Technological developments in mass spectrometry towards molecular structural elucidation of macromolecular assemblies

Please check the document version of this publication:

• A submitted manuscript is the version of the article upon submission and before peer-review. There can be important differences between the submitted version and the official published version of record. People interested in the research are advised to contact the author for the final version of the publication, or visit the DOI to the publisher's website.
• The final author version and the galley proof are versions of the publication after peer review.
• The final published version features the final layout of the paper including the volume, issue and page numbers.

Link to publication

Download date: 26 Apr. 2024

TECHNOLOGICAL DEVELOPMENTS IN MASS SPECTROMETRY TOWARDS MOLECULAR STRUCTURAL ELUCIDATION OF MACROMOLECULAR ASSEMBLIES

ANJUSHA MATHEW

Technological Developments in Mass Spectrometry Towards Molecular Structural Elucidation of Macromolecular Assemblies

Anjusha Mathew

Technological Developments in Mass Spectrometry Towards Molecular Structural Elucidation of Macromolecular Assemblies

DISSERTATION

To obtain the degree of Doctor at Maastricht University,
on the authority of the Rector Magnificus
Prof. dr. Pamela Habibovic
in accordance with the decision of the Board of Deans,
to be defended in public on
Tuesday, 17th of October 2023 at 10:00 hours

by

Anjusha Mathew

Born in Kerala, India, on 16th of October 1994

Promotor:

Prof. dr. Ron M. A. Heeren

Co-promotor:

Dr. Shane R. Ellis, University of Wollongong, Australia

Assessment committee:

Prof. dr. Maarten Honing (Chair)
Prof. dr. M. Eline Kooi
Prof. dr. Anouk Rijs, VU Amsterdam
Dr. Ljiljana Pasa-Tolic, EMSL/PNNL Pacific Northwest National Laboratory, Richland, USA

TABLE OF CONTENTS

1

GENERAL INTRODUCTION

MACROMOLECULAR ASSEMBLIES

Atoms and molecules form the basis of life. They are the building blocks of biomacromolecules, such as proteins and nucleic acids, as well as various small molecular complexes including, carbohydrates and lipids. These biomacromolecules interact with each other and form huge, complex biochemical structures called **macromolecular assemblies (MMAs)** with molecular weight ranging from a few kDa to several MDa.[1-2] The MMAs are defined both by their chemical composition and by their structure. The molecular structure of an MMA enables understanding its biological function as it can determine how the MMA interacts with other molecules and receptors. Hence, the retrieval of higher-order molecular structural features of MMAs is of great interest.
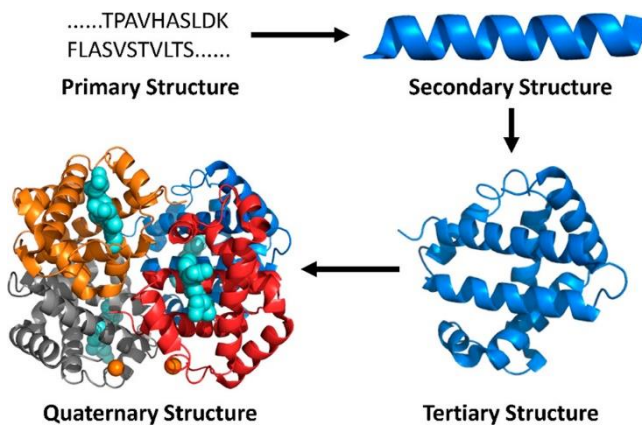
Figure 1. Levels of protein organization exemplified by tetrameric human deoxyhemoglobin (PDB 2HHB). Reprinted from Liu, X. R.; Zhang, M. M.; Gross, M. L., Mass spectrometry-based protein footprinting for higher-order structure analysis: fundamentals and applications. Chemical reviews 2020, 120 (10), 4355-4454, with permission from the American Chemical Society.

As the majority of the previous studies on MMAs targeted protein complexes or the complexes formed by binding of co-factors such as lipids, DNA, RNA, ligands, or metal ions to the proteins, here we exclusively focus on the molecular structural elucidation of **multiproteoform complexes (MPCs)**.[2-9] It is crucial to comprehend the different levels of organization of MPCs to understand how an MPC acquires its final shape or conformation (Figure 1). The amino acid sequence together with various post-translational modifications (PTMs) forms the **primary structure**. The local packing of the polypeptide chain into a-helices and β-sheets due to interactions between the atoms of the backbone results in the **secondary structure**. The overall folding of the entire polypeptide chain into a 3D shape determined by interactions between side chains of amino acids defines its **tertiary structure**. Finally, non-covalently associated polypeptide chain subunits encompass the **quaternary structure**.[10] Each of the primary, secondary, tertiary, and quaternary structural features contribute to the final protein function. Further functional diversification for the MPCs is achieved through the binding of co-

factors. To understand the phenotypic behavior observed in living cells, each protein of interest must therefore be studied in detail at all levels of its molecular complexity.

METHODS TO EXPLORE BIOCHEMICAL STRUCTURE OF MPCs

There are numerous methods available to explore various aspects of MPCs. While some of them retrieve the high-resolution spatial structure of MPCs, others yield information that can be used to deduce amino acid sequence and other molecular characteristics directly linked to structure. The first category includes high-resolution structural biology techniques such as cryogenic-electron microscopy (cryo-EM), nuclear magnetic resonance (NMR), and x-ray crystallography.[11-17] Several structural mass spectrometry (MS)-based tools that interrogate protein structure at the level of peptides, intact proteoforms, or entire MPCs fall within the second category.[18-21]

Non-MS Based Techniques

Proteoform composition, subunit stoichiometry, conformation, topology, and interaction sites, are all examples of higher-order structural features of protein assemblies. The biophysical techniques that fall under the first category are capable of providing snapshots of MPCs at atomic resolution. Although these techniques have significantly advanced the structural biology field, each of them has some limitations. The **x-ray crystallography** requires a large amount of sample and highly dynamic MPCs are difficult to crystalize. **Cryo-EM** provides little molecular detail and is hampered by a low mass limit (> ~40 kDa). **NMR** requires a relatively large amount of purified samples and performs poorly for the identification of large (< ~250 kDa) and highly heterogeneous MPCs. Another drawback of the high-resolution spatial structural approaches is that they require significant structural averaging, which averages out some transient features. In addition to the high-resolution structural approaches, low-resolution biophysical tools such as **small-angle scattering**[22-23] and **circular dichroism**[24-25] can reveal the size, shape, structural transitions, and binding properties of MPCs. Despite the availability of numerous characterization techniques such as those listed above, some classes of MPCs, including intrinsically disordered proteins, membrane proteins, and heterogeneous samples such as heavily glycosylated proteins are still challenging to analyze with any of these approaches.

MS Based Techniques

Investigating Primary Structure

MS-based methods have emerged as a powerful and versatile tool to characterize MPCs in a rapid, sensitive, and selective manner, at all levels of its molecular complexity. The primary structure of a proteoform-amino acid sequence together with PTMs is an essential piece of information. The most basic MS-based method used to characterize the protein sequence is called **shotgun**

proteomics or **bottom-up proteomics**. Here, the protein is first digested, either chemically or enzymatically, producing a mixture of peptides that are then typically analyzed using liquid chromatography-tandem mass spectrometry (LC-MS/MS).[26-27] This approach allows for high throughput and enables de novo investigation of complex protein mixtures. However, it does suffer from sensitivity issues and requires complex computational solutions to interpret the data, often providing the complete sequence only for purified proteins. While the average size of peptides generated by trypsin-the most commonly used protease in bottom-up MS, is below 3 kDa, certain proteases can produce significantly larger peptides. When these proteases are employed, the approach is distinguished from bottom-up proteomics and has been termed "**middle-down proteomics**".[28-29] The main drawback of both bottom-up and middle-down proteomics approaches is the loss of peptide-to-proteoform connectivity, which hampers the direct characterization of proteoform structures and the determination of combinatorial PTM patterns.
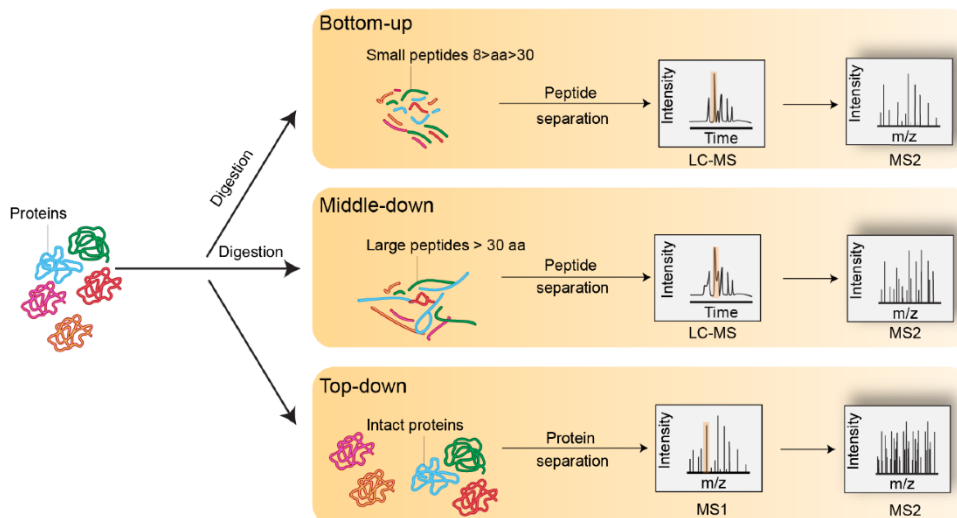
Figure 2. Overview of the bottom-up, middle-down, and top-down proteomics approaches. Reprinted from El Kennani, S.; Crespo, M.; Govin, J.; Pflieger, D., Proteomic analysis of histone variants and their PTMs: strategies and pitfalls. Proteomes 2018, 6 (3), 29, with permission from MDPI.

Top-down proteomics is another tandem MS approach that is capable of providing primary structure details of MPCs.[30-31] This technique allows for the direct identification of intact proteoforms with a molecular weight (MW) up to ~100 kDa and nearly complete characterization of proteoforms with MW below 30 kDa with resolutions up to the residue-level.[32] Like bottom-up and middle-down proteomics approaches, top-down MS also requires a prefractionation step prior to MS analysis, which is accomplished with LC or capillary electrophoresis (less widely used).[33-34] These combinations allow the analysis of samples of medium complexity and often require an additional offline prefractionation. For this

purpose, size-exclusion chromatography or ion-exchange chromatography has been used. Despite the benefits of top-down MS for structural investigations of proteoforms, the technique has significant drawbacks compared to bottom-up MS, including reduced sensitivity and considerably more challenging ionization and MS/MS analysis. An overview of all three approaches is provided in Figure 2.

Investigating Higher-Order Structure

Several MS-based approaches are capable of retrieving secondary, tertiary, and quaternary structural features of MPCs. Although these methods are not able to directly probe the structure of the MPC, they have the potential to characterize very fine structural details in a high-throughput or highly targeted manner. Moreover, the versatility of MS-based approaches allows structural characterization of MPCs that are challenging for the high-resolution biophysical methods. Among the structural MS toolbox (Figure 3), some methods perform surface labeling (eg. **hydrogen-deuterium exchange MS (HDX-MS)**)[35-36] or chemical cross-linking (eg. **chemical cross-linking MS (XL-MS)**)[37-39] in solution and analyze the MPCs in the gas phase. While other methods investigate the gas-phase structure of MPCs by maintaining non-covalent interactions in the gas phase (**native MS (nMS)**)[21, 40] and/or via the collision cross section (CCS) determination in a neutral gas (**ion mobility MS (IM-MS)**).[41-42]

In **HDX**, the labile hydrogen in the protein backbone is exchanged with the deuterium in the solution.[35-36] This method exploits the fact that exposed or disordered regions have a higher rate of H/D exchange compared to tightly folded regions of non-covalently interacting MPCs in solution. Proteins are typically digested into peptides prior to MS analysis in HDX. This method has recently been extended for the structural analysis of MPC in its native state.[43-45]

XL-MS is a technique based on covalently linking specific functional groups in a protein or between proteins. This technique offers information on protein-co-factor interactions as well as analyzes the structures of MPCs, particularly challenging MPCs like membrane proteins and intrinsically disordered proteins. XL-MS employs peptide-centric proteomics approaches and involves a proteolytic digestion step prior to LC-MS analysis.[37-39]

IM-MS is a powerful and rapidly evolving technique in the MS field that enables the separation of MPCs based on a combination of size, charge, and shape under the influence of an electric field, revealing various structural aspects, including the composition and topology. In IM-MS, ions travel through a bath of neutral gas molecules that create resistance, resulting in longer travel times for ions with a larger collisional cross-section. The most commonly used IM approaches include drift-tube ion mobility spectrometry, traveling-wave ion mobility spectrometry, field-asymmetric ion mobility spectrometry, and trapped ion mobility spectrometry.[41-42] Over the last decade, IM-MS has proven valuable for obtaining snapshots of conformational landscapes, which is rather challenging to achieve with other MS-based techniques.[46-47]

nMS exploits the ability of electrospray ionization (ESI)[48] to maintain non-covalent interactions upon ionization, thereby analyzing higher-order structure of the MPCs in the gas phase.[21, 40, 48] A combination of nano-ESI (nESI) source[49-50] and high ionic strength solvents[51-52] is often used in nMS to analyze intact proteoforms as well as large MPCs in their pseudo-native state. Over the past few decades, nMS played a bridging role between MS and structural biology, enabling the inference of composition, stoichiometry, and subunit arrangement.
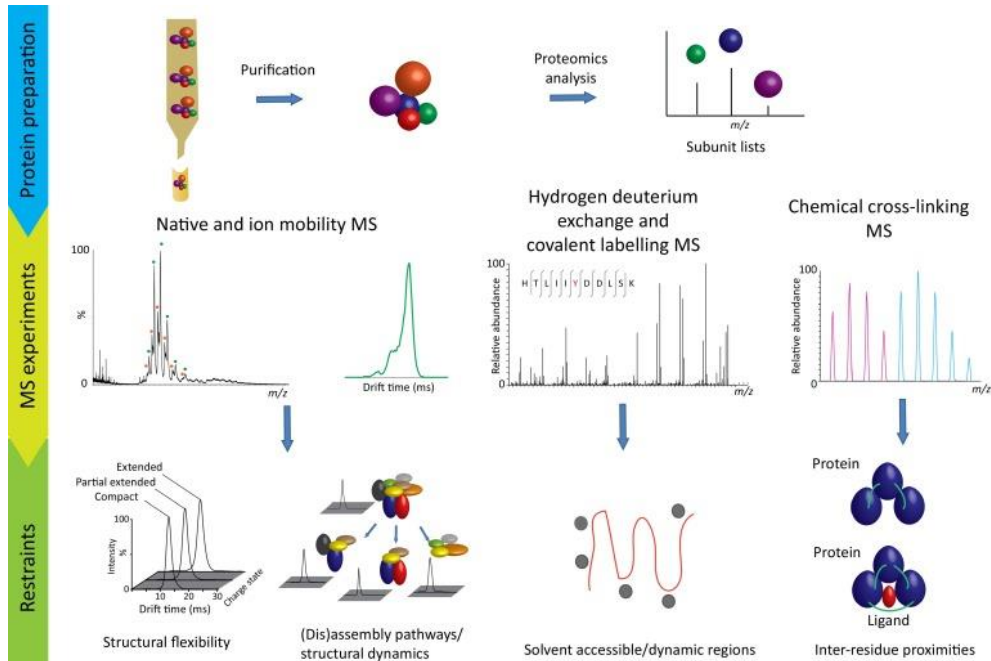
Figure 3. Overview of the MS-based methods for the retrieval of higher-order structural features of MPCs. Reprinted from Ahdash, Z.; Pyle, E.; Politis, A., Hybrid mass spectrometry: towards characterization of protein conformational states. Trends in Biochemical Sciences 2016, 41 (8), 650-653, with permission from Elsevier.

All the above mentioned structural MS tools are often coupled together and/or integrated with various ion fragmentation methods to obtain the most structural features.[53-55] The most used ion fragmentation techniques for MPC characterization are discussed in "Activation and Dissociation of MPCs" section.

IONIZATION OF MPCs

Explosive growth in the utilization of MS for the structural characterization of MPCs occurred after the introduction of "**soft-ionization techniques**"- ESI[48] and matrix-assisted laser desorption/ionization (MALDI)[56] in the late 1980s (Figure 4). These techniques allowed the transfer of intact biomolecules with masses ranging from several daltons to few megadaltons into the gas phase without any fragmentation.[57-59] In **MALDI**, biomolecules immobilized in a crystalline matrix are irradiated with a laser. The matrix absorbs the laser energy inducing desorption of analytes and matrix molecules as well as protons originating from photodissociated matrix molecules from the surface. The ionization mechanism is still not completely understood. However, the most widely accepted theories are that proton transfer occurs either in the solid phase prior to the desorption or in the gas phase from photoionized matrix molecules.
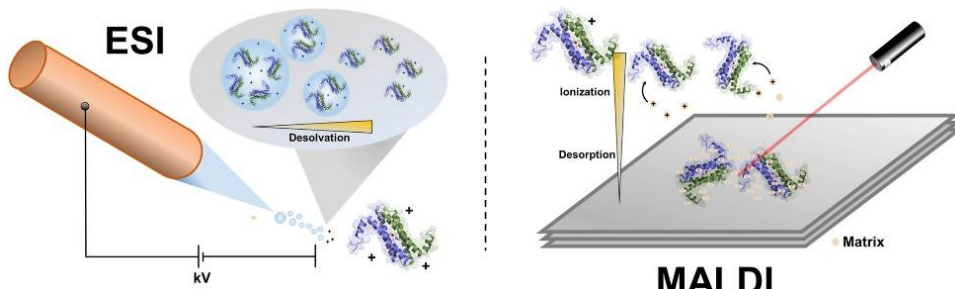
Figure 4. Schematic of two soft-ionization techniques-ESI (left) and MALDI (right). Reprinted from Clarke, D. J., Protein mass spectrometry: structural characterization and clinical diagnosis. Chem 2019, 5 (5), 1019-1022, with permission from Elsevier.

ESI achieves ionization directly from the solution the analytes are dissolved through the creation of a fine spray of highly charged liquid droplets in a strong electric field. In contrast with ESI which produces highly-charged ions, MALDI predominantly results in the formation of singly-charged ionized species. The resulting singly-charged ions in MALDI facilitate mass analysis of complex mixtures, although it largely limits the detection of protein dissociation products, which often depends on the number of charges carried by the ion. ESI makes the analysis of molecules with very high MW possible as the highly-charged species generated by ESI appear at a relatively low mass-to-charge ratio *(m/z)* range, which might not be detected in a singly-charged state at a very high *m/z* value in MALDI. MALDI also prevents direct coupling to pre-fractionation techniques such as LC. Even though MALDI is effective for single protein analysis, it is challenging to maintain MPCs in their native form in the acidic/denaturing matrix. However, the potential of MALDI to produce protein ions directly from tissues or cell samples is remarkable.[60-63] ESI was further improved by the development of **nESI** that utilizes smaller capillary diameters (1-2 µm) and lower flow rates (nL/min) resulting in enhanced sensitivity and reduced sample consumption.[49-50] nESI became the ionization method of choice for LC-MS in tandem MS. Moreover,

because of the delicate ion formation mechanism, nESI preserves most of the non-covalent interactions if the sample is in high-ionic strength solvents (ammonium acetate is most commonly used), enabling nMS of large MPCs.

Several other ionization techniques that have recently demonstrated the ionization of MPCs in their native state from solution/tissue are discussed in "Recent Innovations in MS-based Structural Proteomics of MPCs". In this thesis, nESI (**Chapters 2-3, 5-6**) and MALDI (**Chapter 4**) have been utilized for the ionization of non-covalently bound protein complexes and intact proteins/covalent protein complexes, respectively.

INSTRUMENT MODIFICATIONS FOR MPCs ANALYSIS

The generation of ions is only the first hurdle to be overcome in MS of large native MPCs. For the successful application of MS, it is very important to retain MPC ions in their intact form in various stages of MS, focused and guided towards the mass analyzer. This section briefly discusses the methodological and instrument advancements developed over the past years for the improved transport of high-mass MPC ions.

Increased pressure in the ion guides of the first vacuum stages of the MS improves the transmission of high-mass ions. It is hypothesized that the improved ion transmission at high pressure is due to collisional damping of the radial velocity component of the MPCs, allowing ions to be more efficiently kept on the center axis of the ion guides. Higher ion guide pressures have been obtained in a number of ways: reducing the pumping efficiency by throttling the vacuum lines, leaking additional gas into the source region, or incorporating a flow-restricting valve between the ion guide and pump orifice.[64-71] **Increasing the effective physical length of the ion guide** is an alternate approach for increasing the number of collisions with the surrounding gas, and hence to increase the high m/z transmission while operating at the same pressure.[68]

Lowering the operating frequency of the RF multipoles (while maintaining/increasing the amplitude) not only allows the selection of high m/z ions for MS/MS (MS/MS mode) but also improves the high m/z transmission (MS mode).[65, 68-69, 72-74] In comparison to MS/MS mode, a multipole operating in MS mode can transfer ions up to almost five times their maximum m/z.[65]

The utilization of heavy gases (eg. xenon, argon, sulfur hexafluoride) at high pressure **in the collision cell** improves the MS/MS spectrum of MPCs. Heavier gases increase the ability to focus ions with high m/z values (with relatively low velocity) before and after collisional activation.[54, 70, 75] In addition, the **application of a higher potential across the collision cell** enables the ability to perform higher energy dissociation experiments, resulting in the generation of additional product ions.[70, 74]

One of the challenges MS instruments have encountered for the analysis of high-mass MPCs is the high momentum possessed by the high-mass ions from free-jet expansion during the transfer from atmospheric pressure to high vacuum. This

effect can propel the ions out of the stable trajectories and lead to an overall loss of sensitivity. The implementation of the **in-source ion trapping** within the multipole placed in the first vacuum stages of the MS can be used to reduce the momentum of the high-mass ions and increase the ion transmission efficiency.[74, 76-77] Moreover, the use of **variable voltage gradients when the ions enter the in-source trapping region**, improves desolvation and consequently the mass resolution. The utilization of voltage gradients and in-source trapping provides sufficient energy for MPCs to be fragmented, enabling pseudo-MS[3]. The in-source fragmentation in the front end of the MS is followed by product isolation using the quadrupole and secondary fragmentation. The common fragmentation techniques are conventional collision-induced dissociation (CID)/ higher-energy collisional dissociation (HCD), but custom fragmentation methods such as surface-induced dissociation (SID) and ultraviolet photodissociation (UVPD) are also employed.[78-82]

A **low repetition rate pusher** is often employed in TOF instruments used in the study of large MPCs, considering the prolonged flight period of the slow-moving high m/z ions.[69] Further benefits can be gained from **implementing detectors with enhanced sensitivity** at high m/z values. This is discussed in the "High Mass Detectors" section.

All the studies conducted in this thesis were performed on three MS instruments- a modified Micromass LCT (**Chapters 2-3**), Bruker Ultraflex III (**Chapter 4**), and a Thermo Scientific Q Exactive ultra-high mass range (UHMR) hybrid quadrupole-Orbitrap mass spectrometer integrated with a custom-designed TOF mass analyzer (**Chapters 5-6**), all of which employ one or more of the aforementioned techniques to achieve high mass transmission.

MASS ANALYZERS FOR MPCs

Although a wide range of mass analyzers have been developed and applied to the analysis of biomolecules, only a small subset of these have been employed for the study of large MPCs. Typically, MPCs ionized by ESI under native conditions attain relatively fewer charges than those ionized under denaturing conditions, and intact protein ions generated by MALDI are mostly singly or doubly charged. Thus requires mass analyzers with a wide m/z range and high upper m/z limit for the analysis of MPC ions generated by both ionization techniques. As a result, the field of MPCs analysis largely relied on **TOF** mass analyzers that have a theoretically unlimited m/z range, especially in the early days.[83-86] Development of MS platforms such as **Orbitrap**[76, 87-89] and **Fourier transform ion cyclotron resonance (FT-ICR)**[90-93] mass analyzers with exceptionally high mass accuracy, high mass resolution, broad m/z range, and high upper m/z limit have revolutionized the study of MPCs. A comparison of TOF, FT-ICR, and Orbitrap mass analyzers is given in Table 1.

TOF MS is a technique in which all ions are accelerated with the same kinetic energy per charge as they are all subjected to the same acceleration voltage in

a TOF tube. Then the ions are separated based on their velocity/TOF in the TOF tube. The velocity/TOF of ions is used to derive the m/z values.[83-86] TOF mass analyzers have played a prominent role in the analysis of large MPCs with a record of providing a charge-resolved mass spectrum of 18 MDa capsids from the bacteriophage HK97.[94] TOF-based analysis is inherently sensitive and fast. Furthermore, TOF analyzers enable detection with constant mass resolution over a very broad m/z range. This feature is very distinctive compared to Fourier transform (FT)-based analyzers, where the resolution decreases drastically with increasing m/z. However, TOF analyzers have a substantially lower mass accuracy when compared to FT-based analyzers. Multiple approaches including multipass and multireflection instrumental setups have emerged, which led to significant improvements in mass resolution ($>10^5$ at $m/z = 200$) and mass accuracy ($\sim$5–10 ppm) in TOF systems.[95-97] However, the prolonged flight paths in multireflection and multipass instruments cause reduced sensitivity in the measurement of MPCs, due to the dissociation occurring prior to reaching the detector.

Table 1. Overview of the most commonly used mass analyzers for the studies of MPCs.[89, 98-101]

	TOF	FT-ICR	Orbitrap
Resolving power (@200m/z)	$>10^5$	$>2\times10^6$	$>5\times10^5$
Mass accuracy	<10 ppm	< 0.6 ppm	<3 ppm
Separation principle	Flight time	Angular frequency	Angular frequency
Mass range	The highest	High	High
Speed	Fast	Slow	Moderate
Cost	High	The highest	High
Limitations	Large size, low mass accuracy, moderate mass resolution and limited ion storage	Large size, high cost, difficult to maintain and low dynamic range	Requires ultra-high vacuum

Unlike TOF MS, an **FT-ICR MS** is a trapped ion technique, which determines m/z values by measuring the ion cyclotron frequency in a static magnetic field. It has developed into a wonderful tool for mass measurements that require ultrahigh mass resolution ($>10^6$ at $m/z = 200$) and mass accuracy (sub-ppm to ppb range).[91, 102-103] However, the outstanding resolving power and mass accuracy come at a high cost together with their relatively large size, high maintenance cost, and long measurement times. The high-resolution measurement capability

of FT-ICR instruments makes them well-suited for native top-down MS of MPCs and even provides the isotopically resolved distributions of low-charge dissociation products. However, the inverse dependency of mass resolution with m/z somewhat limits the usability of FT-ICR for the study of large MPCs. The direct dependence of the resolution on the duration of the time-domain signal also hampers high-resolution detection of MPCs. Their ion signals are often susceptible to decay due to magnetic field imperfections, collisions with background gas molecules, and ion-ion interactions. Because of the required ultrahigh-vacuum operation, FT-ICR instruments are less compatible with conventional collision-based ion fragmentation methods. Therefore, alternative photon-based and electron-based fragmentation techniques have been implemented in FT-ICR instruments, which were shown to have benefits over CID in the structural investigation of MPCs.[104-105]

Despite being the youngest among the mass analyzers used for the investigation of MPCs, the **Orbitrap** has experienced substantial advancements over the last decade and is today one of the most prominent technologies for the analysis of large and heterogeneous MPCs. Many characteristics of Orbitrap mass analyzers were derived from earlier developed mass analyzing techniques, such as pulsed ion injection from the orthogonal acceleration (O)-TOF, trapping principles from radiofrequency ion trap, and signal detection and processing from FT-ICR.[76, 87-89] The Orbitrap mass analyzer does not require superconducting magnets and benefits from significantly smaller size compared to FT-ICR instruments while both techniques utilize angular frequency measurement for m/z derivation. In addition, the Orbitrap experiences a less steep drop in resolution with increasing m/z compared to FT-ICR. Similar to an FT-ICR mass analyzer, an Orbitrap also requires longer time-domain signals to better resolve the species of interest that comes at the expense of increasing ion decay, which ultimately limits the mass resolution. The Orbitrap instruments including QExactive plus hybrid Quadrupole-Orbitrap MS, Exactive plus extended mass range (EMR) MS and QExactive UHMR hybrid quadrupole-Orbitrap MS have proven to be indispensable for the high-resolution native MS of large MPCs.[72, 74, 78, 106-108] The implementation of in-source trapping in the front-end of QExactive UHMR MS allows MS[3] analysis of large MPCs. The newest tribrid platform-Orbitrap Eclipse, is capable of addressing difficult analytical challenges through pseudo-MS[4].[81]

All the instruments used in the studies conducted here utilizes TOF mass analyzers, with different configurations-orthogonal reflectron TOF (**Chapters 2-3**), axial TOF (**Chapter 4**), and orthogonal TOF (custom designed) (**Chapters 5-6**). The custom-designed orthogonal TOF mass analyzer and associated high mass transmission ion optics is coupled to a QExactive UHMR hybrid quadrupole-Orbitrap MS (**Chapters 5-6**).

HIGH MASS DETECTORS

This section exclusively focuses on the particle detectors employed in TOF MS as the detection in Orbitrap and FT-ICR is accomplished through the measurement of image current. **Microchannel plates (MCPs)** are the conventional detectors used in TOF MS in combination with a time-to-digital converter (TDC) or analog-to-digital converter (ADC), because of their higher gain, fast response, and large active area. MCP consists of a two-dimensional array of several millions of very small diameter, conductive glass channels, which are fused together and sliced as a thin plate.[109-112] Each channel works as an independent secondary electron multiplier (SEM). When an ion strikes the MCP channel wall, it excites secondary electrons. The secondary electrons are then drawn down the channel by the electric field, where they strike the channel wall and generate more electrons. This is a cascade process that continues through each channel, which eventually results in an avalanche of electrons at the end of the channel. A single MCP typically has a gain of 10^3-10^4, depending on the applied voltage. Two MCPs can be used in a chevron stack configuration to produce an electron gain>10^6. As the detection mechanism in MCP relies on translating particle momentum into electron count, it suffers from 'high-mass roll-off', which limits the detection of high m/z ions produced from MPCs. In MCP, the secondary electron avalanche is proportional to the velocity of the incoming particle. As all particles in TOF MS are given the same kinetic energy per charge ratio, high m/z ions impinge on the detector with a relatively low velocity/momentum. Hence, they deposit insufficient energy to create an electron shower and might remain undetected.

CovalX high mass (HM) detectors and cryogenic detectors are explored as an alternative for MCP detectors in the high-mass low-velocity regime.[111, 113-115] The **Covalx HM detection system** (CovalX, Zurich, Switzerland) uses conversion dynode technology[116-117], which allowed the detection of macromolecules up to an m/z of 1.2 MDa at nano-molar sensitivity.[114] The conversion dynode transforms the impact of the initial slow-moving MPC ions into smaller, faster secondary ions that are then accelerated towards an SEM. Because of the higher velocity of secondary ions, they are detected with more sensitivity than the initial MPC ions would be.

Cryogenic detectors involve a detection mechanism at low, sub-Kelvin, temperatures. Cryogenic detection systems have a mass-independent response, which makes them well-suited for the detection of slow-moving large MPCs with near-unity efficiency. In addition to the TOF, they also measure the energy that the impinging ion deposits on the detector which is directly proportional to the charge state of the ion. Therefore, the energy measurement can be used to determine the charge state of the ion. This is particularly interesting in TOF MS, where the TOF is proportional to the m/z of the ion. Hence, the singly charged monomer and doubly charged dimer, etc., which all have the same m/z values cannot be distinguished solely by their TOF. Therefore, the energy measurement can be used to determine the charge state of the ion and to distinguish oligomers

that appear at the same *m/z*. There are three types of cryogenic detectors: superconducting tunnel junctions (STJ)[58, 118-120], calorimeters and bolometers[121-123], and superconducting stripline detectors (SSLD).[124-126] Although the detection efficiency of cryogenic detectors is greatly improved for high mass compared to MCPs, there are multiple factors that limit the deployment of them in MS. They need to be kept at extremely low temperature (<4 K), have a small effective area and much slower (high-rise time) than MCPs. Despite the few successful studies of singly/doubly charged high *m/z* ions in MALDI TOF MS, highly charged native MPC ions generated by nESI are still challenging to measure with cryogenic detectors. Among the three types of cryogenic detectors, only calorimeters and STJs are capable of charge detection. Poor resolution is another drawback of this method. Despite the fact that cryogenic detectors and CovalX HM detectors are proven more sensitive at high mass measurements, MCP continues to be the most commonly used detector in TOF MS.

Position-Sensitive Detectors

MCPs are generally coupled to charge-collecting anodes, and then the signal is digitized using ADCs and TDCs, yielding only the TOF data, which is used to obtain the mass spectrum.[83, 112, 127] When MCP is coupled with position-sensitive detectors, it can introduce an additional dimension of experimental information to a mass spectrometric measurement. Position-sensitive detection systems include electro-optical imaging detectors, i.e. MCPs in combination with a photon detector, and charge division detectors such as MCPs in combination with a resistive anode, delay-line detector (DLD), a shaped or a cross-strip anode (XSA), or a hybrid active pixel detector (HAPS).[111]

In **electro-optical imaging detectors**, the electron (generated by the impact of ion event at the front MCP plate) to photon conversion is typically performed in a phosphor screen or a scintillation crystal. The photons are then collected by a photo-sensitive detector such as a photo-plate, an array of photo-diodes, a Vidicon camera system, or a charge-coupled device (CCD) camera.[128] The electro-optical imaging detectors explored in bimolecular MS were mostly MCP-phosphor screen-CCD camera assemblies. However, it suffered from the limitation that it is unable to link the ion TOF and the spatial distribution. This can be resolved to some extent by the employment of a pair of fast-switching electrodes called electrostatic blanker that enables the selection of particular *m/z* species.

In **charge division detectors**, the electron shower from the MCP is collected by an anode array, which distributes the charge among several of its elements. Even though some of the charge division detectors (eg. resistive anodes, shaped anodes) are not capable of providing *m/z* resolved images, DLDs can measure both the ion arrival position and time precisely and thereby lifts the limitations of *m/z* selected imaging of MCP-phosphor screen-CCD camera assemblies.[129-131] However, DLDs can only register a few ion events that simultaneously arrive at the detector. This renders it unsuitable for high-count rate experiments.[132]
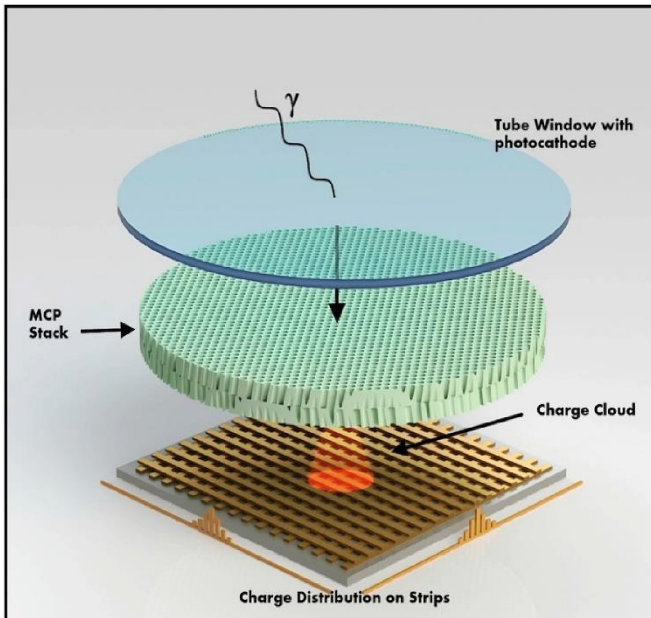
Figure 5. Schematic representation of the particle detection mechanism in MCP-position sensitive detection assembly. A number of electrons are ejected from the front MCP plate upon the impact of the particles (ions/photons/electrons/alphas/neutrons). These electrons generate more electrons that are accelerated to the back MCP plate. The position-sensitive detector (for example TPX) positioned behind the back MCP measures the arrival time, arrival position, and/or energy (TOT) of the emitted electron pulses that spread over multiple pixels in TPX. Reprinted from Siegmund, O.; McPhate, J.; Vallerga, J.; Tremsin, A.; Frisch, H.; Elam, J.; Mane, A.; Wagner, R., Large area event counting detectors with high spatial and temporal resolution. Journal of Instrumentation 2014, 9 (04), C04002, with permission from IOP Publishing.

Hybrid active pixel detectors were able to overcome most of the limitations of the previous imaging detectors. Hybrid active pixel detectors are pixelated image sensors, which are typically composed of an application-specific integrated circuit (ASIC) and a semiconductor substrate layer.[133-138] Each ASIC pixel is connected to a cell of the semiconductor layer. Each pixel has its own charge-to-voltage converter, preamplifier, discriminators, noise correction unit, or other digital signal processing features. The hybrid active pixel detectors from **Medipix (MPX)/Timepix (TPX) detector family** (see Table 2) were chosen for the studies conducted here as they outperform conventional technology easily in the detector dynamic range, signal-to-noise ratio, multiplexed detection, measurement mass range, detector homogeneity, and single-ion sensitivity.[134-135, 137-138] The simultaneous acquisition of arrival time and arrival coordinates corresponding to each ion event in TPX detectors remove the requirement of an electrostatic blanker for m/z selection as in CCD camera-based detectors. Unlike in DLDs, TPX facilitates parallel detection of multiple molecular species. MPX/TPX family detectors have already been implemented in bimolecular MS in combination with MCP amplifiers (see Figure 5) for the detection of relatively

smaller bimolecular assemblies.[139-152] MCP-TPX detection systems were previously coupled to TOF mass spectrometers equipped with micro-ESI, MALDI, or secondary ion MS (SIMS) sources, where the *m/z*-resolved image acquired by the TPX was utilized to obtain insights into the ion transport properties within the MS instrument, as well as to improve the spatial resolution and throughput of MS imaging via stigmatic ion imaging.

Table 2. The summary of the main features of the chips in the Timepix family.[135, 137-138]

	Timepix	Timepix3	Timepix4
Technology	250 nm CMOS	130 nm CMOS	65 nm CMOS
Year	2005	2014	2019
Pixel size (μm)	55	55	55
Pixel array size	256 x 256	256 x 256	448 x 512
TOT/TOA	TOA or TOT	TOA and TOT	TOA and TOT
TOA resolution	10 ns	1.5625 ns	195.3125 ps
TOT resolution	10 ns	25 ns	1.5625 ns
Readout	Frame-based	Data-driven or frame-based	Data-driven or frame-based
Number of sides for tiling	3	3	4

All the instruments used in the studies conducted here utilize TOF mass analyzers equipped with time- and position-sensitive detectors from TPX family coupled with MCP amplifiers. A TPX[135] quad detector with moderate time resolution (>10 ns) and single hit capabilities, coupled directly to a dual MCP stack, floating at high voltage/grounded was employed on LCT MS (**Chapters 2-3**) and QExactive UHMR Orbitrap/TOF MS as axial imaging detector (**Chapter 5)**, respectively. The successor of the TPX, TPX3[137], which offers a time resolution of 1.5625 ns, allows simultaneous measurement of TOF and time-over-threshold values, and operates under data-driven readout mode was coupled to Ultraflex III MS (**Chapter 4**) and QExactive UHMR Orbitrap/TOF MS as orthogonal imaging detector (**Chapters 5-6**). Unlike the MCP-bare TPX quad assemblies, a TPX3CAM containing a silicon-coated TPX3 chip was coupled to a dual MCP stack through a phosphor screen in the TPX3 detection assembly.

ACTIVATION AND DISSOCIATION OF MPCs

The ion activation methods are employed in the studies of non-covalently bound protein complexes to (i) enhance desolvation and to improve mass resolving power[75, 153-154], (ii) **eject protein subunits from non-covalent protein complexes** to yield higher-order structural information[155-157], and (iii) **fragment polypeptide chains of individual subunits to determine amino acid sequences** to obtain primary structural details. In such experiments, the *m/z* selected precursor MPC ions are subjected to a particular type of ion activation with the intention of fragmenting them. Ion activation techniques can be broadly categorized into collision-based methods, irradiation-based methods, and methods based on ion-ion interactions (see Figure 6).
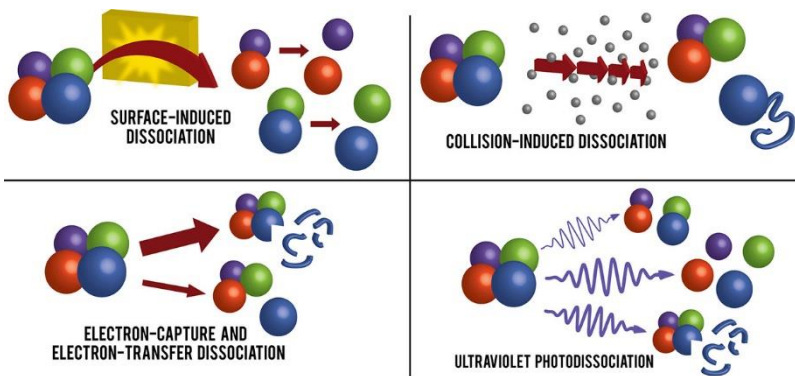
Figure 6. Cartoon illustration of various dissociation methods used in the study of MPCs exemplified by the dissociation of a non-covalent tetramer. Small blue fragments represent the covalent cleavage of an individual protein subunit. Reprinted from Stiving, A. Q.; VanAernum, Z. L.; Busch, F.; Harvey, S. R.; Sarni, S. H.; Wysocki, V. H., Surface-induced dissociation: an effective method for characterization of protein quaternary structure. Analytical Chemistry 2018, 91 (1), 190-209, with permission from the American Chemical Society.

Collisions with inert gas molecules (CID/HCD) is the most commonly used ion activation method in MS, even for the characterization of native MPCs. Although CID/HCD provides excellent fragmentation efficiency, this approach is mainly hampered by slow and stepwise energy deposition that predominantly dissociates the most labile bonds, often leading to small neutral losses and other less informative dissociation products. Infrared multiphoton dissociation (IRMPD, λ=10.6 μm) that falls under the irradiation-based ion activation category, leads to the gradual increase of the internal energy of the subjected MPC ions through the absorption of low-energy IR photons, and hence resulting in low-energy fragmentation pathways similar to CID/HCD.[158-159] Alternative ion activation methods have been developed over the years that provide better access to high-energy dissociation pathways. These include methods based on collisions with a surface (SID)[160-161], interactions with electrons (electron capture dissociation (ECD) and electron transfer dissociation (ETD))[162-163], and absorption of high-energy photons (UVPD, λ=193 nm[159, 164]). While the slow, stepwise, and low-

energy collisional activation works well for desolvating MPC ions and removing adducts (i), faster and more energetic photon- or electron-based fragmentation methods are more suitable to obtain information-rich fragments (particularly UVPD) from subunits of native protein complexes (iii). Both low-energy and high-energy fragmentation approaches can be used to provide complementary structural information by the ejection of subunits from MPCs (ii). However, we have chosen **UVPD** as the fragmentation method for the studies presented in **Chapters 5-6** due to its (i) rapid high-energy deposition, (ii) ability to characterize MPC structure at different levels of its molecular complexity, and most importantly, (iii) ability to preserve the spatial orientation of the subunits post-fragmentation.

UVPD

UVPD utilizes the natural absorbing chromophores present in the backbone of proteins and peptides as well as aromatic amino acids to absorb high-energy photons emitted through nanosecond-scale laser pulses.[159, 164] UVPD (λ=157-351 nm) was initially exploited in the applications of bottom-up and top-down MS.[159, 164-166] Its applicability has been recently extended to the activation and dissociation native MPCs. UVPD is able to deposit substantial amounts of energy (6.4 eV) on a time scale in nanoseconds using 193 nm photons. This provides access to higher-energy dissociation pathways, such as the formation of a, c, x, and z ions in addition to the low-energy pathway of b and y ions, yielding sufficient sequence coverage for the identification of individual subunits.[167] Recent studies demonstrate that high-energy UV laser pulses can eject subunits from non-covalent protein complexes with more symmetrical charge partitioning (like in SID) compared to techniques like HCD, i.e, each subunit is ejected carrying nearly symmetrical number of charges relative to the charge of the entire MPC assembly.[168-169] In HCD, a single subunit of a given MPC undergoes charge rearrangement because of the exposure of the new protonation sites on the unfolding subunit chain. This is followed by the ejection of the most unfolded highly charged subunit, and appears at the low *m/z* range in the mass spectrum. The charge-reduced residual precursor missing the single ejected subunit appears at high *m/z* range. Symmetric charge partitioning behavior in UVPD compared to HCD suggests that the structure of the MPCs undergoes fewer changes during the UVPD process. The efficiency of UVPD also exhibits little dependence on the precursor charge when comparing to CID, making this approach well-suited to study large native protein assemblies that are detected in multiple charge states.[170] Recently, the Heck group has extended UVPD to the MDa mass range by studying 1 MDa AaLS virus-like particles.[80]

RECENT INNOVATIONS IN MS–BASED STRUCTURAL ANALYSIS OF MPCs

1

Single-Molecule Mass Spectrometry

Numerous methods have been exploited over the last years to overcome the limitations of conventional MS for the effective measurements of native MPCs. Despite the fact that more and more MS instruments are being developed with higher mass resolution and accuracy, the high charge states and heterogeneity of the native MPC samples make the analysis extremely difficult. The **single-particle methods** might be able to resolve this challenge posed by mass heterogeneity. In such approaches, individual ions are measured rather than using ensemble ion detection.[115] Single-ion signals can be statistically post-processed, enabling the data to be filtered to remove aberrant ion signals, thereby improving the signal-to-noise ratio, mass resolution, and mass accuracy. There have been many new methods for the measurement of single ions, but they all have some limitations. Typically the deciding factors are the accuracy and the time. The small size of some of the detectors can also cause difficulties. Some of the single-particle methods involve simultaneous measurement of m/z and charge, including **direct charge detection in FT-ICR**, **charge detection mass spectrometry (CDMS)**, and **quadrupole ion trap (QIT) with a charge-detecting plate**. Of these three, CDMS is the most explored single-molecule MS technique.

In **CDMS**, the ions pass through a conducting cylinder, and a charge-sensitive amplifier detects the charge that is induced on the cylinder. If the cylinder is long enough (length to diameter ratio>4), the induced charge equals the charge on the ion.[171-173] In single-pass CDMS, the first developed and simplest type, ions go through a tube, which is equipped with a few charge detectors that are connected in series. The m/z and the charge of the ion are determined based on the TOF and amplitude of the signal collected at the detector, respectively.[174-176] In linear array CDMS, multiple detector tubes are aligned. The multiple measurements of the ion charge reduce the root mean square (RMS) uncertainty in the charge by the square root of the number of measurements.[177-180] The detector tube can be embedded in an electrostatic ion trap to further improve the charge measurement. This allows the measurement of hundreds or thousands times of a single ion's charge as the ion oscillates back and forth through the tube. This version is called ion trap CDMS.[181-183] In this case, the m/z is determined from the ion's oscillation frequency. The most accurate type of CDMS ion trap CDMS, although it is the slowest. Single-pass CDMS is the least accurate but the fastest, while linear array CDMS is in the middle. Ion trap CDMS's eye-catching performance has recently been demonstrated in several exciting studies, including characterizing highly complicated mixtures of proteoforms and their complexes, ribosomes, and genome-packed adeno-associated viruses with much higher resolution and accuracy, and charge state information (Figure 7).[184-188]
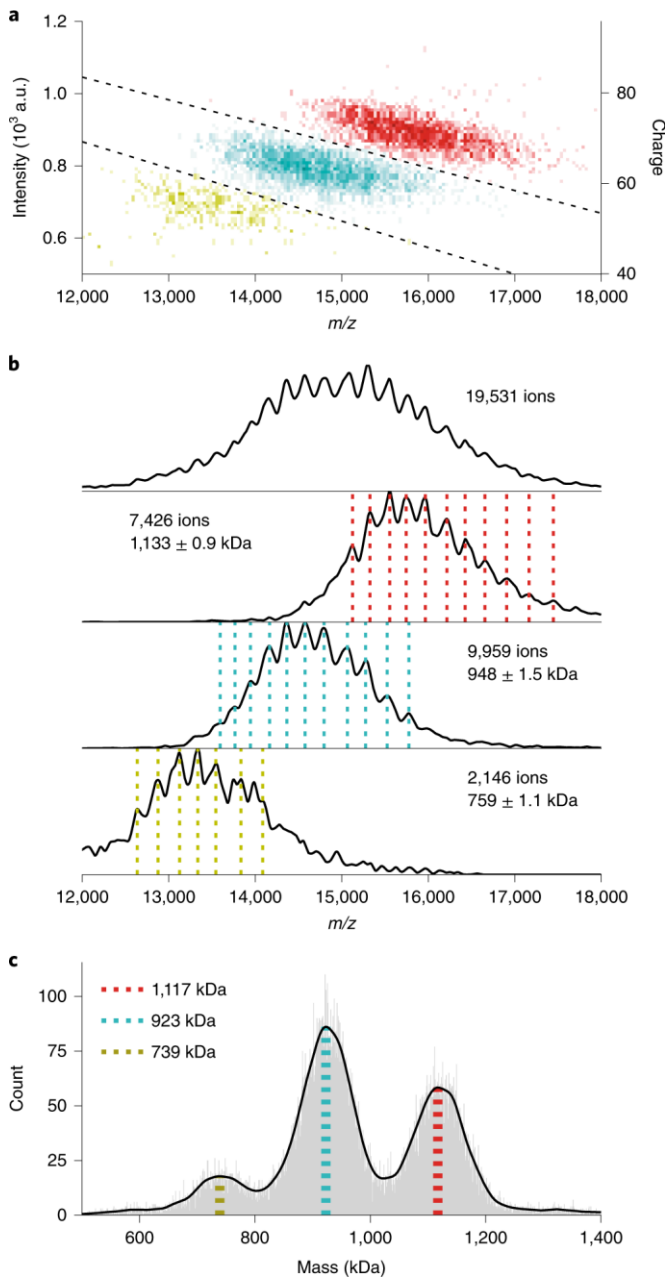
Figure 7. (a) Single-molecule CDMS of IgM oligomers (tetramer-green, pentamer-cyan, and hexamer-red). (b) *m/z* histogram showing the extensively overlapping charge state distributions for the three IgM oligomeric states (top). Below are shown the filtered subsets used for the charge state assignments. (c) Mass histograms, calculated from ion intensities, revealing the distribution and masses of the three co-occurring species. Reprinted from Wörner, T. P.; Snijder, J.; Bennett, A.; Agbandje-McKenna, M.; Makarov, A. A.; Heck, A. J., Resolving heterogeneous macromolecular assemblies by Orbitrap-based single-particle charge detection mass spectrometry. Nature methods 2020, 17 (4), 395-398, with permission from Springer Nature.

Although TOF MS with **cryogenic detectors** can measure *m*/*z* and charge simultaneously at the single molecule level, the technique currently does not perform well for highly charged MPC ions. For further information about the cryogenic detectors, see the section on "High Mass Detectors".[58, 120-121]

Other techniques involve charge stepping, where the *m*/*z* of a single ion is measured for several different values of charge to deduce mass. **Charge stepping** can be performed in an **FT-ICR**[189-193] or in a **QIT with optical detection**.[194-200] The charge stepping-based approach can measure mass very accurately, but it usually takes many measurement cycles and remeasurements. The ion needs to be collisionally focused down in between the measurements as well. These techniques are better suited for analyzing the ion characteristics rather than measuring the mass distributions of heterogeneous samples due to the time-consuming nature of the measurements.

Mass can be measured independently of charge in **nanoelectromechanical systems (NEMS)**, where the resonant frequency of the device changes as mass accretes on it.[201-209] These types of resonators allow the measurement of analytes with very high masses. This method is capable of real-time measurements as the detector measures the accreting mass of the molecule of interest. A limitation of these sensors is their small effective area that reduces the probability of molecules striking the resonator. The measurements performed in NEMS depend not only on the mass of the particles but also on the properties as well. Advancements in data analysis and measurements for multiple modes are still required to account for those properties.

Other Ionization Approaches for the Analysis of Intact MPCs

Currently, ESI is the dominant ionization approach in MPCs analysis, as it is capable of maintaining non-covalent interactions within the MPCs. However, recent studies have demonstrated that the dissociation of non-covalent bonds during the MALDI process can be prevented by the usage of appropriate matrix and chemical cross-linking.[210] The potential of **MALDI** combined with top-down MS for proteomics studies has also been explored over the past years.[211-214]

Recently, the ability to ionize non-covalent protein complexes using **laser ablation electrospray ionization (LAESI)** and **laser-induced liquid bead ion desorption (LILBID)** was demonstrated.[215-216] In addition, we want to draw the reader's attention to MS imaging (MSI) techniques based on MALDI or other ion sources, such as **liquid extraction surface analysis (LESA)**, **desorption electrospray ionization (DESI)** and **nanoDESI** (Figure 8), which have grown to be crucial for the in-situ analysis of intact proteins and protein complexes from tissues.[217-224]
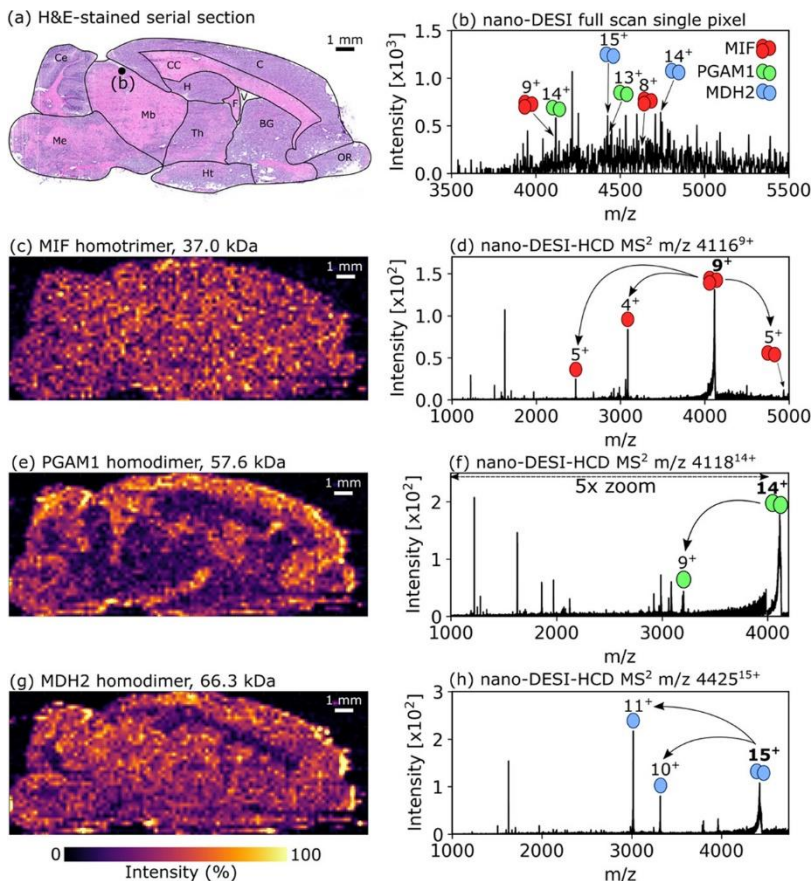
Figure 8. MSI of non-covalent protein complexes from rat brain using nanoDESI. (a) Optical image of H&E-stained tissue section. (b) Nano-DESI full-scan mass spectrum representing the pixel marked "(b)" in Figure 8a. Ion images and HCD MS^2 spectra indicating subunit dissociation for protein complexes Macrophage inhibitory factor homotrimer (c, d), Phosphoglycerate mutase 1 homodimer (e, f) and MDH2 homodimer (g,h) respectively. Ion images were produced with a pixel size of 200 µm × 200 µm (0.04 mm^2). Reprinted from Griffiths, R. L.; Sisley, E. K.; Lopez-Clavijo, A. F.; Simmonds, A. L.; Styles, I. B.; Cooper, H. J., Native mass spectrometry imaging of intact proteins and protein complexes in thin tissue sections. International Journal of Mass Spectrometry 2019, 437, 23-29, with permission from the American Chemical Society.

Bringing Multiple Fragmentation Methods to a Single Platform

The **Omnitrap** (Fasmatech, Athens, Greece) is a unique segmented linear ion trap that incorporates an entire range of ion activation methods, such as CID, ECD/ETD, UVPD, and other gas phase reactions, and enables multidimensional multiple-stage tandem mass spectrometry (Figure 9).[225] The complementary information offered by different ion activation methods allows in-depth top-down MS^n characterization of intact proteins/MPCs.
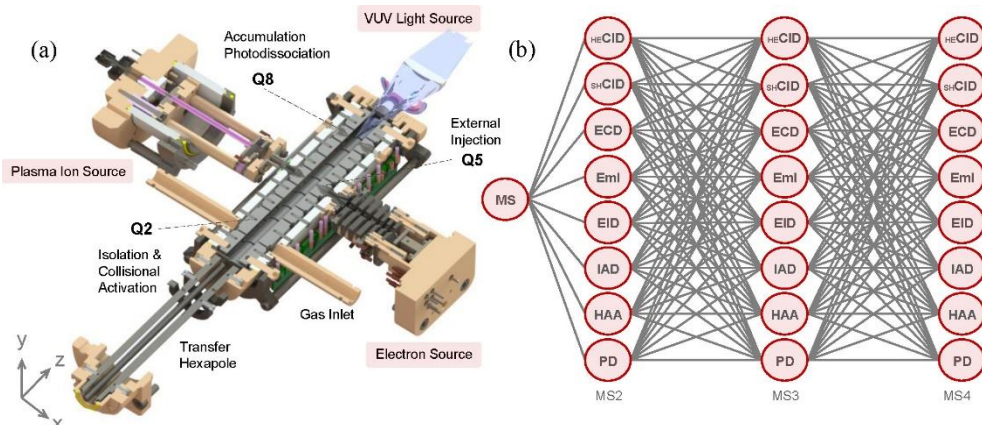
Figure 9. (a) Cross-sectional view of the Omnitrap platform highlighting the trapping regions for processing ions, external sources for injection of ions and electrons, inlets for pulsed gas injection, and the hexapole guide for transferring ions to and from an external source. (b) Ion activation network for multidimensional multiple-stage tandem MS workflows available in the Omnitrap platform (EmI-electron meta-ionization, EID-electron induced dissociation, IAD-ion activated dissociation, HAA-hydrogen atom attachment, and PD-photodissociation). Reprinted from Papanastasiou, D.; Kounadis, D.; Lekkas, A.; Orfanopoulos, I.; Mpozatzidis, A.; Smyrnakis, A.; Panagiotopoulos, E.; Kosmopoulou, M.; Reinhardt-Szyba, M.; Fort, K.; Makarov, A.; Zubarev, R. A., The omnitrap platform: a versatile segmented linear ion trap for multidimensional multiple-stage tandem mass spectrometry. Journal of the American Society for Mass Spectrometry 2022, 33 (10), 1990-2007, with permission from the American Chemical Society.

THESIS OVERVIEW

The technical instrumentation development conducted throughout this thesis enables the structural elucidation of MPCs at different molecular complexity levels. We brought together the aspects from soft-ionization techniques (nESI and MALDI), axial/orthogonal reflectron TOF and high-resolution Orbitrap MS, top-down proteomics (UVPD), and *m/z*-resolved imaging (TPX and TPX3 ASIC based detection assemblies) for resolving the molecular structure of MMAs in the gas phase (Figure 10).

Chapter 2 illustrates the potential of position- and time-sensitive MCP-TPX quad detection assembly to image high mass (~800 kDa) nESI generated non-covalent protein complexes in an orthogonal reflectron TOF (LCT) MS with single ion sensitivity in an *m/z* resolved manner. In addition, the time-resolved imaging capability of the TPX detection assembly was utilized for the identification of an unusual signal that appears at the mass spectrum of high-mass species, which was also observed in earlier studies conducted on modified quadrupole-TOF (q-TOF) I, q-TOF II, and LCT mass spectrometers (Micromass, Manchester, UK) under certain ion optical conditions but could not explained solely by the TOF spectrum generated by conventional mass spectrometers.

In **Chapter 3,** the single ion sensitivity of the MCP-TPX quad assembly demonstrated in Chapter 2 has been utilized for the characterization of MCP

response for the detection of multiply-charged native high-mass single ions. The pixel cluster size on the TPX corresponds to individual ion events from samples that encompass a wide and high mass range of 195 to 800,000 Da was analyzed to develop a better understanding of ion properties and ion optical parameters on the MCP performance in the high-mass low-velocity regime.

Chapter 4 explores the potential of an MCP-phosphor screen (P47)-TPX3CAM imaging assembly that contains a Si-coated TPX3 chip, the successor of the TPX (used for the studies in Chapters 2 and 3) for the enhanced spatially and temporally resolved detection of intact proteins of m/z approaching $1x10^6$ Da, generated by MALDI on an axial TOF MS. This chapter also discusses on the additional features in TPX3 compared to TPX chip that improves the sensitivity of the high m/z detection in the presence of low m/z ions at high pixel occupancies. In addition, the combination of deflectors and space- and time- resolved detection capabilities of the TPX3 detection assembly has been utilized for the detection of metastable fragments generated from the precursor intact protein ions formed at different locations along the TOF tube.

Chapter 5 focuses on the design, development, and evaluation of an innovative Orbitrap/TOF system integrated with UVPD and TPX detection assemblies – MCP-TPX quad (used for studies in Chapters 2 & 3) and MCP-P47-TPX3CAM (used for studies in Chapter 4) for the extensive structural and molecular level characterization of the MPCs. This new instrument enables the high-mass resolution measurement and m/z-resolved imaging of the UVPD or HCD generated fragments from the native precursor MPC ions using the high-resolution Orbitrap analyzer, axial TPX quad detection assembly, and orthogonal TOF analyzer-TPX3 detection assembly.
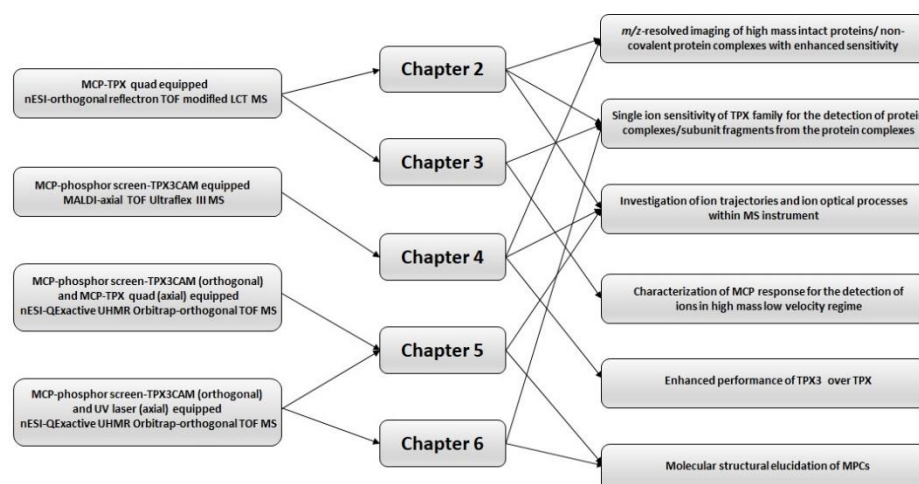
Figure 10. Thesis overview

The custom-developed Orbitrap/TOF system with integrated UVPD and TPX3CAM discussed in Chapter 5 has been employed for the *m/z*-resolved imaging of the UVPD generated subunits from single MPC precursor ions in **Chapter 6**. The relative positions of fragments from a single ion on the TPX3 image were utilized to understand the kinematics of the MPC fragmentation process and to retrieve the 3D geometry and higher-order structural features of the MPCs.

ION IMAGING OF NATIVE PROTEIN COMPLEXES USING ORTHOGONAL TIME-OF-FLIGHT MASS SPECTROMETRY AND A TIMEPIX DETECTOR

Anjusha Mathew[1], Ronald Buijs[2], Gert B. Eijkel[1], Frans Giskes[1], Andrey Dyachenko[3,4], Jerre van der Horst[5], Dimitry Byelov[6], Dirk-Jan Spaanderman[2], Albert J. R. Heck[3,4], Tiffany Porta Siegel[1], Shane R. Ellis[1,7], and Ron M. A. Heeren[1]

[1] Maastricht MultiModal Molecular Imaging (M4i) Institute, Division of Imaging Mass Spectrometry (IMS), Maastricht University, 6229 ER Maastricht, The Netherlands

[2] FOM Institute for Atomic and Molecular Physics (AMOLF), Science Park 104, 1098 XG Amsterdam, The Netherlands

[3] Biomolecular Mass Spectrometry and Proteomics, Bijvoet Centre for Biomolecular Research and Utrecht Institute for Pharmaceutical Sciences, Utrecht University, Padualaan 8, 3584 CH Utrecht, The Netherlands

[4] Netherlands Proteomics Center, Padualaan 8, 3584 CH Utrecht, The Netherlands

[5] MS Vision, Televisieweg 40, 1322 AM Almere, The Netherlands

[6] Amsterdam Scientific Instruments (ASI), Science Park 106, 1098 XG Amsterdam, The Netherlands

[7] Molecular Horizons and School of Chemistry and Molecular Bioscience, University of Wollongong, NSW 2522, Wollongong, Australia
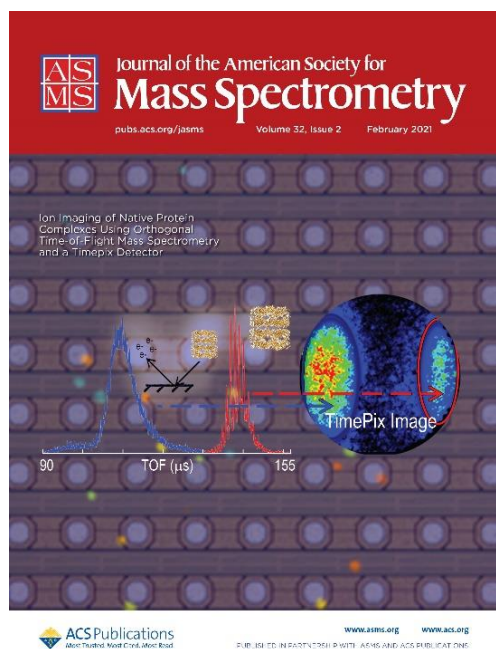
Showcasing *"Ion Imaging of Native Protein Complexes Using Orthogonal Time-of-Flight Mass Spectrometry and a Timepix Detector"*

Journal of the American Society for Mass Spectrometry
February 2021, Volume 32, Issue 2

About the cover: A false colored microscope image of the Timepix detector surface with an image of individual native ion hits superimposed. The inset shows the spatial distinction between GroEL ions and secondary electrons generated by surface collisions inside an O-TOF MS.

2

ABSTRACT

Native mass spectrometry (native MS) has emerged as a powerful technique to study the structure and stoichiometry of large protein complexes. Traditionally native MS has been performed on modified time-of-flight (TOF) systems combined with detectors that do not provide information on the arrival coordinates of each ion at the detector. In this study, we describe the implementation of a Timepix (TPX) pixelated detector on a modified orthogonal TOF (O-TOF) mass spectrometer for the analysis and imaging of native protein complexes. In this unique experimental setup, we have used the impact positions of the ions at the detector to visualize the effects of various ion-optical parameters on the flight path of ions. We also demonstrate the ability to unambiguously detect and image individual ion events, providing the first report of single-ion imaging of protein complexes in native MS. Furthermore, the simultaneous space- and time-sensitive nature of the TPX detector was critical in the identification of the origin of an unexpected TOF signal. A signal that could easily be mistaken as a fragment of the protein complex was explicitly identified as a secondary electron signal arising from ion-surface collisions inside the TOF housing. This work significantly extends the mass range previously detected with the TPX and exemplifies the value of simultaneous space- and time-resolved detection in the study of ion optical processes and ion trajectories in TOF mass spectrometers.
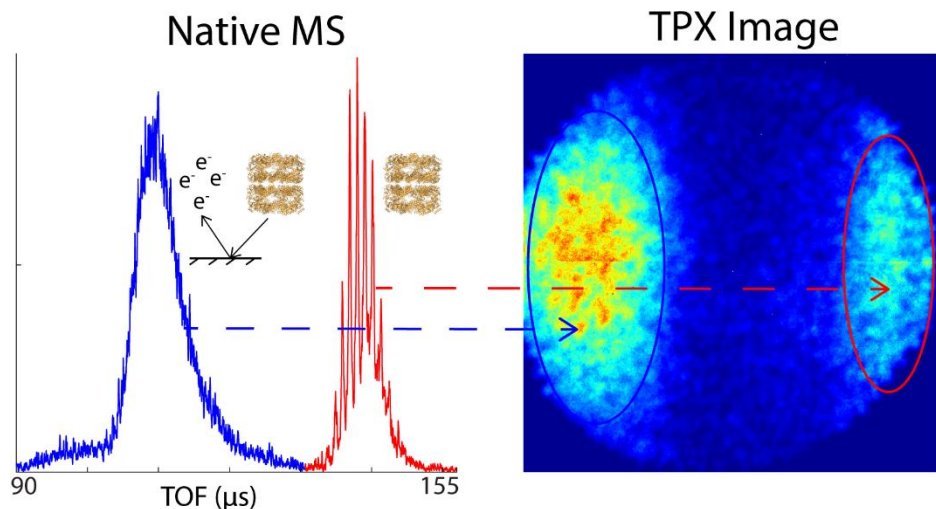
INTRODUCTION

Advances in electrospray ionization (ESI) over the past two decades have enabled the ionization and mass analysis of macromolecular assemblies (MMAs) in their pseudo-native state, where non-covalent interactions are maintained; a method referred to as native mass spectrometry (native MS).[226] Using native MS, various structural details of MMAs such as topology, stoichiometry, subunit connectivity, dynamics, and interaction of large biomolecules like protein complexes[227-228], protein–ligand complexes[81, 229], protein-nucleic acid complexes[108, 230] and virus capsids[94, 231] has been successfully investigated.

A combination of a nano-ESI source[49-50] and an orthogonal time-of-flight (O-TOF) mass analyzer equipped with an ion reflectron[232-233] is widely used for native MS. Careful consideration in the design and operating parameters of the ion transfer optics is critical for the transmission of the high mass-to-charge (m/z) ions produced under native conditions. Elevated gas pressures and radio-frequency ion guides operating with higher amplitudes and/or lower frequencies are often used to enhance the transmission of high m/z ions into the TOF (or other) mass analyzer.[65, 67, 69, 72] Ion detection in TOF-MS is generally accomplished using microchannel plates (MCPs)[109] in combination with time-to-digital converters (TDCs) or analog-to-digital converters (ADCs) that are typically capable of single-ion detection.[83, 127] While these are popular and versatile detection systems deployed in virtually all modern TOF instruments, they do not provide spatial information of ions arriving at the detector surface. This poses a limitation as these impact coordinates can encode critical information on the trajectories that ions take through the intermediate ion optics and TOF analyzer. As a result, they may reveal ion optical processes that remain hidden if only the resulting, integrated mass spectrum is observed. In this study, we have coupled an active pixelated detector (Timepix (TPX)) for the first time to an O-TOF mass spectrometer modified for native MS to study the ion transport processes of large proteins and protein complexes.

The TPX is a position- and time-sensitive charge detector consisting of a 512 x 512 pixel array of 55 μm pitch with each pixel capable of recording both the arrival time and impact coordinates of impinging particles.[135] Initially developed for high energy physics applications where a silicon sensor layer is placed on top of the detector chip for localized charge generation from impacting particles[234-237], it has also been adapted for ion imaging in MS applications.[139-140, 143-148, 151, 238] In MS applications, a TPX detector chip without a silicon sensor layer is positioned behind a dual MCP and directly detects the amplified electron pulses emitted by the MCP. Initial TPX studies focused on the development of stigmatic ion imaging applications using both secondary ion mass spectrometry (SIMS) and matrix-assisted laser desorption/ionization (MALDI) with the goal to improve the spatial resolution and throughput of mass spectrometry imaging experiments.[140, 145, 147] Improvement in detection efficiency for higher mass ions such as intact proteins was subsequently realized by the development of a TPX detection system biased

at a high voltage (HV) of +12 kV/-8 kV for ion post-acceleration prior to ion detection.[144] Furthermore, the coupling of the TPX detector to a commercial MALDI-axial-TOF instrument (Ultraflex III from Bruker Daltonics) demonstrated both the ability to detect ions with m/z values up to 400,000[143] and the study of m/z-dependent ion trajectories defined by mass-independent initial ion velocities and the ion extraction optics.[146] These studies clearly show the significance of spatially and temporally resolved ion detection for studying ion optical processes in mass spectrometry.

In this work, we describe the development of a new HV-floating TPX detection system and its coupling to an O-TOF LCT mass spectrometer modified for high mass transmission and equipped with a nano-ESI ion source, thereby providing the first report for the detection and imaging of highly charged ions with molecular weights in excess of 800 kDa using TPX technology. In this system, we have used the spatial and temporal distributions of ions arriving at the detector as a readout to investigate ion transport properties through the different ion optics elements of the instrument and to resolve individual ion detection events in both space and time. Furthermore, we discuss how both the impact coordinates and arrival time information recorded by the TPX detector are utilized to explain an unusual signal in the native mass spectrum, which was also observed in earlier studies using modified quadrupole-TOF (q-TOF) I, q-TOF II and LCT mass spectrometers (Micromass, Manchester, UK) under certain ion optical conditions, but could not be explained solely by the TOF spectrum generated by conventional mass spectrometers.[239-244]

MATERIALS AND METHODS

Materials

Cytochrome C (12.4 kDa) from equine heart, myoglobin (17.6 kDa) from equine heart, pepsin (35 kDa) from porcine gastric mucosa, bovine serum albumin (BSA, 66.4 kDa), conalbumin (77 kDa) from chicken egg white, concanavalin A (102 kDa) from Canavalia ensiformis, immunoglobulin G (IgG, ~150 kDa) from human serum, beta-amylase (β-amylase, 223.8 kDa) from sweet potato, chaperonin 60 (GroEL, ~800 kDa) from Escherichia coli, ammonium acetate, tris acetate, potassium chloride, ethylenediaminetetraacetic acid (EDTA), adenosine-5'-triphosphate (ATP), magnesium chloride, ammonium hydroxide, and acetic acid were all purchased from Sigma-Aldrich (Zwijndrecht, The Netherlands). Methanol, acetone, and LC-MS grade water were purchased from Biosolve (Valkenswaard, The Netherlands).

Nanospray needles were homemade from preheated borosilicate glass capillaries (Science products GmbH, Hofheim, Germany) using a DMZ universal electrode puller (Zeitz-Instruments Vertriebs GmbH, Munich, Germany) followed by gold coating with an SC7640 sputter coater (Quorum Technologies, Kent, UK.

Sample Preparation

The lyophilized protein assemblies (except GroEL) were dissolved to a stock concentration of 100 µM in LC-MS grade water. These samples were further diluted to a final monomer concentration of 2.5-20 µM in 100 mM ammonium acetate (pH 6.8) prior to MS experiments. The preparation of GroEL samples was performed as follows. A 5.8 µM (monomer concentration) solution of GroEL was made in buffer A (20 mM tris acetate, 50 mM potassium chloride, 0.5 mM EDTA, 1 mM ATP, 5 mM magnesium chloride adjusted to pH 8). This solution vortexed slowly for 1 h followed by the addition of ice-cold methanol (20% of the final volume). The solution was equilibrated by vortexing another 1 h followed by the addition of ice-cold acetone (50% of final volume) and kept overnight at -20°C to precipitate the protein. Precipitated GroEL was redissolved in 500 µL of buffer A, which was subsequently shaken for 20 min at room temperature. This sample was buffer exchanged with 100 mM ammonium acetate at pH 6.8 using 30 kDa molecular weight cutoff (MWCO) Amicon Ultra centrifugal filter (Millipore, Merck KGaA, Germany) to a final monomer concentration of 28 µM.

Timepix Detector

The Timepix (TPX) detector family was developed within the Medipix consortium hosted by the European Organization for Nuclear Research (CERN, Geneva, Switzerland).[135] A single TPX chip consists of a 256×256 pixel array having a pixel pitch of 55 µm and dimensions of 1.4 × 1.6 cm^2. For this study, we used a 2 × 2 quad array consisting of 512 ×512 pixels in total. Each pixel is a single-stop TDC that registers an event once the input charge of a given pixel exceeds a certain threshold (equivalent to ~600 electrons). The TPX is positioned 2 mm behind a dual MCP stack and thus detects the emitted electron pulses that each span multiple pixels.[140] TPX can be operated in three modes: (i) counting mode, in which each pixel counts the number of arriving particles; (ii) time-of-arrival (TOA) mode, in which the arrival time of each particle is measured with respect to an external trigger; and (iii) time over threshold (TOT) mode, in which each pixel registers the time for which it's signal is above a certain detection threshold level. In this study, TOA mode is used and the TPX data is readout via a ReLAXD (high-Resolution Large-Area X-ray Detector) readout board with a speed of 1 Gbit.s^{-1}.[245]

Mass Spectrometer and Detection System

All experiments were performed on two similar LCT O-TOF mass spectrometers (Micromass, Manchester, UK), one is a modified LCT with the described TPX detector (Maastricht University, Maastricht, The Netherlands), and the other is a standard LCT (Utrecht University, Utrecht, The Netherlands). Both instruments were modified to improve the transmission of high *m/z* ions, through the installation of a speedivalve that reduces the pumping efficiency of the rotary pump and thus increases the pressure in the source region. The systems were additionally equipped with a flow restriction sleeve in front of the first hexapole to increase

the pressure in the RF optics. Such elevated pressures in these regions are critical for the gentle transmission of high m/z ions through collisional damping.[65-69]

(a)

(b)
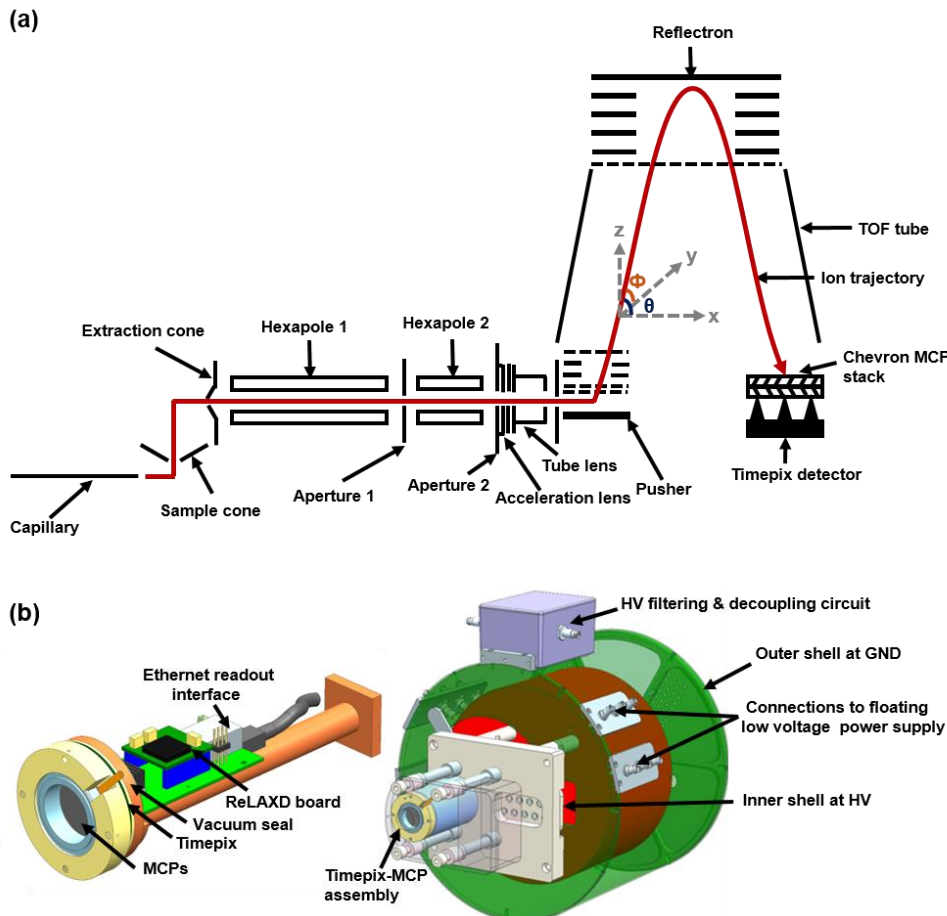
Figure 1. (a) Schematic of the ion optics of modified LCT O-TOF mass spectrometer. The TPX detector is positioned behind the MCP stack. Ions (red trace) are initially accelerated and transported in the x-direction and subsequently accelerated in the z-direction before they enter the O-TOF analyzer. The detector assembly is positioned in the x-y plane. Flight angles Φ and θ define the ion trajectory. (b) Schematic representation of the mechanical design of MCP-TPX setup. The MCP-TPX assembly is isolated from the readout electronics via a vacuum seal (left) and placed within the inner shell kept at HV, and protected by the outer shell at ground potential (right).

A schematic of the ion optics of the instrument is shown in Figure 1a. Ions generated using an in-house built static nano-ESI source are transferred into an orthogonal acceleration TOF mass analyzer via two differentially pumped hexapole RF lenses. The interface between the nano-ESI source and MS consists of two cones: a sample cone and an extraction cone (source region). Apertures 1 and 2 are used to focus ions into the hexapole region and a set of lenses

(acceleration, focus, steering, and tube lenses) are used to transfer the beam into the pusher region for TOF-based mass analysis.

The LCT is designed such that the field-free TOF tube is floating at HV (typically ~ -4.6 kV in positive ion mode) and as such the TPX detector and associated readout electronics must also operate at HV to enable the operation of the instrument using the standard acceleration schemes. A schematic of the detector assembly is shown in Figure 1b and is based on a previously reported HV-TPX design.[144] The inner shell is floated at HV and contains the TPX detector in vacuum and the associated ReLAXD readout system at atmospheric pressure. A multifunctional chip carrier provides both vacuum seal and electrical feedthroughs for connection from the TPX to the ReLAXD board. The inner shell is surrounded by an outer shell shield that is kept at ground potential. A home-built floating low-voltage power supply was used to power up the TPX, ReLAXD readout board, and cooling system. An external power supply (FuG Elektronik GmbH, Schechen, Germany) provides a voltage offset to the TPX relative to the back MCP to attract the amplified electrons towards the TPX surface (typically +800 V offset). The bias between the front and back MCP plates was 1.6 kV and controlled by the standard MassLynx software. An optical fiber protocol via two ethernet media converters (N-Tron 1002MC) was used to transfer the TCP/IP signal output at HV from the ReLAXD board to the acquisition PC at ground potential. The TPX was triggered using a down-sampled version of the main trigger pulse that starts the orthogonal acceleration in the pusher. The trigger was down-sampled to a rate of 30-50 Hz to match the achievable frame rate of the TPX. This down-sampled trigger passed through a digital pulse and delay generator (DG535, Stanford Research Systems) to trigger and open the TPX for the measurement period and have flexible timing control. Trigger was converted to the optical domain for the HV isolation and two home-built converters were used for the signal transmission from the pulse and delay generator to the TPX. All experiments were performed using a 20 ns TPX clock width, corresponding to a maximum measurement window of 236.2 µs for each TOF cycle. Typical flight times were < 155 µs for all data reported here.

Samples were introduced into the mass spectrometer using gold-coated needles via an in-house built static nano-ESI source. 3 µL of each sample was loaded into the needle and a spray voltage of 1.4 kV was applied. Sample cone voltage, extraction cone voltage, RF lens voltage of hexapoles and the pressures in source and TOF analyzer regions were optimized for each protein separately. All spectra were recorded using the following voltage settings; DC offset 1: 10 V, DC offset 2: 6 V, ion energy: 10 V, aperture: 20 V, TOF tube: 4600 V, reflectron: 1000 V, MCP gain: 1600 V and TPX: -2200 V unless stated otherwise. All ion optics parameters except the TPX voltage were defined via MassLynx V4.1 software (Waters, Wilmslow, UK).

Data Acquisition and Analysis

The SoPhy (Software for Physics) software package was used for the TPX chip control and data acquisition (Amsterdam Scientific Instruments, Amsterdam, The Netherlands). 10,000 TOF cycles were collected and summed for each dataset. For each TOF cycle, a separate data file was saved that registers the information about the pixel addresses (location) and corresponding TOA associated with each event. These raw files were subsequently analyzed using in-house developed software written in MATLAB (R2014a, MathWorks Inc., Natick, MA, USA).

Ion Optics Simulations

SIMION 8.1 (Scientific Instrument Services, Ringoes, USA) software was used for all ion optics simulations to evaluate the experimental results. A two-dimensional model of the simplified TOF geometry of the LCT generously provided by Waters Corporation (Wilmslow, UK) was used for the simulations.

RESULTS AND DISCUSSION

Detection of High Mass Native Proteins Using Timepix

We acquired mass spectra of native GroEL (800 kDa) under the same ion optical conditions on both the TPX-equipped LCT and the one equipped with the standard MCP/TDC detection system to first validate the native MS data recorded by the TPX system. The resulting native mass spectra collected on both instruments are shown in Figure 2. Each spectrum represents a 1 s accumulation time corresponding to 45 and 7,143 pusher pulses for MCP-TPX and MCP-TDC data, respectively. In both MCP-TPX and MCP-TDC generated spectra, a series of peaks spanning over the m/z values between 11,290 and 12,740 are observed. This is consistent with the previously reported native GroEL spectrum[246] and corresponds to the 63+ to 71+ charge states. We note the lower mass resolution of the MCP-TPX spectra. In part, this can be explained by known time-walk effects, whereby a single electron pulse is registered across several time bins (Supporting Information Figure S1).[140, 247-249] Previous studies demonstrated that centroiding approaches can be used to correct for time-walk effects and improve the effective mass resolution.[140, 247, 250] Here, we found such approaches to provide a minimal improvement in mass resolution for the detection of the high m/z ions. This suggests the lower mass resolution of the TPX compared to the conventional detection system is caused by some other phenomena. Nonetheless, this mass resolution is still sufficient to resolve the multiply charged high m/z native species generated by ESI.

The differences in absolute intensity values arise from the different nature of each detection approach. In the case of the standard LCT system, the MCP-TDC records the number of time bins for which an ion event is registered during each measurement cycle with a digitization rate of 1 GHz. This detector output is then

converted to counts per second. In the case of the TPX spectrum, the output value corresponds to the average number of pixels activated for each arrival time was used. Each individual ion event results in an electron pulse that spans 6-65 pixels, thus multiple counts are recorded for each ion event. It is noteworthy that the TPX data was acquired with 158 times fewer pusher pulses than that used to acquire the TDC spectrum.

2

Figure 2. Averaged mass spectra of native GroEL acquired on an LCT equipped with TPX detector (top, red trace) and on a standard LCT with conventional MCP-TDC detector (bottom, blue trace). Both spectra were acquired under identical ion optical conditions (DC offset 1: 10 V, DC offset 2: 6 V, ion energy: 30 V, aperture: 20 V, TOF tube: 4600 V, reflectron: 1000 V). The MCP-TPX is the result of the accumulation of 45 pusher pulses, whereas the MCP-TDC is the result of 7143 ion pulses.

The TPX may provide improved sensitivity for high-mass ions due to the lower charge threshold for event registration.[143] Given the high *m/z* range observed, some ion impacts can result in lower ion-to-electron conversion efficiency and thus lower overall amplification. Some of these events may still be registered by the TPX, but do not exceed the detection threshold of the standard TDC (~70 mV). However, such comparisons are difficult to quantify. A second potential advantage of the TPX is the ability to differentially detect simultaneous individual ion events that arrive at different positions, whereas this is not possible with the conventional integrating TDC system. While this can potentially lead to a benefit for the TPX at high-count rates, in such O-TOF instruments, the number of ions per pusher pulse is sufficiently low that is likely not to have a significant effect.

The TPX data also exhibits a broad lower TOF distribution corresponding to arrival times of 90-130 μs (appearing at *m/z* hump ranging from 5,500 to 9,000). The potential origin of this distribution is discussed later in this article.

Single-Ion Imaging of Protein Complexes

Single-ion detection of MMAs has been previously reported on TOF[231, 251], Fourier transform-ion cyclotron resonance (FT-ICR)[189, 252], and Orbitrap[72, 253] platforms. Recent works on individual ion measurement using Orbitrap analyzers demonstrated the ability to significantly improve mass resolution at high m/z values[185], and allowed precise mass determination and charge detection of highly complex mixtures of MMAs.[186-187] In this section, we demonstrate for the first time the capabilities of an LCT-TPX assembly for simultaneous space- and time-resolved detection of single MMA ions.
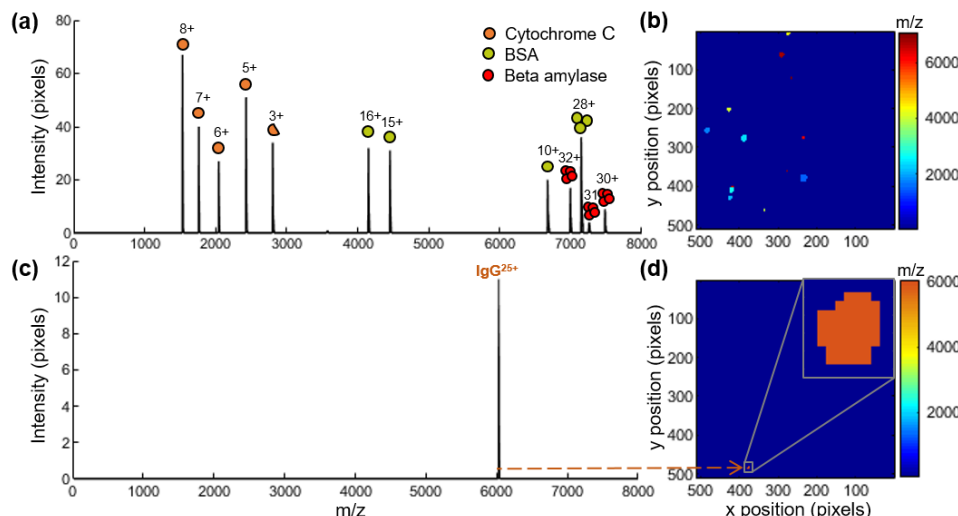
Figure 3. (a) Mass spectrum and (b) TPX image acquired from a single TOF cycle (one TPX frame) using a protein mix of cytochrome C, BSA, and β-amylase sprayed under native conditions. (c) Mass spectrum and (d) TPX image acquired from a second single TOF cycle using IgG. Only a single-ion event that represents IgG[25+] was detected. The y-axis in (a) and (c) represents the number of TPX pixels activated for each ion event. Each color in the single frame TPX image corresponds to a different m/z or arrival time.

Figure 3a,b shows the mass spectrum and measurement frame image generated from a single TOF cycle using a protein mix containing cytochrome C (12.4 kDa), BSA (66.4 kDa), and β-amylase (223.8 kDa), three commonly used molecular weight markers in gel filtration chromatography. Each impact event in the single frame image (Figure 3b) corresponds to the electron footprint of a single ion event at the MCP and is associated with a single peak in the mass spectrum (Figure 3a), thereby demonstrating single-ion detection and imaging of protein complexes. Figure S2 (Supporting Information) contains single-frame spectra and images from four different TOF cycles. Each peak in the single frame spectrum may corresponds to more than one ion event if more ions arrive at the same time but strike at different locations of the detector. The number of pixels activated by each ion event is related to the number of electrons emitted from the MCP, which in turn is related to the efficiency of the initial ion-to-electron conversion,

amplification steps through the channels of MCP, and the space charge-driven expansion of the electron pulse between the MCP and TPX. These processes are expected to follow Poisson statistics and produce a distinctive distribution of the size of each electron showers footprint on the TPX detector.[254]

Figure 3c,d shows data from another single TOF cycle in which only one ion event is recorded. This ion event is assigned to IgG[25+] at m/z = 6029. In this case, the electron footprint of IgG[25+] occupies 46 pixels and results in a maximum time-bin intensity of 11 counts with a TOF spread of 180 ns (Supporting Information Figure S1). Given the fact that the pulse width of a single MCP pulse is expected to be no longer than several nanoseconds, this wide spread of TOF values for a single ion event is due in part to the time-walking effects of TPX.[140, 247-249]

Influence of Ion Optics on the Spatial Distribution of the Ions Arriving at the Detector

We next investigated the ability of the TPX to study ion trajectories as a function of various ion-optical parameters. In the LCT schematic diagram shown in Figure 1a, ions are initially accelerated in the x-direction as they leave the ion source and travel toward the pusher. The pusher pulses the ions in the z-direction for the TOF and spatial profile measurement, and is finally detected by the MCP-TPX assembly in the x-y plane. The impact coordinates of ions at the detector are determined by the flight angles of the ion beam leaving the pusher. The flight angles θ and Φ indicated in Figure 1a and given by,

$$\vartheta = \tan^{-1}\frac{v_z}{v_x} \qquad \Phi = \tan^{-1}\frac{v_z}{v_y} \qquad (1)$$

where v_x, v_y and v_z are the velocity components in the x-, y- and z-directions respectively. In the region prior to the pusher, the velocity components in y- and z-directions are significantly smaller than the axial (x) velocity component of the ion beam. Once the beam is accelerated to the z-direction by the orthogonal pusher, v_z increases significantly, while v_x and v_y remain almost unchanged. Hence, the ion trajectory in the post-pusher region is mainly determined by the flight angles defined by equation set 1. As no voltage source accelerates the ions in the y-direction, v_y is much smaller than v_z, which keeps Φ≈90°. As a result, no shift in impact position is observed along the y-direction when any of the instrument settings are altered, even for the parameters that affect the v_z component. That means θ is the only significant flight angle that defines the impact position of the ion cloud. As a result, only shifts in the spatial profile along the x-direction under normal operating conditions are expected.

We have observed that only four ion-optical parameters have a critical influence on the spatial distribution of ions in the detection plane: TOF tube voltage, axial ion energy, DC offset across the first hexapole, and reflectron voltage. No significant shift in the ion profile along the x-direction was observed for change in any of the other ion optics settings other than these parameters as all other voltage elements only alter the potential energy profile locally. This will be discussed in more detail below.

2

Effect of TOF Tube Voltage

The spatial distribution of the cytochrome C ion cloud recorded at different TOF tube voltages is shown in Figure 4a. The entire *m/z* range that encompasses all detected charge states was summed for this evaluation. The vertical patterns in the y-direction that appear as "ion shadows" in the image are explained by the transmission grids placed in the acceleration region.
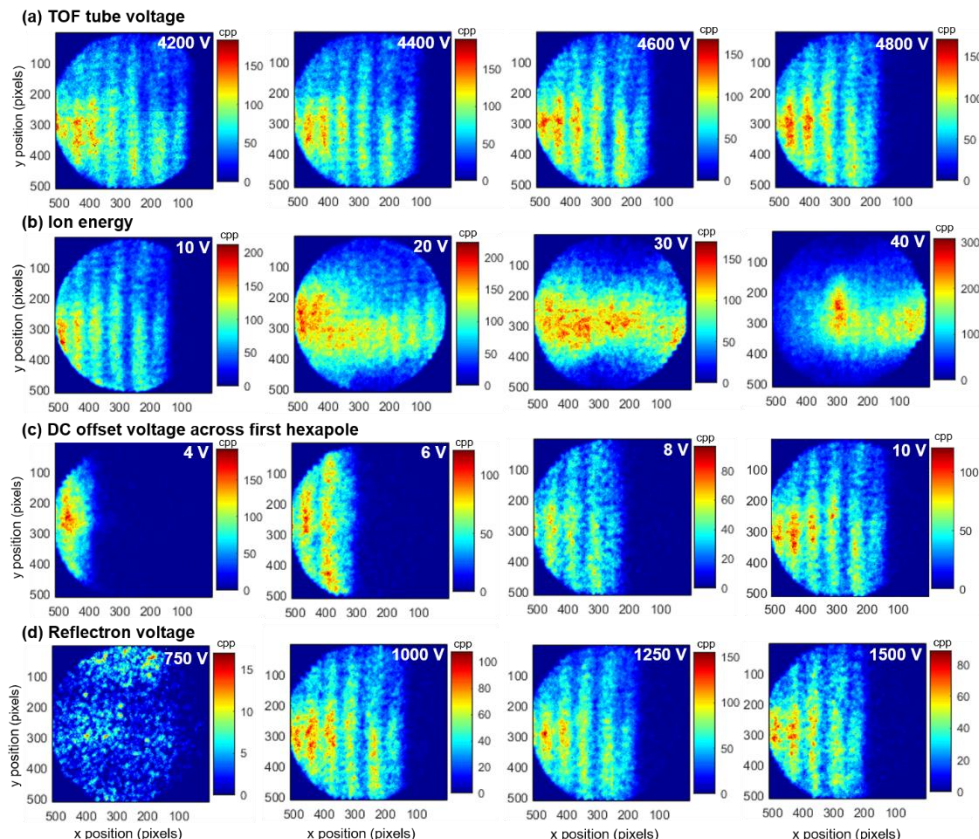
Figure 4. Influence of (a) TOF tube voltage (b) axial ion energy (c) DC offset voltage across the first hexapole, and (d) reflectron voltage on the spatial distribution of cytochrome C ions arriving at the detector. All data represents the sum of 5,000 TOF cycles by spraying native cytochrome C under identical voltage conditions and represent the sum of all charge states. cpp = counts per pixel.

The "TOF tube" defines the voltage at the exit of the pusher and thus determines the orthogonal acceleration energy of the ions as they enter the field-free TOF tube. The cytochrome C mass spectrum appears almost similar for different TOF tube voltages (Supporting Information Figure S3), but the spatial distribution of the ion cloud at the detector shifts towards the left as the TOF voltage increased from 4200 to 4800 V. These results can be explained as follows: a higher TOF tube voltage increases the total acceleration potential of the pusher and thus

increases v_z, while v_x and v_y remain unchanged, and thus raises the flight angle θ. At a TOF tube voltage of 4200 V, the reduced θ angle combined with the width of the ion beam in the x-direction results in most of the ion beam hitting the detector. A higher TOF tube voltage increases the flight angle and thus leads to a larger fraction of the ion beam missing the detector.

Effect of Axial Ion Energy

The impact of "ion energy" on the spatial distribution of the ion cloud is shown in Figure 4b. The "ion energy" setting defines the voltage at aperture 1 and all voltage elements prior to the pusher entrance (except capillary) are defined with respect to the aperture 1; thus this parameter ultimately determines the axial ion energy of ions entering the pusher. Higher ion energies increase the axial velocity and thus reduces θ, so that the ion cloud moves toward the right of the detector.

The intensity distribution of the ion cloud appears different at lower ion energies. This can be explained by the increased sensitivity of the ion optics to voltage changes at lower ion energies since the instrument was designed to operate at a higher ion energy of ~35 V.

Effect of DC Offset Voltage across First Hexapole

The "RF DC offset 1" parameter that defines the DC offset voltage across the first hexapole displays a similar behavior as "ion energy". As this voltage increases, the potential difference between the first hexapole and its exit lens (aperture 1) is increased and leading to an increase in the axial ion energy of ions entering the pusher. Expectedly, this leads to a shift in the spatial distribution of the ion cloud towards the right side of the detector (Figure 4c).

Figure 4c is generated from the data recorded at a fixed "ion energy" setting of 10 V, which resulted in spatial intensity distribution being very sensitive to small variations in the DC offset voltage of the first hexapole. Figure S4 (Supporting Information) is generated for the exactly same "RF DC offset 1" values used in Figure 4c, but for a higher "ion energy" of 40 V, and it is observed that the intensity profile of ions is less sensitive to the DC offset of the first hexapole.

Effect of Reflectron Voltage

The "Reflectron" sets the voltage at the rear of the reflectron. A change in the reflectron voltage does not affect θ, but this voltage does define the point from which the ion beam gets reflected back to the detector. For higher reflectron voltages, this turn-around position is closer to the detector and results in the ion beam hitting more toward the left side of the detector (Figure 4d).

General observations

The equation of θ can be rewritten as,

$$\vartheta = \tan^{-1}\frac{v_z}{v_x} = \tan^{-1}\sqrt{\frac{V_z}{V_x}} \tag{2}$$

V_x and V_z are the acceleration potential components in the x- and z-directions

respectively.[233] Equation 2 clearly shows that θ is independent of the mass of the protein, hence the same spatial distribution is expected to be observed for different proteins under identical ion optics conditions. Figure S5 (Supporting Information) shows the spatial distribution of the ion cloud corresponding to different proteins of masses from 12.4 to 223.8 kDa acquired under similar voltage conditions, and the spatial profiles look similar as expected. Figure S6 (Supporting Information) is generated using the exact same ion optical conditions used in Figure 4, but with a different protein-conalbumin (77 kDa), and the spatial distributions are observed to be identical to those of cytochrome C except for axial ion energy. This is due to the origin of mass-independent secondary particles at higher axial energies, which will be discussed in the next section.

All the experimental data show good agreement with the SIMION ion optical simulation results. Simulated ion trajectories of cytochrome C for different TOF tube voltages are shown in Supporting Information (Figure S7).

Visualization of Secondary Electrons Generated by Protein-Surface Interaction

In this section, the imaging capability of the TPX is further exploited to determine the origin of the unexpected TOF signal observed with flight time less than the corresponding parent protein. Figure 5a shows the TOF spectrum of GroEL recorded at different "ion energy" voltage settings from 10-50 V, while the corresponding TPX images for all the arriving ions are shown in Figure 5b. In addition to the intact GroEL signal (red trace), an additional spectral distribution is observed at lower TOF values that increases in abundance with increasing axial ion energy (blue trace). For an ion energy of 50 V, two distinct distributions are observed in both the mass spectrum and total ion image. Figure 5c shows the corresponding TPX images for the red and blue flight times indicated in Figure 5a and demonstrates the spatial separation of these two populations at the detector. As expected, the high-TOF intact GroEL signal shows a shift in impact position to the right of the detector with an increase in axial ion energy. In contrast, the low-TOF secondary particle distribution does not exhibit a shift in impact position with increasing axial ion energy. Similar spectra and TPX images were also observed at high axial ion energies for a series of different protein ions (Supporting Information Figure S8). The formation of this low-TOF signal at high axial energy was reproduced on a second, unmodified LCT equipped with the standard detector (Supporting Information Figure S9). Surprisingly the impact position of this secondary population was also observed to be insensitive to all other instrument parameters including the reflectron and TOF tube voltages (Supporting Information Figure S10).

Insensitivity to both axial ion energy and the reflector voltage allows the exclusion of two possible sources of this secondary population. First, the possibility of secondary particle formation prior to the pusher can be excluded as the axial ion energy does not alter the impact position of this secondary population. The possibility of secondary particle formation inside the reflectron can also be

excluded due to the fact that neither the flight time of the ions nor their impact position changes with the reflectron voltages. Such behavior would be otherwise expected upon the creation of ions having different *m/z* values within the decelerating/accelerating field of the reflectron.
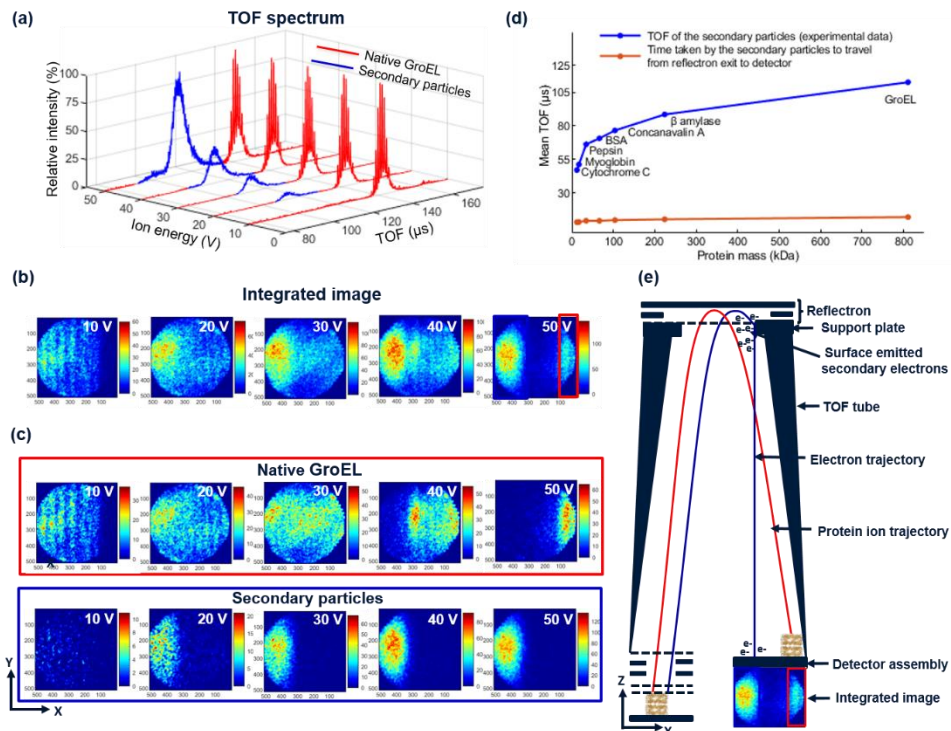
Figure 5. (a) TOF spectra and (b) spatial distribution at the TPX detector recorded at different axial ion energies (10-50 V) by spraying native GroEL. (c) TPX images generated separately for native GroEL (red trace in Figure 5a) and secondary particles (blue trace in Figure 5a) at different ion energies. (d) Comparison between the mean TOF of the secondary particles (blue) and time difference between simulated mean TOF of GroEL to reach the support plate at the exit of the reflectron and measured TOF of secondary particles at the detector. (e) Schematic diagram explains the generation of secondary particles from the parent GroEL ion. At higher ion energies, a fraction of the wide ion beam hits the support plate and generates secondary electrons via protein-surface collisions. cpp = counts per pixel.

Another possibility considered is the occurrence of metastable fragmentation between the reflectron exit and the TPX. However, this is excluded for the following reasons: (i) after metastable fragmentation in the field-free region, fragments travel at the same velocity as the precursor ion and would have identical arrival times and impact positions at the detector (ignoring the small radial kinetic energy discrepancy resulting from dissociation)[83, 255]; and (ii) the spatial profile of metastable ions are expected to also be sensitive to voltages prior to the TOF measurement in a similar manner as their parent ions.

Nonetheless, the above observations provide strong circumstantial evidence for the generation of the secondary particles in the post-reflectron region.

SIMION simulations were employed to investigate these effects further. It was observed that the mean TOF of the secondary particles was very close to the simulated TOF of the intact protein ions to reach the exit of the reflectron. Figure 5d plots the experimentally measured mean TOF of the secondary particle distribution (blue trace) and the time difference between the simulated TOF of the protein ions to the exit of the reflectron and the experimentally measured TOF of the secondary particles (orange trace). Interestingly, there is very little dependency of the time difference plotted as orange trace in Figure 5d on the mass (and thus m/z) of the protein suggesting the identity of the secondary population is the same regardless of the protein being analyzed. This led us to believe the source of this low TOF signal was the creation of secondary electrons by protein-surface collisions near the reflectron exit. As a result of the surface interaction of the primary beam, positively charged/neutral protein fragments and surface-emitted positively charged ions/negatively charged ions/neutrals could also be generated. However, all these possibilities were excluded due to the lower TOF of the secondary particles compared to the parent ions in the field-free region. The LCT contains an uncoated stainless steel support plate placed between the 1st reflectron grid and detector. The position of this support plate is such that it lines up with the detector (Figure 5e). At higher axial higher ion energies, the flight angle becomes wider (lower θ) and leads to an increased probability of the ion cloud to hit the support plate and to generate more secondary electrons from protein-surface collisions. Further evidence for the support plate as the source of this additional signal is the close match in the overlapping area of the support plate with the detector (9.5 mm) and the size of the secondary particle image on the TPX (~9.4 mm). The comparison between the results from the experiments and the LCT ion optics model suggests that an energy of ~4 meV is enough to accelerate the secondary electrons from the support plate to the detector with a mean flight time of ~9.5 μs.

The extent of the surface emitted secondary electrons and its dependency on the parent protein ions were studied for different proteins under similar ion optical conditions; ion energy=50 V, reflectron=1000 V, TOF tube=4600 V, RF DC offset 1=10 V. As expected, it was observed that the spatial profile of all proteins looks similar for same voltage settings (Supporting Information Figure S8). However, the ratio of secondary electrons to parent ion intensity shows an increasing trend with the mass of the protein (Figure 6a). Two possible contributors to this are the reduced detection efficiency (ion-to-electron conversion) of higher m/z ions, an effect known to arise when using MCP-based detectors, and the possibility of higher secondary electron yields per surface impact with increasing m/z of the parent protein ion.[256-257]
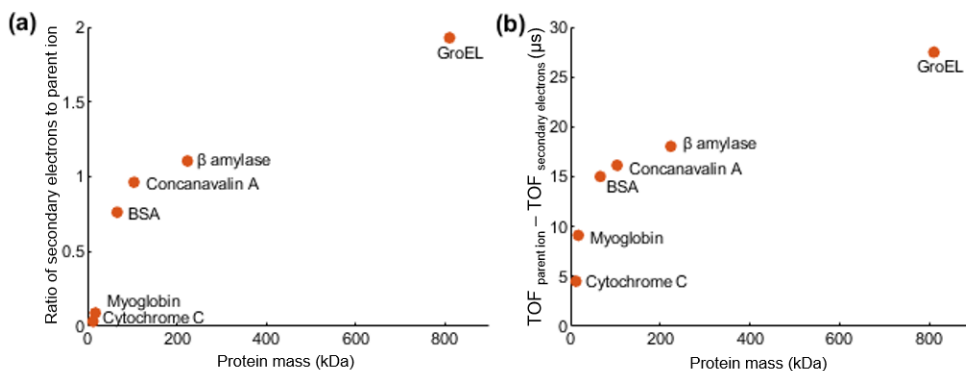
Figure 6. (a) Ratio of the number of surface-emitted secondary electrons to the parent ion plotted for proteins of different masses. The number of parent ions and secondary electrons reaching the detector is calculated by dividing the signal intensity of each by the average number of pixels activated. (b) Difference in the mean arrival time of secondary electrons and parent ion plotted as a function of mass of the protein.

Figure 6b shows the relationship between the mass of the protein and the difference between the time-of-arrival of parent ion and secondary electrons. The time-of-arrival measured at the detector corresponding to the secondary electrons is the sum of time taken by the primary beam to travel from the pusher to the support plate and the surface emitted electrons to reach the detector. Hence, an increasing trend in TOF difference between parent and secondary electron with the size of the protein is expected, which matches with the experimental results.

CONCLUSIONS

In this work, we have described the first implementation of a TPX active pixel detector coupled to an ESI-equipped mass spectrometer modified for high mass transmission. This new experimental setup allows the detection and ion imaging of multiply charged protein complexes of molecular weight in excess of 800 kDa generated by native MS. By utilizing the single ion imaging capabilities of the TPX detector, the spatial distribution of ions at the detector surface has been studied as a function of various ion-optical parameters. The combination of both space- and time-resolved detection was critical to understand the origin of a mysterious signal observed with high entrance energies into the pusher as secondary electrons produced by protein-surface collisions at the exit of the reflectron. The unique imaging capability of TPX allows for more detailed insight into the functionality of each ion optical element within the mass spectrometer. This makes TPX a suitable tool for the optimization of newly developed mass spectrometers and allows for more direct comparisons between the ion optics simulations and experimental data.

This work supports previous studies highlighting the utility of the TPX detector, and other similar detectors such as pixel imaging mass spectrometry (PImMS) camera

for simultaneous imaging of ions with different arrival times and for studying ion optical processes.[146, 258] Active pixel detectors are demonstrated to offer significant advantages over the traditional charge-coupled device (CCD)-based approaches that are widely used in ion imaging applications such as velocity map imaging.[247, 259]

The TPX detector used for this work is limited by a moderate time resolution (20 ns here, at best 10 ns) and single-stop detection for each pixel that can limit the detection of high TOF ions at high-count rates. Future studies will benefit from the implementation of the next-generation Timepix3 detector that amongst other advantages offers 1.56 ns time resolution, per-pixel multi-hit functionality, and kHz readout rates.[137, 260-262]

SUPPORTING INFORMATION
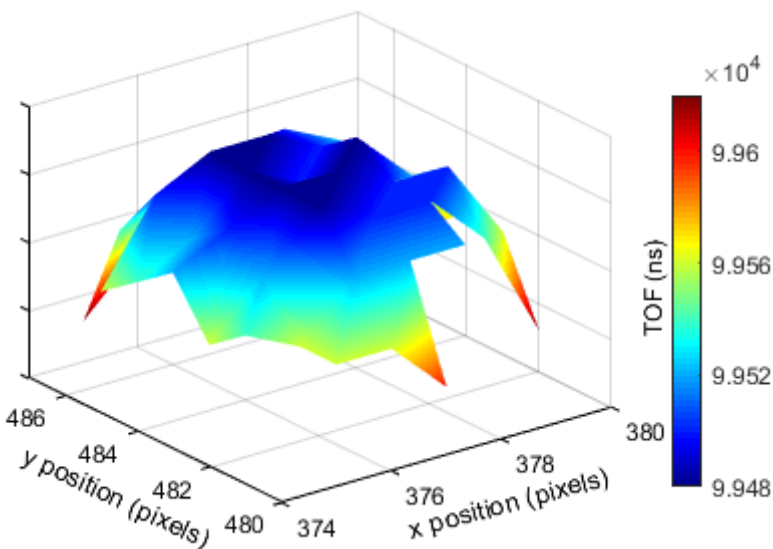
Figure S1. Timepix time-of-arrival data of a single ion event corresponding to IgG[25+]. Outer pixels were activated up to 180 ns after the triggering of the innermost pixels. This time-walk effect is related to the charge density arriving at each pixel from the electron pulse emitted by the MCP. Centre pixels are triggered earlier due to higher charge density.
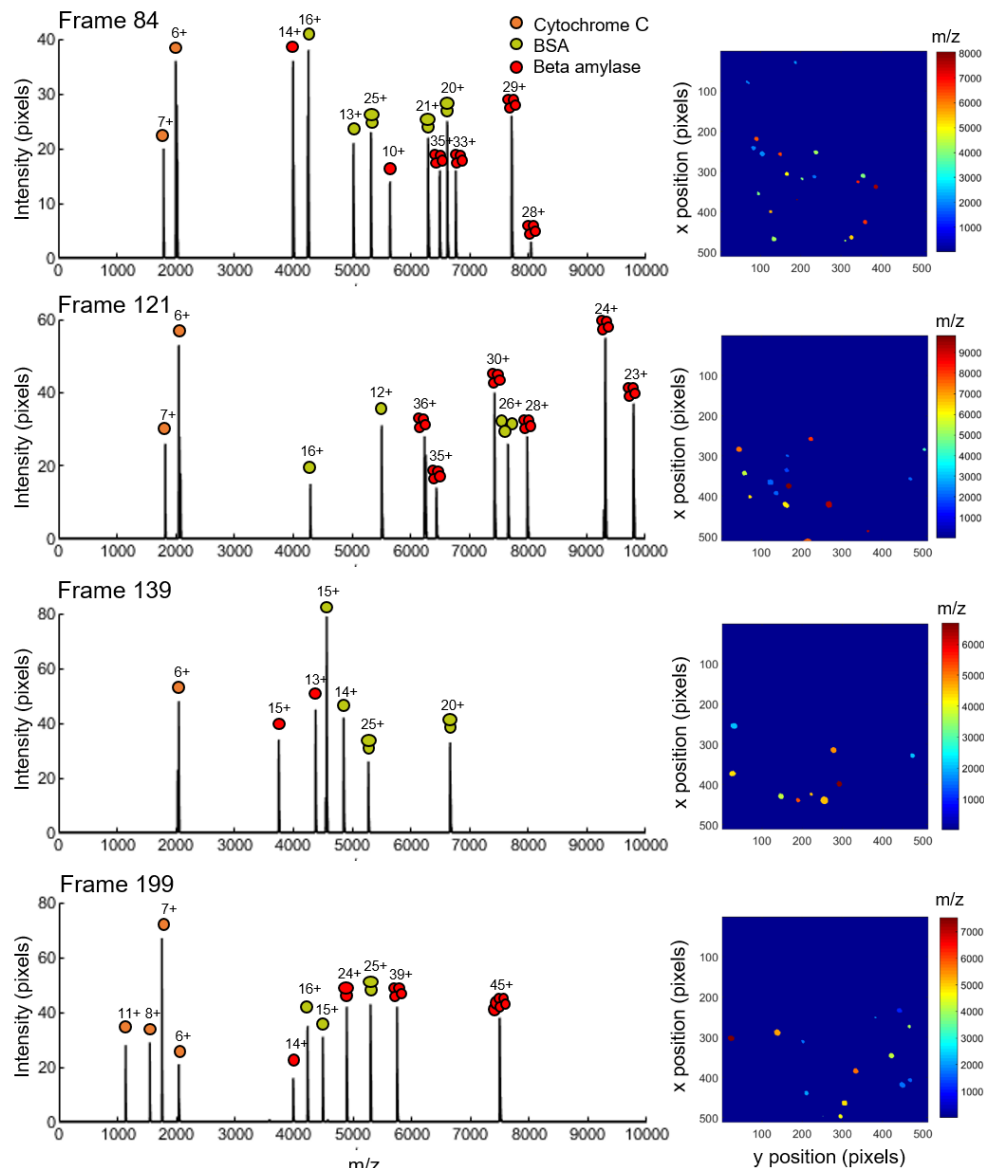
Figure S2. Single frame mass spectrum (left) and TPX image (right) acquired from four different TOF cycles using a protein mix of cytochrome C, BSA and β-amylase sprayed under native conditions. The y-axis in single frame mass spectrum represents the number of TPX pixels activated for each ion event. Each color in the single frame TPX image corresponds to a different *m/z* or arrival time.
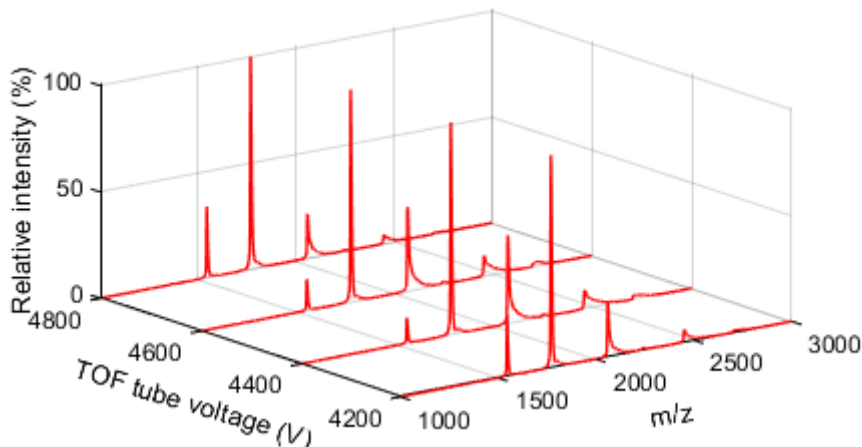
Figure S3. Mass spectra of native cytochrome C recorded at different TOF tube voltages.
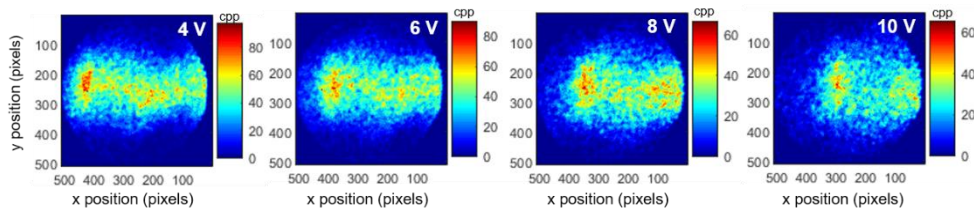
Figure S4. Timepix images showing the ion distributions at the detector for native cytochrome C recorded for different "RF DC offset 1" settings at an "ion energy= 40 V". The entire m/z range that encompasses all detected charge states was summed for the generation of the Timepix image. Absolute ion counts recorded by each pixel (counts per pixel (cpp)) is shown in the corresponding scale bars.
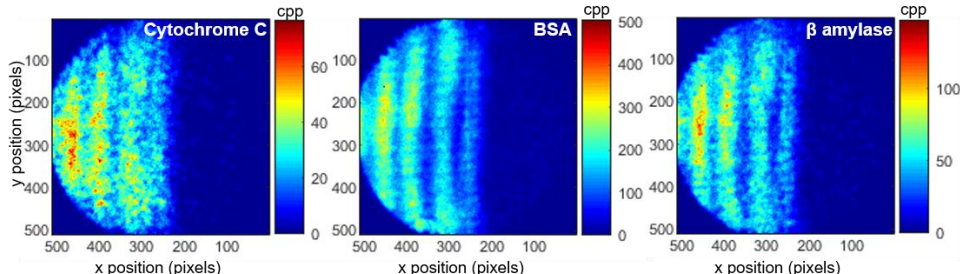
Figure S5. Timepix images showing the ion distributions at the detector for native cytochrome C (left), BSA (middle) and β-amylase (right) under identical voltage settings. All the detected charge states of each protein were used for the generation of the Timepix image. cpp = counts per pixel.
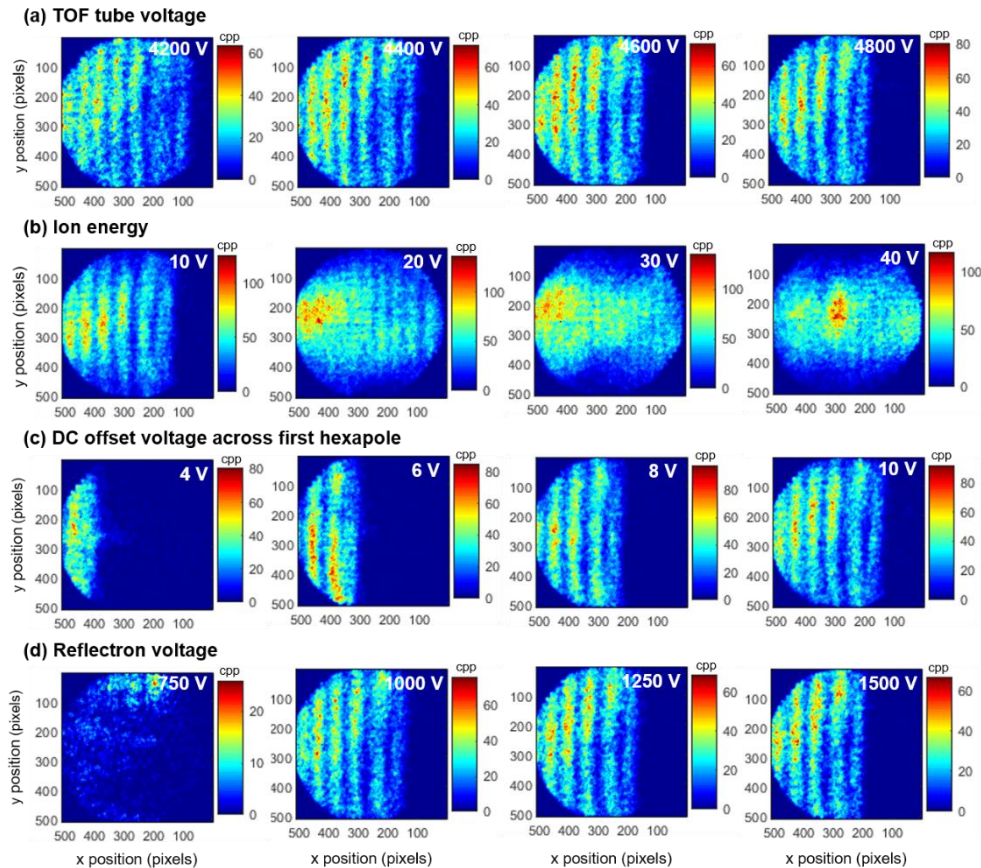
Figure S6. Influence of (a) TOF tube voltage (b) axial ion energy (c) DC offset voltage across first hexapole and (d) reflectron voltage on the spatial distribution of native conalbumin ions arriving at the detector. All data represents the sum of 5,000 TOF cycles and corresponds to an *m/z* range containing all the detected charge states. cpp = counts per pixel.
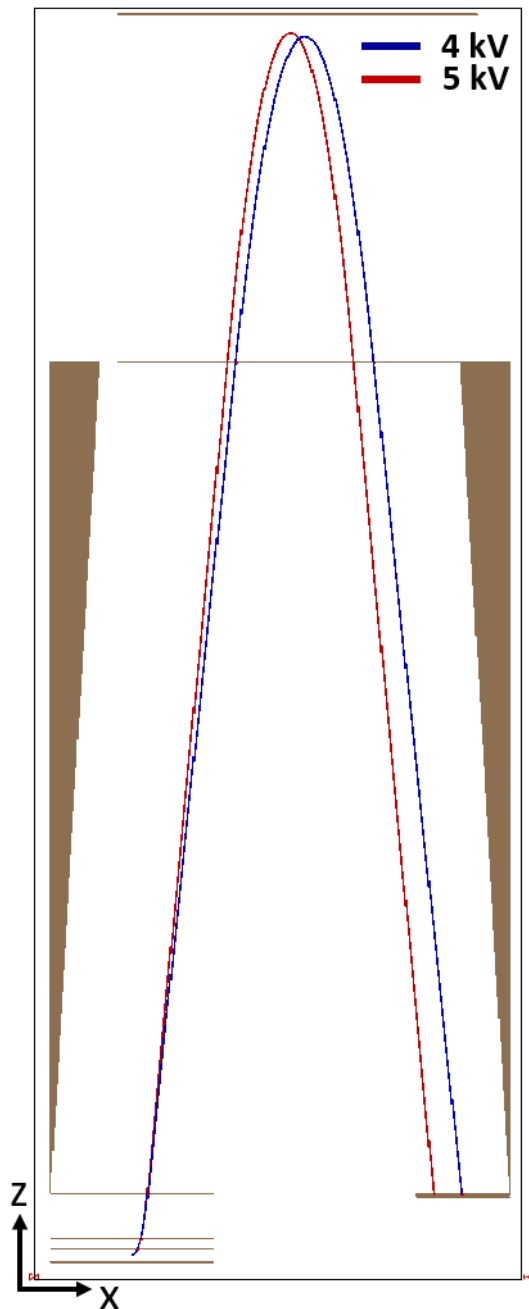
Figure S7. Ion trajectories of native cytochrome C [M+7H]⁷⁺ ions at TOF tube voltages of 4 kV (blue) and 5 kV (red) simulated in SIMION using a simplified TOF geometry of the LCT. Voltage variables were assigned to the following values: pusher voltage = 977 V, Reflectron voltage = 1000 V, and entrance voltage =30 V.

(a)

(b)
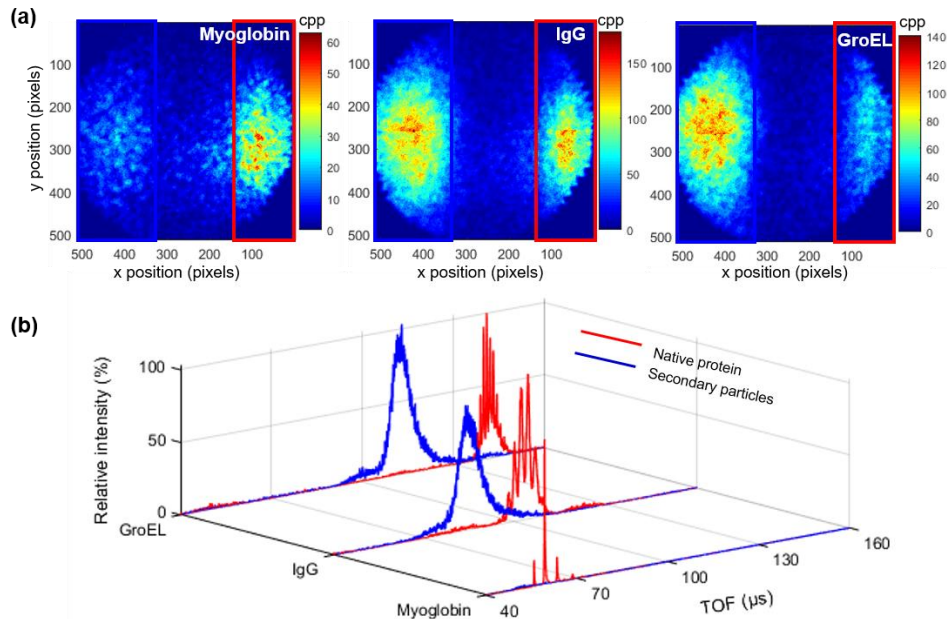
Figure S8. Timepix generated (a) ion distribution images and (b) TOF spectra of intact proteins (red box in (a) and spectra in (b)) and corresponding secondary particle population (blue box in (a) and spectra in (b)), acquired for native myoglobin (17.6 kDa), IgG (150 kDa) and GroEL (800 kDa) under identical voltage settings (DC offset 1: 10 V, DC offset 2: 10 V, ion energy: 50 V, Reflectron: 1000 V, TOF tube: 4600 V). cpp = counts per pixel.
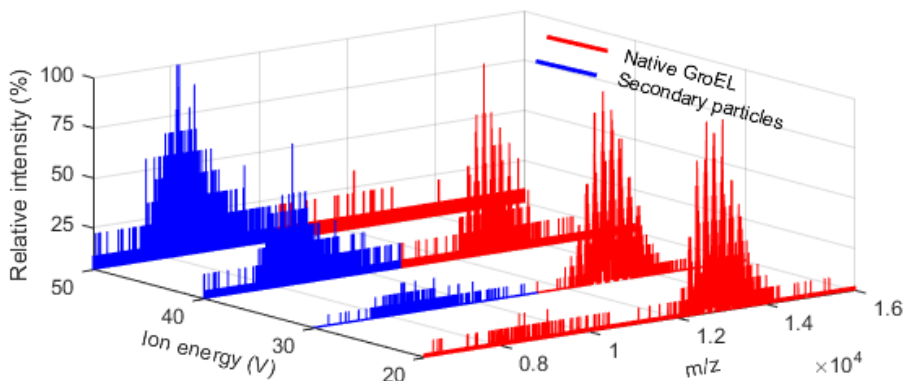
Figure S9. Mass spectra of native GroEL collected for different axial ion energies using a standard LCT instrument equipped with the original detector. Ion optical parameters used for the data acquisition are the same as the native GroEL spectrum collected on the TPX equipped LCT (Figure 5a) except for the MCP gain voltage, which is increased to 2500 V.

(a) Reflectron voltage
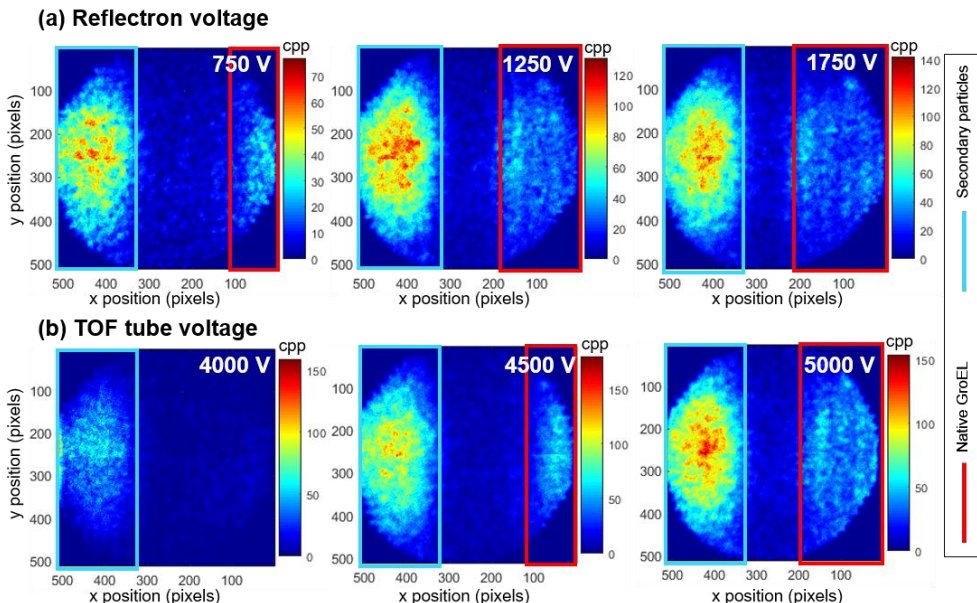
(b) TOF tube voltage

Figure S10. Spatial distribution of the ion cloud recorded at the detector for native GroEL ions upon varying (a) reflectron voltages and (b) TOF tube voltages. All data were acquired using an "ion energy=50 V". All the detected charge states of GroEL were used for the generation of the Timepix image. cpp = counts per pixel.

CHARACTERIZATION OF MICROCHANNEL PLATE DETECTOR RESPONSE FOR THE DETECTION OF NATIVE MULTIPLY CHARGED HIGH MASS SINGLE IONS IN ORTHOGONAL TIME-OF-FLIGHT MASS SPECTROMETRY USING A TIMEPIX DETECTOR

3

CHAPTER

Anjusha Mathew[1], Gert B. Eijkel[1], Ian G. M. Anthony[1], Shane R. Ellis[1,2], and Ron M. A. Heeren[1]

[1] MultiModal Molecular Imaging (M4i) Institute, Division of Imaging Mass Spectrometry (IMS), Maastricht University, 6229 ER Maastricht, The Netherlands
[2] Molecular Horizons and School of Chemistry and Molecular Bioscience, University of Wollongong, NSW 2522, Wollongong, Australia
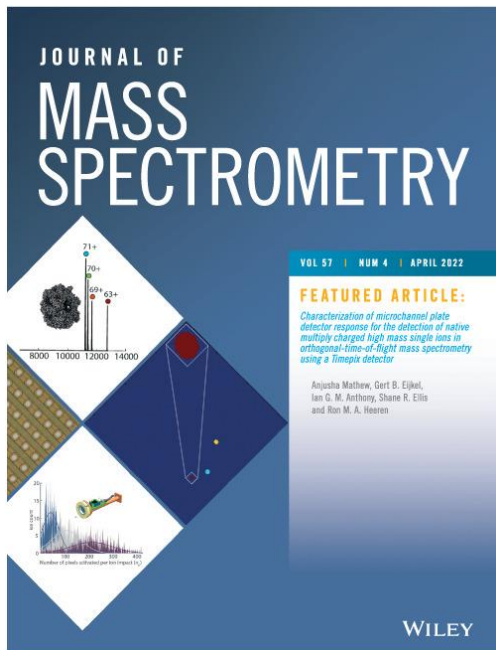
Showcasing *"Characterization of Microchannel Plate Detector Response for the Detection of Native Multiply Charged High Mass Single Ions in Orthogonal Time-of-Flight Mass Spectrometry Using a Timepix Detector"*

Cover page of Journal of Mass Spectrometry April 2022 Edition, Volume 57, Issue 4

3

ABSTRACT

Time-of-flight (TOF) systems are one of the most widely used mass analyzers in native mass spectrometry (nMS) for the analysis of non-covalent multiply charged bio-macromolecular assemblies (MMAs). Typically, microchannel plates (MCPs) are employed for high-mass native ion detection in TOF MS. MCPs are well known for their reduced detection efficiency when impinged by large slow moving ions. Here, a position- and time-sensitive Timepix (TPX) detector has been added to the back of a dual MCP stack to study the key factors that affect MCP performance for MMA ions generated by nMS. The footprint size of the secondary electron cloud generated by the MCP on the TPX for each individual ion event is analyzed as a measure of MCP performance at each mass-to-charge (m/z) value, and resulted in a Poisson distribution. This allowed us to investigate the dependency of ion mass, ion charge, ion velocity, acceleration voltage, and MCP bias voltage on MCP response in the high-mass low-velocity regime. The study of measurement ranges; ion mass = 195 to 802,000 Da, ion velocity = 8.4 to 67.4 km/s, and ion charge = 1+ to 72+ extended the previously examined mass range, and characterized MCP performance for multiply charged species. We derived an MCP performance equation based on two independent ion properties-ion mass and charge from these results, which enables rapid MCP tuning for single MMA ion detection.

Keywords: Microchannel plate detector, Native mass spectrometry, Single ion imaging, Time-of-flight mass spectrometry, Timepix detector

INTRODUCTION

The introduction of soft ionization techniques such as electrospray ionization (ESI)[48] and matrix-assisted laser desorption/ionization (MALDI)[56] in the late 1980s, allowed the mass analysis of intact biomolecules ranging from several daltons to few megadaltons.[57-59] The utilization of nanoESI source[49-50] and volatile high ionic strength solvents[51-52], and advancements in mass spectrometry (MS) instrumentation[65, 69, 72] further extended the mass range to several megadaltons, by enabling the ionization and analysis of non-covalent macromolecular assemblies (MMAs) in their pseudo-native state[94, 263-264], where the quaternary structure is retained, a method referred to as native MS (nMS).[40]

Time-of-flight (TOF) MS is one of the most commonly used mass analyzers for high mass detection due to its unlimited theoretical mass range, high sensitivity, and speed of analysis.[83-84] Ion detection in TOF MS is traditionally accomplished using microchannel plates (MCPs) because of their high gain, fast response, and large active area.[109-111] However, MCP detectors suffer from a reduced detection efficiency when impinged by large slowly moving ions.[257, 265-268] Hence, the key parameters affecting the detection of high mass non-covalent ions generated by nMS must be better understood. Here we conducted a detailed study to gain insight into the influence of critical ion and ion optical parameters on MCP detector performance for high-mass multiply-charged slow-moving protein/protein complex ions, using the spatially and temporally resolved detection of individual ion events.

In previous studies, the performance of the MCP has been examined for the detection of singly charged biomolecules of mass up to 290 kDa, by measuring the secondary electron yield (γ, average number of electrons produced within the MCP per initial ion impact event) or/and detection efficiency (ε, probability of generation of one or more secondary electrons during the initial ion impact event), by comparing the ion counts at different acceleration voltages[265], using a superconducting tunnel junction (STJ) detector[267] or an inductive charge detector (ICD)[257, 268] in parallel with MCP detector. Secondary electron emission from the impacts of low-velocity macro-ions of m/z < 100,000 from various conducting surfaces has also been studied.[256, 269-272] In this work, we have added an active pixelated detector (Timepix (TPX)) to the back of a dual MCP stack on a modified orthogonal reflectron TOF (O/R-TOF) MS (LCT) equipped with a nanoESI source.[71] With this unique setup, we analyzed the individual footprints of secondary electron clouds generated by the MCP on the TPX detector. As the size of each electron cloud depends on the number of electrons produced from an individual ion impact, this allowed us the study of MCP response as a function of various parameters for multiply charged MMA ions of molecular weights up to 802 kDa.

The TPX is a position- and time-sensitive charge detector consisting of a 512 x 512 pixel array with each pixel capable of recording both the arrival time and impact coordinates of impinging particles.[135] Despite the fact that TPX technology has its

origin in high energy physics[273-276], the integration of TPX with MCP amplifier allowed the detection of low energy particles[234, 277-279], which extended its scope to MS applications.[111] MCP-TPX assemblies have been used in MS with the goals (i) to improve the spatial resolution and throughput of MS imaging[139-140, 145, 147]; (ii) to investigate the ion transport properties through different ion optical elements of MS[71, 146, 148]; and (iii) for the enhanced detection of high mass ions.[71, 143-144] A previous study from our group conducted on the same TPX equipped LCT system has demonstrated the capability of TPX to detect non-covalent protein complexes and to image single ion events.[71]

We present a detailed characterization of MCP response for high mass multiple charged non-covalent species using the single ion imaging capability of the TPX detector. We analyzed the electron cloud footprints on the TPX corresponding to each mass-to-charge (m/z) value from a set of 16 samples that encompasses the following measurement ranges; ion mass = 195 to 802,000 Da, TOF = 16 to 155 µs, ion velocity = 8.4 to 67.4 km/s, ion charge = 1+ to 72+, m/z = 195 to 12, 500 Da, ion energy = 4.6 to 331.2 keV. The main objective of this study is to develop a better understanding of the dependency of ion mass, ion velocity, ion charge, acceleration voltage, and MCP bias voltage on MCP performance in high-mass low-velocity regime.

MATERIALS AND METHODS

Materials

Ubiquitin (8.6 kDa) from bovine erythrocytes, cytochrome C (12.4 kDa) from equine heart, myoglobin (17.6 kDa) from equine heart, carbonic anhydrase (29 kDa) from bovine erythrocytes, bovine serum albumin (BSA, 66.4 kDa), conalbumin (77 kDa) from chicken egg white, concanavalin A (102 kDa) from Canavalia ensiformis, alcohol dehydrogenase from Saccharomyces cerevisiae (147.5 kDa), trastuzumab monoclonal antibody (148 kDa), beta-amylase (β-amylase, 223.8 kDa) from sweet potato, pyruvate kinase (232 kDa) from rabbit muscle, apoferritin (480 kDa) from equine spleen, chaperonin 60 (GroEL, ~802 kDa) from Escherichia coli, ammonium acetate, tris acetate, potassium chloride, ethylenediaminetetraacetic acid (EDTA), adenosine-5'-triphosphate (ATP), magnesium chloride, ammonium hydroxide, and acetic acid were all purchased from Sigma-Aldrich (Zwijndrecht, The Netherlands). Pierce™ LTQ ESI positive ion calibration solution (195 to 1,522 Da) and cesium iodide (CsI, 392.7 to 11,304 Da) were purchased from Thermo Fisher Scientific, The Netherlands. Glu-fibrinopeptide B (1.6 kDa) was obtained from Waters, The Netherlands. Methanol, acetone, isopropanol, and LC-MS grade water were purchased from Biosolve (Valkenswaard, The Netherlands).

Sample Preparation

Ubiquitin, cytochrome C, myoglobin, carbonic anhydrase, BSA, conalbumin, concanavalin A, alcohol dehydrogenase, trastuzumab monoclonal antibody,

and beta-amylase were dissolved to a stock concentration of 100 μM in LC-MS grade water. These samples and aqueous solutions of pyruvate kinase and apoferritin were buffer exchanged with 200 mM ammonium acetate at pH 6.8 using 3/10/30 kDa molecular weight cutoff (MWCO) Amicon Ultra centrifugal filter (Millipore, Merck KGaA, Germany) to a final monomer concentration of 5-30 μM. The preparation of GroEL was performed as described previously.[71] Glu-fibrinopeptide B was dissolved in 200 mM ammonium acetate (pH 6.8) to a concentration of 5 μM. Cesium iodide was prepared as 2 mg.ml^{-1} solution in 1:1 isopropanol:water (v:v).

Mass Spectrometer and Detection System

All experiments were performed on a modified LCT nESI-O-TOF mass spectrometer (Micromass, Manchester, UK) equipped with a TPX detector that has recently been described in detail in reference.[71] Samples were introduced into the mass spectrometer using homemade gold-coated needles via an in-house built static nanoESI source. Ions are transferred into an orthogonal acceleration TOF mass analyzer for TOF separation via two differentially pumped hexapole RF lenses. The instrument has been modified for improved transmission of high m/z ions as described previously.[71]

The detector assembly consists of an MCP-TPX system. The dual chevron MCP stack (Type No. F4294-07, Hamamatsu Photonics, Japan) employed in this study has the following properties; 27 mm effective diameter, 0.4 mm plate thickness, 12° bias angle, 12.5 μm channel center-to-center spacing, 10 μm channel diameter, and 4–20 μA strip current. A bare TPX quad application-specific integrated circuit (ASIC) is positioned 2 mm behind the dual MCP stack of the LCT to detect the secondary electron clouds emitted from the MCP during an ion event. The TPX is a position- and time-sensitive charge detector consisting of 512 × 512 pixel array with a pixel pitch of 55 μm, in which each pixel is a single stop time-to-digital converter (TDC) that registers an event once the input charge of a given pixel exceeds a certain threshold (equivalent to ~600 electrons).[135] In this study, TPX has been operated in time-of-arrival (TOA) mode, in which the time of activation of each pixel is measured along with pixel coordinates with respect to an external trigger.[140] The TPX was triggered at a rate of 30-40 Hz using a down-sampled version of the main trigger pulse that starts the orthogonal acceleration in the pusher, via a digital pulse and delay generator (DG535, Stanford Research Systems). All experiments were performed using a 20 ns TPX clock width, corresponding to a maximum measurement window of 236.2 μs for each TOF cycle. All data reported in this paper were recorded using the following voltage settings; DC offset 1: 10 V, DC offset 2: 6 V, ion energy: 10 V, aperture: 20 V, TOF tube: 4,600 V, reflectron: 1,000 V, MCP gain: 1,600 V and TPX: -2,200 V unless stated otherwise. This resulted in typical flight times between 16 and 155 μs. 5 μL of each sample was loaded into the nano-ESI needle and a spray voltage of 0.9-1.8 kV was applied. All ion optics parameters except the TPX and spray voltages were defined via MassLynx V4.1 software (Waters, Wilmslow, UK). External power

supplies (FuG Elektronik GmbH, Schechen, Germany) were used to provide a voltage offset to the TPX relative to the back MCP, and spray voltage.

All samples were characterized using a Q Exactive UHMR Hybrid Quadrupole-Orbitrap mass spectrometer (Thermo Fisher Scientific, Bremen, Germany) prior to the measurements on the LCT-TPX system for the TOF to m/z conversion.

Data Acquisition and Analysis

The SoPhy (Software for Physics) software package version 1.5.2 was used for TPX chip control and data acquisition (Amsterdam Scientific Instruments, Amsterdam, The Netherlands). 5,000-10,000 TOF cycles (frames) were collected and summed for each dataset. SoPhy generates a binary 512 x 512 frame for each TOF cycle. Every x-y position (pixel) in the frame contains information on the number of clock counts passed since the start of the TOF cycle and the arrival of sufficient charge to trigger that pixel. 100 frames are bundled in a zipped output file. An in-house developed algorithm written in MATLAB (R2014a, MathWorks Inc., Natick, MA, USA) was used to convert the data to NetCDF format and to select sub-frames from frames and TOF ranges. The MATLAB functions 'bwlabel' and 'regionprops' were used to detect and measure the properties of connected areas (pixel clusters) in 2D binary sub-frames.

RESULTS AND DISCUSSION

Single Ion Imaging Using MCP-Timepix Assembly

MCP assemblies are particle amplifiers that intensify low-energy particles by the multiplication of electrons via secondary emission and amplification. The amount of secondary electrons generated within the dual MCP stack is related to the impinging particle properties and bias voltage across the MCP plates (MCP bias voltage). Zero to n number of electrons may eject from the front MCP plate upon the impact of a single ion on one of the microchannels, and these electrons generate more electrons and are accelerated to the back MCP plate based on the MCP bias voltage. Under typical MS conditions, the amplification factor is often nominally in the order of 10^5-10^6. The secondary electron multiplicity is described by a Poisson distribution given by

$$P_n = \frac{\gamma^n e^{-\gamma}}{n!} \tag{1}$$

where P_n is the probability of emitting n electrons from the MCP, and γ is the average number of electrons emitted per initial ion impact, known as secondary electron yield.[257] The detection efficiency, ε, is defined as the probability of emitting at least one electron from a single ion impact, and is given by

$$\varepsilon = 1 - P_0 = 1 - e^{-\gamma} \tag{2}$$

where P_0 is the probability of not emitting any electrons, and is calculated as $e^{-\gamma}$ from Equation 1.

In TOF MS, all ions are accelerated with the same kinetic energy per charge since they are all subjected to the same acceleration voltage, $zeV = \frac{1}{2}mv^2$, where ze, V, m, and v are ion charge (e is the charge of an electron and z is the number of charges on the ion), acceleration voltage, ion mass, and ion velocity, respectively. High m/z ions impinge the MCP detector with a lower velocity, resulting in reduced γ, making it harder to detect large slow moving ions.[257, 265-268]
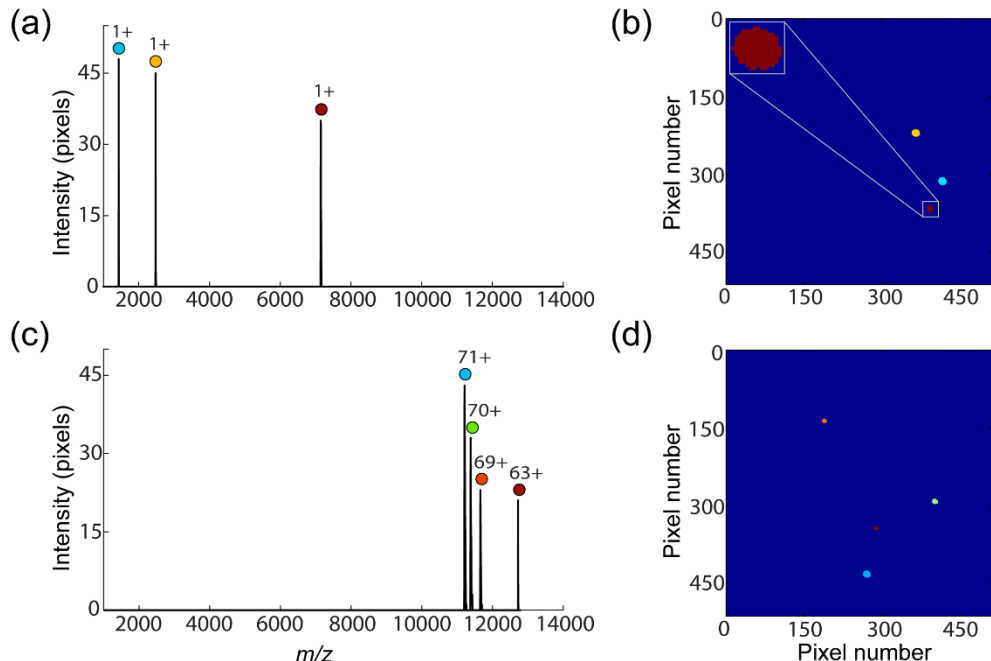
Figure 1. (a) Mass spectrum and (b) TPX image acquired from a single TOF cycle using CsI mix (mass range: 392 to 11,304 Da, charge =1). (c) Mass spectrum and (d) TPX image acquired from a second single TOF cycle by spraying GroEL (mass: 800 kDa, charge range: 63+ to 72+) under native conditions. The y-axis in (a) and (c) represents the number of TPX pixels activated for each ion event. Each color in the single-frame TPX image corresponds to a different m/z or TOA.

Several groups previously examined the performance of the MCP in the high-mass low-velocity regime by measuring γ and/or ε with different approaches. Macfarlane's group has calculated ε through the following procedure. First, the ion intensity at a high acceleration potential was measured to determine the integrated intensity of particular ions under conditions where $P(γ) = 1$ (i.e. γ is a large number). Then, the integrated intensity of the same ions was measured at the velocity of interest by reducing the acceleration voltage. Later, the ratio of two intensities was taken for the calculation of ε. Note that the ion intensity was derived using the single ion counting technique. The study was conducted for the following measurement range; mass = 86-5,734 Da, charge = 1, velocity = 13-32 km/s, and acceleration voltage = < 20 kV.[265] Benner's group measured ion intensity using MCP along with an STJ detector, which has 100% detection efficiency, exposing both the detectors simultaneously to nearly identical ion

fluxes for the following measurement conditions; mass= 1.3-66 kDa, charge = 1, velocity = >5 km/s and acceleration voltage = 10-30 kV.[267] Smith's group calculated γ by detecting ions in parallel using both an in-line non-destructive ICD that provides an absolute measure of the number of ions, and an MCP detector, for the following conditions; mass= 1-290 kDa, charge = ±1, velocity =3.5-68 km/s and acceleration voltage = 10-25 kV. [257, 268] In this work, a time- and position-sensitive TPX detector has been combined with a dual MCP stack for the MCP characterization and thus measures the arrival time and size of the emitted electron pulses that span multiple pixels (Supporting Information Figure S1) but correspond to individual ion events.
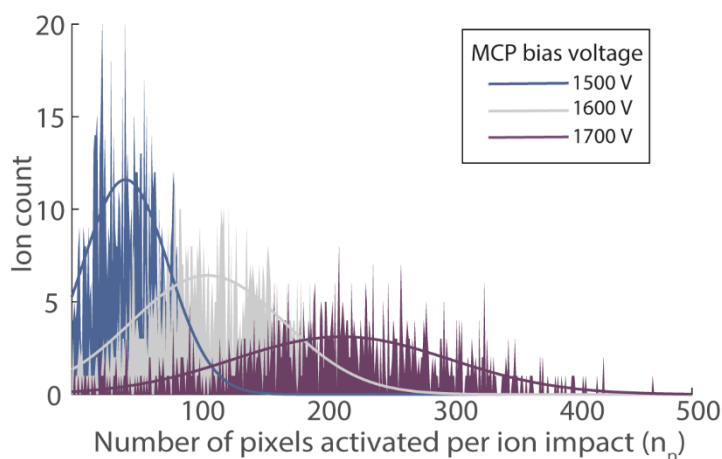
Figure 2. Distribution of pixel cluster area (in pixels, n_p) of ~ 930 cytochrome C [M + 7H]$^{7+}$ ions from 5,000 TOF cycles acquired for different MCP bias voltages, and corresponding Gaussian fits.

The detection in TPX is frame-based, and each frame corresponds to a single TOF cycle. Figure 1a,b shows the single frame spectrum and the image generated by spraying CsI mix (mass range: 392 to 11,304 Da, charge =1), and Figure 1c,d corresponds to the single frame spectrum and image of GroEL (mass: 800 kDa, charge range: 63+ to 71+). Each impact event in the single-frame image corresponds to the electron footprint of a single ion event at the MCP and is associated with a single peak in the mass spectrum. The number of pixels activated by each ion event (n_p) is related to the number of electrons emitted from the MCP, which in turn is related to the efficiency of the initial ion-to-electron conversion, amplification steps through the channels of MCP, and the space charge-driven expansion of the electron pulse between the MCP and TPX. In this work, we have measured n_p instead of γ/ε to investigate the dependency of ion and voltage parameters on the MCP detector response. Figure 1 suggests that n_p increases or MCP response improves with an increase in ion charge and a decrease in ion mass. However, it is hard to draw a conclusion only by analyzing a single frame. Hence, we have analyzed n_p corresponds to a single m/z or TOA from all the frames. This produces a Poisson statistics (Equation 1) as expected. Figure 2 shows the distribution of n_p of ~930 cytochrome C [M + 7H]$^{7+}$ (m/z =

1766.7*)* ions from 5,000 TOF cycles acquired for different MCP bias voltages and corresponding Gaussian fits. A higher MCP bias voltage produces more secondary electrons on average for a single ion event. This in turn leads to higher columbic repulsion of the electron pulse as it travels towards the TPX and thus results in the activation of more pixels. The effect of MCP bias voltage on the detection efficiency will be discussed in more detail later in this article.

Influence of Ion Properties on MCP Performance

In this section, the single ion imaging capability of TPX has been utilized to study the influence of ion properties on ion to electron conversion factor, and thus the MCP response. γ is generally expressed as a function of two dependent parameters-ion mass and velocity[257, 267-268], given by

$$\gamma = k_0 m^a v^b \tag{3}$$

where k_0 is the constant of proportionality, and a and b are fit parameters. Combining Equation 3 with basic TOF MS equation

$$v = \sqrt{\frac{2zeV}{m}} \tag{4}$$

yields the relation

$$\gamma = k_0 m^{\frac{2a-b}{2}} (2zeV)^{\frac{b}{2}} \tag{5}$$

Equation 5 can be rewritten as a function of two independent parameters-ion mass and charge, at a given acceleration voltage as

$$\gamma = k_1 m^c z^d \tag{6}$$

where $k_1 = k_0(2eV)^{b/2}$, c = (2a-b)/2 and d = b/2.
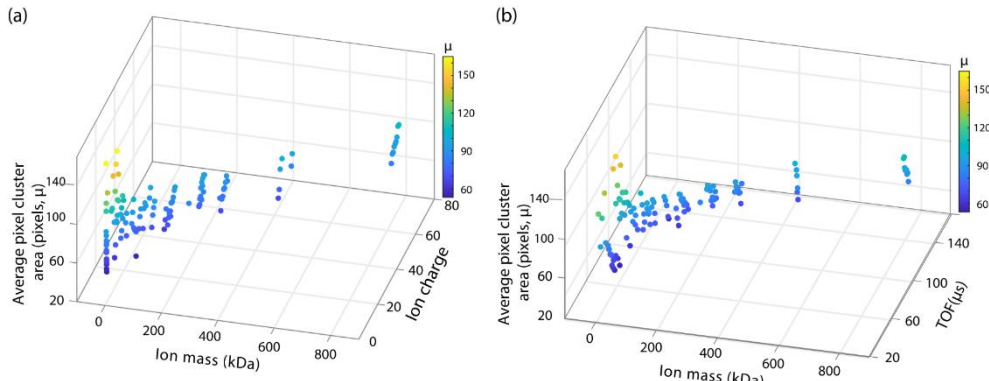
Figure 3. 3D scatter plots showing the effect of (a) ion mass and charge and (b) ion mass and TOF on the average pixel cluster area (in pixels, μ). All the data were acquired using the following conditions; Sample cone: 20-190 V, Extraction cone: 10-80 V, RF lens: 200-2,000 V, DC offset 1: 10 V, DC offset 2: 6 V, ion energy: 10 V, aperture: 20 V, TOF tube: 4,600 V, reflectron: 1,000 V, MCP gain: 1,600 V, TPX: -2,200 V and TOF cycles: 5,000-10,000.

In this study instead of calculating γ, we have measured the mean n_p (μ) that corresponds to each m/z or TOA, which is proportional to γ. This is done by spraying 16 samples that encompass the following measurement range; m = 195 to 802,000 Da, TOF = 16 to 155 μs, v = 8.4 to 67.4 km/s, z = 1+ to 72+, m/z = 195 to 12,500, ion energy = 4.6 to 331.2 keV under identical ion optical conditions. Figure S2 (Supporting Information) shows the TOF to m/z conversion curve, plotted by comparing LCT measured TOF data with the Orbitrap m/z spectrum of each sample. From Equation 4 and calibration curve, v can be written as $k_2TOF^{-0.99}$, where $k_2 = (1.142 \times 10^6)k_0$. Therefore, Equations 3 & 6 can be rewritten to calculate μ as,

$$\mu = k_3 m^c z^d = k_4 m^a TOF^{-0.99b} \tag{7}$$

where $k_3 = (\mu/\gamma)k_1$ and $k_4 = (\mu/\gamma)k_2$.
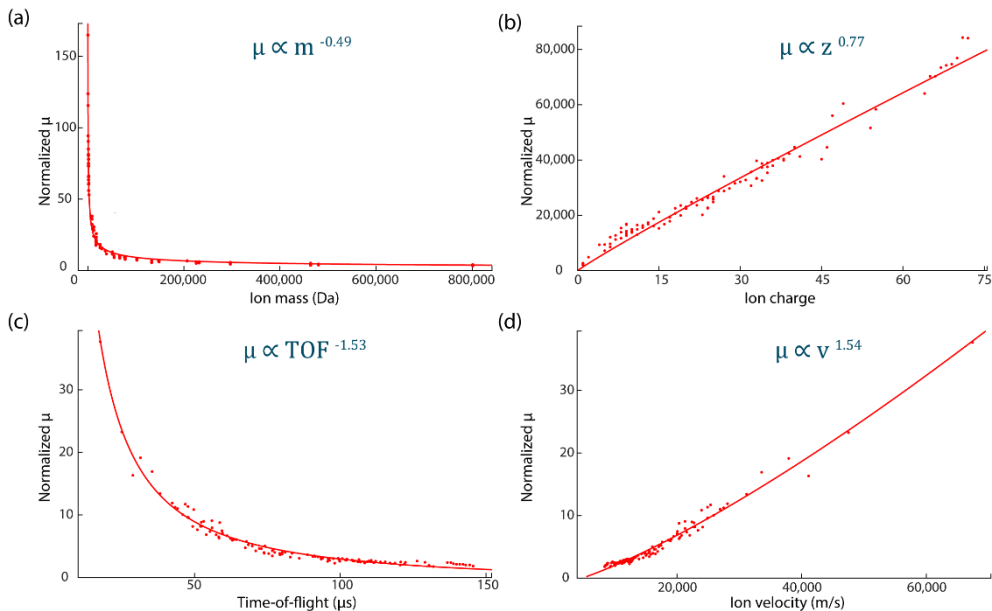
Figure 4. Influence of different ion properties ((a) ion mass (b) ion charge (c) TOF and (d) ion velocity) on the average pixel cluster area (in pixels, μ). μ has been normalized by a factor of $z^{0.77}$ for (a), $m^{-0.49}$ for (b), and $m^{0.28}$ for (c) and (d).

Figure 3a,b are the 3D graphs, in which μ is plotted between m and z, and m and TOF, respectively. 3D curve fitting yields the values of 0.28, 1.54, -0.49, and 0.77 for the power constants a, b, c, and d respectively. Figure 4 and Figure S3 demonstrate the dependency of normalized μ on m (R^2= 0.987), z (R^2= 0.982), TOF (R^2= 0.976), v (R^2= 0.978), m/z (R^2= 0.979) and ion impact energy (E= zeV, R^2= 0.982). The detector performance has been shown to improve with an increase in q, v and E, as well as with a decrease in m, m/z and TOF of the ion beam, which is in good agreement with the previous studies. However, the values of the exponents of mass and velocity appear to be different from the earlier studies, which can be attributed to the difference in the curve-fitting approach. In

previous works, in order to separate out the dependence of γ on m and v, γ has been plotted as $\gamma_{red} = \gamma /m$, called as reduced secondary electron yield, and fitted to a simple power law $\gamma_{red} = k_5 v^f$ [257, 267-268] or exponential function $\gamma_{red} = k_6 e^{gv}$ [265], where k_5 and k_6 constants of proportionality, and f and g are fit parameters. Here instead of assuming a linear dependence of m on γ, 3D curve fitting method was employed, which yields γ or $\mu \propto m^{0.28}v^{1.54}$ or $m^{-0.49}q^{0.77}$. For validating the derived function, the deviation of the experimentally determined γ value from Smith's data[257] from their (2.6×10^{-18} $mv^{3.1}$) and our (1.04×10^{-8} $m^{0.28}v^{1.54}$) fit functions were compared (Supporting Information Figure S4). Interestingly, our function fits better to the Smith data with an RMS error of 0.203 than their fit (RMS error = 0.247). Note that the μ to γ conversion was performed by calculating the ratio of k_0 to k_4, fitting $m^{0.28}v^{1.54}$ to the μ data from this study and the γ values from Smith's group.

Influence of Ion Optics on MCP Performance

We next investigated the influence of ion optics on the MCP detection efficiency. In our previous work, we have shown that the voltage settings "ion energy" and "RF DC offset voltage of first hexapole" has an influence on the axial ion energy of the ion beam, while "TOF tube voltage" affects the orthogonal ion energy.[71] An increase in ion-to-electron conversion efficiency has been expected with a raise in orthogonal voltage as per Equation 5. Figure 5a shows the increasing trend of μ with the orthogonal TOF tube voltage. As per equation 5, a power function of 0.77 was expected to fit with the TOF tube voltage-μ curve. However, the limited control over the TOF tube voltage (4,000 to 5,000 V) allows a change in velocity of the myoglobin $[M+7H]^{7+}$ ions from 17.6 to 19.6 km/s and concanavalin A dimer $[M+13H]^{13+}$ ions from 13.4 to 14.9 km/s, which covers only a very small portion of the velocity range shown in Figure 4d. Therefore, it is difficult to fit a power function to the TOF tube voltage-μ curve with the limited number of data points. As expected μ value remains unaffected by voltage settings "RF DC offset of first hexapole" and "ion energy", since both these voltages contribute to the total energy of the ion beam only through the axial velocity component, which is parallel to the detection plane.

As discussed in the previous section, a higher MCP bias voltage increases the number of secondary electrons generated in each amplification step within the MCP, and thus raises μ (Figure 5b). Figure 5b fits an exponential function as expected. An increase in MCP bias voltage enhances the MCP output signal quality to some extent for high-mass species. However, the independency of the ion-to-electron conversion factor on the MCP bias voltage still limits the detection of large slow moving ions.
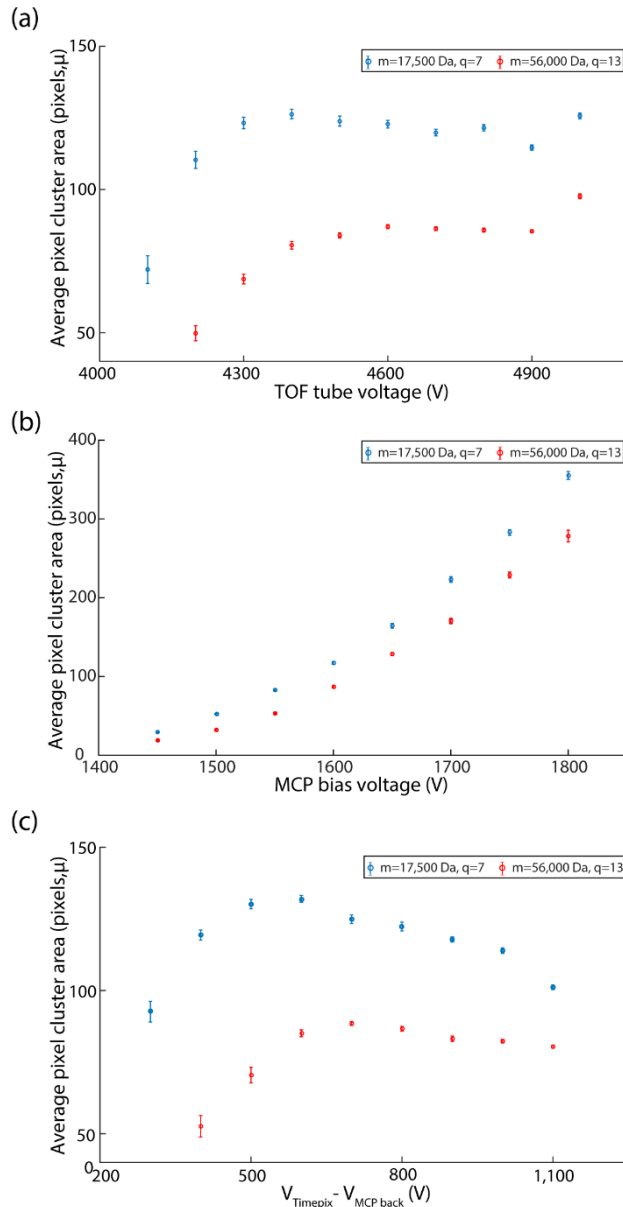
Figure 5. Effect of different ion optics parameters ((a) TOF tube voltage, (b) MCP bias voltage, and (c) voltage difference between MCP back plate and TPX detector ($V_{TPX-MCP\ back}$)) on the average pixel cluster area (in pixels, μ). Red and blue traces correspond to concanavalin A dimer $[M+13H]^{13+}$ and holo-myoglobin $[M+7H]^{7+}$ ions, respectively.

$V_{TPX-MCP\ back}$, the potential gradient between the MCP back plate and TPX detector, is one of the parameters that has an influence on the overall detector performance. Figure 5c shows the dependence of μ on the $V_{TPX-MCP\ back}$. At a lower $V_{TPX-MCP\ back}$, the potential gradient is not strong enough to accelerate and focus the electron clouds from the MCP to the TPX at the low voltage. Most importantly,

the charge deposited into a single pixel by the electron clouds is not adequate for the activation of TPX pixels. A higher amount of charge is deposited with an increase in TPX voltage, which leads to an increase in μ. However, after attaining a maximum value, μ tends to decrease due to the space charge effect. At a higher $V_{TPX-MCP\ back}$, electrons are accelerated much faster toward the TPX detector, providing less time for the electron cloud to expand, which leads to the activation of less number of TPX pixels. The space charge-driven expansion of the electron cloud was expected to fit a cosine distribution.[280-281]

Understanding the influence of ion optics on MCP detector efficiency or electron cloud footprint size is crucial in the context of using an MCP as an image intensifier when combining with position readout systems such as charge-coupled device (CCD), resistive anode encoder, delay line detector, discrete anode array detector, wedge and stripe anodes, hybrid active pixel detector (Medipix/Timepix, Pixel Imaging Mass Spectrometry (PImMS) camera, etc.) for the imaging of low energy photons (soft X-ray, UV and visible), alpha particles, ions, and neutrons in various applications.[111-112, 282-285] Optimization of the event charge footprint is required to achieve high spatial resolution and appropriate image linearity. A narrow charge cloud can cause image distortion, whereas excessive spreading of the charge footprint leads to distortion at the image edges. It was observed that the TOF tube voltage, MCP bias voltage, and potential gradient between the back plate of the MCP and TPX can be used to fine-tune the electron cloud footprint to achieve optimum image quality. These results are in good agreement with the previous studies conducted on the MCP electron charge cloud analysis using MCP in combination with split-strip anode, cross-strip anode, phosphor screen-CCD assembly, and discrete anode array, where they have shown that the charge cloud can be expressed as a function of MCP bias voltage, acceleration bias voltage and distance between the back plate of the MCP and position readout system.[286-289]

CONCLUSIONS

This study comprises the comprehensive analysis of MCP detector performance in terms of ion properties and ion optics parameters for high-mass multiply-charged non-covalent protein/protein complex ions that encompass a wide mass range from 195 to 802,000 Da. The utilization of a TPX detector combined with the dual MCP stack allowed the characterization of MCP performance by analyzing the footprints of secondary electron clouds generated by the MCP on TPX corresponding to each individual ion event. Oversampling each individual ion event by a number of pixels for a number of TOF cycles makes this the best method to examine the MCP response. The MCP detector performance is shown to improve with an increase in ion charge, velocity, and energy, and deteriorates with an increase in ion mass, m/z, and TOF. The dependence of ion optical parameters such as TOF tube voltage, MCP bias voltage, and potential gradient between the back plate of the MCP and TPX on the MCP charge cloud footprint can be utilized to achieve optimum image quality when MCP is used in imaging

systems, as well as to improve native macromolecular ion detection efficiency in the high-mass low-velocity regime.

SUPPORTING INFORMATION
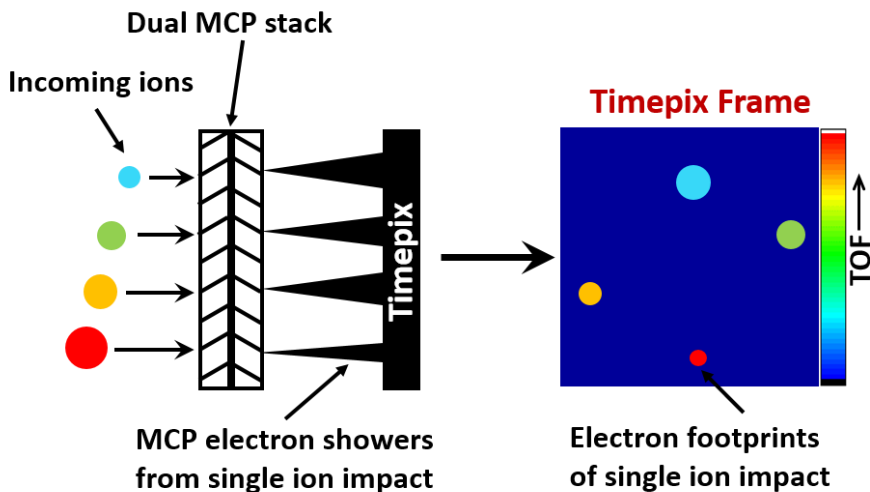
Figure S1. Schematic of the ion detection mechanism in MCP-TPX detection assembly. A number of electrons are ejected from the front MCP plate upon the impact of the ions. These electrons generate more electrons that are accelerated to the back MCP plate based on the MCP bias voltage. The TPX detector positioned behind the back MCP measures the arrival time, position, and size of the emitted electron pulses that span multiple pixels.
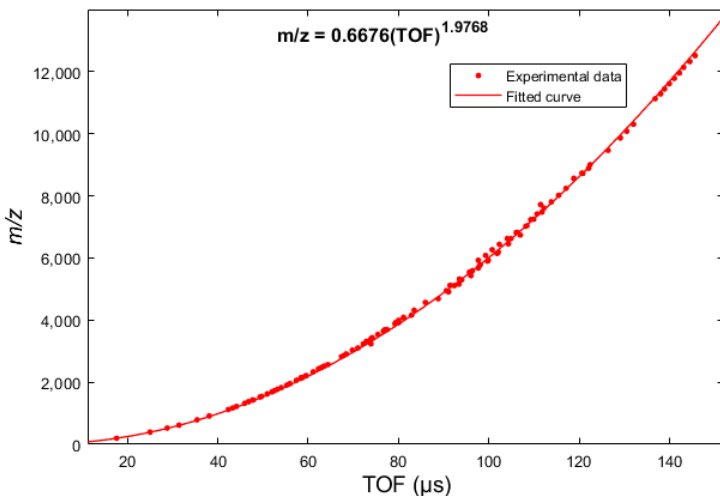
Figure S2. TOF to *m/z* conversion curve, plotted by comparing LCT measured TOF data with the Orbitrap *m/z* spectrum of each sample. Calibration was performed by spraying 16 samples that encompass the following mass range; m = 195 to 802,000 Da. All LCT TOF data were collected using the following voltage settings; TOF tube: 4,600 V, reflectron: 1,000 V, MCP gain: 1,600 V, and TPX: -2,200 V.
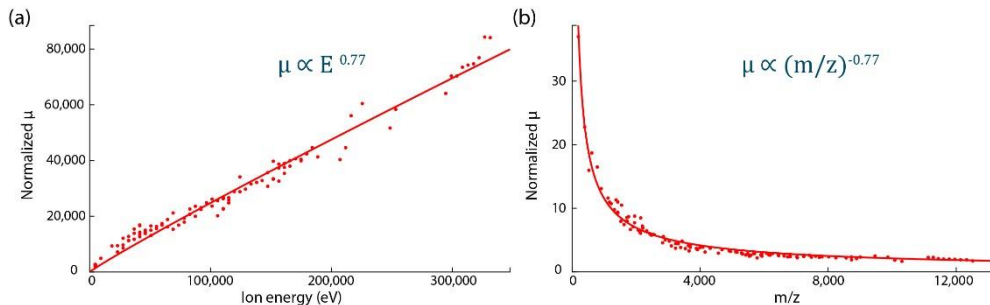
Figure S3. Influence of different ion properties ((a) ion energy (b) m/z) on the average pixel cluster area (in pixels, μ). μ is normalized by a factor of m^{-49} for (a) and $m^{0.28}$ for (b).
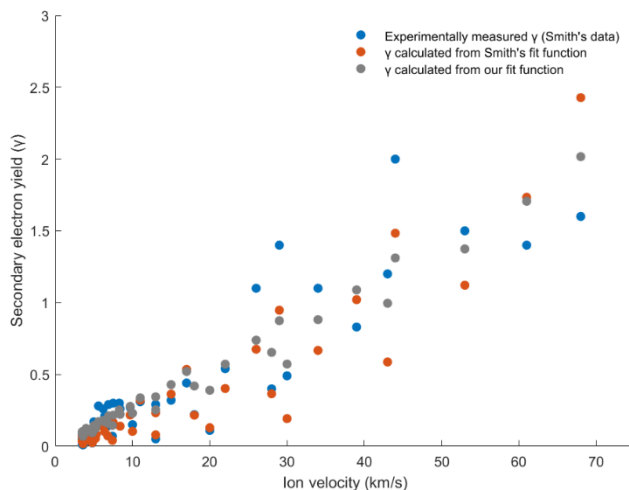
Figure S4. Secondary electron yield plotted as a function of ion velocity. The data shown in blue corresponds to the experimentally measured γ values from Smith's group.[257] Orange and grey markers are the γ values calculated using Smith's ($2.6 \times 10^{-18} \, mv^{3.1}$) and our ($1.04 \times 10^{-8} \, m^{0.28}v^{1.54}$) fit functions, respectively.

3

TIME-RESOLVED IMAGING OF HIGH-MASS PROTEINS AND METASTABLE FRAGMENTS USING MATRIX-ASSISTED LASER DESORPTION/IONIZATION, AXIAL TIME-OF-FLIGHT MASS SPECTROMETRY, AND TPX3CAM

4

CHAPTER

Anjusha Mathew[1], Joel D. Keelor[2], Gert B. Eijkel[1], Ian G. M. Anthony[1], Jingming Long[2], Jord Prangsma[2], Ron M. A. Heeren[1], and Shane R. Ellis[1,3]

[1] Maastricht MultiModal Molecular Imaging (M4i) Institute, Division of Imaging Mass Spectrometry (IMS), Maastricht University, 6229 ER Maastricht, The Netherlands
[2] Amsterdam Scientific Instruments (ASI), Science Park 106, 1098 XG Amsterdam, The Netherlands
[3] Molecular Horizons and School of Chemistry and Molecular Bioscience, University of Wollongong, NSW 2522, Wollongong, Australia

ABSTRACT

The Timepix (TPX) is a position- and time-sensitive pixelated charge detector that can be coupled with time-of-flight mass spectrometry (TOF MS) in combination with microchannel plates (MCPs) for the spatially and temporally resolved detection of biomolecules. Earlier generation TPX detectors used in previous studies were limited by a moderate time resolution (at best 10 ns) and single-stop detection for each pixel that hampered the detection of ions with high mass-to-charge (m/z) values at high pixel occupancies. In this study, we have coupled an MCP-phosphor screen-TPX3CAM detection assembly that contains a silicon-coated TPX3 chip to a matrix-assisted laser desorption/ionization (MALDI)–axial TOF MS. A time resolution of 1.5625 ns, per-pixel multihit functionality, simultaneous measurement of TOF and time-over-threshold (TOT) values and kHz readout rates of the TPX3 extended the m/z detection range of the TPX detector family. The detection of singly charged intact immunoglobulin M ions of m/z value approaching 1×10^6 Da has been demonstrated. We also discuss the utilization of additional information on impact coordinates and TOT provided by the TPX3 compared to conventional MS detectors for the enhancement of the quality of the mass spectrum in terms of signal-to-noise (S/N) ratio. We show how the reduced dead time and event-based readout in TPX3 compared to the TPX improves the sensitivity of high m/z detection in both low and high mass measurements (m/z range: 757 to 970,000 Da). We further exploit the imaging capabilities of the TPX3 detector for the spatial and temporal separation of neutral fragments generated by metastable decay at different locations along the field-free flight region by simultaneous application of deflection and retarding fields.

4
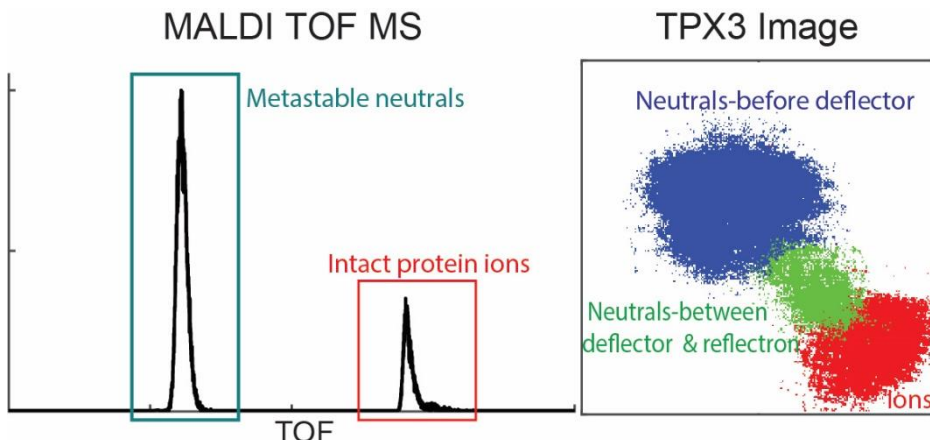
Keywords: High m/z detection, Matrix-assisted laser desorption/ionization, Metastable fragmentation, Time-of-flight mass spectrometry, Timepix detector

INTRODUCTION

The Timepix (TPX) detector family consists of position- and time-sensitive pixelated charge detectors, with each pixel capable of recording both the arrival time and impact position coordinates of impinging particles.[135, 137-138] Although TPX detectors originate from high-energy physics, the integration of TPX with microchannel plate (MCP) amplifiers has enabled the detection of low-energy particles[234, 279, 285] that extended their scope to biomolecular mass spectrometry (MS).[71, 139-151, 290] MCP-TPX detection systems were previously coupled to time-of-flight (TOF) mass spectrometers equipped with nano/micro-electrospray ionization (ESI), matrix-assisted laser desorption/ionization (MALDI) or secondary ion MS (SIMS) sources, where the arrival time information at the TPX detector was used for the generation of the mass spectrum. The additional impact position information provided by the TPX compared to conventional MS detectors has previously been utilized to obtain insight into the ion transport properties and ion optical processes within the MS[71, 146, 148, 150], as well as to improve the spatial resolution and throughput of MS imaging via stigmatic ion imaging.[139, 141-142, 145, 147, 151] The TPX detector used for previous studies was limited by a moderate time resolution (at best 10 ns) and single-stop detection for each pixel that can result in a low intensity of higher mass-to-charge (m/z) signals (longer flight time) due to the occupancy of pixels by earlier arriving ions.[135]

In this study, we have coupled an MCP-phosphor screen-TPX3CAM detection assembly[291-293] that contains a silicon (Si)-coated TPX3 chip, the successor of the TPX, for the first time to a MALDI-axial TOF MS (Bruker Ultraflex III). The TPX3 offers a time resolution of 1.5625 ns, allows simultaneous measurement of time-of-arrival (TOA) and time-over-threshold (TOT) values, and operates under data-driven readout mode.[137] Unlike the previous MCP-bare TPX single/quad systems that had to be placed in vacuum, the additional signal conversion steps in MCP-phosphor screen-TPX3CAM detection assembly allowed the TPX3CAM to be installed at atmospheric pressure that brings considerable flexibility, elimination of several elements, and flexible mapping between phosphor screen and sensor area.

Previous investigations conducted on the Ultraflex III MS coupled with MCP-TPX assembly and the modified LCT (nanoESI-orthogonal acceleration reflectron TOF) MS coupled with HV-floating MCP-TPX quad system demonstrated the ability of TPX to detect intact protein ions with m/z values up to 400,000 Da[143] and multiply charged non-covalent protein complexes of molecular weight up to 800,000 Da (m/z < 13,000 Da).[71, 290] Here, we extend the m/z detection range of TPX family up to 970,000 Da by the measurement of single-charged intact immunoglobulin M (IgM) ions using the MCP-phosphor screen-TPX3CAM assembly, which has previously been used with great success in velocity map imaging to investigate small-molecule reaction dynamics.[261, 294-300] In addition, we demonstrate the utilization of multiple information provided by TPX3 such as TOA, pixel coordinates and TOT for better visualization of the mass spectrum. We discuss how the reduced dead time and event-based readout in TPX3 compared to the TPX

enhances both the low and high mass measurements (m/z/mass range: 757 to 970,000 Da) and enables the operation of the whole system ten times faster. These capabilities of the TPX3 detector allowed us to explore the spatial detection and separation of precursor ions and neutral fragments formed via metastable decay at the different locations within the field-free TOF tube. These spatio-temporal studies provide insights into the molecular processes, such as post-source decay (PSD) that occur in axial TOF systems.

MATERIALS AND METHODS

Materials

Insulin chain B oxidized (3.5 kDa) from bovine pancreas, insulin (5.7 kDa) from bovine pancreas, cytochrome c (12.4 kDa) from equine heart, myoglobin (17.6 kDa) from equine heart, immunoglobulin G (IgG, ~150 kDa) from human serum, immunoglobulin A (IgA, ~400 kDa) from human colostrum, a-cyano-4-hydroxycinnamic acid (CHCA), sinapinic acid (SA) and trifluoroacetic acid (TFA) were all purchased from Sigma-Aldrich (Zwijndrecht, The Netherlands). The peptide calibration standard II (m/z range: 700-3200 Da), protein calibration standard I (m/z range: 5 to 18 kDa), and protein calibration standard II (m/z range: 10 to 70 kDa) were purchased from Bruker GmbH (Bremen, Germany), and C450 IgM MALDI MS Calibration Kit (~970 kDa) was purchased from CovalX (Zürich, Switzerland). Acetonitrile and liquid chromatography-mass spectrometry (LC-MS) grade water were purchased from Biosolve (Valkenswaard, The Netherlands).

Sample Preparation

Insulin chain B, insulin, cytochrome c, myoglobin, IgG, and IgA were prepared as 0.5-2 mg/mL solution in water. One tube of peptide calibration standard II/protein calibration standard I/protein calibration standard II was dissolved in 125 µL 0.1% TFA solvent according to the manufacturer's instructions. The SA was prepared as a 20 mg/mL solution in 50% acetonitrile + 0.1% TFA. The CHCA matrix was prepared as 10 mg/mL solution in 70% acetonitrile + 0.2% TFA. The prepared aliquots of proteins/peptides were mixed 1:1 (v:v) with matrix solutions. 1 µL aliquots of each analyte:matrix solution were then deposited onto a stainless steel target plate and air-dried prior to the MS analysis.

TPX3CAM

The TPX3CAM (Amsterdam Scientific Instruments, Amsterdam, The Netherlands) is a fast optical imager based on a specialized Si sensor bump-bonded to the Timepix3 application-specific integrated circuit (TPX3 ASIC) readout chip (Medipix3 collaboration, CERN, Geneva, Switzerland).[137, 261, 293] The 300 µm thick silicon sensor has a thin entrance window and anti-reflective coating, and provides an enhanced quantum efficiency (QE) about 90% over the wavelength range 400-1000 nm. The TPX3 chip is produced in 130 nm CMOS technology and

consists of a 256 × 256 pixel matrix having a pixel pitch of 55 μm and dimensions of 1.4 × 1.4 cm^2. Unlike its precursor TPX chip[135] where the readout is frame-based, the readout from TPX3 is data-driven, whereby data is immediately sent out upon the activation of each pixel. Each pixel has a customizable energy threshold level that determines when a hit is registered. If a signal causes a crossing of this threshold, then the hit is registered along with the pixel coordinates, time-of-hit/arrival (TOA), and time taken for the signal to fall below the threshold, which is referred to as the time-over-threshold (TOT). The light detection threshold is about 600-800 photons per pixel, depending on the wavelength. The dead time of individual pixels to process and store the information after they were hit is about 475 ns plus the corresponding TOT. TOA is recorded in a 14-bit register operating at 40 MHz giving a temporal resolution of 25 ns, and improved further to 1.5625 ns using the local 4-bit counter operating at 640 MHz. The data from the TPX3 ASIC is acquired by Speedy PIxel Detector Readout (SPIDR) system (Nikhef, Amsterdam, The Netherlands), which provides both 10 and 1 Gbps ethernet interfaces, and the former can deal with high data output of 80 Mhits per chip per second.[301] The SPIDR has an internal time-to-digital converter (TDC) which is able to time-stamp incoming digital pulses with 260 ps precision synchronously with the TPX3 hits. This feature is useful to provide an external time reference.

Mass Spectrometer and Detection System

All experiments were performed on an Ultraflex III MALDI TOF MS (Bruker Daltonik GmbH, Bremen, Germany)[146] equipped with a TPX3CAM detection assembly (Figure 1). The MALDI ions generated by the Smartbeam 355 nm Nd:YAG laser are extracted, accelerated, and time-focused through a two-stage acceleration region (target plate, second voltage plate, and a ground electrode) employing delayed ion extraction, before passing through a lens system and entering the drift region (Figure 1a). Ions can either be detected in the linear/axial mode or reflectron mode by the reflection of ions using a two-stage reflectron. The reflectron voltage can also be used to apply a retarding field to ions prior to axial mode detection. The drift region is equipped with a deflection unit that allows the deflection of ions in a plane perpendicular to the flight direction.

The conventional Ultraflex linear detector has been replaced by a microchannel plate (MCP)-phosphor screen-TPX3CAM detection assembly. The mechanical schematic of the detection system coupled with the Ultraflex III MS is shown in Figure 1b. The dual chevron MCP stack generates secondary electrons based on the impinging particle properties. The P47 phosphor screen placed behind the MCPs produces fast flashes of light when impinged by the MCP electrons, which are imaged and time-stamped by the sensor in the TPX3CAM. The two imaging MCPs (40 mm quality diameter, 8° bias angle, 12 μm channel center-to-center spacing, 10 μm pore size, 4 x 10^6 electron gain at 2000 V) and phosphor screen (40 mm quality diameter, maximum emission at 430 nm, rise time 7 ns, decay time 70 ns)[302] were mounted to a stainless steel vacuum flange (Photonis USA, Sturbridge, USA) that is equipped with four BSHV feedthroughs. The phosphor

screen feedthrough is rated up to 7.5 kV and the other three are rated up to 5 kV (two MCPs and one spare). The signals from the MCP differential current and phosphor screen current were capacitively decoupled and recorded simultaneously with the TPX3 signal using a fast oscilloscope (~500 MHz and 4 GS/s, LeCroy LT372). The TPX3CAM with 50 mm f/0.95 lens and 25 mm c-mount extension was installed outside of the vacuum via two support rods ~55 mm from the vacuum flange. When compared to the previously employed MCP-TPX arrangement, where the entire detecting assembly was placed in vacuum, the TPX3CAM which is completely decoupled from the rest of the setup, brings considerable flexibility. Furthermore, the direct electron detection approach in the previous studies required close proximity of the MCP and TPX chip (~2 mm) and/or floating detection assembly and readout electronics at high voltages (kV range) that resulted in severe complications of the design as well as the addition of several other elements.[71, 144, 146] Lastly, the optical approach employed here allows flexible mapping between the phosphor screen and TPX3 sensor by magnification/demagnification using appropriate lenses. In this study, the TPX3CAM has been operated in TOF mode, in which the arrival time of each particle (along with TOT and pixel coordinates) is measured with respect to an external trigger. The TPX3 and internal TDC of the SPIDR were triggered at a rate of 10-100 Hz using the laser pulse photodiode signal through the four channels of the digital pulse and delay generator (DG535, Stanford Research Systems, USA). The falling-edge pulse from channels A and B that defines the TOF window was sent to TPX3 through a trigger box, whereas the pulse signal from channels C and D was fed directly to the TDC. The data acquisition parameters are listed in Table S1. All parameters except the linear detection assembly voltages, pulse generator, and oscilloscope settings were defined via FlexControl 3.4 software (Bruker Daltonik GmbH, Bremen, Germany). External power supplies from AMOLF, Amsterdam, The Netherlands, and FuG Elektronik GmbH, Schechen, Germany were used to define the MCPs and phosphor voltages, respectively. TOF to m/z calibration was performed using the 2nd order polynomial function generated from the TOF-m/z conversion curve using 10 samples that encompass an m/z range from 750 to 970,000 (Figure S1). All of the TOF data were acquired using an initial acceleration voltage (target plate voltage) of 25 kV.

Data Acquisition and Analysis

The SoPhy (Software for Physics) software package version 1.6.3 was used for the TPX3CAM control and data acquisition (Amsterdam Scientific Instruments, Amsterdam, The Netherlands). The raw files were subsequently analyzed using open-source Python 3.7.6 with Spyder IDE environment from Anaconda (Anaconda 3, Anaconda Inc., Texas, USA) and GUI built in MATLAB (R2019b, MathWorks Inc., Natick, USA).

All TPX3 spectra were recorded with a time resolution of 1.5625 ns. The "total pixels spectrum" (Figure 2c, 3b, 4a, c, e) was generated by the summation of the number of activated pixels over successive 1.5625 ns time windows in each TOF

cycle for a number of measurement cycles. The total pixels spectrum in Figure 3b was resampled to 100 ns. The "total TOT spectrum" (Figure 2d) was generated by the summation of the TOT values of the pixels triggered in each 1.5625 ns window in a TOF cycle over a number of measurement cycles. Figure 5g-i was generated by the summation of the number of ion events over successive 1.5625 ns time windows in each TOF cycle for a number of measurement cycles. For single ion counting, TOF cycles were divided into 500 ns (475 (dead time) + 25 (minimum TOT)) time slices. The time dimension was then removed to create a 2D binary subframe. MATLAB function "regionprops" was used to detect and measure the properties of connected areas (pixel clusters) in these subframes. The TOF of the centroid pixel in the detected pixel blob was used to add one at that TOF position in the reconstructed spectrum to build the "ion events spectrum." The simulated TPX data (Figure 4) was produced from the TPX3 data by converting each frame (TOF cycle) to binary 256 x 256 data, by considering the earliest TOA event and ignoring the rest for each pixel.
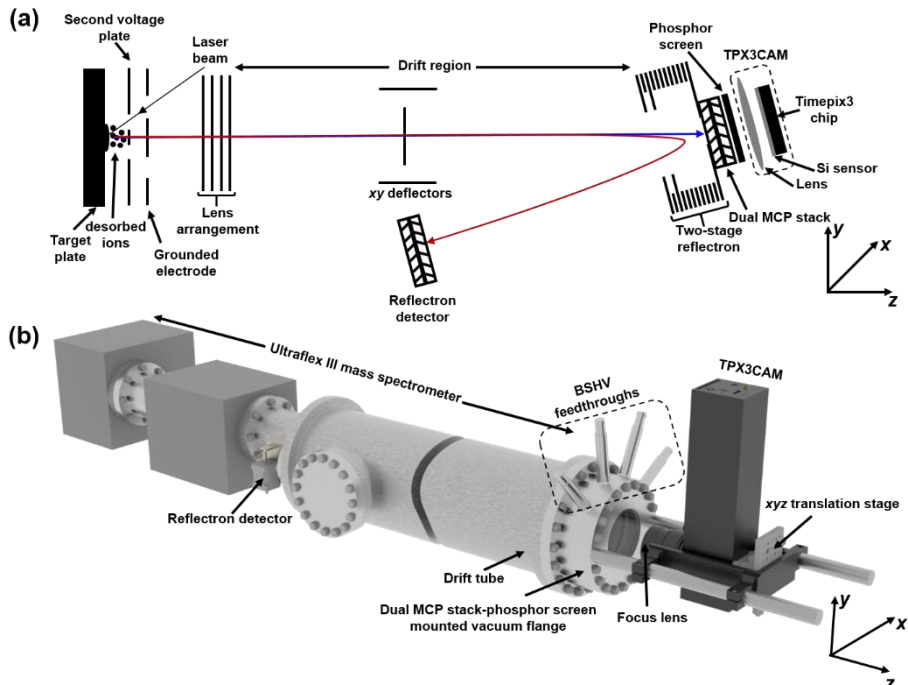
Figure 1. (a) Schematic of the ion optics of Ultraflex III MS. Conventional linear detector is replaced by the MCP-phosphor screen-TPX3CAM assembly. Ions are accelerated in the z-direction and sent either to the linear imaging detector (blue trace) or to the standard reflectron detector (red trace). (b) Mechanical schematic of Ultraflex MS coupled with the MCP-phosphor screen-TPX3CAM assembly. MCP-phosphor screen assembly mounted to the vacuum flange that is positioned at the end of the drift tube, and the TPX3CAM is kept at atmospheric pressure via support rods behind the flange.

The "m/z-resolved TPX3 images" in Figure 2e were generated by summing up the number of pixels activated corresponding to each TOF/m/z value over a number of measurement cycles. The "pixel histograms" in Figure 4b, d, f were plotted by converting the 256 x 256 pixel array total ion image into a 1 x 65,536 row vector. To create Figure 5d-f, each of the ion clouds in the total ion image was extracted from the MATLAB figure using a binary mask and exported to the GNU image manipulation program (GIMP), where each ion cloud was given a distinct color, and then all of the ion clouds were recombined.

The MCP and phosphor screen data (Figures 2a, 2b, and 3a) collected at 100 MHz sampling rate on the oscilloscope (LeCroy LT372) were saved as text files using the Scope Explorer software (LeCroy Corporation, New York, USA). The MCP spectrum in Figure 3b was resampled to 100 ns.

RESULTS AND DISCUSSION

Detection of High m/z Ions Using TPX3CAM

We initially acquired the MALDI-axial TOF mass spectra of IgG (~150 kDa) to investigate the performance of the TPX3CAM assembly for the detection of high m/z ions. IgG is a covalently bounded heterotetramer comprised of two heavy chains (HC, ~50 kDa) and two light chains (LC, ~25 kDa), where the HCs are linked to each other and to a LC each by disulfide bonds.[303] Figure 2 shows the MALDI spectra of IgG acquired simultaneously from MCP (Figure 2a), phosphor screen (Figure 2b), and TPX3 (Figure 2c,d) channels by summing 5000 laser shots. Note that the analog signals registered on the MCP and phosphor screen are recorded at a 100 MHz digitation rate using an oscilloscope, whereas TPX3 data is acquired with a time resolution of 1.5625 ns. The singly charged IgG, doubly charged IgG, triply charged IgG, and singly charged LC ions were observed at m/z values of ~150,000, ~75,000, ~50,000, and ~25,000, respectively. The m/z-resolved TPX3 images of LC[1+], IgG[3+], IgG[2+], and IgG[1+] ions collected from 5000 laser shots are shown in Figure 2e. All m/z values are observed to have distorted elliptical spatial distributions with diameters that increase as the m/z value increases. This m/z-dependent focusing phenomenon has previously been investigated in detail using MCP-TPX assembly on the same Ultraflex instrument.[143, 146]

Both the MCP and phosphor screen spectra yield similar S/N and are comparable to the spectrum from the earlier studies using the conventional MCP/analog-to-digital converter (ADC) detection system on the Ultraflex.[143] In Figure 2c, the TPX3 data has been plotted by summing the number of pixels activated across each 1.5625 ns TOA bin. Each ion impact on the detection assembly leads to a cascade of secondary electrons within the MCP that is in turn converted to photons by the scintillator and electron-hole pairs in the Si-coated TPX3 that results in a detectable current within an individual pixel. The footprint of a single ion event typically spans around an average of ~4 pixels (Supporting Information Figure S2). This indicates that the detection of a single ion is effectively

oversampled by a factor of 4 pixels in Figure 2c. This is consistent with earlier TPX detection of high m/z ions that yields significantly improved S/N values compared to the traditional MCP/ADC approach when using reduced MCP bias conditions.[143]
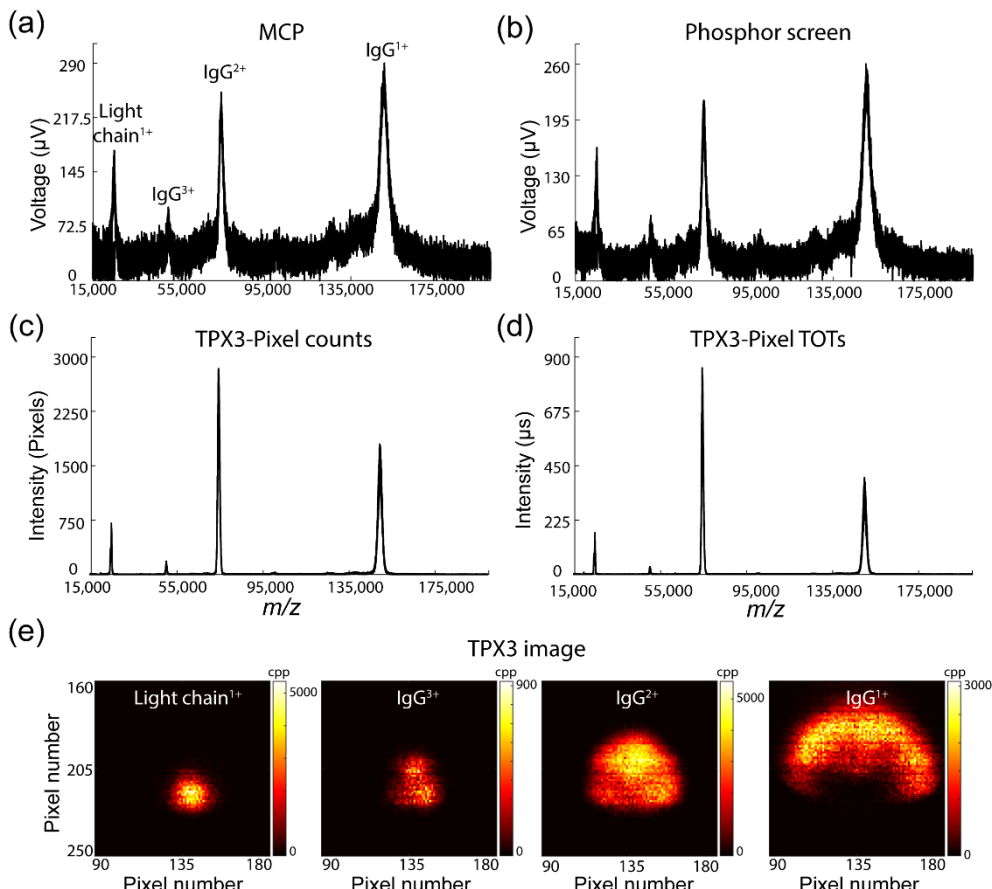
Figure 2. MALDI mass spectra of IgG (in SA matrix) acquired simultaneously from MCP (a), phosphor screen (b), and TPX3 (c,d) detectors for 5000 laser shots. The signal intensity in each case represents different parameters. In panels (a) and (b), the mass spectrum is plotted by integrating the voltage pulses corresponding to each ion event using an oscilloscope with a sampling rate of 100 MHz. TPX3 data are plotted by summing up the number of pixels activated for each ion event (c) and TOT values corresponding to each pixel hit (d) across 1.5625 ns. (e) m/z-resolved TPX3 images of LC[1+], IgG[3+], IgG[2+] and IgG[1+] ions (cpp = counts per pixel). Data acquisition parameters are listed in Table S1 (Supporting Information).

A new feature of the TPX3 is the capability to simultaneously record both TOA and TOT data for each pixel. The TOT corresponds to the time each pixel is over the threshold value required for event registration and is proportional to the number of electron-hole pairs generated. Figure 2d shows the TPX3 data represented in terms of the summed TOT values recorded for each TOA bin across 5000 laser shots. Typical TOT values for these experiments were ~25-1050 (in ns) (Figure S3),

which means each ion event is oversampled by a factor of 25-1050 (in ns) in Figure 2d. The significantly higher S/N ratio of TPX3 mass spectrum in Figure 2c,d compared to MCP and phosphorus screen spectrum is mainly due to the larger oversampling factor, which depends on various parameters such as MCP bias voltage, phosphor screen voltage, and camera aperture f-stop value.[71, 290]

Figure 3. MALDI MS spectra of IgM (in SA matrix) acquired simultaneously on MCP (a) and TPX3 (b) channels for 5000 laser shots. The TPX3 spectrum is generated by summing up the number of pixels activated for each TOA bin. The MCP spectrum was recorded at a 100 MHz digitization rate using an oscilloscope, whereas TPX3 data was acquired using time bins of 1.5625 ns. Both spectra were resampled to 100 ns and baseline subtracted. Data acquisition parameters are listed in Table S1 (Supporting Information).

Next, we evaluated the performance of TPX3CAM at higher m/z values utilizing intact IgM (~970 kDa). IgM exists as a pentamer, in which each of the five monomers is composed of two LCs (~25 kDa) and two HCs (~70 kDa). Monomers are bound together by disulfide bonds and a joining chain (~15 kDa). Within the monomer, HCs are linked to each other and to a LC each by disulfide bonds.[304] Figure 3 shows the MALDI mass spectra of IgM simultaneously acquired using both the MCP (a) and TPX3 (b) channels for 5000 laser shots. The TPX3 spectrum is generated by summing up the number of pixels activated for each TOA bin

(similar to the approach used for plotting Figure 2c). The MCP spectrum was recorded at a 100 MHz digitization rate using an oscilloscope, whereas TPX3 data was acquired using time bins of 1.5625 ns. Both spectra were resampled to 100 ns and baseline subtracted. Only the IgM 2^+-5^+ ions with m/z values of ~485,000, ~323,333, ~242,500, and ~194,000 were detected using the MCP signal with poor S/N ratios. In contrast, TPX3 data yields significantly higher S/N values and even detects singly charged IgM ions at an m/z of 970,000. The application of high MCP bias voltage (2 kV) and low TPX3CAM aperture f-stop value (0.95) generated large clusters with an average size of ~18-37 pixels (Figure S4) and resulted in a high-quality TPX3CAM spectrum when compared to the MCP spectrum. Given the decrease in efficiency of the ion-to-electron conversion of MCPs with an increase in the m/z (decreasing velocity)[257, 265-267, 290, 305], the ability of the TPX3 to detect intact protein ions with m/z approaching 1,000,000 is remarkable and corresponds to ~ 2.5 times increase in m/z range comparable to previous TPX studies, and its performance is comparable to other high mass detection systems such as CovalX HM detectors[114], cryogenic detectors based on superconducting tunnel junctions[58, 118-120, 306], calorimeters/bolometers, superconducting nanostripline detectors/nanomembrane detectors[126] and nanoelectromechanical system (NEMS) detectors.[204, 207]

Event-Based Readout Using TPX3CAM

The benefits of switching the readout from frame-based (TPX) to packet-based architecture (TPX3) is discussed in this section. Data from the earlier generation TPX chip is formatted in frames (TOF cycles) of binary data from all of the pixels, including pixels that did not activate during the measurement window. This results in a readout time >300 μs for each frame. In addition, the measurement had to be paused during the data readout of each frame in TPX. Due to these reasons, previous TPX studies had to be performed at reduced frame rates.[71, 143] Unlike the TPX chip, the on-chip zero suppression scheme implemented in the TPX3 chip allows only pixels with event data to be read out simultaneously during the data acquisition. This reduces the dead time per pixel (475 ns + TOT) and the total readout time of the pixel matrix for occupancies (% of pixel hits) below 50%.[135, 137, 236] This unique data-driven readout system allows the TPX3 to operate at least 10 times faster compared to the previous Ultraflex-TPX experimental setup, where the data is read out by 1 Gbps in both cases.[143] The 10 Gbps ethernet interface at the SPIDR readout system allows the instrument to operate with a higher speed, which would be beneficial in high-throughput mass spectrometry imaging experiments.[152, 307]

Further, the single-stop pixels in the TPX limited the detection of higher m/z values, especially at high count rates (e.g., those encountered using MALDI MS) and high MCP voltages that lead to high pixel occupancies, as pixels are deactivated by lower m/z (earlier arriving) ions. In contrast, TPX3 is designed to enable multihit functionality such that each pixel can record multiple events within a single measurement cycle (in this case, for each laser shot). This makes TPX3 better

suited for the analysis of complex mixtures and ensures that spectra better reflect the true abundances of ions generated.
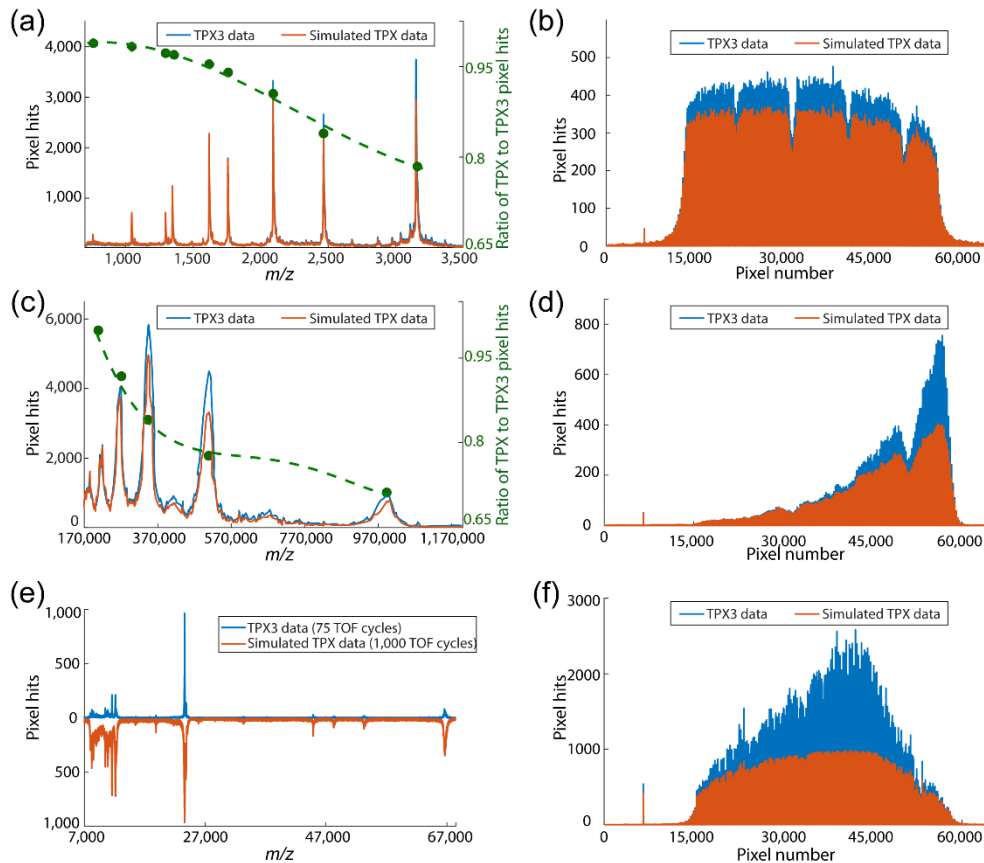
Figure 4. Mass spectra (a, c) and pixel histograms (b, d) plotted in event-based (TPX3, blue trace) and frame-based (TPX, orange trace) modes for two different mass ranges: Bruker peptide calibration standard II (*m/z* range: 700-3200 Da, data 1 (top), in CHCA matrix) and IgM (*m/z* range: 190 to 970 kDa, data 2 (middle), in SA matrix) for 1000 laser shots. Green trace in (a) and (c) plots the ratio of signal intensity in TPX and TPX3 modes. Bruker protein calibration standard II (*m/z* range: 10-70 Da, data 3 (bottom), in SA matrix) mass spectrum (e) plotted in event-based mode by the accumulation of 75 TOF cycles and in frame-based mode by the accumulation of 1000 laser shots, and pixel histograms (f) plotted for 1000 laser shots in both modes. The spectra are generated by summing up the number of pixels activated for each 1.5625 TOA bin. The pixel histograms are generated by summing up the frequency of pixel activation of each pixel in the 256 x 256 TPX3 pixel array (65,536 pixels) for 1000 laser shots. Data acquisition parameters are listed in Table S1 (Supporting Information).

Figure 4 shows the mass spectra (a, c) and pixel histograms (b, d) plotted in event-based (TPX3, blue trace) and single-stop frame-based (simulated TPX, orange trace) modes for two different mass ranges: (a, b) Bruker peptide calibration standard II (*m/z* range: 700-3200 Da, case 1); and (c, d) IgM (*m/z* range: 190 to 970 kDa, case 2). The number of pixels activated per TOA bin is the sum of 1000

laser shots. The pixel parameters corresponding to the earliest TOA were used to simulate frame-based TPX data, and the rest were ignored in each TOF cycle. This has the effect of simulating the single-stop behavior of TPX. In both cases 1 and 2, the TPX3 data registers more events than the simulated TPX data due to its multihit capabilities. The green trace in Figure 4a,c shows the ratio of signal intensities in simulated TPX and TPX3 modes and shows a decreasing trend with an increase in m/z, and thus demonstrates that utilizing TPX3 over TPX improves detection efficiency for higher m/z species when detected in the presence of ions with lower m/z. The average number of ion events per TOF cycle and pixel cluster size for case 1 are ~2942 and ~3-6 pixels (Supporting Information Figure S5), and for case 2 are ~144 and ~18-37 pixels (Figure S4). In case 1, the high count rate at low m/z causes some high m/z ions to be missed in TPX mode, as the pixels they strike may have been rendered inactive by the earlier arrival of lower m/z ions. Case 2 has a much lower number of ions arriving at the detector per TOF cycle than case 1, however the pixel cluster size is larger due to the higher MCP bias voltage used for the detection of heavy ions, and thus each ion event occupies more pixels. The higher pixel occupancy by low m/z ions causes the inactivation of pixels when struck by high m/z ions and results in a low detection efficiency at high m/z in TPX mode. Figure 4e shows the mass spectrum produced from the Bruker protein calibration standard II (m/z range: 10-70 Da, case 3) plotted in event-based mode by the accumulation of 75 laser shots (blue trace) and in frame-based mode by the accumulation of 1000 TOF cycles (orange trace). Figure 4f shows the number of pixels activated for the same data shown in Figure 4e for 1000 laser shots, revealing again the additional events registered in TPX3 mode. Despite the reduced number of laser shots, the event-based TPX3 data in Figure 4e shows similar signal intensity of the most intense peak ($m/z=$ 23,983) as that of the simulated single-stop TPX data, again highlighting the benefits of the event-based TPX3 acquisition. This enhanced performance in TPX3 mode in case 3 is attributed to the fact that many different ions can strike the same pixels due to the large spatial overlap of the ion clouds of different m/z values (Figure 4f and S6).

Visualization of Metastable Fragments Produced in the TOF Tube

The spatially resolved detection capability of TPX3CAM can be employed for the evaluation of fragments produced by metastable decay (post-source decay, PSD) at different locations within the field-free flight tube. Typically, in linear TOF mode, metastable fragments produced in the field-free region have flight times and impact positions identical to the precursor ion (ignoring small deviations caused by fragment recoil).[308-310] Following MALDI, PSD will generally produce a singly charged ionic and neutral fragment pair (assuming a singly charged precursor). Here, we have combined the imaging capability of the linear TPX3 detector with an electrostatic deflector and retarding fields of the reflectron to spatially separate neutral fragments formed at different locations along the ion flight path in the field-free region.
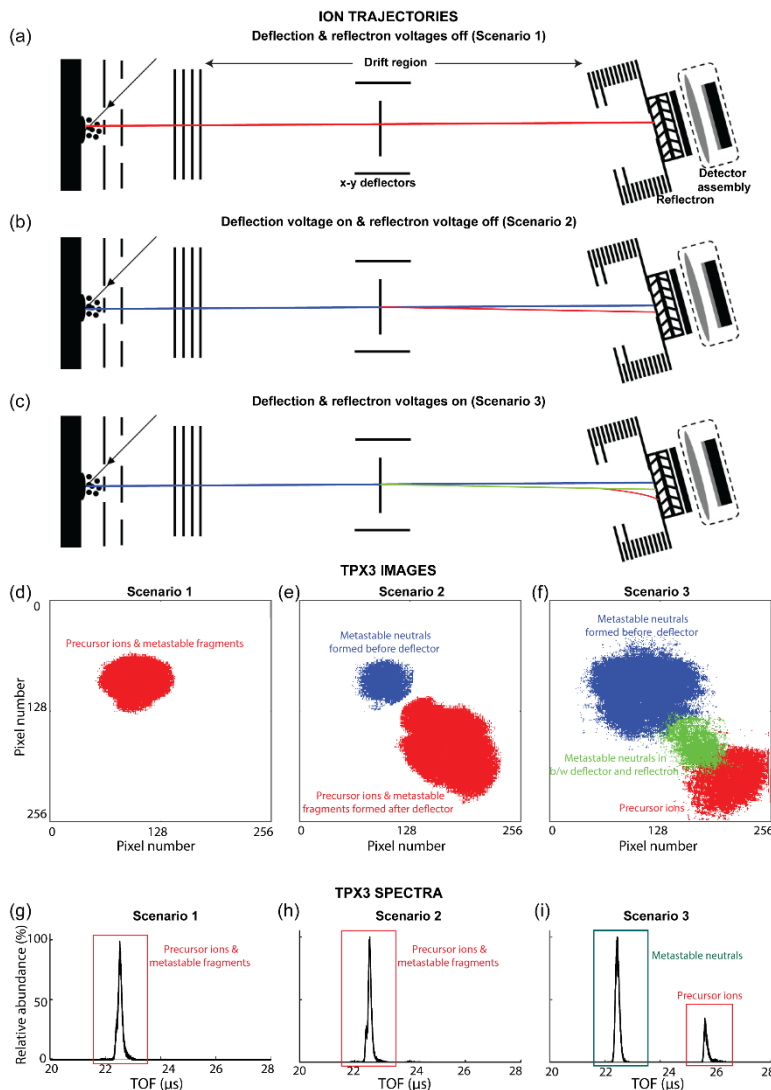
Figure 5. Ion trajectory (a-c), and the resulting total ion TPX3 image (d-f) and TOF spectrum (g-i) produced from insulin chain B [M+H]$^{1+}$ ions (in CHCA matrix) for three different conditions; (1) without deflection and reflectron voltages, (2) with deflection voltage (x and y deflection voltages: -55 V and -65 V), and (3) with deflection and reflectron voltages (x and y deflection voltages: -55 V and -65 V, reflectron voltage: 19.5 kV). The ion trajectories and corresponding spatial distributions at the TPX3 detector of each type of ion cloud are represented using the same color in all three scenarios. The mass spectra were generated by the summation of the number of ion events over successive 1.5625 ns time windows in each TOF cycle for 5000 laser shots. The details on the plotting of TPX3 images and ion events spectrum are provided under the 'Data Acquisition and Analysis' section. Data acquisition parameters are listed in Table S1 (Supporting Information).

The adjustable *x-y* deflectors positioned within the flight tube prior to the reflectron were used to spatially separate ions and neutral fragments formed between the source and deflector. The application of retarding field using the reflectron along with the deflector voltage leads to (i) temporal separation of ions and neutral fragments (ions shifted to longer TOF) and (ii) spatial separation of neutral fragments formed between the source and deflector, and the deflector and reflectron. This spatial separation of the fragments arises as the neutral fragments produced after the deflectors travel on the same path as deflected ions until they reach the reflectron, whereas neutrals formed before the deflector travel on a path unperturbed by the deflection voltages. In addition, due to the greater residence time of ions in the reflectron, neutral fragments formed after the deflector are also spatially separated from intact ions. The combination of deflection and retarding voltages thus results in three impact zones, one corresponding to intact ions reaching the reflectron at longer TOF, and two impact regions corresponding to neutrals at different locations along the flight path (one group formed prior to the deflector, a second group formed in between the deflector and reflectron). This is exemplified in Figure 5.

Figure 5a,d,g shows the ion trajectory and the resulting TPX3 image and TOF spectrum produced from insulin chain B [M+H]$^{1+}$ ions (in CHCA matrix) when no deflection or retarding fields are applied (scenario 1). Ion source voltages were adjusted to spatially focus the ion packet to a small circular cloud for all the data acquisition in this section. However, it should be noted that these conditions are different from those needed for time focusing of the ions on the detector, and thus broader peaks are observed.[146] As expected, these conditions yield one impact zone on the detector and one peak in the TOF spectrum corresponding to protonated insulin chain B. When the deflection voltage is activated (scenario 2, *x* and *y* deflection voltages: -55 V and -65 V), the deflected ions strike closer toward the bottom right of the detector (Figure 5b,e, red) whereas neutral fragments formed prior to the deflector remain on their original trajectory (Figure 5b,e, blue). These conditions still result in a single TOF peak (Figure 5h). Smaller pixel clusters (a parameter that is related to the MCP detection efficiency) were observed for neutrals compared to the precursor ions. This is caused by a reduced ion-to-electron conversion efficiency when neutrals impact the MCP.[290] The average pixel cluster size for metastable product neutrals and precursor ions are 3.5 and 5.5 pixels, respectively (Figure S7). Figure S8 (Supporting Information) compares the TOF spectra generated for precursor ions (red trace) and metastable neutrals (blue trace) from the TPX3 image. The result clearly shows that the metastable fragments arrive at a slightly later time compared to the precursor ions. This could be attributed to the post-acceleration of ions at the end of the TOF tube because of the negative potential at the front MCP. When both the deflection and retarding fields are applied (scenario 3, *x* and *y* deflection voltages: -55 V and -65 V, reflectron voltage: 19.5 kV), ions are further deflected due to the greater residence time in the reflectron (Figure 5c,f, red). Note that not the full reflectron voltage is applied but a reduced voltage, enough to

deflect the ions slightly from their original flight path. An additional packet of neutrals (Figure 5c,f, green) is observed at the same location ions are observed to strike the detector in Figure 5b,e (red) that are assigned to neutral fragments formed by PSD events between the deflector and reflectron. The ions are shifted to longer TOA due to the retarding field, while neutrals are detected at the original ion TOA time (Figure 5i). Figure S9 (Supporting Information) shows the evolution of the total ion TPX3 images and linear TPX3 detector TOF spectra with an increase in the reflectron voltage (a deflection voltage is also applied). The square patterns that are only observed in the precursor ion clouds and not in the metastable product neutral clouds in the TPX3 images are explained by the transmission grids placed in the reflectron. The TOF of the ions increases with an increase in reflectron voltage as the ions spend more time in the reflectron, whereas the TOF of metastable neutrals is insensitive to the reflectron voltage. While outside the scope of this work, the unique ability of space and time-resolved detection to detect metastable fragments formed at different locations along the flight path provides an interesting avenue to study the kinetics of metastable ion decay.

CONCLUSIONS

In this work, we have described the first implementation of a TPX3CAM detection assembly on a MALDI TOF (Ultraflex III) MS for the detection and ion imaging of high-mass biomolecules. This new experimental setup significantly extended the m/z range previously detected with the TPX family by the measurement of the intact protein ions of m/z approaching 1,000,000 Da. The enhanced time resolution, simultaneous measurement of TOT and TOA, and multihit capabilities of the TPX3 chip compared to its predecessor, the TPX chip, allowed the generation of the TOF/mass spectra with a better S/N ratio and improved the sensitivity of the high m/z detection in the presence of low m/z ions at high count rates and detector voltages. The utilization of deflectors and time-resolved imaging capabilities of TPX3 allowed us to distinguish PSD events occurring at different locations along the flight path, and provides a unique approach to explore the kinetics of PSD as well as the influence of parameters such as laser fluence, MALDI matrix, protein mass and extraction conditions on the metastable decay rate.[308-309, 311-313]

SUPPORTING INFORMATION

Table S1. List of the data acquisition parameters.

Parameter	Figure 2 (IgG)	Figure 3 (IgM)	Figure 4a & b (Peptide std II)	Figure 4e & f (Protein std II)	Figure 5 (Insulin chain B)	Figure S9 (Insulin chain B)
Number of laser shots/measurement cycles	5000	5000	1000	1000	5000	5000
Laser repetition rate (Hz)	100	100	100	100	10	10
Laser power (%)	50	70	30	50	30	30
Target plate voltage (kV)	25	25	25	25	25	25
Second plate voltage (kV)	21	21	23.6	23.1	22.45	22.45
Lens voltage (kV)	12	12	7	6	6	6
Reflectron voltage (kV)	0	0	0	0	0, 0 and 19.5 (Scenario 1, 2 and 3)	0, 5, 10, 15, 20, 25
Pulsed ion extraction (PIE, ns)	500	2000	0	500	0	0
Matrix suppression deflection (Da)	15000	100000	700	10000	1000	1000
Global attenuator offset (%)	65	65	45	65	45	45
Attenuator offset (%)	15	15	25	15	25	25
Focus offset (%)	0	0	0	0	0	0
Focus range (%)	100	100	100	100	100	100
Focus position (%)	33	33	33	33	33	33
x-deflection voltage (V)	0	0	0	0	0, -55 and -55 (Scenario 1, 2 and 3)	-55
y-deflection voltage (V)	0	0	0	0	0, -65 and -65 (Scenario 1, 2 and 3)	-70
Linear MCP front plate voltage (V)	-2150	-2600	-2100	-2200	-2100	-2100
Linear MCP back plate voltage (V)	-600	-600	-600	-600	-600	-600
Phosphor screen voltage (V)	5000	5000	5000	5000	5000	5000
TPX3CAM t-stop value	0.95	0.95	0.95	0.95	0.95	0.95
DG535 channel A pulse width (delay for TPX3, µs)	75	125	20	20	20	20
DG535 channel B pulse width (measurement window for TPX3, µs)	1000	2000	150	500	100	100
DG535 channel C pulse width (delay for internal TDC SPIDR, µs)	75	125	20	20	20	20
DG535 channel D pulse width (measurement window of internal TDC SPIDR, µs)	100	100	100	100	100	100
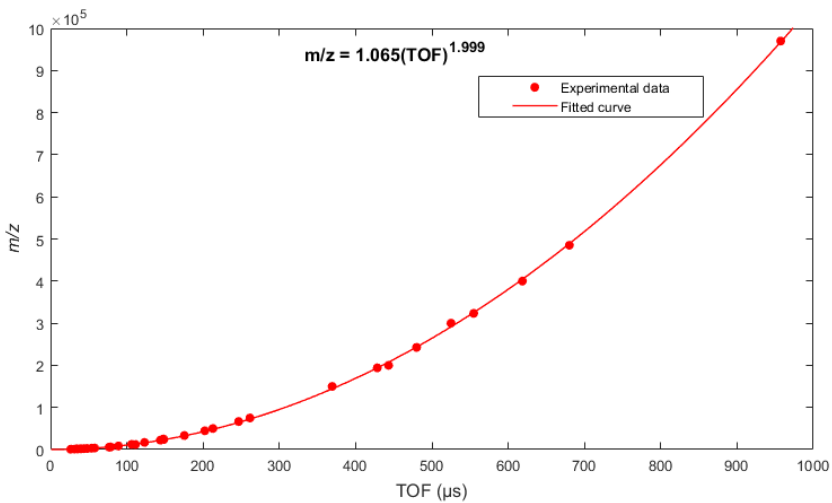
Figure S1. TOF to *m/z* conversion curve plotted using 10 samples that encompass an *m/z* range from 750 to 970,000 Da. All the TOF data were acquired using an initial acceleration voltage (target plate voltage) of 25 kV.
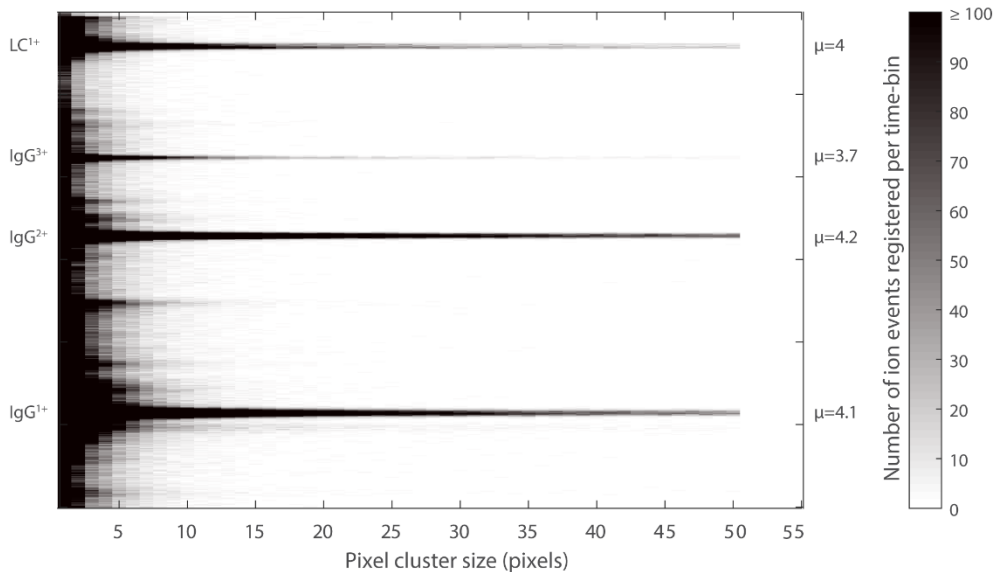
Figure S2. The distribution of pixel cluster area (in pixels) of LC^{1+}, IgG^{3+}, IgG^{2+}, and IgG^{1+} ions, and corresponds to the data shown in Figure 2. A time-bin size of 500 ns was used for the generation of the histogram. μ is the average pixel cluster size that is calculated by $\frac{\sum_{i=1}^{k}(i \times N_i)}{\sum_{i=1}^{k} N_i}$, where i=pixel cluster size (in pixels), N_i=number of ion events with pixel cluster size of 'i', and k= maximum pixel cluster size (in pixels).
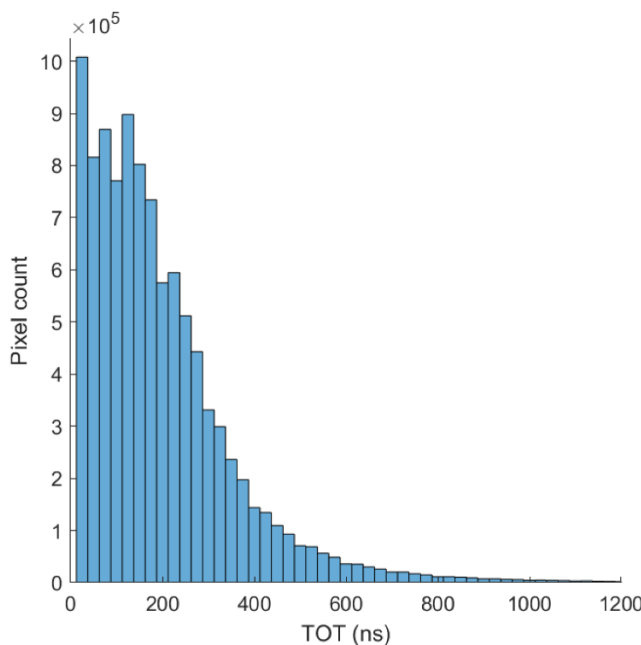
Figure S3. TOT distribution of the TPX3 pixels triggered by IgG ions (*m/z* range: 25-150 kDa), and corresponds to the data shown in Figure 2. A time-bin size of 25 ns was used for the generation of the histogram.
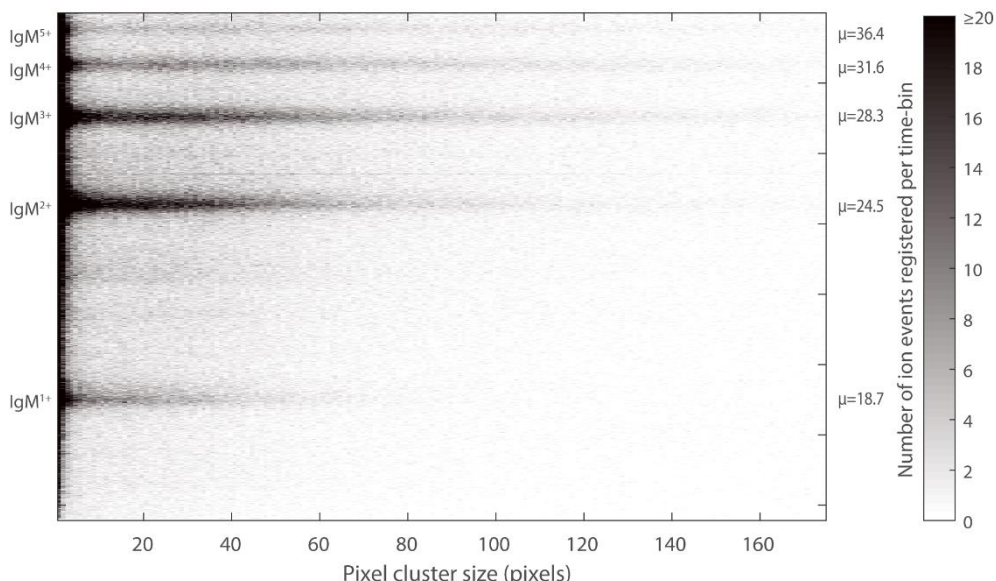
Figure S4. The distribution of pixel cluster area (in pixels) of IgM 1+-5+ ions, and corresponds to the data shown in Figure 3. A time-bin size of 500 ns was used for the generation of the histogram. μ is the average pixel cluster size that is calculated as previously described (Figure S2).
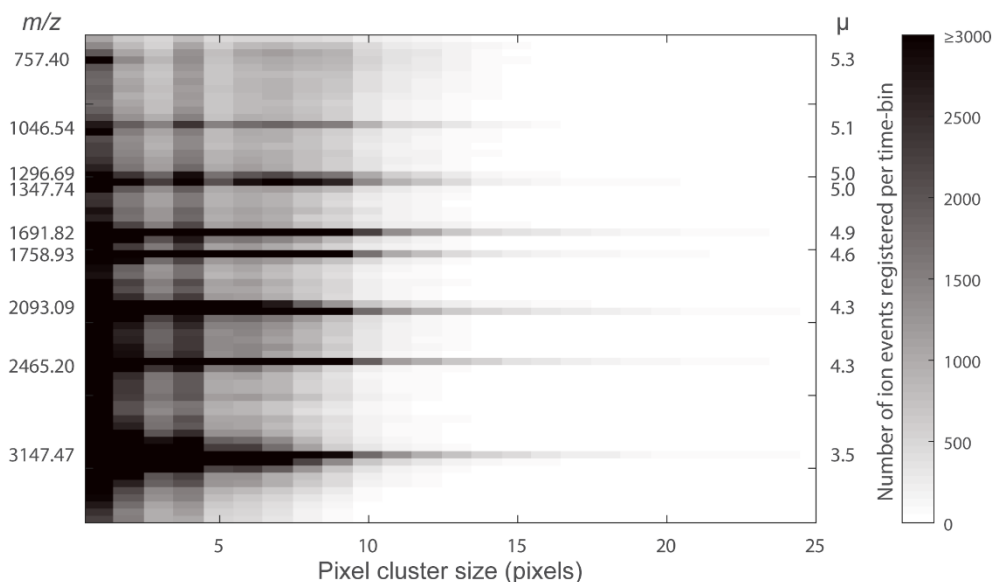
Figure S5. Distribution of pixel cluster area (in pixels) of the ions generated from Bruker peptide calibration standard II (*m/z* range: 700-3200 Da), and corresponds to data shown in Figure 4a,b. A time-bin size of 500 ns was used for the generation of the histogram. μ is the average pixel cluster size that is calculated as previously described (Figure S2).
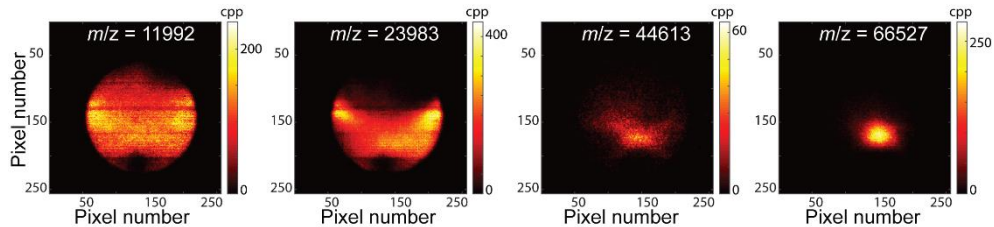
Figure S6. *m/z* resolved TPX3 images of trypsinogen^{2+} (*m/z*=11,992), trypsinogen^{1+} (*m/z*=23,983), protein A^{1+} (*m/z*=44,613), and BSA^{1+} (*m/z*=66,527) from Bruker protein calibration standard II, and generated from data shown in Figure 4e,f by the accumulation of 1000 laser shots (cpp=counts per pixel).

(a)
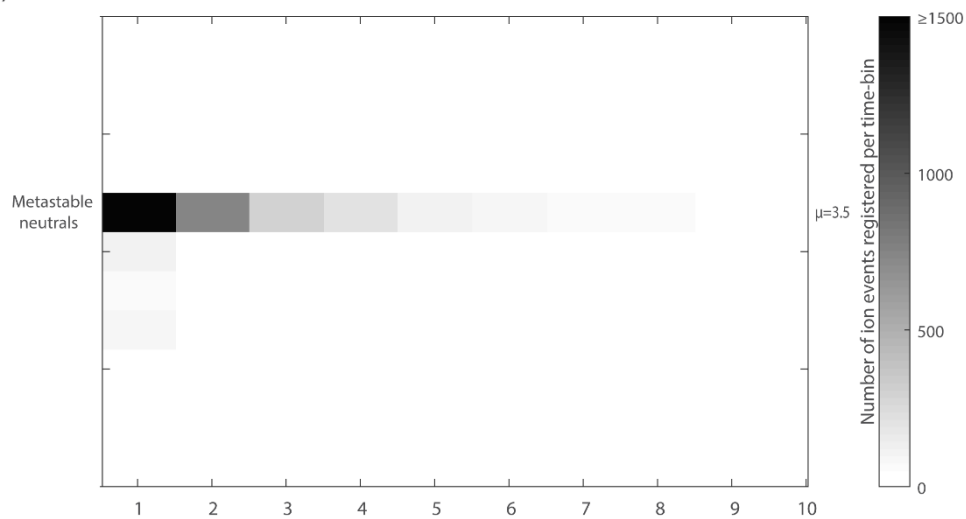
(b)
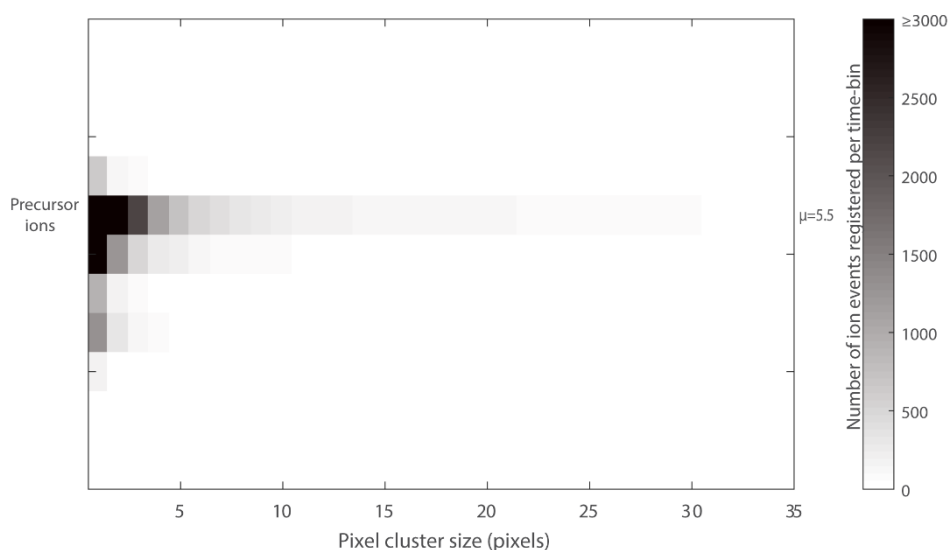
Figure S7. Distribution of pixel cluster area (in pixels) of metastable neutrals formed in between the source and deflector (a), and precursor insulin chain B $[M+H]^{1+}$ ions (b), and corresponds to data shown in Figure 5b,e,h (scenario 2). A time-bin size of 500 ns was used for the generation of the histogram. μ is the average pixel cluster size that is calculated as previously described (Figure S2).
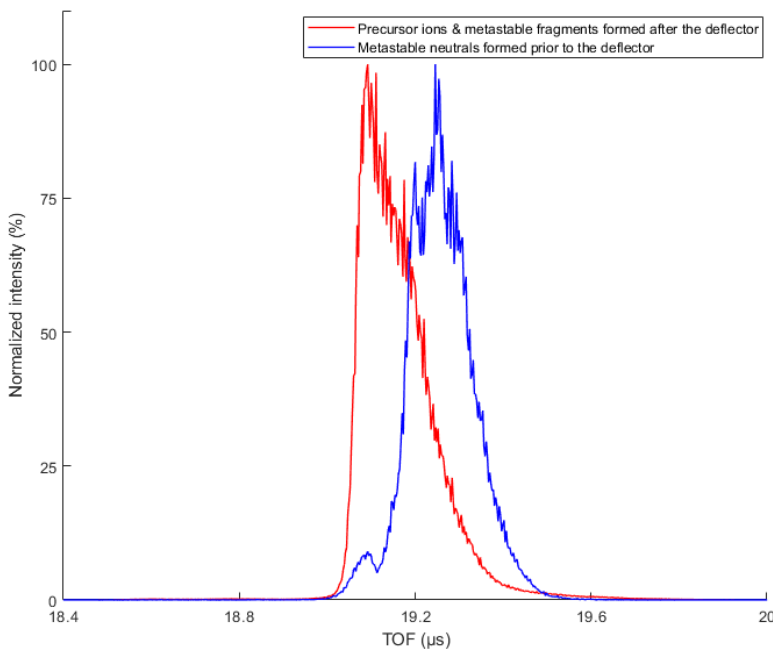
Figure S8. TOF spectra correspond to the intact insulin chain B $[M+H]^{1+}$ions (red trace) and metastable neutrals formed prior to the deflector (blue trace). Data was acquired with deflector voltage on and reflectron voltage off (scenario 2, Figure 5). Note that the intensities in both cases are normalized to their respective maximum for easier comparison of the TOF values.

(a)

(b)
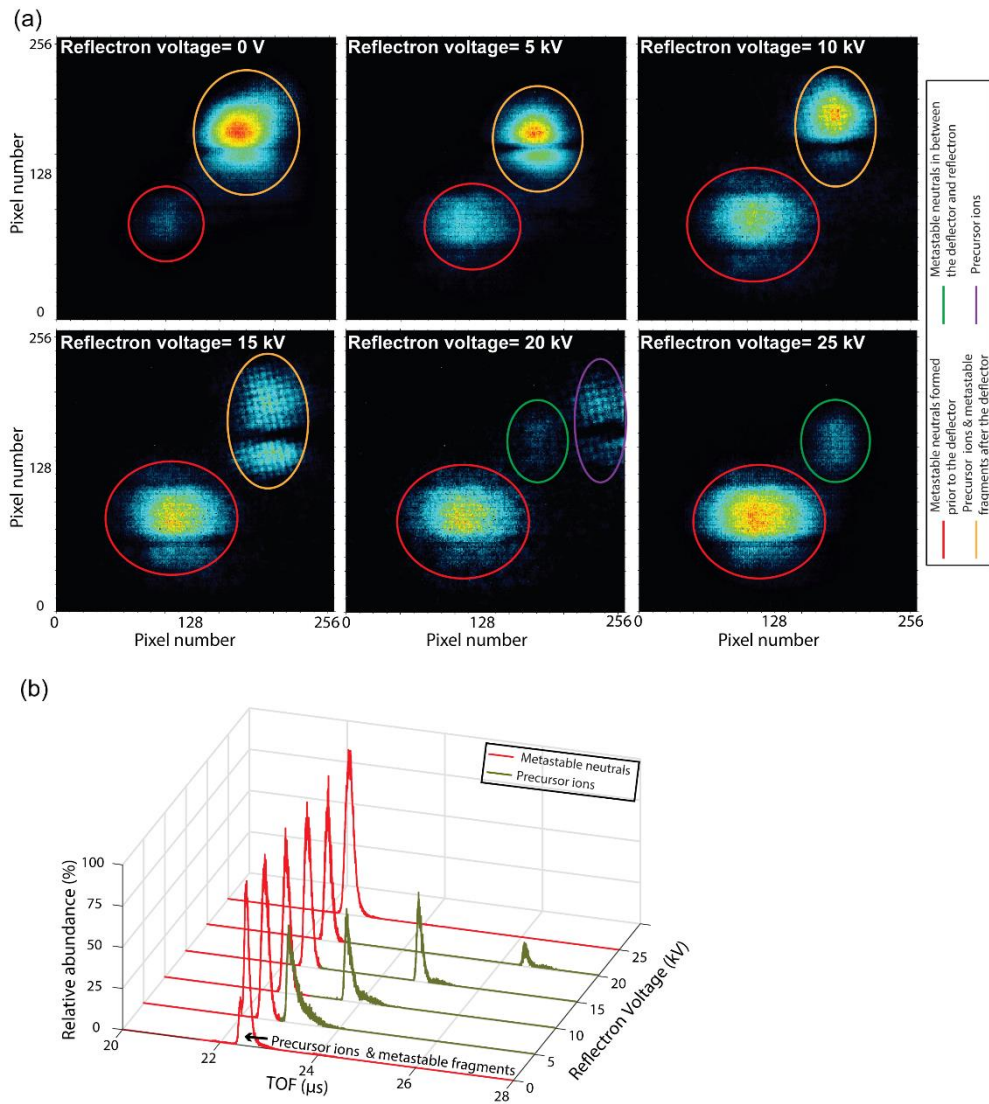
Figure S9. Evolution of the (a) total ion TPX3 images and (b) linear TPX3 detector TOF spectra with an increase in the reflectron voltage (a deflection voltage is also applied). Note that the intensities are normalized to their respective maximum for all the TOF spectra. The data acquisition parameters are listed in Table S1.

4

5

AN ORBITRAP/TIME–OF–FLIGHT MASS SPECTROMETER FOR PHOTOFRAGMENT ION IMAGING AND HIGH–RESOLUTION MASS ANALYSIS OF NATIVE MACROMOLECULAR ASSEMBLIES

Anjusha Mathew[1], Frans Giskes[1], Alexander Lekkas[2], Jean-François Greisch[3,4], Gert B. Eijkel[1], Ian G. M. Anthony[1], Kyle Fort[5], Albert J. R. Heck[3,4], Dimitris Papanastasiou[2], Alexander A. Makarov[3,5], Shane R. Ellis[1,6], and Ron M. A. Heeren[1]

[1] Maastricht MultiModal Molecular Imaging (M4i) Institute, Division of Imaging Mass Spectrometry (IMS), Maastricht University, 6229 ER Maastricht, The Netherlands

[2] Fasmatech Science and Technology, Demokritos NCSR, 15310 Agia Paraskevi, Athens, Greece

[3] Biomolecular Mass Spectrometry and Proteomics, Bijvoet Centre for Biomolecular Research and Utrecht Institute for Pharmaceutical Sciences, Utrecht University, Padualaan 8, 3584 CH Utrecht, The Netherlands

[4] Netherlands Proteomics Center, Padualaan 8, 3584 CH Utrecht, The Netherlands

[5] Thermo Fisher Scientific (Bremen) GmbH, 28199 Bremen, Germany

[6] Molecular Horizons and School of Chemistry and Molecular Bioscience, University of Wollongong, NSW 2522, Australia

ABSTRACT

We discuss the design, development, and evaluation of an Orbitrap™/time-of-flight (TOF) mass spectrometry (MS) based instrument with integrated UV photodissociation (UVPD) and time/mass-to-charge ratio (m/z)-resolved imaging for the comprehensive study of the higher-order molecular structure of macromolecular assemblies (MMAs). A bespoke TOF analyzer has been coupled to the higher-energy collisional dissociation cell of an ultra-high mass range hybrid quadrupole-Orbitrap™ MS. A 193 nm excimer laser was employed to photofragment MMA ions. A combination of microchannel plates (MCPs)-Timepix (TPX) quad and MCPs-phosphor screen-TPX3CAM assemblies have been used as the axial and orthogonal imaging detectors, respectively. The instrument can operate in four different modes, where the UVPD generated fragment ions from the native MMA ions can be measured with high-mass resolution or imaged in a mass-resolved manner to reveal the relative positions of the UVPD fragments post-dissociation. This information is intended to be utilized for retrieving higher-order molecular structural details that include the conformation, subunit stoichiometry, and molecular interactions as well as to understand the dissociation dynamics of the MMAs in the gas phase.
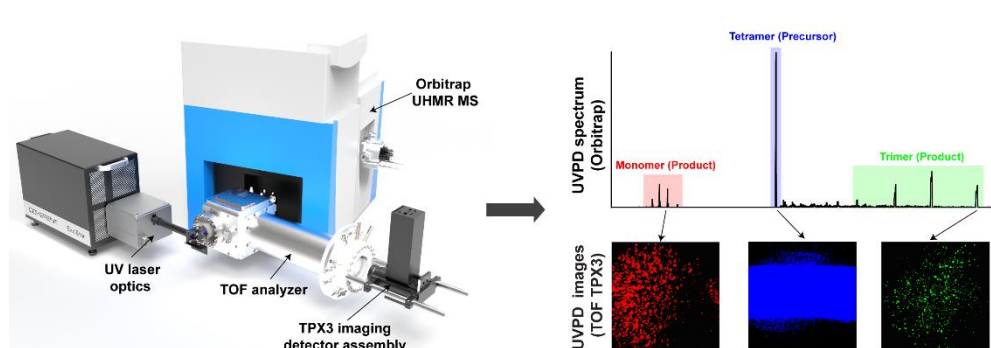
5

Keywords: Macromolecular assemblies, Orbitrap mass spectrometry, Orthogonal time-of-flight mass spectrometry, Photofragment ion imaging, Timepix detector, UV photodissociation

INTRODUCTION

Mass spectrometry (MS) has emerged as a versatile and powerful tool to study molecular structural features of macromolecular assemblies (MMAs).[18-20, 314] The MMAs are a broad range of important large (molecular weight range: kDa to MDa) complex biological ensembles of proteins, nucleic acids, carbohydrates, lipids, metabolites, metal ions, ligands, etc. The majority of the previous studies on MMAs targeted protein complexes or the complexes formed by binding of co-factors such as lipids, DNA or RNA, ligands, and metal ions to the proteins, termed as multiproteoform complexes (MPCs).[3-7, 9] Here we exclusively focus on the techniques for the molecular structural elucidation of MPCs.

With the advancements in MS instrumentation, mass spectrometers that provide ultra-high mass resolution (> 10^6 at m/z (mass-to-charge ratio) = 200), ppb to sub-ppm mass accuracy, wide and high m/z range, and femtomole to attomole detection sensitivity are now available.[89, 94, 98, 100-103, 315-317] Often a combination of liquid chromatography (LC) coupled online to a nano-electrospray ionization (nESI) source, and mass spectrometers with the above-mentioned features and MS/MS capabilities are used for the characterization of the protein sequence. Several MS-based approaches such as native MS (nMS), ion mobility MS (IM MS), affinity purification MS (AP MS), hydrogen-deuterium exchange MS (HDX MS), hydroxyl radical footprinting MS (HRF MS), and cross-linking MS (XL MS) have proven to be complementary to the structural biology tools such as cryogenic-electron microscopy, nuclear magnetic resonance, and x-ray crystallography.[18-21, 35-38, 41-42, 226, 318] These MS-based tools are capable of retrieving several higher-order structural features like subunit stoichiometry and interaction sites of MPCs along with the high-resolution molecular information. These methods are often coupled together and/or integrated with various ion fragmentation methods such as collision-induced dissociation (CID)/higher-energy collisional dissociation (HCD), electron-capture dissociation (ECD), electron-transfer dissociation (ETD), surface-induced dissociation (SID), ultraviolet photodissociation (UVPD), infrared multiphoton dissociation (IRMPD), EThCD (ETD supplemented with HCD), activated ion ETD (AI-ETD, IRMPD followed by ETD), etc. to obtain structural information.[53, 55, 105, 159, 161-164, 319] However, little information on the 3D conformation of the MMA has been provided with any of these MS-based techniques.

Here, we discuss the design and development of an innovative MS-based instrument that allows comprehensive molecular and structural analysis of MMAs at the same time using only picomoles of sample from solution.[320] A combination of a Thermo Scientific™ Q Exactive™ ultra-high mass range (UHMR) hybrid quadrupole-Orbitrap mass spectrometer[74, 108, 169, 186, 224] and a custom-designed orthogonal time-of-flight (TOF) mass analyzer, with an integrated 193 nm excimer laser[167-169, 321] and two position-and-time sensitive Timepix (TPX) detectors[71, 143, 146, 152, 290, 322] were used for the initial characterization of the system presented here. The Orbitrap/TOF system allows the m/z-resolved imaging of UV generated products from the precursor MMA ions, which can be utilized to understand the

energetics of the MMA dissociation process as the TOF analyzer can retain the relative positions of the product ions following the fragmentation process until they reach the imaging detector. Moreover, the instrument is capable of sending the UV generated product ions back to the Orbitrap mass analyzer to obtain the high-resolution UVPD mass spectrum that provides several higher-order structural details of MMAs including conformation, subunit stoichiometry, and molecular interactions.

The work described in this paper focuses on the ion optics design, development, and evaluation of the Orbitrap/TOF system using pixelated TPX detectors and UVPD. A description of the instrument design, the system configurations, modes of operation, and the associated ion optics simulations of the custom-designed TOF analyzer are provided in the first section. That is followed by a comprehensive characterization of the system divided into three sections: characterization of the Orbitrap/TOF system with (i) axially and orthogonally coupled discrete-dynode electron multiplier (EM) detectors (ii) axial microchannel plates (MCP)-TPX quad and orthogonal MCP-phosphor screen (P47)-TPX3CAM imaging detector assemblies, and (iii) coaxial 193 nm excimer laser optics and an orthogonal MCP-P47-TPX3CAM imaging detector assembly.

MATERIALS AND METHODS

Materials

Ubiquitin (8.6 kDa) from bovine erythrocytes, concanavalin A (102 kDa) from Canavalia ensiformis and ammonium acetate were all purchased from Sigma-Aldrich (Zwijndrecht, The Netherlands). Cesium iodide (CsI; 392.7 to 11,304 Da) was obtained from Thermo Fisher Scientific, The Netherlands. Methanol, isopropanol, and LC–MS grade water were purchased from Biosolve (Valkenswaard, The Netherlands).

Sample Preparation

Ubiquitin was dissolved in 1:1 methanol:water (v:v) to a concentration of 5 μM. Concanavalin A was first dissolved to a stock concentration of 100 μM in LC–MS grade water, and then buffer exchanged with 200 mM ammonium acetate at pH 6.8 using 30 kDa molecular weight cutoff (MWCO) Amicon Ultra centrifugal filter (Millipore, Merck KGaA, Germany) to a final monomer concentration of 5 μM. CsI was prepared as 2 mg/mL solution in 1:1 isopropanol:water (v:v).

Instrumentation

Orbitrap/TOF MS

A commercial Q Exactive™ UHMR hybrid quadrupole-Orbitrap™ mass spectrometer (Thermo Fisher Scientific, Bremen, Germany) was coupled with a custom-designed orthogonal TOF analyzer, a 193 nm ExciStar XS 200 series excimer laser (Coherent Laser Systems GmbH & Co. KG, Göttingen, Germany),

and two imaging detectors; herein referred to as MCP-TPX quad and MCP-P47-TPX3CAM (Figure 1a and 2). The electrometer located at the rear of the HCD cell of the Orbitrap MS was removed, and a transfer hexapole (Element 12, Figure 2) was installed to control ion transport into the TOF region. The ion cloud is collisionally cooled in a linear quadrupole trap (LQ-trap, Element 14, Figure 2) that is positioned in between the hexapole and TOF analyzer (Element 18, Figure 2), and it can be further conditioned by the correction lens (Element 16, Figure 2) as it travels to the TOF region. The ions are either directed towards the axial MCP-TPX quad assembly (Elements 28-29, Figure 2 (top)) or to the orthogonal MCP-P47-TPX3CAM assembly (Elements 19-23, Figure 2) through the TOF analyzer. The details regarding the geometry and ion optical design of the TOF analyzer will be discussed in the next section.

Laser optics

A parallel coherent beam of 193 nm UV photons with a maximum repetition rate of 200 Hz was generated with an ExciStar XS 200 series excimer laser filled with an argon fluoride gas mixture (Element 24, Figure 2). The laser produces 7 ns rectangular pulses of dimensions 6 x 2.5 mm (V x H), with functional energies ranging from 0.5 to 5 mJ/pulse. The UV laser beam was guided to the mass spectrometer through a quartz window via a periscope assembly, equipped with 45° 193 nm mirrors (Laseroptik GmbH, Garbsen, Germany) mounted on micropositioners, and ring-actuated iris diaphragms (Thorlabs, Newton, USA). Two UVPD configurations were evaluated (Figures 1a and 2). In configuration 1, the laser beam is aligned orthogonally (y) to the ion optical axis (z), and interacts with the precursor ion cloud in one of the electrodes of the LQ-trap or correction lens. Whereas, in configuration 2, the laser beam is coaxially aligned with the longitudinal ion optical axis (z) of the instrument to maximize the overlap with the ion cloud and hence improve the fragmentation efficiency. All the UVPD experiments shown in this paper were conducted in system configuration 2. A manually operated attenuator module (Coherent Laser Systems GmbH & Co. KG, Göttingen, Germany) was installed in front of the 193 nm laser for the fine control of the laser energy in configuration 2 (Element 30, Figure 2). The HCD exit test point signal was used to generate TTL trigger pulses with a digital pulse generator (DG535, Stanford Research Systems, Sunnyvale, USA) for the laser.
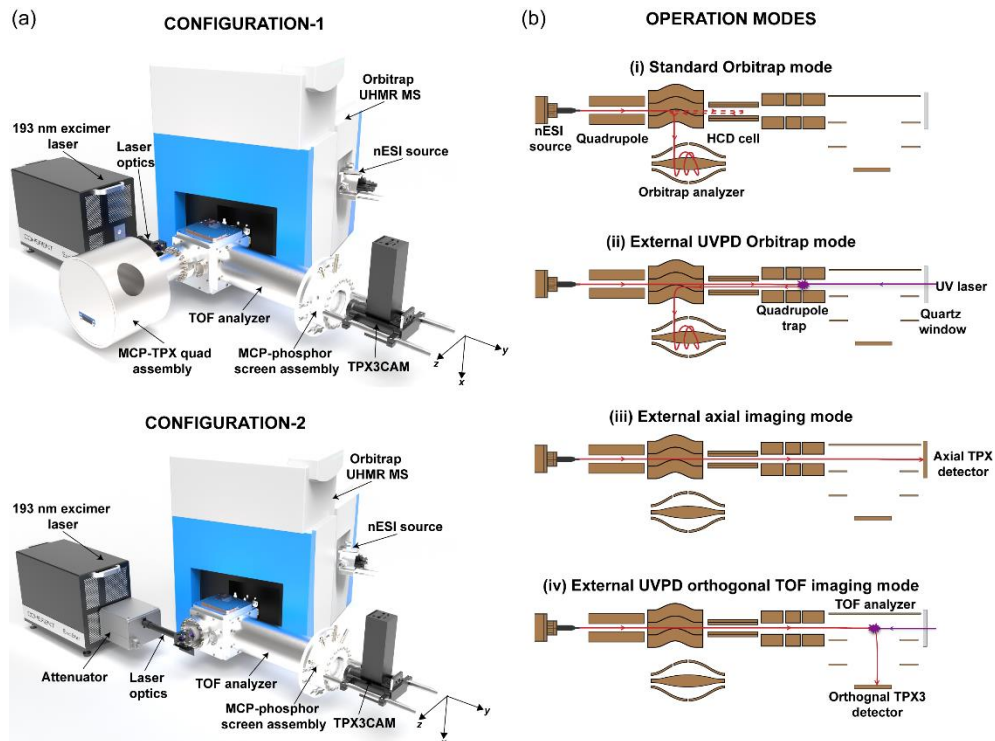
Figure 1. (a) Schematics (not to scale) of the two different configurations of the Orbitrap/TOF system. Configuration 1 (top) utilizes two imaging detectors: an axial MCP-TPX quad and an orthogonal MCP-P47-TPX3CAM. The laser beam interacts orthogonally with the ion cloud at any segments of the LQ-trap or correction lens. In configuration 2, the axial TPX quad assembly has been replaced by a quartz window that allows the laser beam to interact coaxially with the ion cloud. The rest of the experimental setup is exactly the same as configuration 1. (b) Different operation modes of the instrument. The trajectories of the precursor/product ions and laser beam are shown in red and violet, respectively.

Discrete-dynode EM detection systems

Two discrete-dynode EMs (ETP Electron Multipliers, Clyde, Australia) with dimensions of 10x14 and 8x12 mm were coupled axially and orthogonally through the TOF analyzer, respectively for the initial characterization of the custom-designed part. The discrete-dynode EM signals were extracted using a fast oscilloscope (~500 MHz and 4 GS/s, LeCroy LT372). The signal from the HCD exit test point was used to trigger the oscilloscope. The data acquired using the oscilloscope is saved as text files using the Scope Explorer software (LeCroy Corporation, New York, USA).

TPX detection systems

The discrete-dynode EMs were replaced after the initial characterization by time- and position-sensitive charge detectors from the Timepix (TPX) family (Medipix consortium, CERN, Geneva, Switzerland). The axial imaging detection assembly consists of a dual MCP chevron stack–TPX[135] quad system mounted in vacuum.

This system has previously been coupled to MALDI (matrix-assisted laser desorption/ionization)-axial TOF Bruker Ultraflex™ III MS.[143, 146] In this study, TPX has been operated in time-of-arrival (TOA) mode, in which the time of activation of each pixel is measured along with pixel coordinates with respect to an external trigger. The TPX data is read out via a ReLAXD (high-Resolution Large-Area X-ray Detector) readout board with a speed of 1 Gbit/s.[245] The TPX was triggered at a rate of 1-2 Hz using the HCD exit lens trigger pulse, via a digital pulse and delay generator (DG535, Stanford Research Systems). The axial TPX data were recorded using a 100 ns TPX clock width, corresponding to a maximum measurement window of 1181 µs for each measurement cycle.

The imaging assembly mounted on the orthogonal TOF MS consists of an MCP-P47-TPX3CAM detector system that was previously employed in Ultraflex III MS.[322] Briefly, each ion impact on the MCP-P47-TPX3CAM detection assembly leads to a cascade of secondary electrons within the MCP that is subsequently converted to photons by the scintillator (P47). The photons create local electron-hole pairs in the Si-coated TPX3[137] within the TPX3CAM that results in a detectable current on individual pixels of the TPX3 chip. The TPX3 chip consists of a 256 × 256 pixel matrix with a pixel pitch of 55 µm. In contrast to its predecessor TPX chip, where the readout is frame-based, the readout from TPX3 is event-based, and event data is immediately sent out upon the activation of each pixel. If a signal causes a crossing of the energy threshold then the hit is registered along with the pixel coordinates, TOA, and the time taken for the signal to fall below the threshold, which is referred to as the time-over-threshold (TOT). The dead time of individual pixels to process and store the information after they were hit is about 475 ns plus the corresponding TOT. The TPX3 data is acquired by Speedy PIxel Detector Readout (SPIDR) system (Nikhef, Amsterdam, the Netherlands) and transferred to the acquisition computer with a speed of 1 Gbit·s⁻¹.[301] The SPIDR has an internal time-to-digital converter (TDC), which is able to time-stamp incoming digital pulses with 260 ps precision synchronously with the TPX3 hits. This feature is needed to provide an external time reference. The TPX3 and internal TDC of the SPIDR were triggered at a rate of 1-2 Hz using the HCD exit trigger pulse, via a digital pulse and delay generator (DG535, Stanford Research Systems). The TPX3 data was recorded at a time resolution of 1.5625 ns, with a maximum measurement window of 180 µs for each measurement cycle.

The external high-voltage power supplies from Applied Kilovolt (West Sussex, UK), AMOLF (Amsterdam, The Netherlands), and FuG Elektronik GmbH (Schechen, Germany) were used to power the discrete-dynode EMs, MCPs, and phosphor voltages, respectively. The pulse generator and oscilloscope settings were set manually. All other parameters are controlled by the Q Exactive UHMR tune software (version 2.11 build 3005, Thermo Fisher Scientific, Bremen, Germany) and custom-developed instrument control software (Fasmatech, Athens, Greece). The data acquisition parameters and event sequences used for the generation of each figure are shown in Tables S1-S4 and Figures S12-16, S20, S23-24 (Supporting Information).

CONFIGURATION-1

Orbitrap UHMR MS

New development

CONFIGURATION-2

Orbitrap UHMR MS

New development

5

1. nESI source
2. Ion inlet
3. S-lens
4. Injection flatapole
5. Bent flatapole
6. Quadrupole
7. Tranfer multipole
8. C-trap
9. Orbitrap mass analyzer
10. HCD cell
11. Lens 1

12. Tranfer hexapole
13. Lens 2
14. Quadrupole trap
15. Lens 3
16. Correction lens
17. Lens 4 (Slit)
18. TOF analyzer
19. Dual MCP stack 1
20. Phosphor screen
21. Focus lens
22. Si sensor

23. TPX3 chip
24. 193 nm excimer laser
25. Mirror 1
26. Mirror 2
27. Iris1
28. Dual MCP stack 2
29. TPX quad chip
30. Attenuator unit
31. Mirror 3
32. Iris 2
33. Quartz window

Figure 2. Detailed ion and laser optics schematic (not to scale) of the two different configurations of the Orbitrap/TOF system.

Data Analysis

The SoPhy (Software for Physics, Amsterdam Scientific Instruments, Amsterdam, The Netherlands) software package versions 1.5.7 and 1.6.3 were used for the TPX and TPX3 chip's control and data acquisition, respectively. A total of hundred measurement cycles (frames) were collected and summed for each TPX/TPX3

dataset. The raw files were subsequently analyzed using in-house developed software written in MATLAB (R2018a, MathWorks Inc., Natick, MA, USA).

Ion Optics Simulations

SIMION® 8.1 (Scientific Instrument Services, Ringoes, USA) and SIMAX (MSCUBE, Ponsonby, New Zealand) software packages were used for the ion optics design of the custom-built TOF analyzer. The 3D potential arrays (.pa files) of the TOF analyzer and associated ion optics of the custom-designed part built and refined using the SIMION were exported to the SIMAX software. The time-dependent voltage signals and isotropically distributed ion groups (.ic8 files, without initial axial velocity (v_z)) were defined using the SIMAX GUI. v_z component was added to the .ic8 files in excel, and the updated .ic8 files were then reloaded to the SIMAX. All ion optical simulations were performed using SIMAX.

RESULTS AND DISCUSSION

System Configurations and Modes of Operation

The new instrument consists of two mass analyzers: a modified commercial high-resolution Orbitrap MS and a newly developed orthogonal TOF system. The instrument is equipped with a static nESI source at the entrance of the Orbitrap MS (Element 1, Figure 2) for the ionization of the MMAs in their pseudo-native state, by maintaining the non-covalent interactions. This versatile system allows different modes of operation using advanced ion optics for ion manipulation and steering. These operational modes are: 1) standard Orbitrap MS acquisition; 2) external Orbitrap MS acquisition with or without (w/wo) UVPD; 3) external axial imaging and, 4) external orthogonal TOF MS imaging w/wo UVPD (Figure 1b). Each of these modes can take advantage of the quadrupole mass filter (Element 6, Figure 2) within the Orbitrap MS to select a specific *m/z* of interest. Selected ions can be directed towards the LQ-trap (Element 14, Figure 2) of the custom-designed system, where they are stored for later usage. The different operational modes will be elaborated in the following paragraphs.

Standard Orbitrap Mode

The ability to maintain normal Orbitrap UHMR MS operation was an essential design criterion. As a result, the new LQ-trap-TOF analyzer addition only replaces the HCD cell electrometer and does not interfere with normal operation.

External UVPD Orbitrap Mode

A hexapole ion guide (Element 12, Figure 2) transfers the ions from the Orbitrap MS through the HCD cell to the segmented LQ-trap of the new instrument. In external UVPD Orbitrap mode, the UV laser beam interacts with a large number of precursor ions at the LQ-trap. The precursor ions are radially and axially confined to a well-focused ion cloud by the collision with argon gas in the LQ-trap prior to UVPD to ensure maximum ion-photon interaction. The UV generated

fragments are sent back to the Orbitrap analyzer (Element 9, Figure 2) to obtain a high-resolution UVPD mass spectrum. This mode is employed for the retrieval of several higher-order structural features of MMAs including proteoform composition, subunit stoichiometry, and interactions.

External Axial Imaging Mode

In configuration 1 (Figures 1a and 2), the system can be operated in the external axial imaging mode, in which the MMA ions stored in LQ-trap are directed to the axial MCP-TPX quad detection assembly for imaging. The TPX registers both the arrival time and arrival position of the ion cloud. This mode is extremely suitable for the temporal and spatial analysis of the ion package emitted from the LQ-trap. Note that the TOF spectrum acquired on the TPX quad is of poor quality due to the absence of a strong acceleration field and a short flight path from the LQ-trap to the axial detector.

External UVPD Orthogonal TOF Imaging Mode

The main purpose of this instrument is to determine the spatial and temporal distribution of the MMA's fragments using a TOF MS imaging approach. This is achieved in the external UVPD orthogonal TOF imaging mode. The precursor MMA ions stored in the LQ-trap are sent toward the orthogonal TOF analyzer, on the way they interact with photons in one of the locations between the LQ-trap and the TOF analyzer (Elements 14-18, Figure 2). The TOF-separated UV-generated MMA fragments are then accelerated towards the MCP-P47-TPX3CAM imaging assembly for time (m/z)-resolved imaging. The ion optical design of the TOF analyzer ensures that the relative positions of the fragments are maintained as they separate from each other following the dissociation process until they reach the TPX3 detector assembly. The TPX3 registers both the arrival time and arrival position of each subunit released from the MMA ions. The arrival time information can be used for the generation of the mass spectrum. The arrival coordinates provide the spatial distribution of the product ions at the detection assembly, which is hypothesized to reflect their relative positions and trajectories following the fragmentation process. This can be used to retrieve a large amount of critical information related to the translational energetics of the fragmentation process of the MMAs.[310]

TOF Analyzer Design

The TOF analyzer design criteria encompass the following; (i) sufficient time resolution to distinguish complementary subunit fragments generated from MMA ions, (ii) maintaining the relative positions of subunit fragments formed from a single MMA ion, following the dissociation process until they reach the orthogonal TPX3CAM detection assembly, and (iii) ensure that all ions, regardless of angular divergence hit within a maximum 40 mm diameter area of the MCP detector. A TOF analyzer with a two-stage acceleration field (s and d fields) and a bias electrode was designed to meet the aforementioned requirements. The voltage division and dimensions of each electrode are shown in Figure S1 (Supporting

Information). In the design phase, the whole system and its behavior was modeled using SIMION and SIMAX. The supporting information describes in detail the ion optical design and simulations of the TOF analyzer (Section "Ion Optical Design of TOF analyzer" and Figures S2-S10). Briefly, the expected fragments from two commonly used proteins in MS, ubiquitin (~8.56 kDa) and dimeric concanavalin A (~51.32 kDa) were sent to the orthogonal detector to simulate the performance of the TOF analyzer. The simulated fragment ion trajectories, detector images, and TOF spectra were examined under various ion optics settings. The simulation results suggest that the optimum conditions for the operation of the instrument in the external UVPD orthogonal TOF imaging mode are the following: ratio of V_s to $V_d \geq 0.5$, distance from the pusher to the detector=655 mm, fragmentation location at the center of the pusher, and detector required to be off-centered in the z-direction by 20 to 40 mm.

System Configurations

Two different configurations were employed for the comprehensive characterization (Figures 1a and 2) of the system. Configuration 1 utilizes two imaging detectors: an axial MCP-TPX quad and an orthogonal MCP-P47-TPX3CAM. The laser optics (Elements 24-27, Figure 2 (top)) have been installed in such a way that the laser beam can interact with the ion cloud orthogonally at any segment of the LQ-trap or correction lens. However, even at high laser energies (>3.5 mJ at the laser device exit) and high repetition rates (>175 Hz), the fragmentation efficiency was extremely low in the external UVPD Orbitrap mode and no fragment ions were detected at all in the external UVPD orthogonal TOF imaging mode due to the non-optimal overlap of the orthogonal laser beam with the precursor ion cloud in configuration 1. The experimental setup has been modified in configuration 2 by replacing the axial TPX quad assembly with a quartz window (Element 33, Figure 2), which allows the UV laser beam to interact coaxially with the ion cloud that resulted in a higher fragmentation efficiency compared to the configuration 1. All the UVPD experiments shown in this paper were conducted in system configuration 2. Note that configuration 1 has solely been employed for testing purposes as that allows the visualization of the axial ion cloud using the TPX quad assembly.

Characterization of the Orbitrap/TOF Instrument with Imaging Detectors

The spectral, non-imaging performance of the instrument was evaluated under normal operational conditions (see Supporting Information, Section "Characterization of the Orbitrap/TOF Instrument without Imaging Detectors and UV Laser", Tables S1-2, and Figures S11-20). Subsequently, the influence of the custom-built TOF analyzer and the associated ion optics on the ion trajectories was investigated by the visualization of the spatial distribution of the ion cloud with axial and orthogonal imaging detectors. The MCP-TPX quad[71, 140-144, 146-151, 290] and MCP-P47-TPX3CAM[152, 261, 294, 296-300, 322-325] assemblies coupled with the

Orbitrap/TOF instrument are deployed for this purpose (Configuration 1, Figure 1a and 2). Singly charged CsI ions of mass 5589 Da were selected using the quadrupole mass filter. The spatial distribution of these selected ions was studied with the orthogonal TPX3CAM and axial TPX quad assemblies by operating the instrument in external orthogonal TOF imaging and external axial imaging modes, respectively.

The ions are initially accelerated in the z-direction as they leave the HCD cell of the Orbitrap MS and travel toward the TOF region/axial detector (Figure 2). Ions are imaged in the xy plane when operated in the external axial imaging mode. In external orthogonal TOF imaging mode, the pusher pulses ions in the y-direction for the TOF separation and orthogonal spatial profile measurements, and detected by the TPX3 assembly in the xz plane. The ion impact position z and x at the orthogonal TPX3 detector is determined by the flight angles θ and Φ of the ion beam leaving the pusher [71], which is given by

$$\vartheta = \tan^{-1}\frac{v_y}{v_z} \qquad \Phi = \tan^{-1}\frac{v_y}{v_x} \qquad (1)$$

where v_x, v_y and v_z are the velocity components in x-, y-, and z-directions respectively. We have observed that the TOF analyzer & LQ-trap parameters have a critical influence on v_y and v_z components of the ion beam, respectively, hence on the θ, and that leads to a shift in the z-impact position at the orthogonal TPX3 detector. This will be discussed in detail below. As no voltage source accelerates the ions in the x-direction, v_x is much smaller than v_y, which keeps $\Phi \approx 90°$, which means the x-impact position at the orthogonal detector is least sensitive to most of the ion optical parameters.

Orthogonal Ion Energy (E_y)

The impact of the TOF analyzer parameters on the z-impact coordinate of the orthogonal TPX3 image is shown in Figures 3a and S21a-d. The orthogonal velocity component (v_y) of the ion beam as it enters the TOF analyzer is defined by the potential at the midpoint of E_1 and E_2 (Figure S1). This potential rises when (i) both V_s and V_d are increased while keeping κ as 1 (Figure 3a), (ii) V_s is increased at V_d=5 kV (Figure S21a), and (iii) V_d is increased at V_s=5 kV (Figure S21b), which leads to an increase of v_y in all three cases, raises θ, and results in a shift towards –z direction in the orthogonal TPX3 image. No significant z-shift in the ion profile was observed for a change in (i) V_s and V_d by retaining pusher voltage (V_s+V_d) at 10 kV (Figure S21c) and (ii) bias electrode voltage while keeping V_s=5 kV and V_d=5 kV (Figure S21d) as all these changes do not significantly alter the potential profile at the midpoint of E_1 and E_2.

Axial Ion Energy (E_z)

The DC offset voltage of the HCD cell ($VDC_{HCD\ cell}$) defines the axial energy of the ion cloud as it leaves the HCD cell. But afterwards, these ions are collisionally focused in the third segment of the LQ-trap (Q3) and ejected into the TOF region. Hence, the initial ion axial velocity (v_z) when the beam enters the TOF region is

determined by the DC component of the Q3 voltage (VDC$_{Q3}$), not by the VDC$_{HCD}$ $_{cell}$. An increase in v_z reduces θ, which causes a shift towards the +z-direction in the orthogonal TPX3 image. As expected, a rise in VDC$_{Q3}$ results in a higher v_z velocity and shifts the ion trajectory more to the +z-direction (Figure 3b), whereas the z-impact position remains insensitive to the variations in the VDC$_{HCD\ cell}$ (Figure S21f). The voltages of the adjacent electrodes of Q3-Q2 (second segment of the LQ-trap, Figure S21e) and L3 (Lens 3, Figure S21g-h) are also observed to influence v_z. L3 is biased at a higher voltage during the ion storage in LQ-trap (V$_{L3\ (Q-trapping)}$) and switches to a lower value when the ions from the LQ-trap are ejected into the TOF region (V$_{L3\ (Ejection\ to\ pusher)}$). A change in V$_{L3\ (Q-trapping)}$ and V$_{L3\ (Ejection\ to\ pusher)}$ have totally opposite effects on the z-impact position of the ion distribution at the orthogonal TPX3 image. Supporting Information provides a detailed description on the influence of Q2 and L3 on the axial ion energy, and consequently on the spatial profile at the orthogonal imaging detector (Section "Influence of Ion Optics on Orthogonal Spatial Profile" and Figures S21e, g-h).

Transmission and Collisional Focusing of the Ion Cloud

The effect of RF amplitude of the hexapole and LQ-trap (VRF) on the ion transmission has already been explored by evaluating the Orbitrap spectrum acquired in the external Orbitrap mode (Supporting Information, Section "Characterization of the Orbitrap/TOF Instrument without Imaging Detectors and UV Laser", and Figure S17). Here, we investigated the spatial profile of the quadrupole-isolated ions with *m/z* values of 5589 (Figure 3c and d), 3510.5 (Figure S21i and j), and 7407.7 (Figure S21k and l) using the orthogonal TPX3 and axial TPX quad detectors at different VRF values. The axial TPX quad images indicate that higher VRF is an absolute requirement for the effective transmission of high *m/z* ions. The utilization of VRF=300 V was sufficient for the efficient transmission of *m/z*=3510.5 ions. Meanwhile, a VRF of 375 V was necessary for *m/z*=5589 and 7407.7 ions. The orthogonal TPX3 images provide a clearer picture of the VRF dependency on the *m/z*. For instance, the shape of the ion cloud remains the same or the ion trajectory stabilizes when VRF>300 V for *m/z*=3510.5 ions. However, the ion trajectories do not stabilize even when the VRF approaches 450 V for ions with *m/z*= 5589 and 7407.7.

m/z Dependency

A previous study by our group conducted on the TPX quad-equipped LCT (ESI-orthogonal reflectron TOF) demonstrated that the centroid of the spatial distribution of the ion cloud at the TPX detector is insensitive to *m/z* values.[71] Despite the fact that both the LCT and Orbitrap/TOF instruments utilize ESI sources, the centroid of the *m/z* resolved images acquired on the Orbitrap/TOF instrument shifts in the z-direction (Figure 3e). In LCT, a continuous ion beam produced by the ESI source is pulsed by the pusher towards the detector, causing ions to strike at the same detector area regardless of the *m/z* values. Whereas in the Orbitrap/TOF instrument, the ESI-generated ions are later collisionally focused in the LQ-trap. This well-focused ion cloud pulsed from the LQ-trap is *m/z* separated

in the time domain (z-position) while travelling the substantial distance from the LQ-trap to the pusher. This causes the fast-moving low m/z ions to appear more to the right of the pusher (more towards +z-direction) compared to the slow-moving high m/z ions, prior to the pulsing of the ion cloud to the orthogonal detector. Figure S22a further supports this explanation. The dependency of the spatial distribution of the ion cloud at the orthogonal detector on the time difference between the ion ejection from the LQ-trap and pusher pulse ($T_{Pusher\ pulse}-T_{Ejection\ from\ LQ-trap}$) is depicted in Figure S22a (Supporting Information). At a lower $T_{Pusher\ pulse}-T_{Ejection\ from\ LQ-trap}$, the ions appear more to the left of the pusher prior to the pulsing, and are imaged more to the –z direction of the detector. When the $T_{Pusher\ pulse}-T_{Ejection\ from\ LQ-trap}$ is higher, the ions have the time to travel further to the right of the pusher and are more likely to strike the detector towards the +z direction.

Focusing and Deflection of the Ion Beam

Figures 3f, S22b, and S22c demonstrate the dependency of the spatial profile of the ion cloud at the orthogonal TPX3 detector on the applied voltages on the third, first, and second electrodes of the correction lens (C1-3). The correction lens positioned between the LQ-trap and pusher focuses and defocuses the ion beam based on the applied voltages on the three electrodes, which leads to a change in the shape as well as a shift in the centroid ($\bar{z}$, $\bar{x}$) of the ion cloud that is projected onto the orthogonal detector. Note that the variations in the voltage of the electrode near the exit of the correction lens, lens 4 (L4) have an impact on the shape of the ion cloud as well (Figure S22d). The middle electrode of the correction lens, C2, has the least effect on the ion beam spatial profile of the three electrodes. C2 is a segmented four-electrode steering lens. The voltage of each segment can be adjusted separately to function as a xy deflector. A change in the x-deflection voltage (V_{+x}) of C2 alters the x-position of the ions at the pusher region prior to pulsing and leads to a considerable shift in the x-impact coordinate of the ion cloud at the TPX3 detector image (Figure 3g). Similarly, a variation in the y-deflection voltage (V_{-y}) affects the y-position of the ions at the pusher region prior to pulsing as well. However, the modification of the ion trajectories in the y-direction is not translated to the ion image as the orthogonal detector is placed in the xz plane (Figure 3h).

Size of the Ion Cloud

Figure 3i shows the effect of the m/z isolation window on the axial TPX quad detector image. At high m/z isolation window values, a large ensemble of ions is transported from the quadrupole of the Orbitrap MS to LQ-trap, which results in increased columbic repulsion within the ion packet and it expands in all directions. An x-y slit (Element 17, Figure 2) of 2x12 mm cuts the collisionally focused ion cloud ejected from the LQ-trap as a rectangular beam. The ion cloud is then enlarged further as it is traveled through the field-free zone between the slit and exit of the pusher. A tilted, distorted rectangular-shaped ion cloud is observed at the axial imaging detector as the rectangular TPX quad chip is

positioned at an angle in the xy plane. The dimensions of the ion cloud are measured as ~2x3, 2.2x5.4, 2.2x6.3, and 2.3x11 mm (x-y) at different m/z isolation windows of values 20, 80, 320, and 1280, respectively.
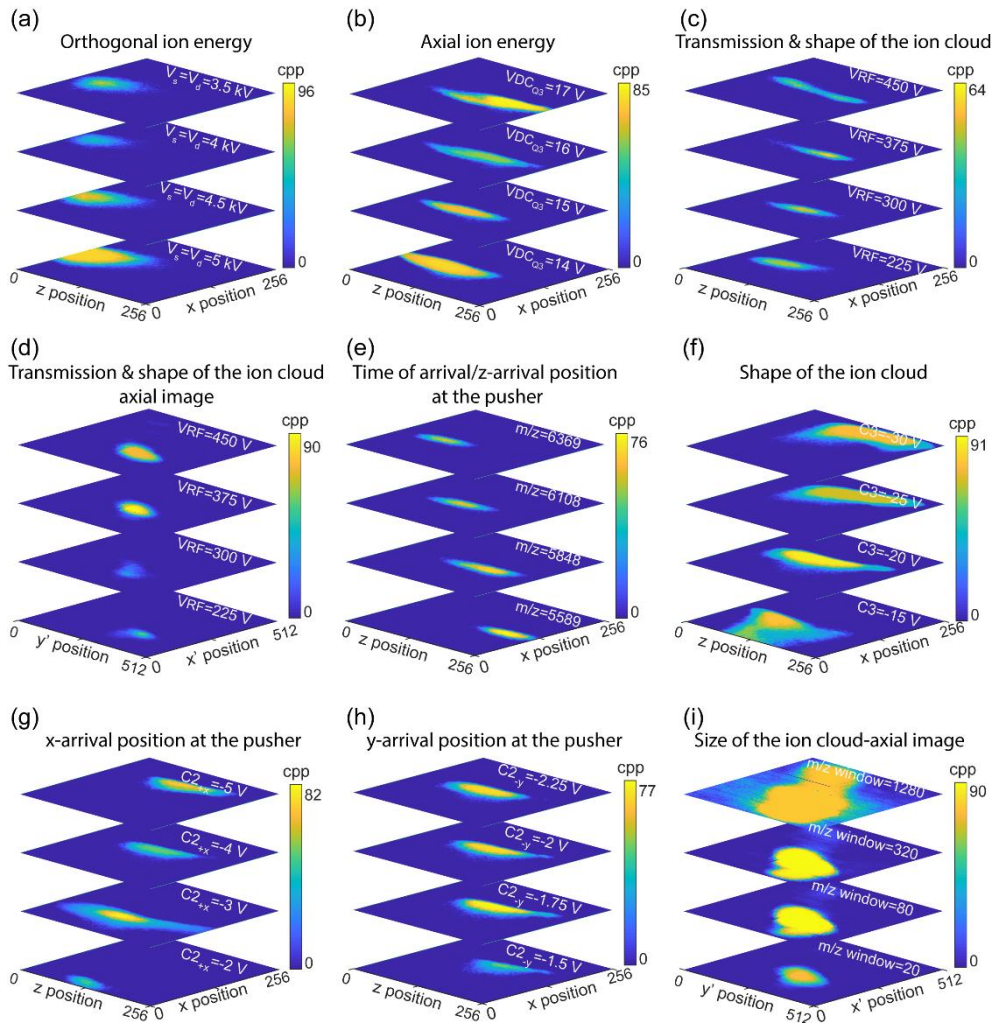
Figure 3. Influence of (a) s & d TOF fields (κ=1), (b) DC voltage on the third segment of the LQ-trap (VDC$_{Q3}$), (c) RF amplitude of the hexapole and LQ-trap (VRF), (e) m/z value, (f) voltage on the third electrode of the correction lens (C3), (g) voltage on the top segment of the second electrode of the correction lens (C2$_{+x}$) and (h) voltage on the left segment of the second electrode of the correction lens (C2$_{-y}$) on the spatial distribution at the orthogonal TPX3 detector, and (d) VRF and (i) width of the m/z isolation window on the spatial distribution at the axial TPX quad detector. All data were collected by spraying the CsI mix and selecting singly charged ions with m/z of 5589 (except for Figure 3e) using the quadrupole mass filter. All images represent the sum of a hundred measurement cycles. cpp = counts per pixel.

Characterization of the Orbitrap/TOF Instrument With External UVPD Imaging

In this section, the implementation of UVPD using the 193 nm excimer laser on the Orbitrap/TOF instrument equipped with the orthogonal imaging detector is discussed. High-resolution measurements in external UVPD Orbitrap mode were initially performed followed by the m/z-resolved spatial distribution determination in external UVPD orthogonal TOF imaging mode of the UV generated fragments from the MMA. The UVPD experiments were conducted in system configuration 2 (Figure 1a & 2) as the axial UVPD implementation in configuration 2 enables maximum overlap of the photons with the ion cloud. Concanavalin A (102 kDa), a non-covalently bounded homotetramer, was injected into the MS under native-like conditions. The tetrameric concanavalin A $[M+21H]^{21+}$ ions were selected with an m/z window of 10 Da using the quadrupole mass filter. The laser beam interacts with the selected precursor ions at one of the locations in between the LQ-trap and pusher, and the UV fragments are then sent either to the Orbitrap analyzer or to the orthogonal TPX3 detector.

High-Resolution UVPD

Figure 4a shows the UVPD spectra of tetrameric concanavalin A $[M+21H]^{21+}$ ions acquired at different laser pulse energies in external UVPD Orbitrap mode. In this mode, a single UV laser pulse interacts with the precursor $[M+21H]^{21+}$ ions in the LQ-trap for 100 ms (ion storage time) per measurement cycle. The generated UV fragments were sent back to the Orbitrap analyzer for the high-resolution molecular analysis. In Figure 4b, the HCD spectra of the tetrameric concanavalin A $[M+21H]^{21+}$ ions measured at various collision energies (normalized collision energy, NCE) are displayed for better comparison. Both the UVPD and HCD spectra were recorded under the same Orbitrap MS settings. Table S3, Figures S12 and S23 show the relevant data acquisition parameters and event sequence used in external UVPD Orbitrap mode. The UVPD data indicates that the tetramer is predominantly dissociating into monomers and trimers, in line with the results from the HCD and previous UVPD[169] measurements. As the laser pulse energy increases, the signal intensity of the precursor peak reduces as expected. However, fragment peak intensities do not significantly increase. This can be attributed to the following reasons: (i) ion beam divergence due to the increased space-charge effect; and (ii) insufficient focusing of the UV generated fragments in the LQ-trap. The ratio of monomers to trimers is low in our study when compared to the UVPD spectrum of the concanavalin A $[M+21H]^{21+}$ ions obtained by the interaction of 3mJ 193 nm photons at the HCD cell in previous investigations.[169] This can be attributed to the discrepancy between the UV dissociation conditions and data acquisition parameters used in the two experimental setups. However, we believe that in our case, the high RF voltage of the hexapole and LQ-trap (VRF=600 V) may contribute to the preferential transmission of the high m/z trimer product ions. Note that a higher VRF (>450V) and a lower LQ-trap pressure (<1e-

4 mbar) were essential requirements for the measurement of UVPD fragments in external Orbitrap UVPD mode.

(a) UVPD **(b) HCD**
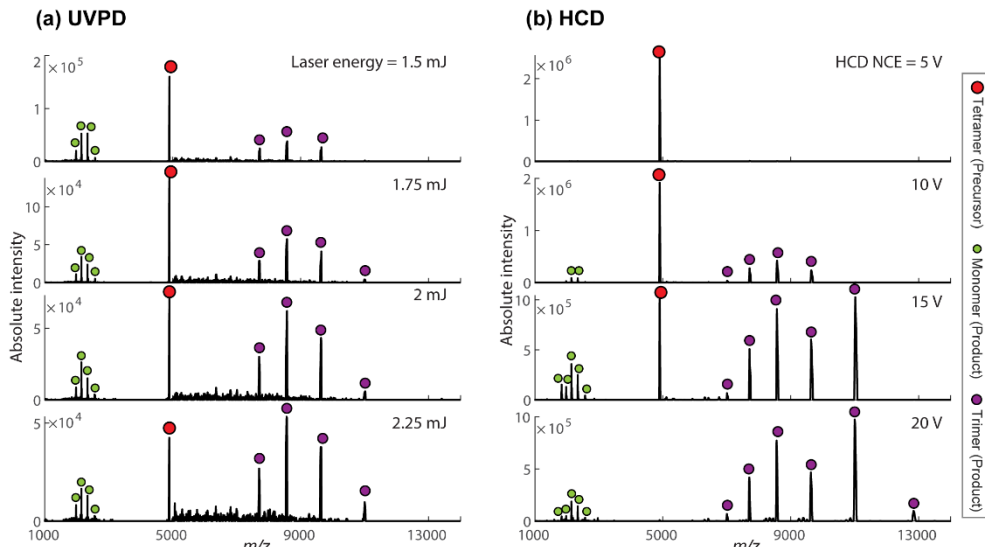
Figure 4. (a) UVPD spectra of tetrameric concanavalin A [M+21H][21+] ions acquired at different laser pulse energies in external UVPD Orbitrap mode. A single UV laser pulse interacts with the precursor ions in the LQ-trap for 100 ms (ion storage time) per measurement cycle. (b) HCD spectra of the tetrameric concanavalin A [M+21H][21+] ions measured at various collision energies (normalized collision energy, NCE). Both the UVPD and HCD spectra were recorded under the same Orbitrap MS settings. Table S3, Figures S12 and S23 show the important data acquisition parameters and event sequence used in external UVPD Orbitrap mode.

UVPD Fragment Orthogonal TOF MS Ion Imaging

The UVPD fragments can also be studied with the orthogonal TOF MS. Figure 5a shows the UVPD spectrum of the concanavalin A [M+21H][21+] precursor ions measured at the orthogonal TPX3 detector by the interaction of 193 nm photons with the ion cloud at different locations of the instrument (Elements 14-18, Figure 2). A single laser pulse with an energy of 0.5 mJ (measured at the exit of the attenuator) per TOF cycle was used. One hundred of TOF measurements were added to produce the total ion spectrum. Table S4, Figures S14 and S24 show the relevant data acquisition parameters and event sequence used in external UVPD orthogonal TOF mode. In all five cases, tetramer is fragmenting to monomers and trimers, which is consistent with the results of high-resolution UVPD. The orange trace corresponds to the photon-ion interaction right after the precursor ion injection from the HCD cell to LQ-trap. The light blue trace displays the result of the interaction of the laser beam with precursor ions, stored in the LQ-trap for 100 ms, just before the ion ejection into the TOF analyzer region. The yellow, dark blue and maroon traces represent the UVPD spectra generated by the interaction of the laser beam with the moving precursor ion cloud at different locations. These are respectively the correction lens (Element 16, Figure 2), the slit (Element 17, Figure 2), and the middle of the TOF analyzer (Element 18, Figure 2). The

interaction locations were predicted by comparing the experimentally measured time between the ion injection from the HCD cell to LQ-trap and the pusher pulsing with the Simion ion optics model. The orange, light blue, and yellow UVPD spectra were plotted by combining the TPX3 spectrum collected for six different $T_{Pusher\ pulse}$-$T_{Ejection\ from\ LQ-trap}$ (time taken by the ion cloud to travel from LQ-trap to middle of the TOF analyzer) of 140 μs, 160 μs, 180 μs, 200 μs, 220 μs, and 240 μs. The $T_{Pusher\ pulse}$-$T_{Ejection\ from\ LQ-trap}$ had to be tuned to 200 μs to ensure that the precursor $[M+21H]^{21+}$ (m/z=4901) ions strike at the center of the imaging detector assembly. However, when UVPD takes place at a location prior to the middle of the pusher, the ion beam will be axially dispersed (in the z-direction) based on the m/z values of the product ions, when they arrive at the pusher. A lower $T_{Pusher\ pulse}$-$T_{Ejection\ from\ LQ-trap}$ (~ 140 to 180 μs) for the fast-moving monomer product ions that spans over a lower m/z range from 1700 to 4300 Da and a higher $T_{Pusher\ pulse}$-$T_{Ejection\ from\ LQ-trap}$ (~ 200 to 240 μs) for the slow-moving trimer product ions that span over a higher m/z range from 5100 to 9700 Da had to be used in order to ensure that the ions in the entire m/z range strike at the MCP detector area (40 mm diameter). The effect of the axial velocity spread of the product ions is minimized when the ion-photon dissociation location is close to the midpoint (z-component) of the pusher, where the pusher pulses the ions towards the TPX3 detector. A single measurement with $T_{Pusher\ pulse}$-$T_{Ejection\ from\ LQ-trap}$ of 200 μs was adequate to encompass the whole m/z range of the UVPD spectrum, when the ion-photon interaction occurs at the midpoint of the pusher region (Maroon curve, Figure 5a). The dark blue curve is generated by the interaction of the laser beam with precursor ions at the slit using a single $T_{Pusher\ pulse}$-$T_{Ejection\ from\ LQ-trap}$ of 200 μs. Several product ions (mainly high m/z's) weren't detected in this case due to the axial separation as they move through a potential gradient of 40 V from the slit to the middle of the pusher (65mm). To minimize the TOF-effect that results in the axial dispersion of the product ions, the UVPD fragment imaging experiments were performed by the interaction of the UV laser beam with the precursor ion cloud at the midpoint of the pusher.

The spatial distribution of the product ions and unfragmented precursor ions at the orthogonal TPX3 detector generated by the photon-ion interaction close to the middle of the pusher is shown in Figure 5b (image corresponds to maroon trace in Figure 5a). A well-focused 21+ charged precursor ion cloud dissociates predominantly into fragment ions that are either 13+ charged monomers and 8+ charged trimers, 12+ charged monomers and 9+ charged trimers, or 11+ charged monomers and 10+ charged trimers, which spread all over the detector area in both x and z-directions. The monomer and trimer product ions are unambiguously separated in both time and space. While outside the scope of this study, a better understanding of the kinetics of the dissociation process can be gained by analyzing the relative distance and angular distribution of the product ions with respect to the impact position of the precursor MMA ions, which may reveal critical details about the higher order structural characteristics of the MMA such as bond strength and 3D conformation.

5
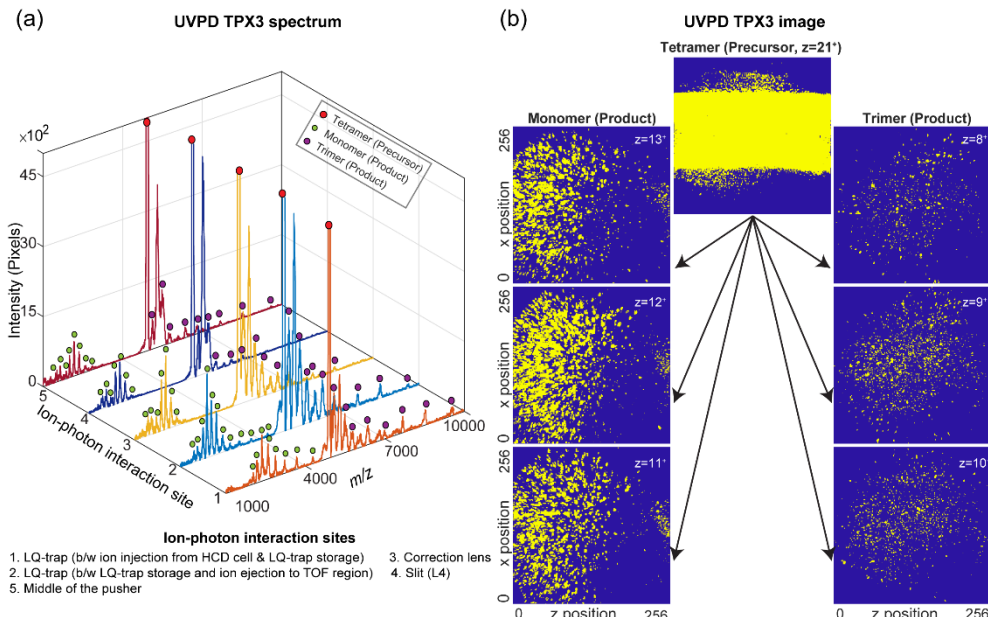
Figure 5. (a) UVPD spectra of tetrameric concanavalin A $[M+21H]^{21+}$ ions acquired at the orthogonal TPX3 detector by the interaction of 193 nm photons with the ion cloud at different locations of the instrument. (b) Spatial distribution of the product ions and unfragmented precursor ions at the TPX3 detector generated by the photon-ion interaction close to the middle of the TOF region (image corresponds to maroon trace in 5a). 21+ charged precursor ion cloud dissociates predominantly into fragment ions that are either 13+ charged monomers and 8+ charged trimers, 12+ charged monomers and 9+ charged trimers, or 11+ charged monomers and 10+ charged trimers. A single laser pulse with an energy of 0.5 mJ (measured at the exit of the attenuator) per TOF cycle was used. A hundred of TOF measurement frames were added to produce the total ion spectrum. Table S4, Figures S14 and S24 show the important data acquisition parameters and event sequence used in external UVPD orthogonal TOF mode.

CONCLUSIONS

With the development of a unique Orbitrap/TOF system with integrated UVPD and TPX3CAM, we have brought together aspects from high-resolution Orbitrap and TOF MS, top-down proteomics, and photofragment ion imaging for the first time. This paves the way for an entirely new approach for resolving the higher-order molecular structure of MMAs in their pseudo-native state in the gas phase. The custom-developed instrument, which is operational in four different modes, enables the high mass resolution measurement and mass-resolved imaging of the UVPD generated fragments from the native MMA ions using the Orbitrap mass analyzer and TOF analyzer-TPX3 imaging assembly, respectively.

UVPD on high-resolution Orbitrap and TOF MS instruments has already been employed by several groups for the high-level structural and functional characterization of MMAs.[80, 164, 169, 326-329] However, the TOF imaging approach implemented in this study with the TPX3 detection assembly allows the

visualization of the 3D UV dissociation event of the MMA's as the TOF analyzer is designed to maintain the relative positions of the fragment subunits until reaching the detector. A better understanding of the dissociation dynamics can be gained through the analysis of the relative distance and angular distribution of the product ions with respect to the impact position of the precursor MMA ions from the m/z-resolved TPX3 images. We hypothesize that this approach will provide crucial information regarding the higher-order structural characteristics of the MMA, including bond strength, conformation, etc as well as the behavior of the MMAs in the gas phase. In addition, the evaluation of the m/z-resolved TPX3 images after the integration of other fragmentation methods such as ECD, ETD, SID and IRMPD to the Orbitrap/TOF system is anticipated to yield significant information on different fragmentation mechanisms.

5

SUPPORTING INFORMATION

Ion Optical Design of TOF Analyzer

This section describes the ion optical design and simulations of the TOF analyzer. The TOF analyzer and the associated ion optics of the custom-designed system was modeled using SIMION and SIMAX. An isotropic spherical expansion of some of the expected covalently/non-covalently dissociated fragments from ubiquitin (~8.56 kDa) and dimeric concanavalin A (~51.32 kDa) was generated for the simulations, where the velocity vectors of the fragments were determined by assuming a kinetic energy (E) release of 2 to 5 eV/fragment ($E_{Fragmentation}$) following the dissociation (Supporting Information Figure S2). The ion beam was considered to be initially accelerated in the axial (z) direction by 30 V (V_{axial}). The precursor ubiquitin ion of $m/z=1428$, $z=6$ and axial kinetic energy (E_{Axial})=180 eV dissociates either into two fragment ions of mass=4.28 kDa ($m/z=1428$, $z=3$) or fragment ions of masses 1.25 kDa ($m/z=1247$, $z=1$) and 7.31 kDa ($m/z=1463$, $z=5$). While the precursor concanavalin A homodimer of $m/z=3422$, $z=15$ and $E_{Axial}=450$ eV dissociates into two monomer fragment ions of $m/z=3209$ ($z=8$) and $m/z=3667$ ($z=7$).

Figure S3 demonstrates the effect of V_s, V_d, and bias electrode voltage ($V_{bias\ electrode}$) on the time focus at a nominal acceleration potential of 15 kV (pusher voltage). The time focus value displayed in the y-axis was calculated by measuring the distance from the pusher to the TOF region with the minimum spatial spread of the ion beam in the y (orthogonal)-direction. κ is the ratio of V_s to V_d. A concanavalin A [M+8H]$^{8+}$ monomer fragment ion cloud formed at the midpoint of the pusher was used for the determination of time focus. The time focus has been observed to be least sensitive to the $V_{bias\ electrode}$ at higher κ values. At higher κ values, for example, when $\kappa=0.5$ ($V_s=5$ kV and $V_d=10$ kV), the time focus drifts only by a maximum distance of 130 mm for a change in $V_{bias\ electrode}$ from -15 to +15 kV (Figure S4). Figures S5 and S6 show the ion trajectories (in xy plane) of the concanavalin A [M+8H]$^{8+}$ and [M+7H]$^{7+}$ monomer fragment ion clouds formed at the midpoint of the pusher, which correspond to different $V_{bias\ electrode}$ at two relatively high κ values, $\kappa = 0.364$ ($V_s=4000$ V, $V_d=11000$ V) and 0.5, respectively. Note that the relative positions of the fragment ions following the dissociation process are maintained at both κ values. However, when the fragmentation occurs in the middle of the second segment of the correction lens (C2) and $\kappa = 0.364$, the ion trajectories cross on their way to the detector and result in the distortion of the relative positions of the ions at the detector image (Figure S7). Whereas, the relative positions of the ions are preserved regardless of the fragmentation location when $\kappa = 0.5$ (Figure S8). In addition, the angular divergence of the fragments is least sensitive to the variations in the $V_{bias\ electrode}$ at $\kappa=0.5$ compared to 0.364. The simulation results suggest that the optimum conditions for the operation of the instrument in the external UVPD orthogonal TOF imaging mode are the following: $\kappa \geq 0.5$, distance from the pusher to the detector=655 mm and the fragmentation location at the center of the pusher. In

order to enhance the time resolution and maximize the number of ions striking the detector, V_s, V_d, and $V_{bias\ voltage}$ should be fine-tuned.

Figures S9 and S10 show the simulated total ion images and TOF spectra collected at the orthogonal detector at different dissociation energies and locations by sending concanavalin A and ubiquitin ions, respectively. There is a shift in the z-impact position of the ion cloud at the detector image (Figures S9 and S10a, c, e, and g) based on the m/z that is caused by the difference in the flight angle (θ). θ is defined as the ratio of orthogonal (y) and axial (z) velocity components. The product ions have the same v_z as the precursor ions regardless of the m/z values. In contrast, as all ions are accelerated with the same kinetic energy per charge in the TOF analyzer resulting in higher v_y for low m/zs and low v_y for high m/zs. This causes $\theta_{low\ m/z} > \theta_{high\ m/z}$. The reduced θ angle causes the high m/z ion beam to strike more towards the left of the detector. The detector required to be off-centered in the z-direction by ~20 mm when operated with a nominal acceleration potential of 15 kV because of the shift in the z-impact position due to the flight angle and to prevent the ions from traveling through the TOF region with non-straight equipotential lines. This has been considered during the mechanical design, and the detector assembly flange is constructed in such a way that it can be shifted by a maximum of 40 mm in the z-direction.

The effect of fragmentation location, $E_{Fragmentation}$, and m/z on the detector images as well as TOF spectra are evident in Figures S9 and S10. Even though the TOF spectra have improved time resolution when the fragmentation occurs in C2 and C3 (Figure S9b,d), the shape of the ion cloud (Figure S9a,c) is distorted due to the axial fragment ion acceleration following the dissociation process. Moreover, the ion transmission is significantly affected in both cases because of the slit (Element 17, Figure 2) that is positioned between the correction lens and TOF analyzer, which cuts the ion beam in the y-direction. This also suggests that the higher time resolution in Figures S9b and d compared to f and h is due to the absence of the fragments with the high angular spread in the y-direction. In Figures S9f and d, all of the fragments including the one with high angular spread, reach the detector and result in poorer quality TOF spectra as the fragmentation occurs at the pusher. However, this time resolution is still adequate to distinguish the complementary fragment pairs generated from single MMA ions in single ion UVPD fragment imaging mode. Also note that the detector image (xz plane) in Figures S9e and g resembles more to the projection of the initial distribution of the ion cloud (Figure S2e), demonstrating once again that relative positions of the ions are better retained when fragmentation occurs in the pusher region.

Characterization of the Orbitrap/TOF Instrument Without Imaging Detectors and UV Laser

To experimentally characterize the performance of the custom-designed TOF analyzer and the associated transmission ion optics, two discrete-dynode EMs were connected axially and orthogonally to the TOF analyzer instead of the imaging detectors. As this instrument is intended for the investigation of high-mass

ions, cesium iodide (CsI) mix was sprayed due to its high and wide m/z range (392 to 11,304 Da), and the signal was analyzed in all modes of operation under identical ion optical conditions (Figure S11). The important data acquisition parameters and event sequences used in different modes of operation are shown in Table S1 and Figures S12-16. Spectra recorded in the external Orbitrap mode and standard Orbitrap mode are very similar, as expected. In external axial non-imaging mode, the CsI signal is measured without distinguishable spectral information due to the lack of a mass analyzer between the LQ-trap and axial discrete-dynode EM detector. The CsI signal measured at the axial discrete-dynode EM detector has therefore been determined as a function of arrival time. The spectrum measured in external orthogonal TOF non-imaging mode resembles the standard Orbitrap spectrum in terms of the m/z peaks identified. Although the mass resolution in TOF mode is not that high, it still adequately resolves the adjacent peaks in the high m/z CsI mix spectrum. In addition, there is a slight difference in the relative intensities of each of the m/z peaks in the Orbitrap and TOF spectra. For example, the base peak in the Orbitrap spectrum is m/z= 2471, while the base peak in the TOF spectrum has a higher m/z value of 3510. The difference in the intensity profiles can be attributed to the m/z dependency of the arrival time of the ions at the pusher region. The fast-moving low-m/z ions appear more to the right of the pusher (Figure 2) compared to the slow-moving high m/z ions prior to the pulsing of the ion cloud to the orthogonal detector. At a lower $T_{Pusher\ pulse}$-$T_{Ejection\ from\ LQ-trap}$ (time difference between the ion ejection from LQ-trap and pusher pulsing, Figure S16), for example at 50 µs, the TOF spectrum is dominated by low m/z ion signal, as most of the high m/z ions appear to be lost on the left side of the detector. Whereas, when the $T_{Pusher\ pulse}$-$T_{Ejection\ from\ LQ-trap}$ is high, for example at 350 µs, mostly high m/z ions appear in the spectrum, as they get sufficient time to reach the pusher zone before being pulsed to the detector area. The majority of the low m/z ions is not measured in this case as they are lost on the right side of the detector. For the acquisition of the TOF spectrum in Figure S11, $T_{Pusher\ pulse}$-$T_{Ejection\ from\ LQ-trap}$=270 µs was used which prefers mostly the high m/z ions to be pulsed to the detector area.

We have observed that only a few ion-optical parameters associated with the custom-designed part of the instrument have a critical influence on the resulting spectrum: RF amplitude of the hexapole and LQ-trap, trapping gas pulse width and time delay between Ar gas injection to the LQ-trap and the ion ejection from the HCD cell to LQ-trap. The effect of the aforementioned parameters on the m/z profile is briefly discussed below.

RF Amplitude of the Hexapole and LQ-trap

Figure S17 shows the denatured ubiquitin spectrum measured in external Orbitrap mode at different RF amplitude of the hexapole and LQ-trap (VRF). An increase in the RF amplitude shifts the m/z transmission window to a higher m/z range.[330-331] When VRF is low, for example, at VRF=50 V, the mass spectrum is dominated

by low m/z ions with a z=13+ to 6+. Whereas, at a higher VRF=350 V, mostly lowly charged (9+ to 4+) high m/z ions appear at the mass spectrum.

Trapping Gas Pulse Width

Figure S18 demonstrates the effect of the amount of trapping gas (Ar) injected into the LQ-trap (Ar gas pulse width) on the mass spectrum. Denatured ubiquitin was measured in external Orbitrap mode. At a pulse width of 60 μs, the amount of Ar gas required to collisionally focus the ion cloud in the LQ-trap was insufficient that resulted in reduced signal intensity. A change in the gas pulse width from 60 to 70 μs, increased the ion intensity by threefold. The ion intensity continues to increase until the pulse width reaches 75 μs. Even if the pulse width is increased to a value as high as 100 μs, there is no significant change in ion intensity after 75 μs. A higher value of Ar gas pulse width was required for the efficient trapping of high molecular weight (MW) species. For instance, a minimum pulse width of 80 μs was required for the sufficient trapping and focusing of tetrameric concanavalin A with a MW of 102 kDa in the LQ-trap.

$T_{Ar\ gas\ injection\ to\ LQ\text{-}trap\ -\ Ion\ injection\ to\ LQ\text{-}trap}$

The impact of the $T_{Ar\ gas\ injection\ to\ LQ\text{-}trap\ -\ Ion\ injection\ to\ LQ\text{-}trap}$ (time delay between the Ar gas injection into the LQ-trap and ion ejection from HCD cell to the LQ-trap) on the Orbitrap spectrum of denatured ubiquitin is depicted in Figure S19. Table S2, Figures S13 and S20 show the important parameters and event sequence used for the acquisition of Figures S17-19. All of the left-sided spectra (Figure S19a, c, and e) were recorded in the external Orbitrap mode. All of the right-sided Orbitrap spectra (Figure S19b, d, and f) were collected by sending the ions from the HCD cell to the LQ-trap and storing them there instead of sending back to the Orbitrap MS by applying a high voltage of 50 V to lens 1. Ideally, the left-sided Orbitrap spectrum is expected to have a maximum intensity of 10^6 (maximum intensity measured in standard Orbitrap mode) and the right one should not contain any signal at all. At $T_{Ar\ gas\ injection\ to\ LQ\text{-}trap\ -\ Ion\ injection\ to\ LQ\text{-}trap}$=2 ms, the base peak of the left spectrum has the same intensity as the base peak of the standard Orbitrap mode spectrum, and very few ions were measured in the right spectrum, indicating that most of the ions are efficiently transmitted from the HCD cell to LQ-trap. When $T_{Ar\ gas\ injection\ to\ LQ\text{-}trap\text{-}Ion\ injection\ to\ LQ\text{-}trap}$ = 0 ms, the ion cloud is poorly trapped in the LQ-trap as there is no time between the Ar gas and ion injection into the LQ-trap (Figure S19a). Whereas, at a higher $T_{Ar\ gas\ injection\ to\ LQ\text{-}trap\text{-}Ion\ injection\ to\ LQ\text{-}trap}$=27 ms, the Ar gas expands to more ion optics components placed in between the LQ-trap and HCD cell that prevents the ion cloud leaving from the HCD cell and reaching the LQ-trap. This leads to the detection of the high-intensity mass spectrum in both cases as the ions are not even leaving the Orbitrap MS (Figure S19e and f). $T_{Ar\ gas\ injection\ to\ LQ\text{-}trap\text{-}Ion\ injection\ to\ LQ\text{-}trap}$ between 1 and 20 ms is recommended for the optimum operation of the instrument.

5

Influence of Ion Optics on Orthogonal Spatial Profile

Axial Ion Energy (E_z)

Despite the fact that the defined potential well is at Q3, ions may be oscillating between the second segment of the LQ-trap (Q2) and Q3 during the collisional focusing of the ion cloud in the LQ-trap. This means that the DC component of Q2 voltage (VDC_{Q2}) is also likely to have an impact on v_z. A shift towards +z direction has been observed with an increase of VDC_{Q2} (Figure S21e). The lens 3 (L3), the electrode placed next to the Q3, is also observed to have an effect on v_z. L3 is at a higher voltage during the ion storage in LQ-trap ($V_{L3\ (Q\text{-trapping})}$) and switches to a lower value when the ions from the LQ-trap are ejected to the TOF region ($V_{L3\ (Ejection\ to\ pusher)}$) (Figure S14). A change in $V_{L3\ (Q\text{-trapping})}$ and $V_{L3\ (Ejection\ to\ pusher)}$ have opposite effects on the z-impact position of the ion distribution at the orthogonal TPX3 image. A higher $V_{L3\ (Q\text{-trapping})}$ shifts the ion trapping location more towards Q2. This causes the ions to gain more v_z as VDC_{Q2} is higher than VDC_{Q3} and results in the ion beam striking more towards the +z direction (Figure S21g). In contrast, the potential gradient between the LQ-trap and L3 during the ion ejection reduces when the $V_{L3\ (Ejection\ to\ pusher)}$ is higher, which causes the ions to travel slowly. This slow-moving ion cloud appears more to the right of the pusher compared to the position where it appear when subjected to low $V_{L3\ (Ejection\ to\ pusher)}$, prior to the pulsing of the ions to the orthogonal TPX3 detector. Thus an increase in $V_{L3\ (Ejection\ to\ pusher)}$ causes the ion beam to strike more to the –z direction of the orthogonal detector (Figure S21h).

Table S1. Data acquisition parameters correspond to Figure S11.

Parameter	Value
Orbitrap MS parameters	
Mas resolution (@200 *m/z*)	70,000
Polarity	Positive
Average	0
Microscans	1
nESI source spray voltage (kV)	1.2
Capillary temperature (°C)	320
In-source trapping desolvation voltage (V)	-50
Noise threshold	4.64
Inject time (ms)	90
Ion tranfer *m/z* optimization	High *m/z*
Detector *m/z* optimization	Low *m/z*
Trapping gas pressure setting	3
Extended trapping (eV)	3
Orbitrap settings for external instrument mode of operation (External Orbitrap, axial non-imaging and orthogonal TOF non-imaging modes)	
HCD external instrument mode	On
HCD offset to external instrument (V)	35
HCD offset from external instrument (V)	2
HCD gradient to external instrument (V)	-200
HCD gradient from external instrument (V)	45
HCD and C-trap exit lens close (V)	35
HCD exit lens open to external instrument (V)	25
HCD exit lens open from external instrument (V)	-25
HCD ion tranfer (ms)	25
HCD waiting for external instrument back transfer (ms)	250
HCD exit lens trigger voltage low (V)	35
HCD exit lens trigger voltage high (V)	-35
TOF analyzer & associated tranfer ion optics settings	
LQ-trap pressure (mbar)	1.00E-04
TOF analyzer pressure (mbar)	9.00E-07
RF voltage of the hexapole and LQ-trap (V)	350
C1 (1st electrode of correction lens) voltage (V)	16 (Axial non-imaging and orthogonal TOF non-imaging modes)
Voltages on the 4 segments (top, bottom, left, right) of C2 (2nd electrode of correction lens) (V)	-7, -7, -4, -4 (Axial non-imaging and orthogonal TOF non-imaging modes)
C3 (3rd electrode of correction lens) (V)	-15 (Axial non-imaging and orthogonal TOF non-imaging modes)
Lens 4 voltage (V)	-35 (Axial non-imaging and orthogonal TOF non-imaging modes)
Vs (V)	3333 (Orthogonal TOF non-imaging mode)
Vd (V)	6666 (Orthogonal TOF non-imaging mode)
Axial detector voltage (V)	-1800
Orthogonal detector voltage (V)	-2800
Oscilloscope sampling rate (ns)	0.5

5

Table S2. The parameters used for the acquisition of data correspond to Figures S17-19.

Parameter	Value
Orbitrap MS parameters	
Mas resolution (@200 *m/z*)	70,000
Polarity	Positive
Average	10
Microscans	1
nESI source spray voltage (kV)	1.2
Capillary temperature (°C)	320
In-source trapping desolvation voltage (V)	-100
Noise threshold	3.64
Inject time (ms)	90
Ion tranfer *m/z* optimization	Low *m/z*
Detector *m/z* optimization	Low *m/z*
Trapping gas pressure setting	1
Extended trapping (eV)	3
Orbitrap settings for external instrument mode of operation (External Orbitrap mode)	
HCD external instrument mode	On
HCD offset to external instrument (V)	35
HCD offset from external instrument (V)	2
HCD gradient to external instrument (V)	-200
HCD gradient from external instrument (V)	45
HCD and C-trap exit lens close (V)	35
HCD exit lens open to external instrument (V)	25
HCD exit lens open from external instrument (V)	-25
HCD ion tranfer (ms)	25
HCD waiting for external instrument back transfer (ms)	250
HCD exit lens trigger voltage low (V)	35
HCD exit lens trigger voltage high (V)	-35
TOF analyzer & associated tranfer ion optics settings	
LQ-trap pressure (mbar)	5.00E-05
TOF analyzer pressure (mbar)	6.00E-07
RF voltage of the hexapole and LQ-trap (V)	200

Table S3. The parameters used for the acquisition of data correspond to Figure 4a.

Parameter	Value
Orbitrap MS parameters	
Mas resolution (@200 *m/z*)	4,375
Polarity	Positive
Average (Data aquistion)	0
Microscans	1
Number of scans averaged	3
nESI source spray voltage (kV)	1.2
Capillary temperature (°C)	320
In-source trapping desolvation voltage (V)	-50
Noise threshold	4.64
Inject time (ms)	90
Ion tranfer *m/z* optimization	High *m/z*
Detector *m/z* optimization	Low *m/z*
Trapping gas pressure setting	5
Extended trapping (eV)	3
Orbitrap settings for external instrument mode of operation	
HCD external instrument mode	On
HCD offset to external instrument (V)	35
HCD offset from external instrument (V)	2
HCD gradient to external instrument (V)	-200
HCD gradient from external instrument (V)	45
HCD and C-trap exit lens close (V)	35
HCD exit lens open to external instrument (V)	25
HCD exit lens open from external instrument (V)	-25
HCD ion tranfer (ms)	25
HCD waiting for external instrument back transfer (ms)	250
HCD exit lens trigger voltage low (V)	35
HCD exit lens trigger voltage high (V)	-35
TOF analyzer & associated tranfer ion optics settings	
LQ-trap pressure (mbar)	3.40E-04
TOF analyzer pressure (mbar)	1.20E-06
RF voltage of the hexapole and LQ-trap (V)	600
Lens 3 voltage (V)	35
Laser pulse energy (mJ)	1.5 to 2.25
Atttenuator knob position & laser pulse exit energy (mJ)	680 & 0.43 to 0.65

5

Table S4. The parameters used for the acquisition of data correspond to Figure 5.

Parameter	Value
Orbitrap MS parameters	
Polarity	Positive
nESI source spray voltage (kV)	1.4
Capillary temperature (°C)	320
In-source trapping desolvation voltage (V)	-50
Inject time (ms)	90
Ion tranfer m/z optimization	High m/z
Detector m/z optimization	Low m/z
Trapping gas pressure setting	3
Extended trapping (eV)	3
Orbitrap settings for external instrument mode of operation	
HCD external instrument mode	On
HCD offset to external instrument (V)	35
HCD offset from external instrument (V)	2
HCD gradient to external instrument (V)	-200
HCD gradient from external instrument (V)	45
HCD and C-trap exit lens close (V)	35
HCD exit lens open to external instrument (V)	25
HCD exit lens open from external instrument (V)	-25
HCD ion tranfer (ms)	25
HCD waiting for external instrument back transfer (ms)	250
HCD exit lens trigger voltage low (V)	35
HCD exit lens trigger voltage high (V)	-35
TOF analyzer & associated tranfer ion optics settings	
LQ-trap pressure (mbar)	8.50E-05
TOF analyzer pressure (mbar)	7.00E-07
RF voltage of the hexapole and LQ-trap (V)	400
C1 (1st electrode of correction lens) voltage (V)	11
Voltages on the 4 segments (top, bottom, left, right) of C2 (2nd electrode of correction lens) (V)	0, -2, -0, 0
C3 (3rd electrode of correction lens) (V)	-20
Lens 4 voltage (V)	-35
Vs (V)	3333
Vd (V)	6666
Laser pulse energy (mJ)	1.75
Atttenuator knob position & laser pulse exit energy (mJ)	680 & 0.5
Orthogonal MCP front plate voltage (V)	-2200
Orthogonal MCP back plate voltage (V)	-600
Phosphor screen voltage (V)	5000
TPX3CAM f-stop value	0.95
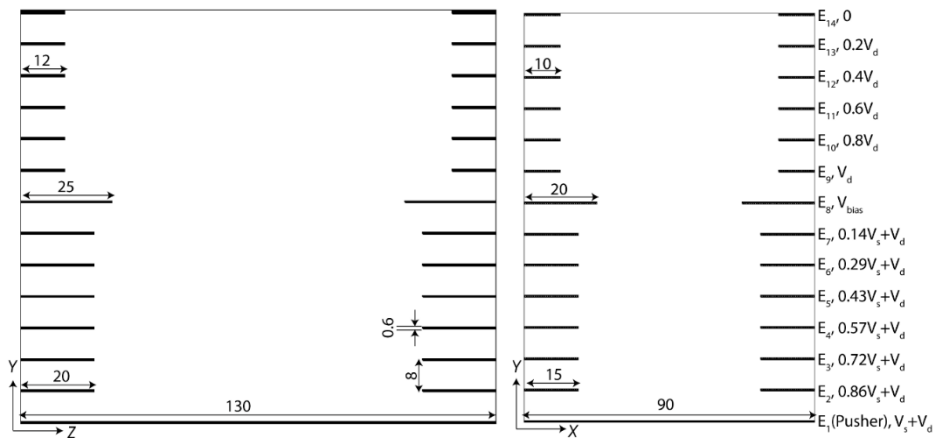
Figure S1. Ion optics schematic of the custom-designed TOF analyzer. TOF analyzer consists of 14 electrodes with a two-stage acceleration field (s and d fields) and a bias electrode. The dimensions (in mm) and voltage division between the electrodes are shown.
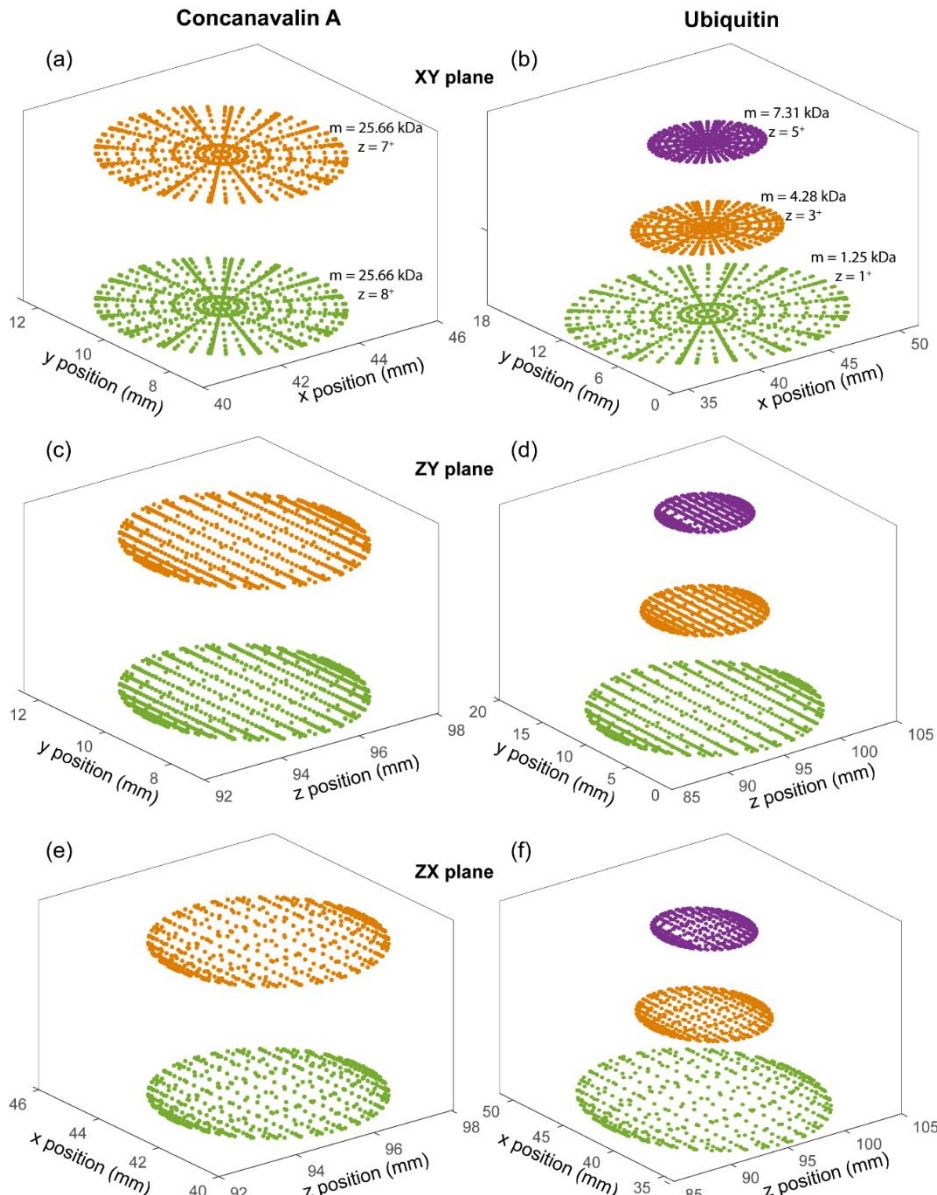
Figure S2. Projections of the simulated isotropic distribution of the fragments formed from concanavalin A and ubiquitin in XY (a and b), ZY (c and d), and ZX (e and f) plane in the field-free region after 20 μs of the dissociation. Note that $E_{Fragmentation}$ of 2 eV/fragment was considered.
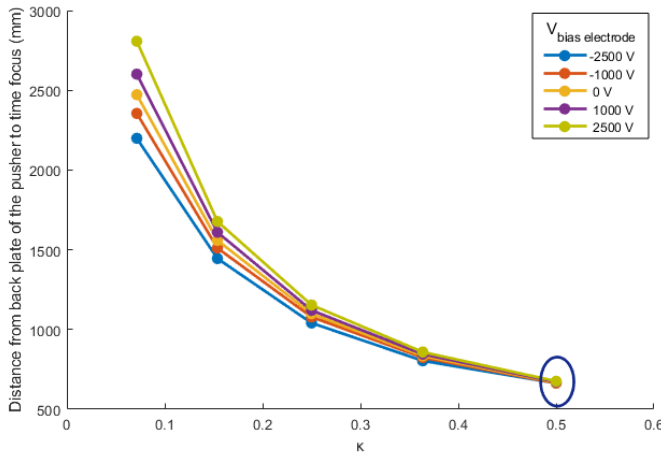
Figure S3. Simulation results showing the effect of V_s, V_d, and $V_{bias\ electrode}$ on the time focus at a nominal orthogonal acceleration potential of 15 kV (pusher voltage). The time focus value displayed in the y-axis is calculated by measuring the distance from the pusher to the TOF region with the minimum spatial spread of the ion beam in the y (orthogonal)-direction. κ is the ratio of V_s to V_d. 8+ charged concanavalin A monomer fragment ion cloud with the following properties was used for the determination of time focus; E_{Axial}=225 eV, $E_{Fragmentation}$=2 eV, Fragmentation location: midpoint of the pusher.

5
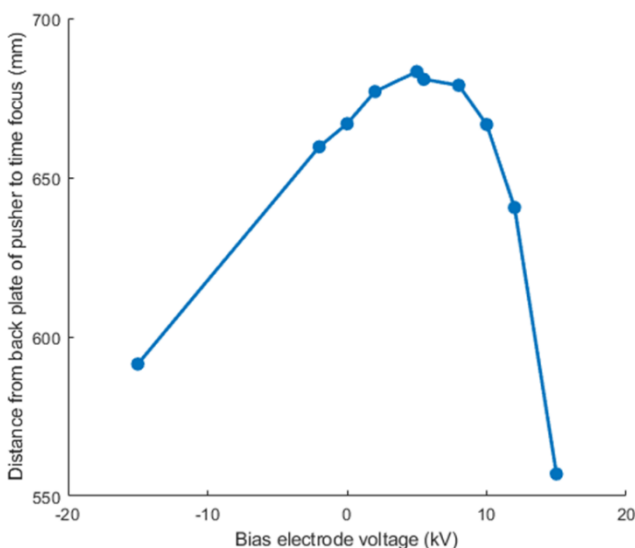
Figure S4. Simulation results showing the effect of the $V_{bias\ electrode}$ on the time focus at κ=0.5 (V_s=5 kV and V_d=10 kV). The time focus drifts by a maximum distance of 130 mm for a change in the $V_{bias\ electrode}$ from -15 to +15 kV. 8+ charged concanavalin A monomer fragment ion cloud with the following properties was used for the determination of time focus; E_{Axial}=225 eV, $E_{Fragmentation}$=2 eV, Fragmentation location: midpoint of the pusher.

Vd = 11,000 V, Vs= 4,000 V, Fragmentation location: Middle of pusher

V_{bias}= 0 kV   2 kV   5 kV   8 kV   10 KV
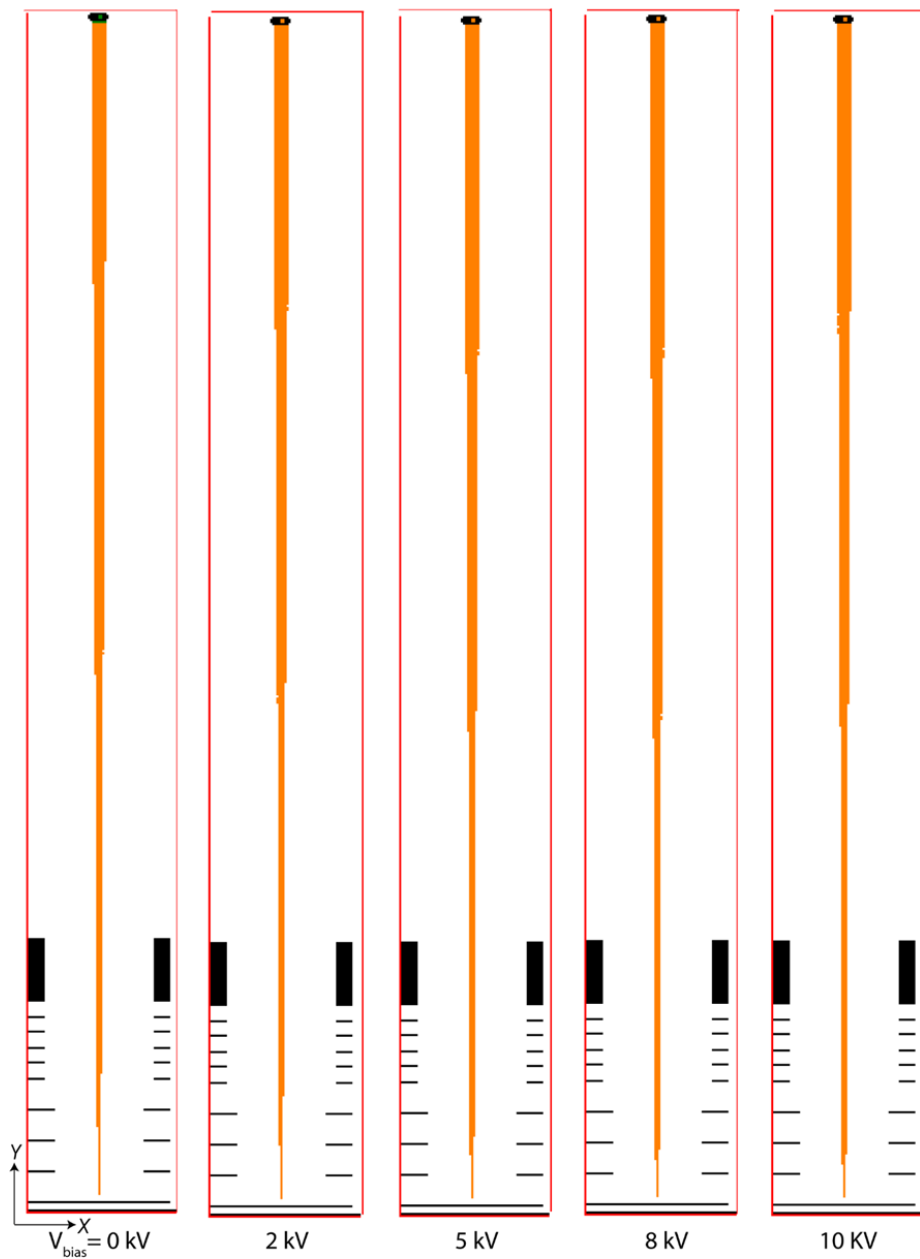
Figure S5. Simulated ion trajectories (in xy plane) of the concanavalin A $[M+8H]^{8+}$ and $[M+7H]^{7+}$ monomer fragment ion clouds, and correspond to different $V_{bias\ electrode}$ at $\kappa = 0.364$ (V_s=4000 V, V_d=11,000 V). E_{Axial}=225 eV, $E_{Fragmentation}$=2 eV, Fragmentation location: midpoint of the pusher.

Vd = 10,000 V, Vs= 5,000 V, Fragmentation location: Middle of pusher

$V_{bias} = 0$ kV   2 kV   5 kV   8 kV   10 KV
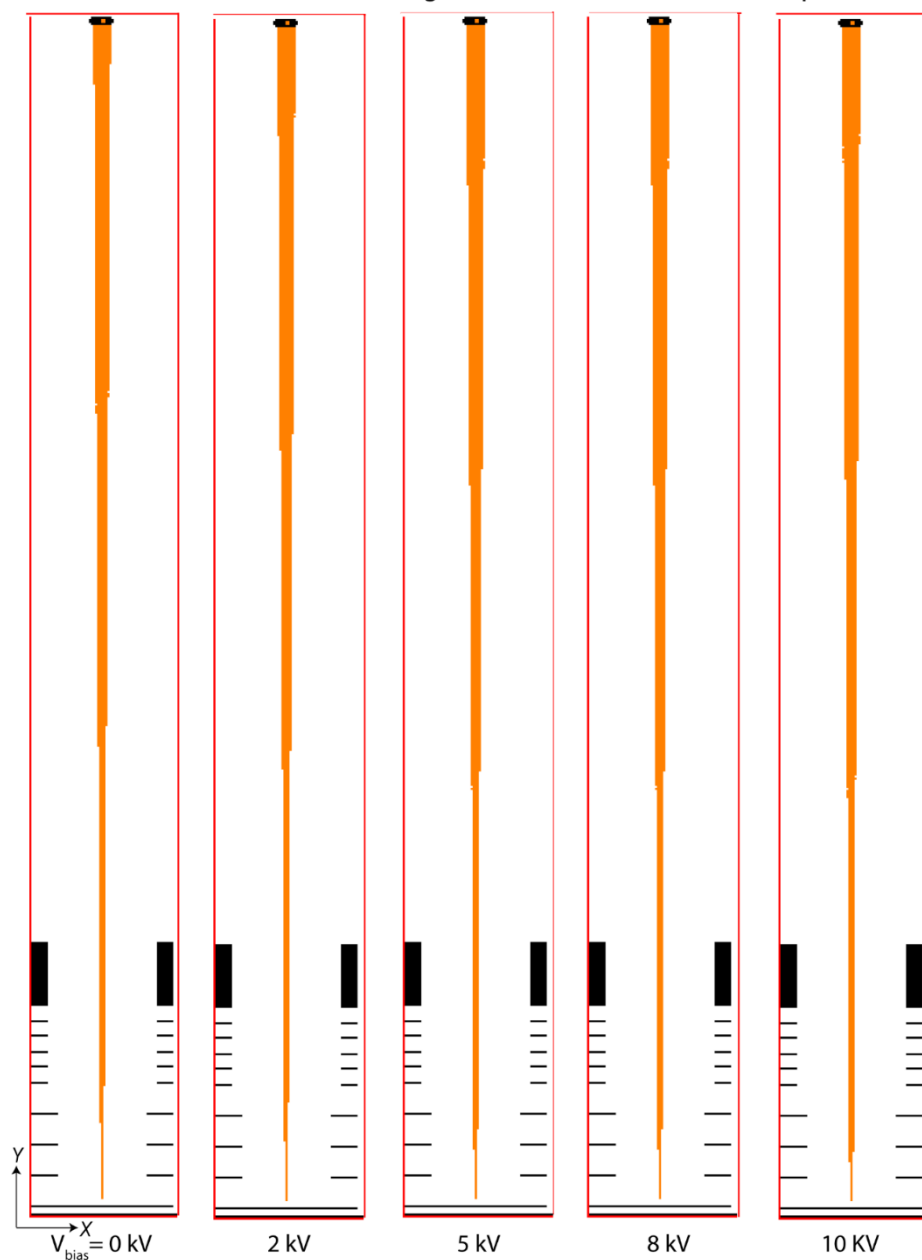
Figure S6. Simulated ion trajectories (in xy plane) of the concanavalin A [M+8H]$^{8+}$ and [M+7H]$^{7+}$ monomer fragment ion clouds, and correspond to different $V_{bias\ electrode}$ at κ = 0.5 (V_s=5000 V, V_d=10,000 V). E_{Axial}=225 eV, $E_{Fragmentation}$=2 eV, Fragmentation location: midpoint of the pusher.

Vd = 11,000 V, Vs= 4,000 V, Fragmentation location: Middle of C2
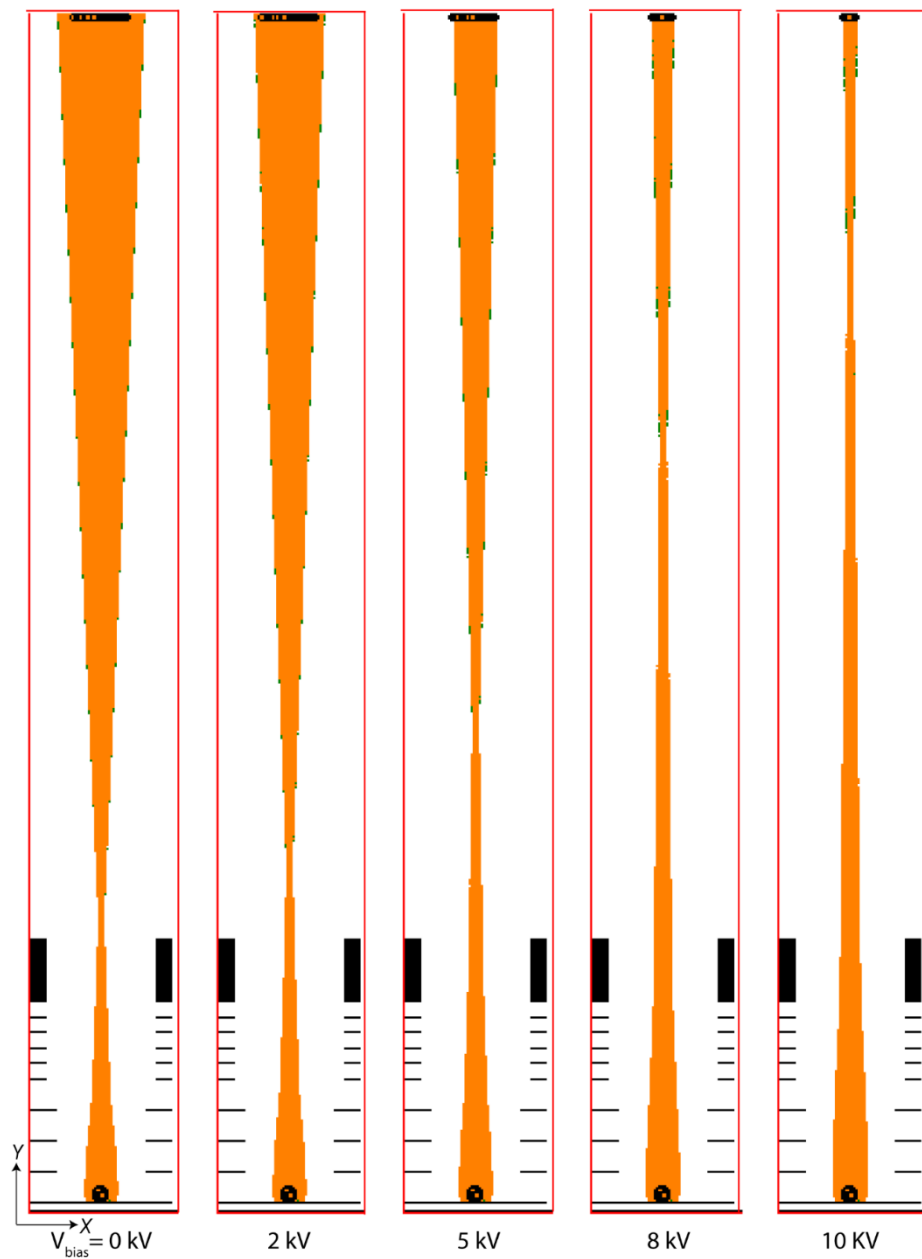
Figure S7. Simulated ion trajectories (in xy plane) of the concanavalin A [M+8H]$^{8+}$ and [M+7H]$^{7+}$ monomer fragment ion clouds, and correspond to different $V_{bias\ electrode}$ at κ = 0.364 (V_s=4000 V, V_d=11,000 V). E_{Axial}=225 eV, $E_{Fragmentation}$=2 eV, Fragmentation location: middle of the second segment of the correction lens (C2).

Vd = 10,000 V, Vs= 5,000 V, Fragmentation location: Middle of C2
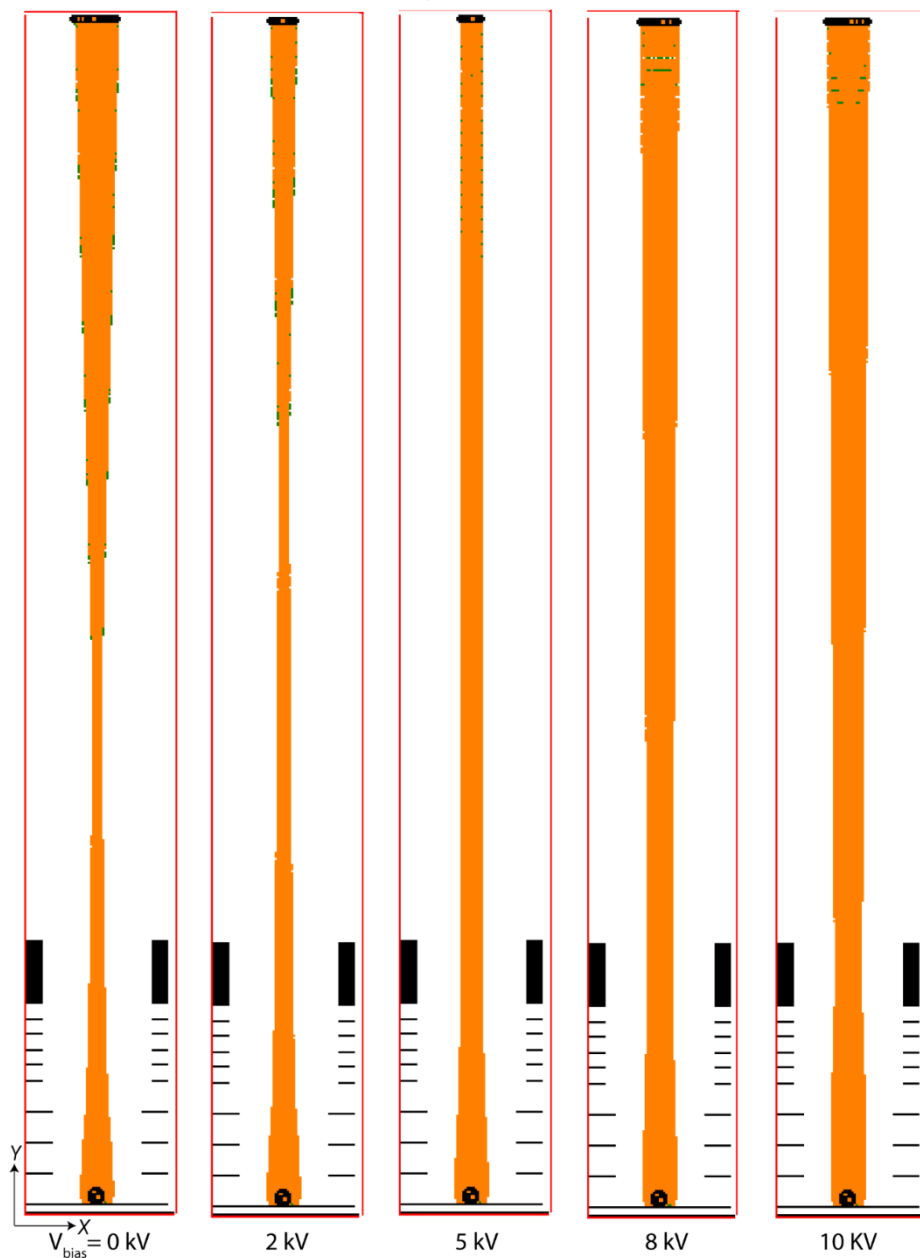
Figure S8. Simulated ion trajectories (in xy plane) of the concanavalin A [M+8H]8+ and [M+7H]7+ monomer fragment ion clouds, and correspond to different $V_{bias\ electrode}$ at κ = 0.5 (V_s=5000 V, V_d=10,000 V). E_{Axial}=225 eV, $E_{Fragmentation}$=2 eV, Fragmentation location: middle of the second segment of the correction lens (C2).
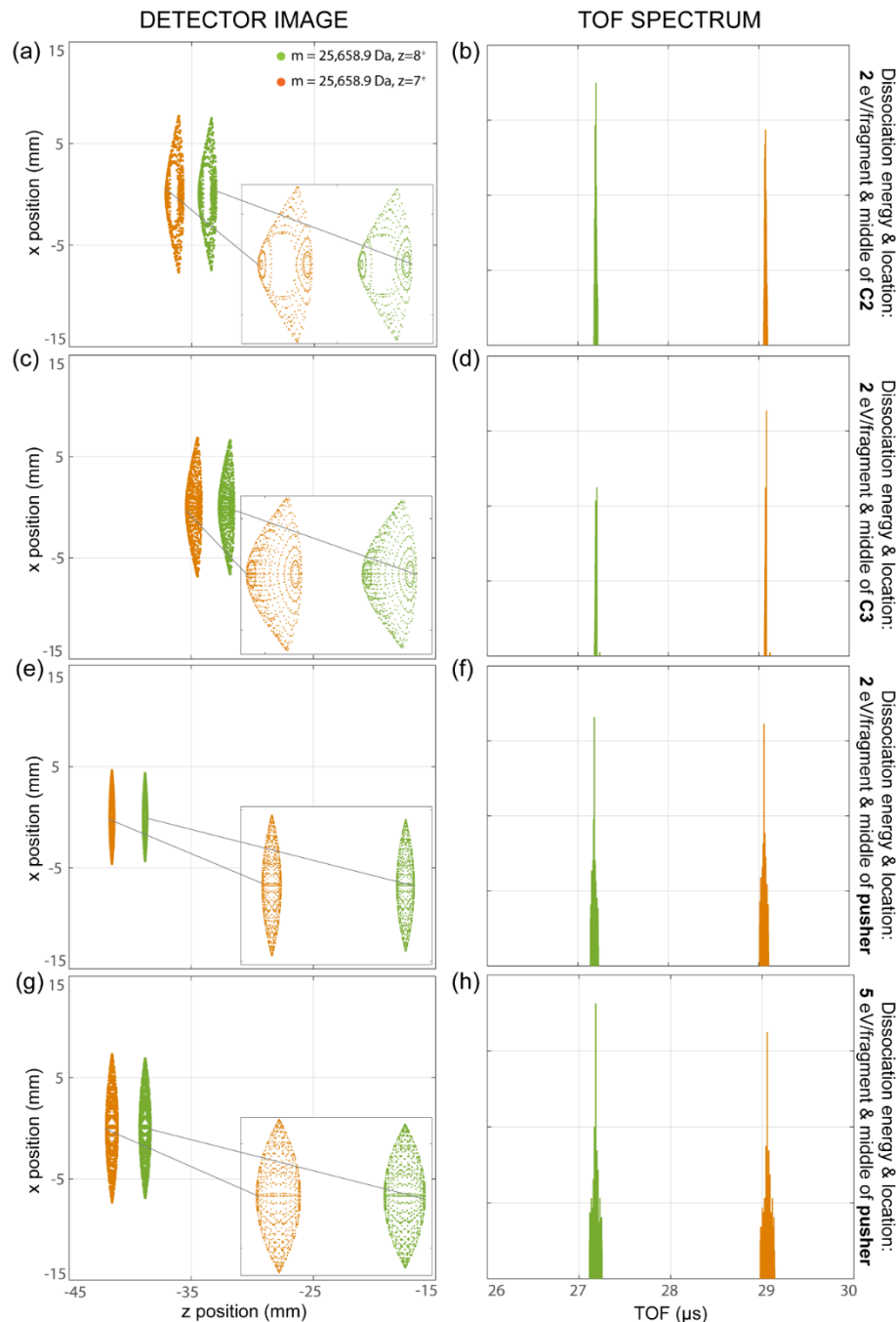
Figure S9. Simulated detector images and TOF spectra collected at the orthogonal detector at different dissociation energies (2-5 eV/fragment) and locations (C2, C3, and pusher) by sending concanavalin A monomer [M+8H]$^{8+}$ (green) and [M+7H]$^{7+}$(orange) fragment ions with an axial energy of 225 eV per fragment.

DETECTOR IMAGE   TOF SPECTRUM
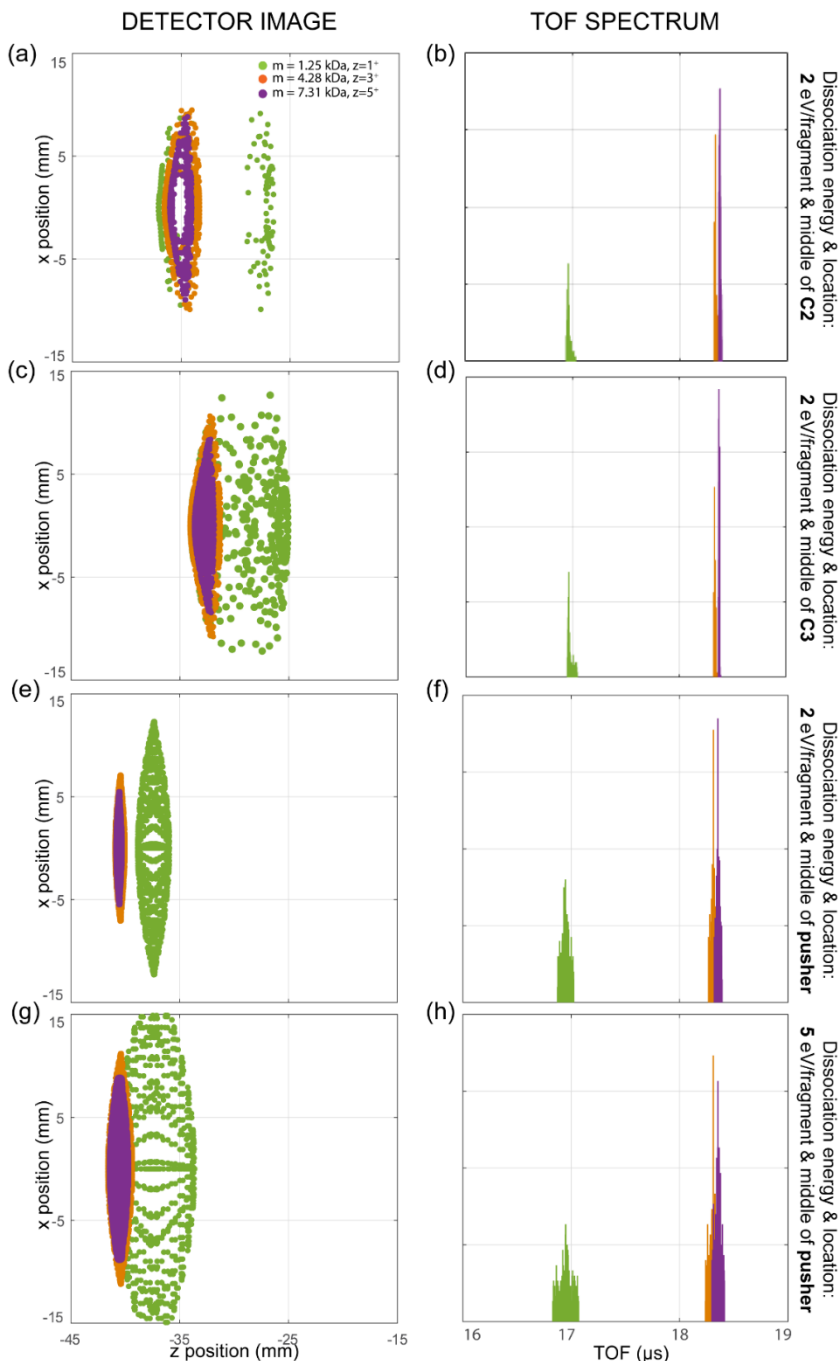
Figure S10. Simulated detector images and TOF spectra collected at the orthogonal detector at different dissociation energies (2-5 eV/fragment) and locations (C2, C3, and pusher) by sending ubiquitin fragments of *m/z*=1247 (green), 1428 (orange) and 1463 (purple) fragment ions. Precursor ubiquitin ion was accelerated with an axial voltage of 30 V.
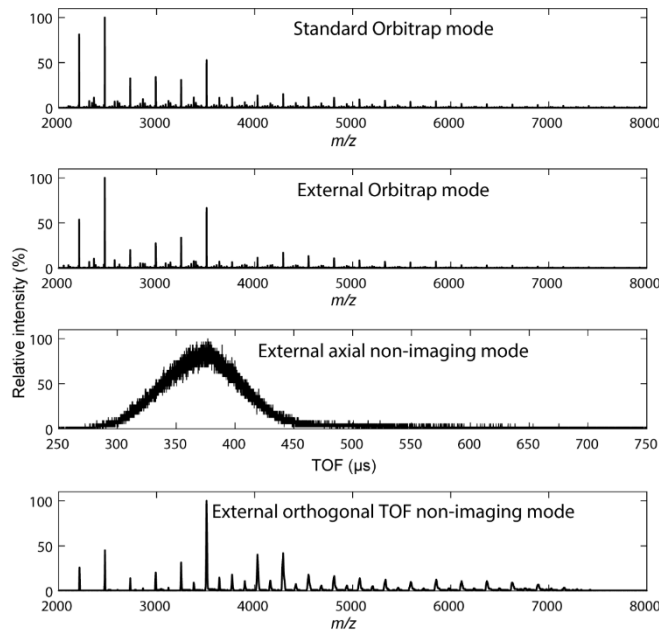
Figure S11. Mass spectra of CsI mix acquired by operating the Orbitrap/TOF instrument in different modes using Orbitrap and discrete-dynode EM detectors (non-imaging) under identical ion optical conditions. Table S1 and Figures S12-16 show the relevant data acquisition parameters and event sequences used in different operation modes.
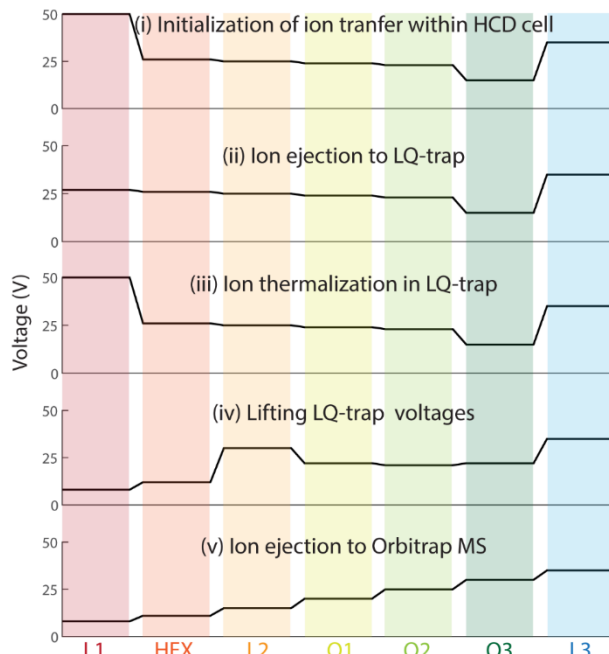
Figure S12. Transitions of the DC voltage profile across the ion optics during each event used for the acquisition of the CsI mix (Figure S11) and concanavalin A (Figure 4a) spectra in external Orbitrap mode (L1-3: Lens 1-3, HEX: Hexapole, Q1-3: Quadrupole electrode 1-3).
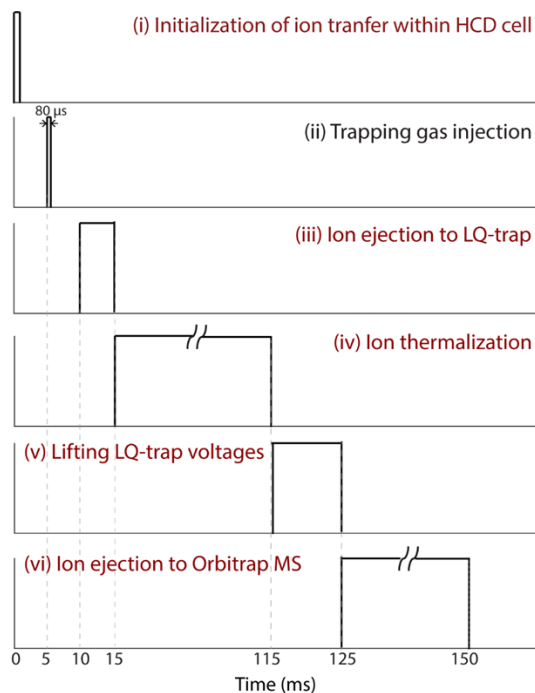
Figure S13. Timing diagram of the events used for the acquisition of the CsI mix (Figure S11) and ubiquitin (Figures S17-19) spectra in external Orbitrap mode. Note that the timing signals labeled in red (title) are associated with a change in the DC voltage profile of the ion optics elements 11-15 (Figures 2, S12 (CsI mix), and S20 (Ubiquitin)).
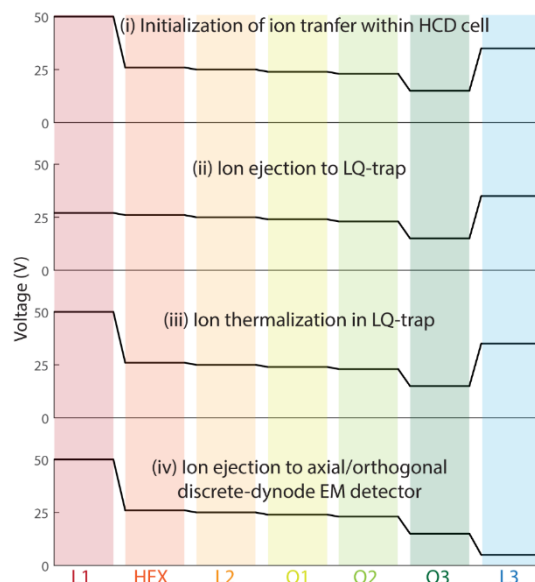
Figure S14. Transitions of the DC voltage profile across the ion optics during each event used for the acquisition of the CsI mix spectrum in external axial non-imaging and orthogonal TOF non-imaging modes (Figure S11) and concanavalin A UVPD spectrum in external UVPD orthogonal TOF imaging mode (Figure 5) (L1-3: Lens 1-3, HEX: Hexapole, Q1-3: Quadrupole electrode 1-3).
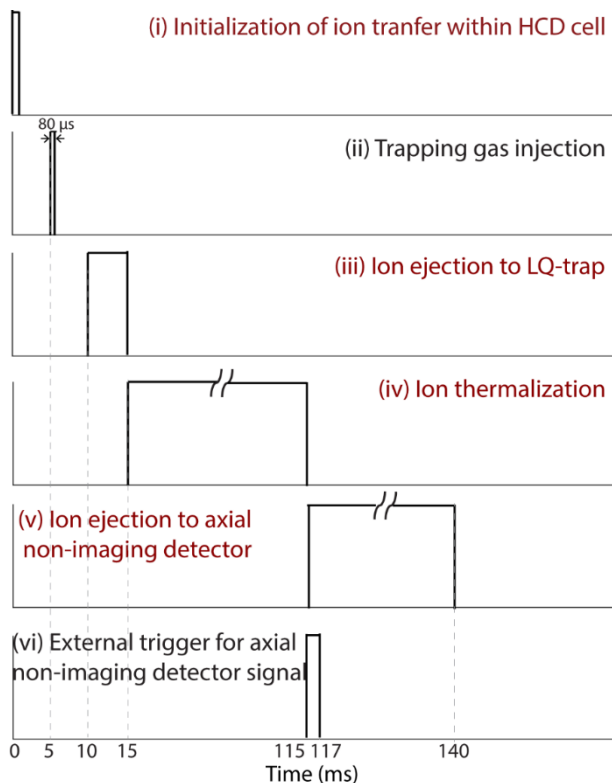
Figure S15. Timing diagram of the events used for the acquisition of the CsI mix spectrum in external axial non-imaging mode (Figure S11). Note that the timing signals labeled in red (title) are associated with a change in the voltage profile of ion optics elements 11-15 (Figures 2 and S14 (CsI mix)).
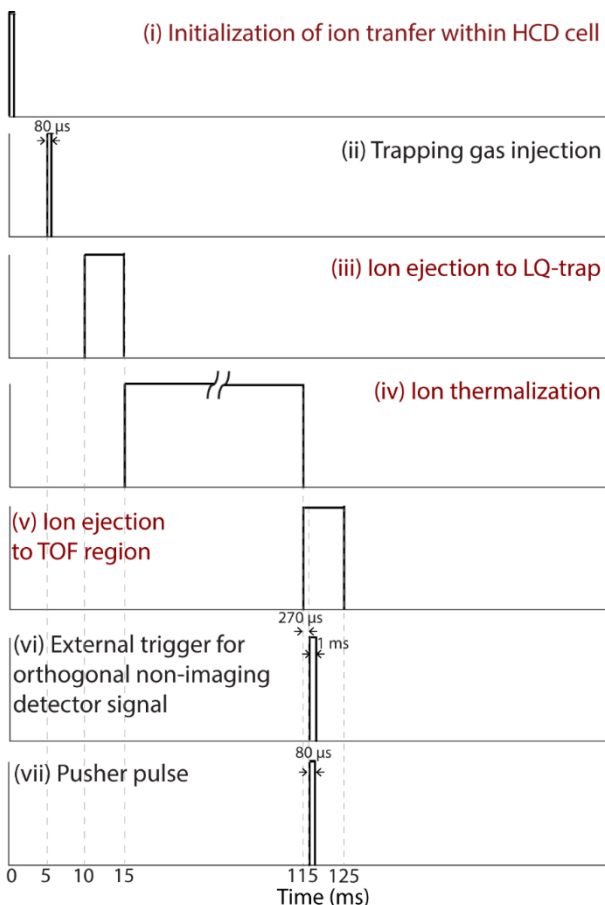
Figure S16. Timing diagram of the events used for the acquisition of CsI mix spectrum in external orthogonal TOF non-imaging mode (Figure S11). Note that the timing signals labeled in red (title) are associated with a change in the voltage profile of ion optics elements 11-15 (Figure 2, S14 (CsI mix)).
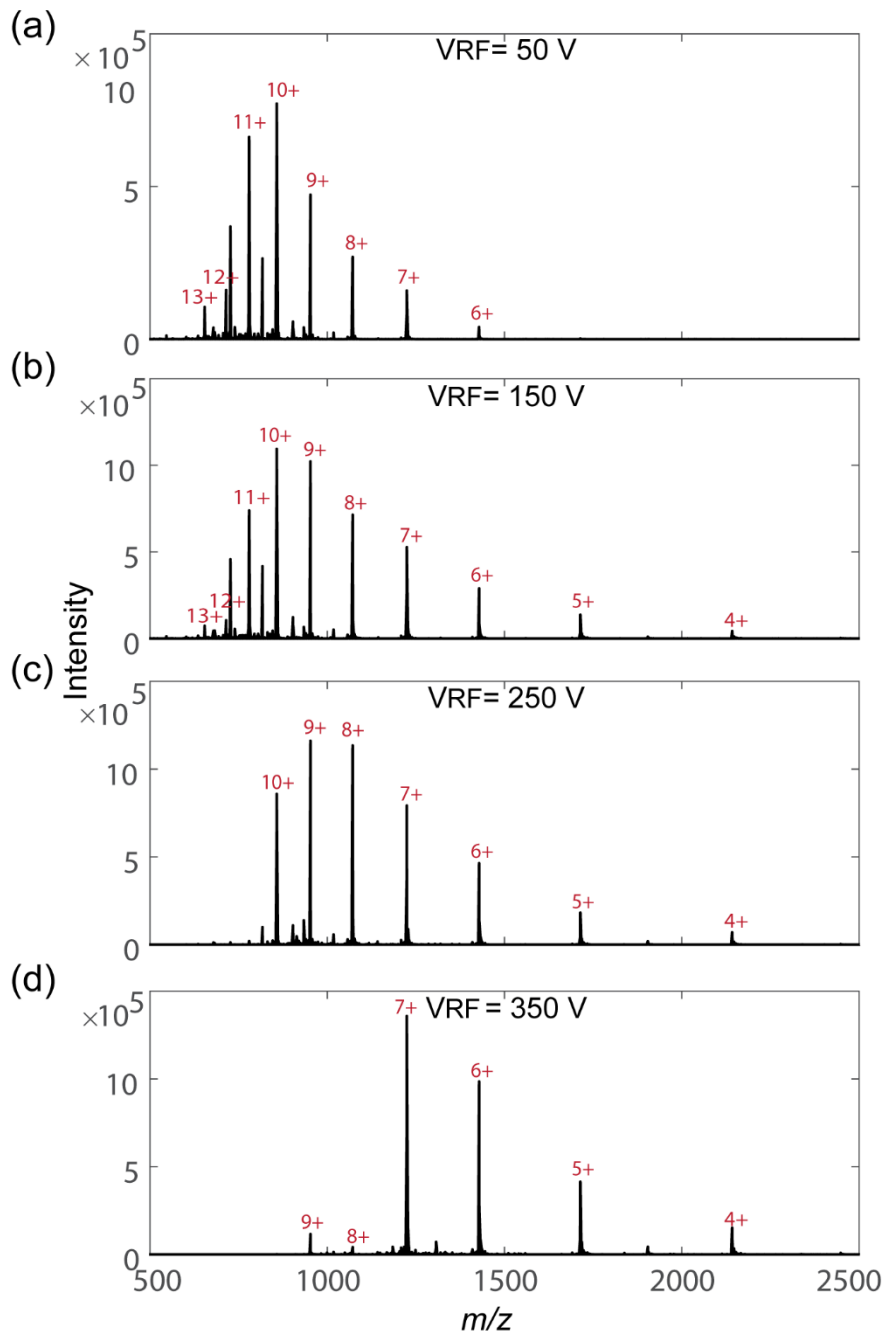
Figure S17. Denatured ubiquitin spectrum measured in external Orbitrap mode at different RF voltages of the hexapole and LQ-trap (VRF).
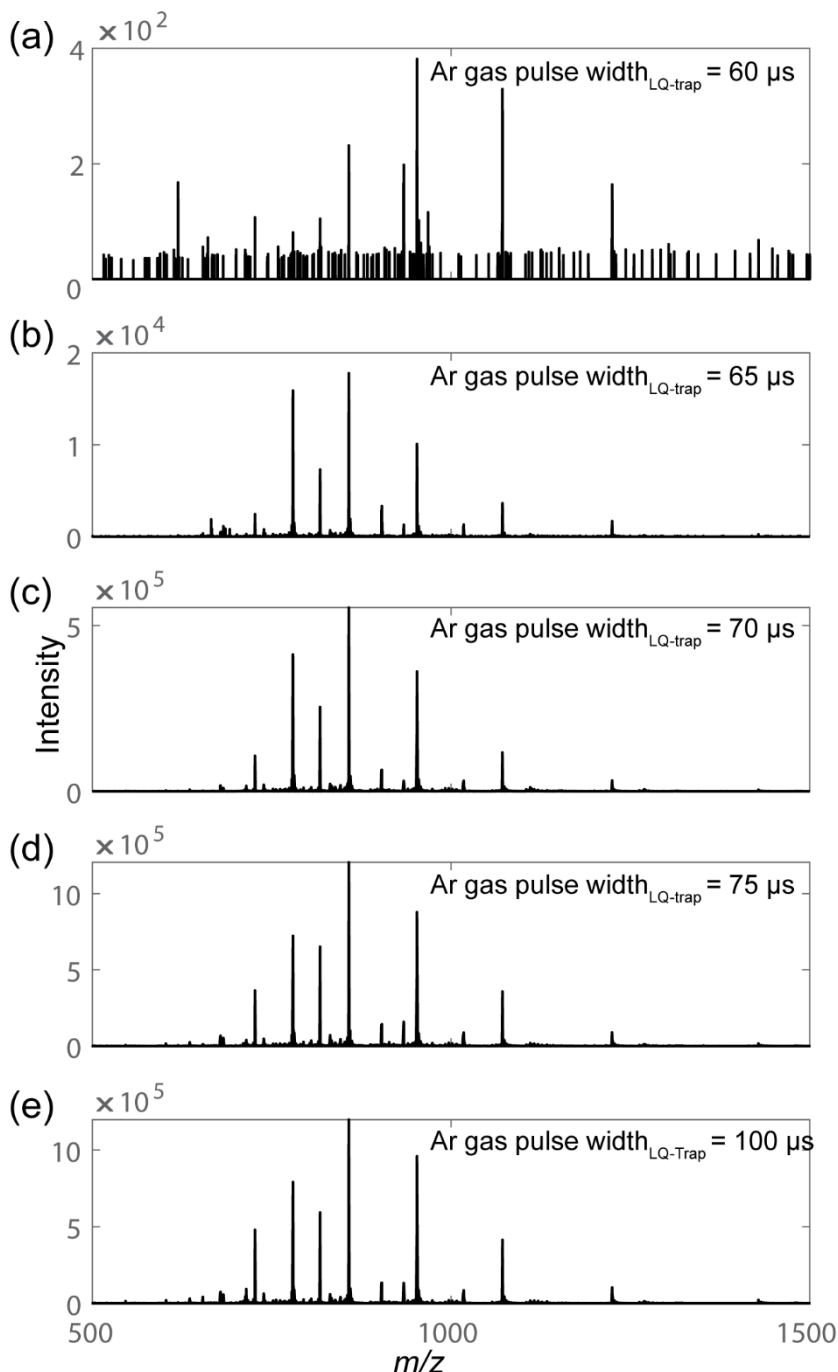
Figure S18. Denatured ubiquitin spectrum measured in external Orbitrap mode at different trapping gas (Ar) gas pulse widths.
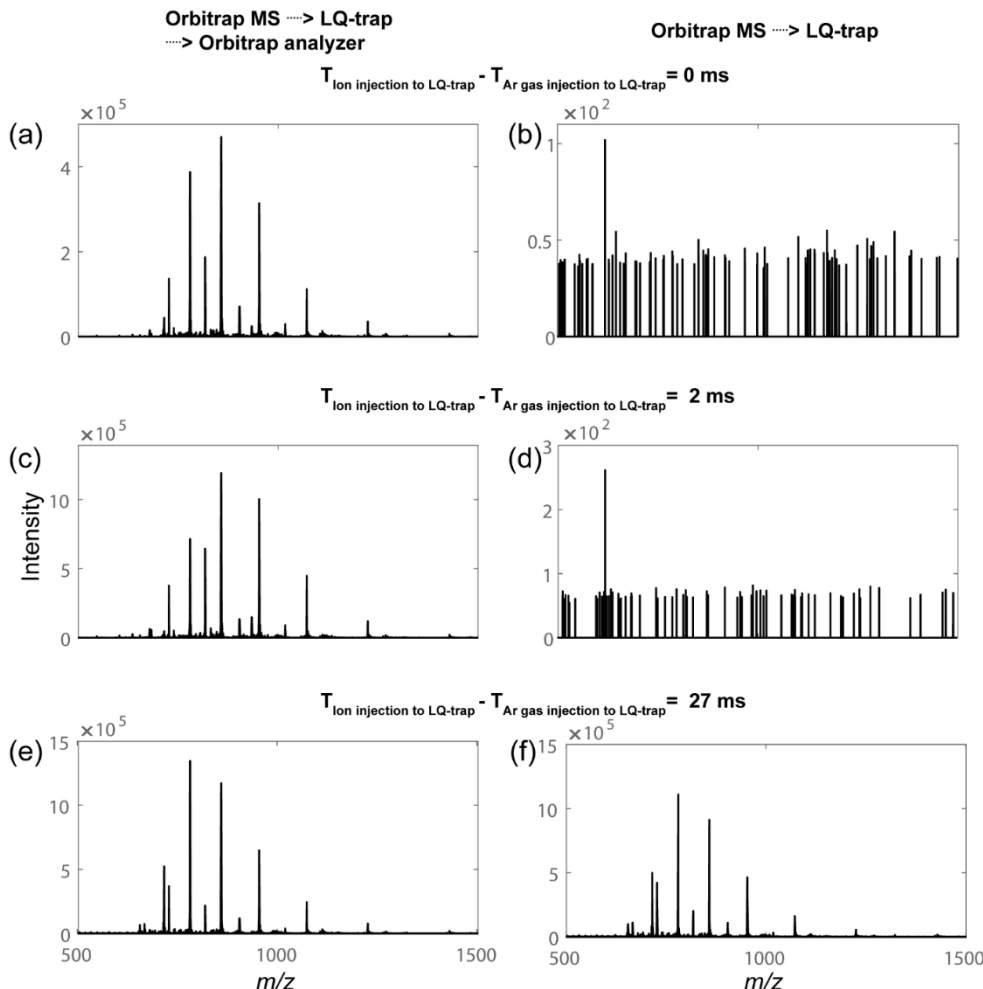
Figure S19. Influence of $T_{Ar\ gas\ injection\ to\ LQ\text{-}trap\ -\ Ion\ injection\ to\ LQ\text{-}trap}$ on the Orbitrap spectrum of denatured ubiquitin. All of the left-sided spectra were recorded in the external Orbitrap mode. All of the right-sided Orbitrap spectra were collected by sending the ions from the HCD cell to the LQ-trap and storing them there instead of sending back to the Orbitrap MS by applying a high voltage of 50 V to lens 1.
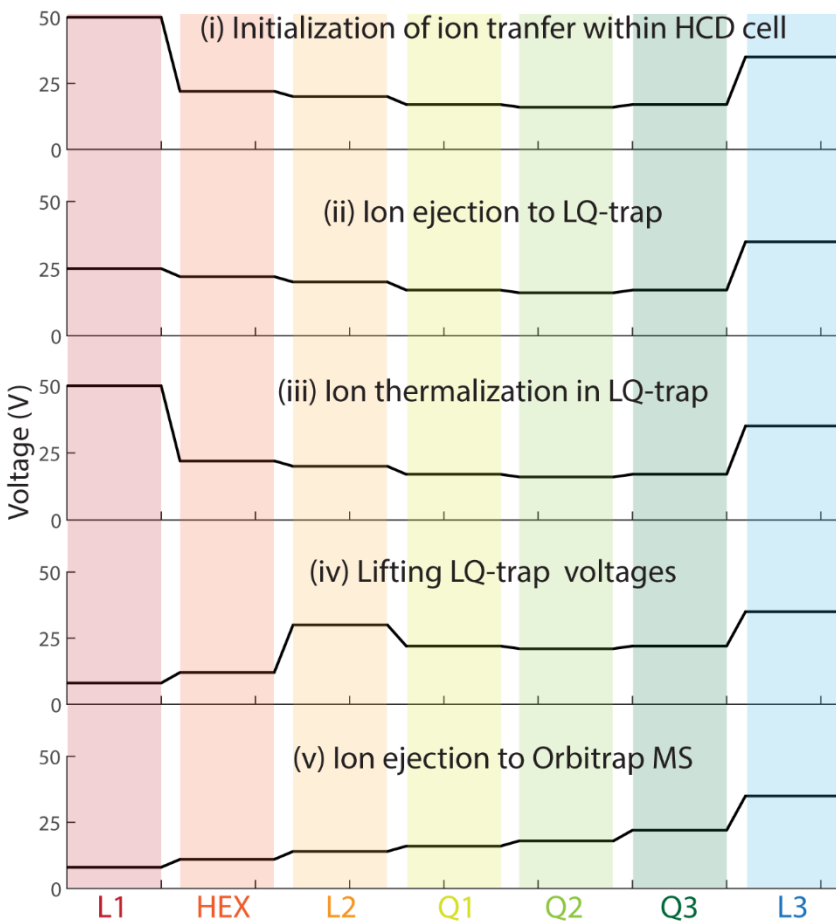
Figure S20. Transitions of the DC voltage profile across the ion optics during each event used for the acquisition of the ubiquitin spectrum in external Orbitrap mode (Figure S17-19) (L1-3: Lens 1-3, HEX: Hexapole, Q1-3: Quadrupole segment 1-3).
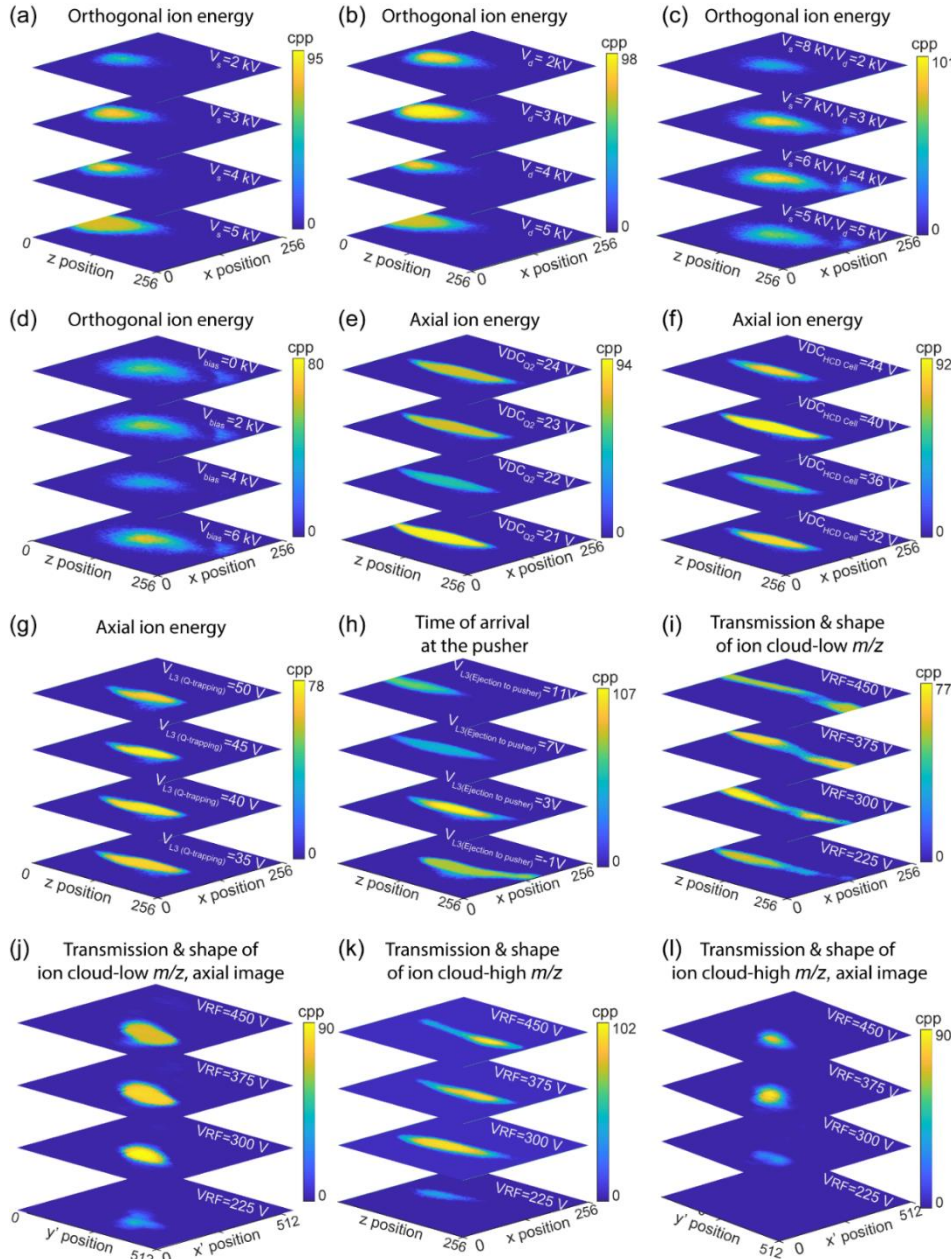
Figure S21. Influence of (a) V_s (V_d=5 kV), (b) V_d (V_s=5 kV), (c) s & d fields (V_s+V_d=10 kV), (d) V_{bias} (V_s=5 kV, V_d=5 kV), (e) voltage on the second segment of the LQ-trap (VDC_{Q2}),(f) DC offset voltage of the HCD cell ($VDC_{HCD\ cell}$), (g) lens 3 voltage during the ion storage in LQ-trap ($V_{L3\ (Q\text{-}trapping)}$) and (h) lens 3 voltage during the ejection from the LQ-trap to TOF region ($V_{L3\ (Ejection\ to\ pusher)}$) on the spatial distribution of quadrupole selected CsI singly charged ions with m/z=5589 at the orthogonal TPX3 detector. Spatial profiles of the quadrupole isolated ions with m/z values of 3510.5 (i and j) and 7407.7 (k and l) at the orthogonal TPX3 and axial TPX quad detectors at different RF voltages of the hexapole and LQ-trap (VRF) values. All images represent the sum of hundred measurement cycles. cpp = counts per pixel.
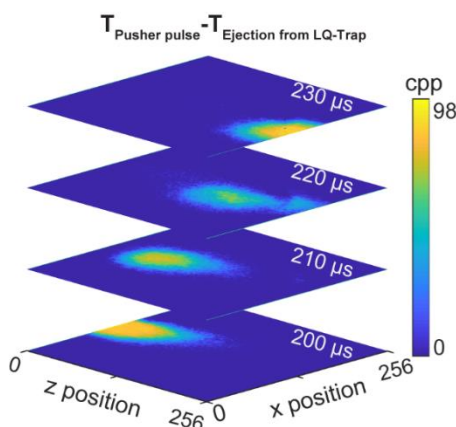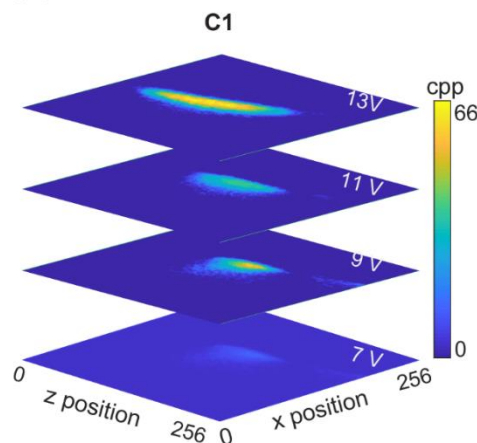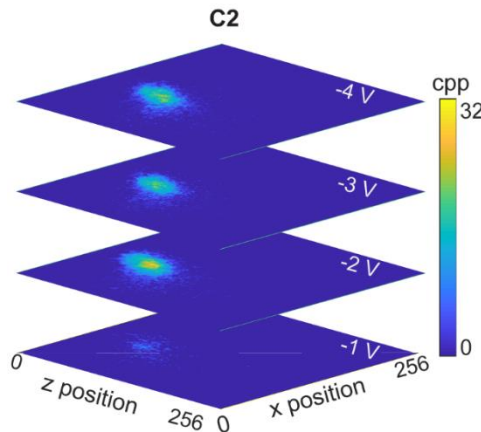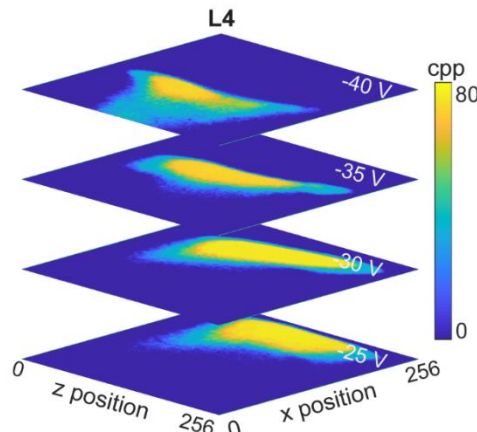
Figure S22. Influence of (a) $T_{Pusher\ pulse}$-$T_{Ejection\ from\ LQ-trap}$ (time difference between the ion ejection from the LQ-trap and pusher pulsing), voltage on the first (b, C1) and second (c, C2) electrode of the correction lens, and (d) lens 4 (L4) voltage on the spatial distribution of quadrupole selected CsI singly charged ions with m/z=5589 at the orthogonal TPX3 detector. All images represent the sum of hundred measurement cycles. cpp = counts per pixel.

(i) Initialization of ion tranfer within HCD cell

80 µs

(ii) Trapping gas injection

(iii) Ion ejection to LQ-trap

1 ms

(iv) External trigger to DG535

30 ns

(v) DG535 to laser device

15 µs

7 ns

(vi) Laser pulse

(vii) Ion thermalization

(viii) Lifting LQ-trap voltages

(ix) Ion ejection to Orbitrap MS

0   5   10   15   115   125   150
                          Time (ms)
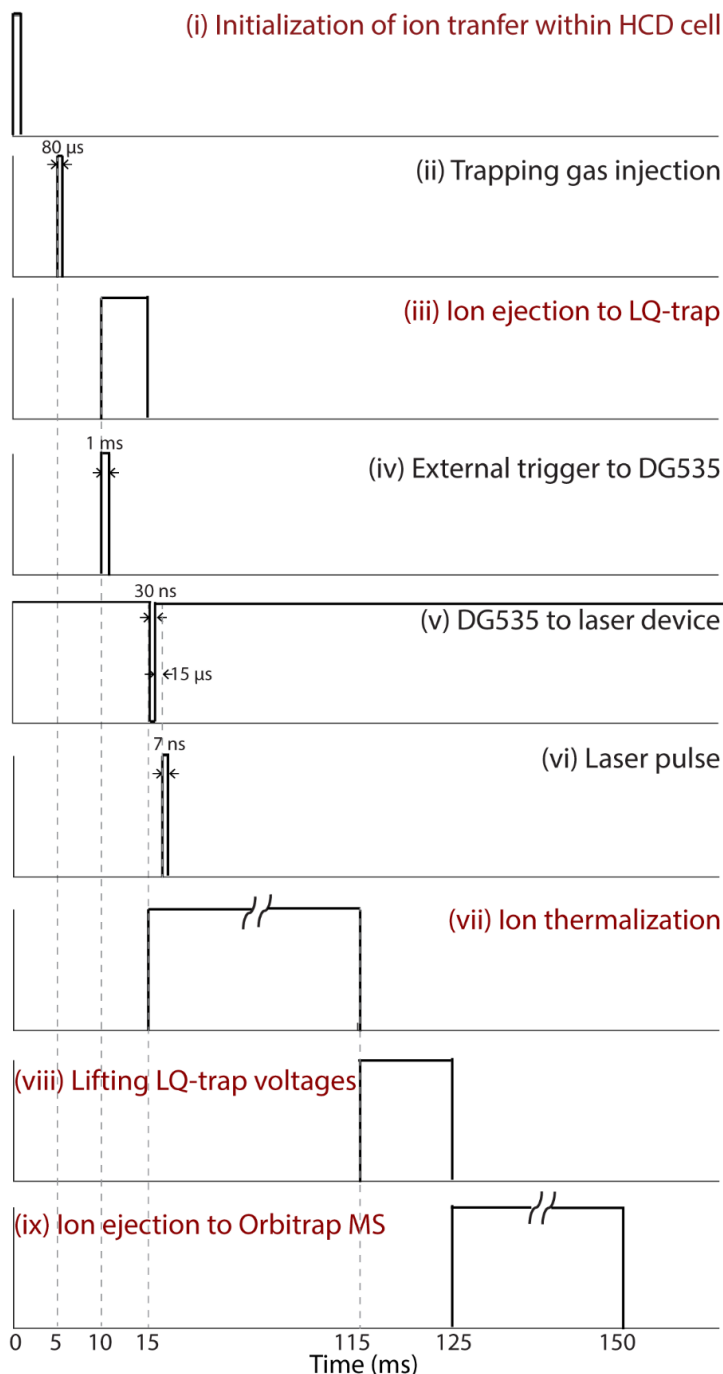
Figure S23. Timing diagram of the events used for the acquisition of concanavalin A UVPD spectrum in external UVPD Orbitrap mode (Figure 4a). Note that the timing signals labeled in red (title) are associated with a change in the voltage profile of ion optics elements 11-15 (Figures 2 and S12 (Concanavalin A)).
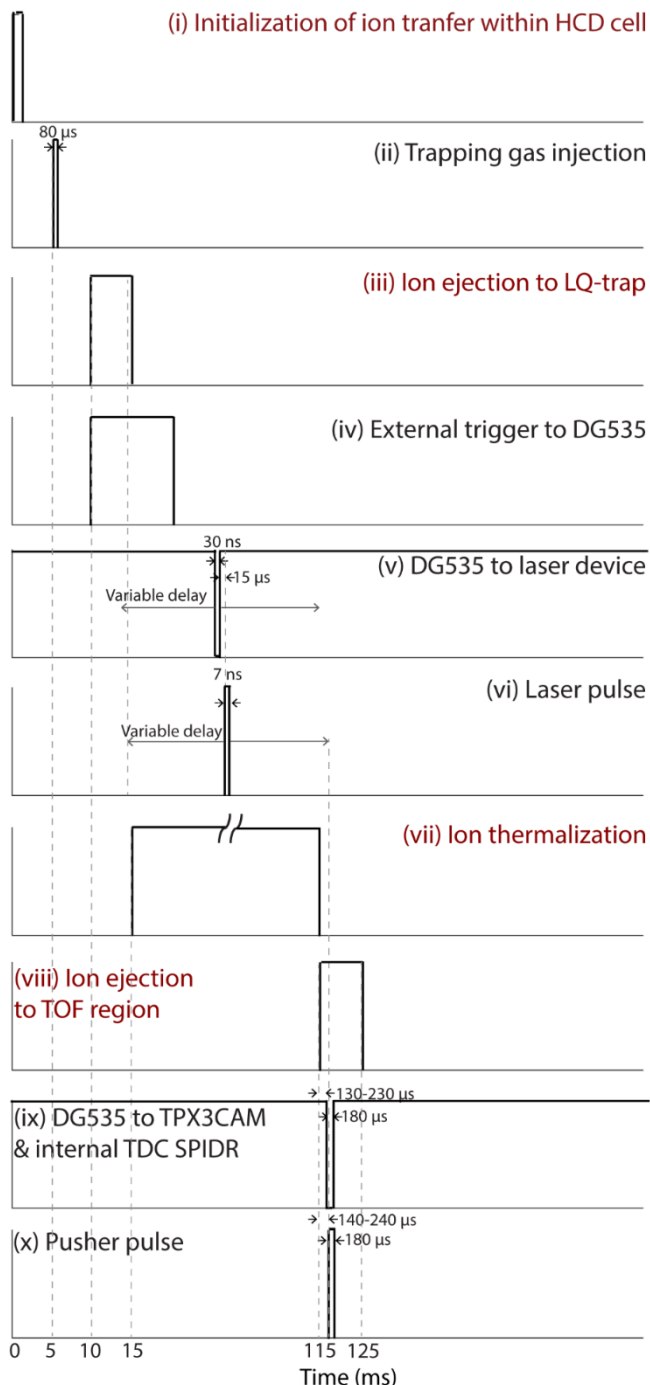
Figure S24. Timing diagram of the events used for the acquisition of concanavalin A UVPD spectrum in external UVPD orthogonal TOF imaging mode (Figure 5). Note that the timing signals represented in red (title) are associated with a change in the voltage profile of ion optics elements 11-15 (Figure 2 and S14 (concanavalin A)).

# TOWARDS GEOMETRIC STRUCTURAL ELUCIDATION OF MACROMOLECULAR ASSEMBLIES USING SINGLE ION IMAGING MASS SPECTROMETRY AND ULTRAVIOLET PHOTODISSOCIATION

6

CHAPTER

Anjusha Mathew[1], Frans Giskes[1], Gert B. Eijkel[1], Ian G. M. Anthony[1], Dimitris Papanastasiou[2], Albert J. R. Heck[3,4], Alexander A. Makarov[3,5], Shane R. Ellis[1,6], and Ron M. A. Heeren[1]

[1] Maastricht MultiModal Molecular Imaging (M4i) Institute, Division of Imaging Mass Spectrometry (IMS), Maastricht University, 6229 ER Maastricht, The Netherlands

[2] Fasmatech Science and Technology, Demokritos NCSR, 15310 Agia Paraskevi, Athens, Greece

[3] Biomolecular Mass Spectrometry and Proteomics, Bijvoet Centre for Biomolecular Research and Utrecht Institute for Pharmaceutical Sciences, Utrecht University, Padualaan 8, 3584 CH Utrecht, The Netherlands

[4] Netherlands Proteomics Center, Padualaan 8, 3584 CH Utrecht, The Netherlands

[5] Thermo Fisher Scientific (Bremen) GmbH, 28199 Bremen, Germany

[6] Molecular Horizons and School of Chemistry and Molecular Bioscience, University of Wollongong, NSW 2522, Australia

7

CHAPTER

PERSPECTIVE AND OUTLOOK

The work described in this thesis brought together the aspects of soft-ionization, high mass analyzers, top-down proteomics, and mass-resolved imaging through different combinations of nano-electrospray ionization (nESI), matrix-assisted laser desorption/ionization (MALDI), time-of-flight (TOF) and Orbitrap mass analyzers, ultraviolet photodissociation (UVPD), and position- and time-sensitive detectors from Medipix (MPX)/Timepix (TPX) family for the ion imaging and structural elucidation of multiproteoform complexes (MPCs) at all levels of its molecular complexity. The focus of this thesis was mainly on the instrument developments toward the retrieval of higher-order molecular structural features. To illustrate the emerging possibilities of the technological developments conducted here, an outlook on some of the future applications is provided below.

Additional Dimension for Gas-Phase Separation of Large and Heterogeneous MPCs

The characterization of the single MPC ion events through the measurement of the pixel cluster size on the TPX positioned on the back of the microchannel plate (MCP) detection assembly demonstrated in **Chapter 3** opens a new chapter in single-molecule MS. The equation of the MCP response/ pixel cluster size derived in terms of ion mass and charge in Chapter 3 clearly indicates that the separation based on the pixel cluster size can add another dimension to the MS analysis. This will be highly beneficial in the analysis of large intrinsically heterogeneous MPC samples, where the analytes do not have a single, well-defined mass. In that case, the ratio of the number of masses present in the sample to the number of ions is much higher, and results in a very complex mass spectrum with unresolved m/z peaks. The charge state, and thus also the mass, can only be accurately measured when multiple charge states of the same molecular species can be resolved and assigned. The TPX pixel cluster size corresponds to each charge state of different molecular species is expected to be different, hence this approach can be used to improve the analysis of large heterogeneous MPCs, and complements other single-molecule MS techniques described in Chapter 1, particularly charge detection mass spectrometry (CDMS) which has recently been demonstrated in Orbitrap MS systems.[184-188] Additionally, this approach will be also beneficial for the separation of oligomeric species that appear at the same m/z values, which is usually impossible to separate just from the mass spectra. For instance, the singly-charged monomer and doubly-charged dimer of the same molecular species appear at the same m/z value. However, these two species are expected to have different pixel cluster sizes.

Kinetics of Metastable Fragmentation in MALDI-TOF MS

Chapter 4 utilized the unique ability of space and time-resolved detection of TPX3 detection assembly to distinguish metastable fragments formed at different locations along the flight path, which provides an interesting avenue to study the kinetics and dependency of different parameters on metastable ion decay. The

most important factors leading to metastable fragment formation in MALDI MS are the energy transfer by the impact of the laser shot and gas-phase collisions with matrix molecules or matrix decomposition products during ion acceleration. Therefore, the metastable decay rate is influenced by the choice of the MALDI matrix, laser fluence, the delay between the laser shot and ion extraction (pulsed ion extraction (PIE) delay), and field strength used for the extraction of ions from the source region (extraction voltage).[308-309, 311-313] Figure 1 shows the increasing trend of metastable decay rate with an increase in laser power, which is acquired for (a) insulin chain B in different matrices and (b) different proteins in a-cyano-4-hydroxycinnamic acid (CHCA) matrix on Ultraflex-TPX3CAM experimental set up. It is observed that the extent of metastable fragmentation for proteins is strongly related to the matrix compound used (Figure 1a). In UV-MALDI, the matrix ions form gas-phase acidic ions (typically protonated matrix molecules), which then act as proton donors for desorbed neutral analyte molecules. As a consequence of this approach, the internal energy of the analyte ion will depend on the exothermicity of the proton-transfer reaction, which in turn is dependent on the specific matrix used. It is noteworthy that CHCA produces a significantly higher number of metastable fragments compared to other matrices, this can be attributed to its relatively low proton affinity value.[352-354] However, the metastable decay rates of 2, 5-dihydroxybenzoic acid (DHB), 2',6'-dihydroxyacetophenone (DHA) and sinapinic acid (SA) are comparable even though there is a difference in the gas-phase proton affinity (PA) values. Therefore, the high metastable decay rate of the oxidized B chain of bovine insulin and CHCA as matrix suggests that some form of highly specific photon activation process may be occurring, but the nature of this process is not readily apparent. Figure 1b shows how the metastable decay rate varies for different proteins. It has been observed that metastable fragmentation decreases with an increase in the mass of the protein. This can be explained on the basis of the quasi-equilibrium theory, meaning that the energy gained during the MALDI process is distributed statistically to all vibrational degrees of freedom (DOF).[355] Thus, if the same amount of energy is spread over a larger number of DOF, less energy is conferred to each DOF. This results in slower fragmentation rates correlating with the size of the ions. Similar dependency of metastable decay rate on the extraction voltage, PIE, and other parameters are expected to be observed. In addition, the quantification of the metastable fragments formed at different locations along the flight tube by the application of both retarding and deflection voltages provides a better understanding of the metastable fragmentation process, which can be investigated further with time-resolved imaging approach.
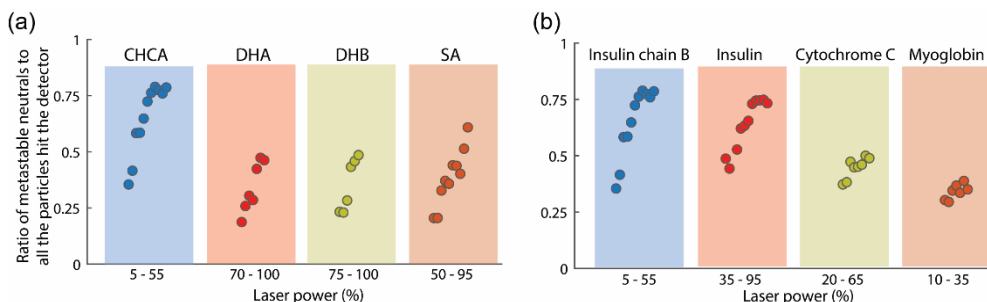
Figure 1. Influence of laser power on the metastable decay rate, acquired for (a) insulin chain B in different matrices and (b) different proteins in CHCA matrix on Ultraflex-TPX3CAM experimental setup. The metastable decay rate is calculated by dividing the number of metastable neutrals by the total number of ions.

Exploring Orbitrap/TOF Instrument to Expose the Structural Features and to Understand Energetics of MPCs Through Different Ion Fragmentation Mechanisms

The TOF imaging approach implemented in Orbitrap/TOF instrument described in **Chapters 5 and 6** allows the visualization of the *m*/z-resolved TPX3 images of UV generated subunits from non-covalent protein complexes from the ion-photon interaction at the middle of the pusher. The *m*/z-resolved TPX3 images reflect the 3D spatial UV dissociation event of the MPCs as the imaging TOF analyzer is capable of maintaining the relative positions of the expanding fragment subunits from the UVPD event to the TPX3 detector. The integration of other fragmentation methods such as electron capture dissociation (ECD), electron transfer dissociation (ETD), surface-induced dissociation (SID), and infrared multiphoton dissociation (IRMPD) to the Orbitrap/TOF system, and allowing the ion interaction with electrons/ IR photons/ surface might produce product ion images that differ from those generated by UV photons, which may help in understanding the fundamentals of each fragmentation process. Previous investigations conducted on the same non-covalent protein complexes using different ion fragmentation techniques have shown multiple dissociation pathways. In most of these studies, energy-resolved mass spectrometry (ERMS) plots corresponding to each precursor/product *m*/z value were analyzed. Figures 2 and 3 show SID, HCD (higher-energy collisional dissociation), CID (collision-induced dissociation), and UVPD spectra of tetrameric streptavidin with square-planar geometry.[168, 356] Different fragmentation mechanisms led to multiple fragmentation pathways, which reveals important information on the energetics of the fragmentation mechanism and the structural features of this MPC. The ability of the TPX3 imaging detection assembly in the Orbitrap/TOF instrument developed here to spatially visualize the fragmentation events in addition to the ERMS plots will undoubtedly provide better insight into the fragmentation process.

7
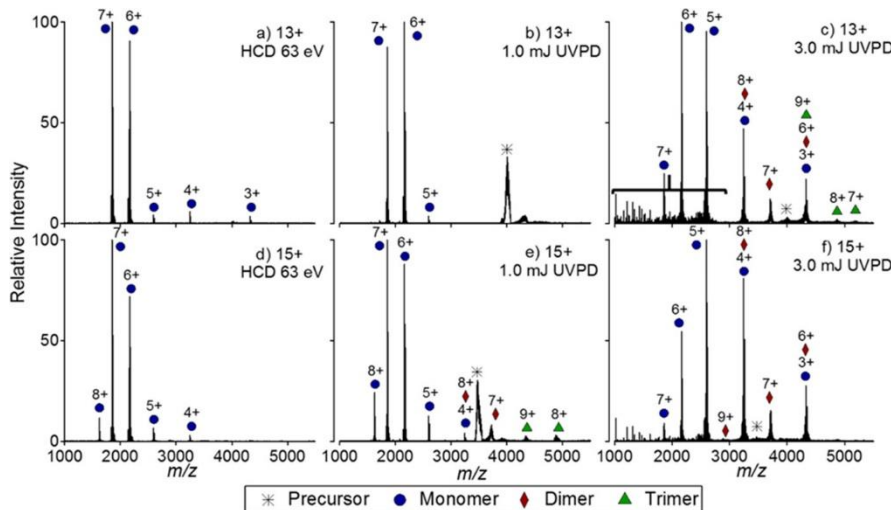
Figure 2. HCD and UVPD spectra of 13+ and 15+ tetrameric streptavidin measured on a Thermo Scientific Orbitrap Elite mass spectrometer. Reprinted from Morrison, L. J.; Brodbelt, J. S., 193 nm ultraviolet photodissociation mass spectrometry of tetrameric protein complexes provides insight into quaternary and secondary protein topology. Journal of the American Chemical Society 2016, 138 (34), 10849-10859., with permission from the American Chemical Society.

Chapter 6 also demonstrates the potential of the TOF imaging approach to detect the subunit fragments produced from single precursor MPC ions in a position and time (*m/z*)-resolved manner. The ability of the instrument to analyze the fragmentation process at the single precursor MPC level allows the quantification of M+T, D+D, 2Ms+D and 4Ms dissociations in the case of a tetramer (Q) (M:monomer, D:dimer and T:trimer) under different dissociation conditions, as well as to understand how the charge division among the subunits occurs during the dissociation process. The dissociation of single tetrameric concanavalin A into 4Ms was observed in only 5% of the total frames of the collected TPX3 data (Chapter 6, Figure 9). More information on the MPC fragmentation process is expected to be revealed by a more detailed analysis of the remaining 95% of the data.
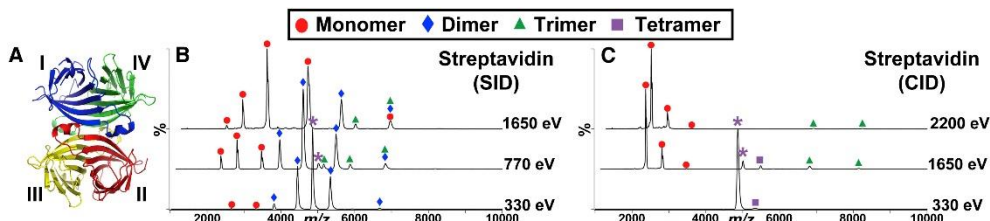
Figure 3. SID and CID spectra of charge-reduced 11+ tetrameric streptavidin measured on a Waters Synapt G2-S mass spectrometer. Reprinted from Quintyn, R. S.; Yan, J.; Wysocki, V. H., Surface-induced dissociation of homotetramers with D2 symmetry yields their assembly pathways and characterizes the effect of ligand binding. Chemistry & Biology 2015, 22 (5), 583-592., with permission from Elsevier.

Oligomer	Interfacial Analysis: interface area (IA)/ Å², salt bridges (SB), hydrogen bonds (HB)	Subunits produced Corresponding interfacial area broken on dissociation						Expected product	Observed Product
	Triose Phosphate isomerase (PDB 8TIM)								
	IA:1607 SB:8 HB: 26	M: 1607						2M	2M
	Phosphorylase B, 196 kDa (PDB 1ABB)								
	IA:2498 SB: 14.5 HB:38	M: 2498						2M	2M
	Streptavidin, 53 kDa (PDB 1SWB)								
	A: IA:1551 SB:2 HB: 12.5	B: IA:415 SB:0 HB:2	C: IA:173 SB:0 HB:0.5	**D(I-IV + III-II): 1176**	D(I-II + III-IV): 3448	D(I-III + IV-II): 3932	M + T: 2139	4M: 4278	2D	2D
	Neutravidin, 59 kDa (PDB 1VYO)								
	A: IA:1889 SB:6 HB:28.5	B: IA:550 SB:0 HB:5	C: IA:144 SB:0 HB:5	**D(I-IV + III-II): 1388**	D(I-II + III-IV): 4066	D(I-III + IV-II): 4878	M + T: 2593	4M: 5166	2D	2D
	Pyruvate Kinase 237 kDa (PDB 1AQF)								
	A: IA: 2733 SB:4 HB:14.5	B: IA:1270 SB:2 HB:10	C: IA:37 SB:0 HB:0	**D(I-IV + III-II): 2614**	D(I-II + III-IV): 5540	D(I-III + IV-II): 8066	M+T: 4040	4M: 8080	2D	2D
	Concanavalin A, 103 kDa (PDB 3CNA)								
	A: IA: 1085 SB:0 HB:10	B: IA: 982 SB:6 HB:2	C: n/a SB: HB:	**D(I-IV + III-II): 1964**	D(I-II + III-IV): 2170	D(I-III + IV-II): n/a	M+T: 2067	4M: 4134	2D, M+T	2D, M+T
	Transthyretin, 55 kDa (PDB 1F41)								
	A: IA:874 SB:0 HB:16	B: IA:379 SB:0 HB:2	C: IA:320 SB:0 HB:3	**D(I-IV + III-II): 1398**	D(I-II + III-IV): 2506	D(I-III + IV-II): 2388	M+T: 1573	4M: 3146	2D, M+T	2D, M+T
	D-Sialic acid aldolase 135 kDa (PDB 3LBM)								
	A: IA: 1148 SB:3.5 HB:12	B: IA:998 SB:6 HB: 16.5	C: IA:401 SB: 2 HB:3	**D(I-IV + III-II): 2798**	D(I-II + III-IV): 3098	D(I-III + IV-II): 4292	**M+T: 2547**	4M: 5094	2D, M+T	2D, M+T
	Hemoglobin, 65 kDa (PDB 1GZX)								
	A: 846 SB:0 HB:7	B: 663 SB:0.5 HB:5	C: 258 SB:1 HB:2	**D(I-IV + III-II): 1842**	D(I-II + III-IV):2208	D(I-III + IV-II): 3018	**M + T: 1767**	4M: 3534	2D, M+T	2D, M+T
	Tryptophan Synthase, 144 kDa (PDB 1WBJ)								
	A: 1624 SB:4 HB:18	B: 1362 SB:1 HB:19		D(I-III + IV-II): 1624	**M+T (I + III-IV-II): 1362**	D+ 2M (III-IV + I +II): 2724		4M: 4610	M+T	M+T
	Cholera toxin B, 58 kDa (PDB 1FGB)								
	A: 1227 SB:3 HB:12.6			**M + Q: 2454**	D + T: 2454	5M: 135			M+Q, D+T	M+Q, D+T
	C-reactive protein, 115 kDa (PDB 1GNH)								
	A: 666 SB:4.4 HB:2.4			**M + Q: 1332**	D + T: 1332	5M: 330			M+Q, D+T	M+Q, D+T
	Serum amyloid P, 125 kDa (PDB 1SAC)								
	A: 735 SB: 2.2HB:5			**M + Q: 1470**	D + T: 1470	5M: 675			M+Q, D+T	M+Q, D+T
	Bovine glutamate dehydrogenase , 336 kDa (PDB 3MVO)								
	A: IA: 1691 SB:0.3 HB:10	B: IA: 991 SB:2 HB:9	C: IA:298 SB:0 HB:0	**2T(I-II-III + IV-V-VI): 3867**	3D(I-IV+ II-V + III-VI): 1040	D (I-IV) + Q: 7360	D (I-II) + Q: 5960	M + P: 4671 | 6M: 14013	2T	2T
	Urease, 549 kDa (PDB 3LA4)								
	A: IA:4888 SB:13.8 HB:53.7	B: IA: 749 SB:0 HB:2	C: IA:228 SB:0 HB:0	**2T(I-II-III + IV-V-VI): 2931**	3D(I-IV+ II-V+III-VI): 30012	D (I-IV) + Q: 20008	D (I-II) + Q: 11730	M+ P: 10753 | 6M: 32259	2T	2T
	Insulin, 35 kDa (PDB 2AIY)								
	A: IA: 1796 SB:4 HB:16.3	B: IA:458 SB:1.2 HB:5.3	C: IA:844 SB:0 HB:14	**2T (II-V-VI + I-III-VI): 4014**	3D (I-IV+II-V,+III-VI): 5280	D (I-IV) + Q: 3520	D (I-II) + Q: 6276	M + P: 3556 | 6M: 10668	D+Q, M+P	D+Q, M+P

Table 1. Interfacial information, and predicted and observed SID products for a number of MPCs with different oligomeric states and conformations. The largest interface in each complex is represented by a solid black line, the second largest interface in each complex is represented by a gray dashed line, and the smallest interface is represented by a gray dotted line. M-monomer; D-dimer; T-trimer; Q-tetramer; P-pentamer; H-hexamer. Reprinted from Harvey, S. R.; Seffernick, J. T.; Quintyn, R. S.; Song, Y.; Ju, Y.; Yan, J.; Sahasrabuddhe, A. N.; Norris, A.; Zhou, M.; Behrman, E. J., Relative interfacial cleavage energetics of protein complexes revealed by surface collisions. Proceedings of the National Academy of Sciences 2019, 116 (17), 8143-8148., with permission from the National Academy of Science.

The dependence of the charge state of the precursor MPC on its gas-phase structure may be understood by the derivation of dissociation energetics parameters from the m/z-resolved TPX3 images corresponding to the UVPD product ions from the different charge states of the precursor MPC ion. Even precursor MPCs with the same charge state can dissociate into subunit fragment pairs of different charges. The evaluation of TPX3 images of those product pairs may reveal differences in the velocity distribution post-fragmentation that can be related to the different conformations of the MPC with the same charge state in the gas phase. We have demonstrated in Chapter 6 that the 2D TPX3 detector images can be used for the reconstruction of the 3D geometry of MPCs, through the UVPD of a single tetrameric concanavalin A to four monomers. However, this study must be extended to larger oligomers with different conformations in order to demonstrate that indeed we are obtaining 3D conformation with this method. Some of the interesting MPCs, which were used in the past for revealing the energetics of MPCs by SID are shown in Table 1.[337] The list of these MPCs can be used for the validation of the photofragment ion imaging (PFI)-based method described in Chapter 6 for the retrieval of MPC's 3D conformation.

7

8
CHAPTER

IMPACT

Defining the overall impact of basic scientific instrumentation research, such as the work presented in this thesis, is a difficult undertaking. The effects of such research that will eventually translate into biological applications may not be immediately apparent on short or medium-term timescales. Multiple analytical tools are necessary to understand the omics of complex biological systems, and even with their usage, it is impossible to comprehend all aspects when trying to answer a biological question. Nonetheless, we believe that the technological developments in mass spectrometry accomplished here have pushed forward that envelope and will likely have a long-term impact on molecular/structural biology.

The main focus of this thesis was on the technological advancements in mass spectrometry (MS) for the retrieval of structural features of multiproteoform assemblies (MPCs) at all levels of its molecular complexity using a single instrument platform. **Chapters 2-4** detail the characterization of the imaging systems from the Medipix (MPX)/Timepix (TPX) family for the detection of high-mass native single MPC ions, while **Chapters 5-6** outline the utilization of these TPX-based detection assemblies along with ultraviolet photodissociation (UVPD) in a custom-built Orbitrap/TOF (time-of-flight) instrument for TOF-resolved imaging and high-resolution Orbitrap analysis of MPCs. This innovative Orbitrap/TOF instrument paves the way to resolve the higher-order molecular structure of MPCs in their pseudo-native state in the gas phase. The high-resolution UVPD Orbitrap spectrum is capable of characterizing the molecular structure of the MPCs at all levels of its organization by retrieving information such as proteoform sequence, subunit stoichiometry, conformation, and molecular interactions. The energetics of the MPC dissociation process is revealed by the TOF imaging approach, which also has great potential in elucidating the quaternary structural features of MPCs including 3D geometry and interface area. However, it might take a few more years to reconstruct the 3D conformation of the MPC as this method still has to be validated on a number of oligomers with different conformations and requires the development of computational tools. Once this is accomplished, this instrument will serve as a unique platform for the extensive molecular, structural, and functional characterization of complex MPCs with biological relevance. The successful application of this unique MS-based platform will complement the structural research of cryogenic electron microscopy (cryo-EM), nuclear magnetic resonance (NMR), x-ray crystallography, and other structural MS-based methods by offering new perspectives on a shared goal. This approach will be a great addition to the MS-based structural toolkit and allows researchers to interrogate protein systems that are challenging to conventional high spatial resolution biophysical methods, e.g., intrinsically disordered and membrane proteins for x-ray crystallography, small proteins for cryo-EM, and highly heterogeneous MPCs for NMR.

The innovative Orbitrap/TOF instrument developed here is expected to have a significant impact in both clinical and pharmaceutical research settings. The study and elucidation of the complex MPC structures can be accomplished using

8

only minute amounts of simple solution-phase samples, which may eventually be applied in clinical settings in which only small amounts of patient samples can be obtained. The MPC structural information is critical in understanding structure-function relationships and drug/ligand binding sites, two essential parameters for pharmaceutical product development. It is foreseen that our novel technologies will draw the interest of pharmaceutical and biotechnology companies. Although of immediate interest to clinical and pharmaceutical research, extensions of the technology presented in this thesis can be applied for the extensive characterization of non-biological materials like nanoparticles as well.

This research emphasizes the importance of collaboration between research institutes and industrial partners as well as among research institutes. During different phases of my PhD, I had the privilege to visit and explore the MS facilities in Fasmatech Science and Technology (Athens, Greece), the provider of the custom-designed and built TOF analyzer used for the studies conducted in **Chapters 5-6**. Working on the ion optics design and testing of the TOF analyzer and associated ion optics with Fasmatech, along with inputs from ThermoFisher Scientific (Bremen, Germany), one of the leading companies in MS instrumentation and research, and the provider of the Q Exactive Orbitrap ultra-high mass range (UHMR) mass spectrometer to which the custom-built TOF analyzer was integrated, was an incredible experience. The joint research between M4i, Fasmatech, and ThermoFisher Scientific led to further collaborations between M4i and these companies, including the integration of a custom-built matrix-assisted laser desorption/ionization (MALDI) ion source (Fasmatech) to an Orbitrap Elite mass spectrometer with an aim of improving the spatial resolution to 1 μm in mass spectrometry imaging (MSI) and coupling an Aquilos cryo-focused ion beam/scanning electron microscope and an Orbitrap Exploris 480 mass spectrometer to enhance the spatial and mass resolution in MSI (ThermoFisher Scientific). Throughout my thesis, I had the wonderful opportunity to work closely with Amsterstedm Scientific Instruments (ASI, Amsterdam, the Netherlands), the supplier of the TPX3CAM (TPX3 based camera), the imaging detector used for the research conducted in **Chapters 4-6**, which facilitated the exchange of knowledge, experience, and insight from both perspectives. While I communicated the added value of position-sensitive detectors in the MS field from a user's point of view, ASI provided valuable resources and expertise in hardware and software development and tailored solutions in TPX-based detection technology. Furthermore, ASI is actively collaborating on a number of projects with M4i, including the integration of TPX3CAM to a BioTRIFT mass spectrometer to enhance the throughput in MSI[152], as well as the employment of TPX3 detectors to Artica and Polara microscopes with an aim to operate EM at a broader range of energies, at higher throughput and higher dynamic range (Department of Nanoscopy, M4i).[357-358] Besides the successful collaborations with the industry partners, I gained hands-on experience on native MS and UVPD implemented on the Q Exactive UHMR and Exactive plus extended mass range (EMR) mass spectrometers from the Hecklab, Utrecht University (Utrecht, the

Netherlands). Without this knowledge transfer, it would have been challenging to implement native MS (**Chapters 2, 3, 5 and 6**) and UVPD (**Chapters 5-6**) at M4i with the same level of ease and success. In addition, for the studies conducted in **Chapter 2** two similar LCT TOF mass spectrometers were utilized; one modified with the TPX detector at M4i and the other a standard LCT at Hecklab. The incorporation of TPX imaging detectors to LCT and Ultraflex III mass spectrometers for the visualization of time-resolved images of the electrospray ionization (ESI)/MALDI ion cloud provides insights into the ion trajectories and ion optical processes (**Chapters 2-4**), which led to the in-depth discussions with the leading MS instrument manufacturers such as Waters Corporation (Wilmslow, UK), MS Vision (Almere, the Netherlands) and Bruker Daltonics (Bremen, Germany).

Even though the focus of my Ph.D. was on the technical aspects of MS, I devoted considerable time performing native MS to address some relevant biological questions that were not included in this thesis. Through an ongoing collaboration between the Technical University of Munich and both divisions of M4i - Mass Spectrometry and Nanoscopy, native MS and cryo-EM have been utilized as tools to characterize exosome samples from different breast cancer cell lines and SARS-CoV2 Spike protein transfected and non-transfected HEK cells, in addition to flow cytometry. Native MS has been a valuable tool for the structural and functional characterization of ESX1 (one of the molecular machinery of Mycobacterium tuberculosis)-secretion system related proteins, in addition to the biophysical techniques such as x-ray crystallography, cryo-EM, and circular dichroism spectroscopy. These studies were carried out in collaboration with the Department of Nanoscopy, M4i. Additionally, I had the opportunity to explore various ionization sources and solvent conditions to characterize the molecular structure of some of the challenging MPCs that include intrinsically disordered proteins, membrane proteins etc. in their pseudo-native state in the gas phase. These projects were conducted in collaboration with various research institutes and companies, including the National Research Council (Catania, Italy), Indian Institute of Technology (Kanpur, India), University of Amsterdam (Amsterdam, the Netherlands), and Cristal Therapeutics (Maastricht, the Netherlands).

The majority of the studies presented in this thesis are published in open-access journals to enable fellow researchers and industry entities to benefit from them for their own purposes. In addition, these findings have been presented at various academic meetings, which have attracted individuals from diverse scientific backgrounds.

8

From an industry perspective, the development of innovative and powerful tools for the structural elucidation of MPCs is one of the most active areas of research for MS manufacturers due to the rapidly growing market demanding this technology. The novel Orbitrap/TOF instrument platform developed from this research will open new markets and revenue streams for both MS instrument manufacturers such as ThermoFisher Scientific and SMEs including Fasmatech Science and Technology and Amsterdam Scientific Instruments.

From a fundamental science perspective, the research conducted here has utilization in many different research fields. Specifically, the structural proteomics research will be accelerated both with the instrumentation platform and corresponding algorithms which will be developed for the reconstruction of the 3D structure of MPCs. The 3D structural data will benefit investigators working in proteomics, specifically by providing structure-function relationships. The technological enhancements achieved through the utilization of the active pixelated detectors from the Medipix (MPX)/Timepix (TPX) family (**Chapters 2-6**) will benefit diverse and broad research fields including fast mass microscopy, structural biology, applied physics, and engineering, where the MPX/TPX detection technology has been applied.[140, 145, 147, 152, 357-367] Through the strong embedding of M4i's detector research within the Medipix consortium at the European Organization for Nuclear Research (CERN, Geneva, Switzerland), the future research will provide new outlets for the expansion of technology developed within this large, international consortium. For instance, the future studies will be benefited from the deployment of Timepix4[138], the latest detector from the MPX/TPX family, which is the first large area (448 x 512) high-resolution pixel detector readout application-specific integrated circuit (ASIC), which provides significantly higher time-of-arrival (TOA) and time-over-threshold (TOT) resolutions than its predecessors TPX[71, 135, 290] and TPX3[137, 322] ASICs used in this research.

8

9

SUMMARY
SAMENVATTING

SUMMARY

The higher-order molecular structural elucidation of multiproteoform complexes (MPCs) is one of the most attention-grabbing applications in the field of mass spectrometry (MS), as the MS-based structural toolbox has the ability to characterize the structure of MPCs at its all molecular complexity levels. MS has demonstrated the ability to retrieve important structural information typically missed by high-resolution biophysical approaches. The work presented in this thesis focused on the technological advancements towards the molecular structural characterization of large MPCs by bringing together soft-ionization techniques, high mass analyzers, top-down proteomics, and mass-to-charge ratio (m/z)-resolved imaging. Nano-electrospray ionization (nESI) and matrix-assisted laser desorption/ionization (MALDI), axial/orthogonal reflectron time-of-flight (TOF) and high-resolution Orbitrap MS, ultraviolet photodissociation (UVPD), and position- and time-sensitive Timepix (TPX) and TPX3 application-specific integrated circuit (ASIC) based detection assemblies were all explored to evaluate the different elements of our approach.

Although the TPX ASIC has been successfully implemented in biomolecular MS in combination with microchannel plate (MCP) amplifiers in the past, it has only been used in the detection of relatively small biomolecules. No native, non-covalent large MPCs were detected using TPX-based detection systems. The MCP-TPX quad detection assembly equipped with nESI-orthogonal reflectron TOF LCT MS employed for the studies conducted in **Chapter 2** enabled the detection and imaging of the multiply charged non-covalent 14-mer (GroEL) with a molecular weight in excess of 800 kDa. Moreover, GroEL was measured using TPX as well as by a conventional detector on two LCTs under identical ion optics conditions, and the results were compared and contrasted. The better quality GroEL TPX spectrum supports the previous investigations conducted on TPX-based systems, where the TPX detector provided spectra with enhanced signal-to-noise (S/N) ratio and sensitivity compared to conventional detectors. The potential of the TPX to detect and image individual MPC ion events demonstrated in this Chapter forms the foundation of the investigations performed in Chapters 3 and 6. The ability of the TPX detector to provide both the TOF spectrum and the spatial distribution of the ions striking at the detector offers a more detailed insight into the functionality of each ion optical element within the mass spectrometer as well as the corresponding ion trajectories. This makes TPX a suitable tool for the optimization of newly developed MS instruments and allows for more direct comparisons between the ion optics simulations and experimental data. For instance, in the LCT system, a strangely behaved secondary, low resolution, low m/z signal at the TOF spectrum of high mass species was observed. Similar, low m/z signals when spraying high-mass species were previously observed in quadrupole (Q)-TOF I, II, and LCT MS instruments from Waters. It was impossible to understand the origin of this signal merely by examining the mass spectrum. Here, using the unique capabilities of TPX

9

detectors and the ion optics SIMION model of the LCT, we were able to identify this unknown signal as "secondary electrons formed by the interaction of intact precursor MPC species with the TOF housing", which appears as a secondary distribution in both time and space domain.

The ability of the TPX positioned at the back of the MCP to measure the pixel cluster size corresponding to individual ion events was utilized to understand the response of the MCP to the ion optics parameters and ion properties (**Chapter 3**). This allowed us to characterize the MCP's performance in the high-mass low-velocity regime, where the MCP has reduced detection efficiency. The pixel cluster size of the secondary electron cloud generated by the MCP on the TPX for each individual ion event is analyzed as a measure of the MCP performance at each m/z value for the following measurement ranges; ion mass = 195 to 802,000 Da, ion velocity = 8.4 to 67.4 km/s, and ion charge = 1+ to 72+, and resulted in a Poisson distribution. The MCP detector performance is shown to improve with an increase in ion charge, velocity, and energy and deteriorates with an increase in ion mass, m/z, and TOF. The dependence of ion optical parameters such as TOF tube voltage, MCP bias voltage, and potential gradient between the back plate of the MCP and TPX on the MCP charge cloud footprint can be utilized to achieve optimum image quality when MCP is used in imaging systems, as well as to improve native macromolecular ion detection efficiency in the high-mass low-velocity regime. We were able to derive an MCP performance equation for individual TPX registered single ion events based on two independent ion properties, ion mass, and charge; pixel cluster size/MCP performance $\propto m^{-0.49}q^{0.77}$. This equation indicates the oligomers of MPCs that appear at the same m/z values in the mass spectrum are expected to have different pixel cluster sizes. Separation based on pixel cluster size can be beneficial for the analysis of highly heterogeneous native MPCs samples and complements the single particle MS methods such as charge detection mass spectrometry (CDMS).

Chapters 2 and 3 utilized an earlier generation TPX chip from the TPX detector family that was limited by a moderate time resolution (at best 10 ns) and single-stop detection for each pixel, which hampered the detection of ions with high m/z values at high pixel occupancies. In **Chapter 4**, a Si-coated TPX3 chip, the successor of TPX, has been employed as the linear detector in a MALDI-axial TOF Ultraflex III MS instrument. The enhanced time resolution (1.5625 ns), simultaneous measurement of time-over-threshold (TOT) and time-of-arrival (TOA), and multihit capabilities of the TPX3 chip, allowed the generation of the TOF/mass spectra with a better S/N ratio and improved the sensitivity of high m/z detection in the presence of low m/z ions at high count rates and detector voltages. In contrast to the previous detector setup discussed in Chapters 2 and 3, where the TPX chip is directly coupled to the MCP, a P47 phosphor screen is placed in between the MCP and Si-coated TPX3 chip in Chapter 4. This allowed the TPX3 assembly to be installed at atmospheric pressure which brings considerable flexibility, elimination of several technically challenging elements, and flexible mapping between the

phosphor screen and sensor area compared to the previous MCP-TPX setup. This experimental setup significantly extended the *m/z* range previously detected with the TPX family by the measurement of the intact singly charged immunoglobulin M (IgM) ions of *m/z* approaching 1,000,000 Da. In addition, the ability of the TPX detector to provide both TOF spectrum and spatial distribution of the ions striking at the detector along with the application of deflector and retarding voltages allowed the examination of the metastable fragments formed at different parts of the flight tube. The unique ability of space and time-resolved detection to distinguish metastable fragments formed at different locations along the flight path provides an interesting avenue to study the kinetics of metastable ion decay. Additionally, the influence of both MALDI and parameters such as laser fluence, MALDI matrix, and extraction conditions on the metastable decay rate can be investigated with this approach.

Next, we have developed a unique Orbitrap/TOF MS-based instrument for the extensive structural and molecular characterization of MPCs at different levels of its organization. **Chapter 5** focused on the detailed design, development, and evaluation of the QExactive ultra-high mass range (UHMR) Orbitrap/TOF MS instrument with integrated UVPD and TPX detection assemblies– MCP-TPX quad (used for studies in Chapters 2 & 3) and MCP-P47-TPX3CAM (used for study in Chapter 4). This instrument has four modes of operation that enabled the high-mass resolution measurement and mass-resolved imaging of HCD or UVPD generated fragments from the native MPC ions using the Orbitrap mass analyzer and TOF analyzer-TPX3 imaging assembly, respectively. UVPD on high-resolution Orbitrap and TOF MS instruments has already been employed by several groups to obtain the tandem MS spectra that allow high-level structural and functional characterization of MPCs by extracting information on amino acid sequence, conformation, subunit stoichiometry, and molecular interactions. However, the TOF imaging approach implemented with the TPX3 detection assembly allows the visualization of the 3D spatial UV dissociation event of the MPCs. This is a direct result of the unique capability of the imaging TOF analyzer that was designed to maintain the relative positions of the expanding fragment subunits from the UVPD event to the TPX3 detector. There, both the arrival time and impact position of each subunit are recorded simultaneously with the ultimate goal to reconstruct the 3D geometry of the MPC prior to the UVPD event.

In **Chapter 6**, the *m/z*-resolved TPX3 images of UV generated subunit fragments from non-covalent protein complexes at the middle of the pusher have been explored using the TOF imaging approach implemented in the custom-developed Orbitrap/TOF instrument described in Chapter 5. The *m/z*-resolved TPX3 images were utilized to interpret the energetics of the 3D MPC dissociation event. The relative distance and angular distributions of the product ions with respect to the impact position of the precursor MPC ions from the *m/z*-resolved TPX3 images were determined. This information will be crucial in retrieving higher-order structural characteristics of the MPC, such as bond strength, conformation, etc., as well as the influence of the charge state on the behavior of the MPCs in

9

the gas phase. In addition, the evaluation of the *m/z*-resolved TPX3 images after the integration of other fragmentation methods such as electron capture dissociation (ECD), electron transfer dissociation (ETD), surface-induced dissociation (SID) and infrared multiphoton dissociation (IRMPD) to the Orbitrap/TOF system is expected to yield significant information on various fragmentation mechanisms. We were also able to show the spatially- and temporally (*m/z*)-resolved detection of the subunit fragments produced from single precursor MPC ions of dimeric β-lactoglobulin (36.5 kDa) and tetrameric concanavalin A (102 kDa). The potential of this instrument to probe the fragmentation process at the single molecule level can be used to gain a thorough understanding of the fragmentation pathways. Most importantly, the TPX3 images generated by the UVPD of single precursor tetrameric concanavalin A ions to four monomer subunits at high laser energy resembled the projection of concanavalin A's 3D geometry. The analysis of thousands of these types of single ion UVPD fragment *m/z*-resolved images might allow the reconstruction of the 3D molecular structural model of MPCs. However, the shift in the impact position in one direction due to the ion acceleration in the axial direction prior to the fragmentation process has to be deconvolved before the reconstruction process as this shift might introduce some distortions to the conformation of the MPCs. Also, better computational tools need to be developed in order to fit various geometries to the 2D detector images. This study must be extended to larger oligomers with different conformations in to demonstrate the effect on the 3D conformation observed with this method.

SAMENVATTING IN HET NEDERLANDS

De opheldering van de hogere-orde moleculaire structuur van meervoudige proteine complexen (multiproteoform complexes, MPC's) is op dit moment een gebied van massaspectrometrie (mass spectrometry, MS) waar veel aandacht naar uit gaat. De op MS gebaseerde structuuranalysegereedschappen biedt de mogelijkheid om de structuur van MPC's op alle moleculaire complexiteitsniveaus te karakteriseren. MS heeft het vermogen aangetoond om belangrijke structurele informatie wordt doorgaans gemist door de biofysische benaderingen. Het in dit proefschrift gepresenteerde werk richtte zich op de technologische vooruitgang in de richting van moleculaire structuurkarakterisering van grote MPC's door zachte ionisatietechnieken, hoge massa analyzers, top-down proteomics en massa-lading verhouding (mass-to-charge ratio, m/z)-resolutie beeldvorming samen te brengen. Nano-elektrospray ionisatie (nano-electrospray ionization, nESI) en matrix-geassisteerde laser desorptie/ionisatie (matrix-assisted laser desorption/ionization, MALDI), axiale/orthogonale reflectron-vluchttijd (time-of-flight, TOF) en hoge-resolutie Orbitrap MS, ultraviolette fotodissociatie (ultraviolet photodissociation, UVPD) en positie- en tijdgevoelige Timepix (TPX) en TPX3 applicatie-specifieke geïntegreerde schakelingen (application-specific integrated circuit, ASIC) werden alle onderzocht om de verschillende elementen van onze aanpak te evalueren.

Hoewel de TPX ASIC in het verleden met succes is geïmplementeerd in bio moleculaire MS in combinatie met microkanaal plaat (microchannel plate, MCP)-versterkers is deze alleen gebruikt bij de detectie van relatief kleine biomoleculen. Er werden geen grote, native, niet-covalente MPC's gedetecteerd met behulp van op TPX gebaseerde detectiesystemen. Het MCP-TPX quad-detectie-systeem, gekoppeld met nESI-orthogonale reflectron TOF LCT MS werd gebruikt voor de studies uitgevoerd in **Hoofdstuk 2.** Het maakte de detectie en beeldvorming mogelijk van het meervoudig geladen niet-covalente tetradecameer (GroEL) met een moleculgewicht van meer dan 800 kDa. Bovendien werd GroEL gemeten met zowel de TPX als een conventionele detector op twee LCT's onder identieke ion optische omstandigheden, en vervolgens werden de resultaten vergeleken. Het GroEL TPX-spectrum is van betere kwaliteit en ondersteunt de eerdere onderzoeken die zijn uitgevoerd met op TPX gebaseerde systemen, waarbij de TPX-detector spectra opleverde met een verbeterde signaal - ruis (signal-to-noise, S/N)-verhouding en gevoeligheid in vergelijking met conventionele detectoren. Het vermogen van de TPX om individuele MPC-ionen te detecteren en in beeld te brengen, zoals aangetoond in dit hoofdstuk, vormt de basis van het onderzoek dat is uitgevoerd in de hoofdstukken 3 en 6. Omdat met de TPX-detector zowel het TOF-spectrum als de ruimtelijke verdeling van de opvallende ionen kan worden gemeten maakt dit een gedetailleerde studie mogelijk naar de optimale werking van elk ionen optisch element in de massaspectrometer alsmede naar de ionentrajecten. Dit maakt TPX een geschikt hulpmiddel voor de optimalisatie van nieuw ontwikkelde MS-instrumenten en maakt een directe vergelijking tussen de ionoptica-simulaties

en experimentele gegevens mogelijk. In de LCT-MS werd bijvoorbeeld een vreemd secundair, lage resolutie, lage m/z-signaal waargenomen bij het TOF-spectrum van moleculen met een hoge massa. Soortgelijke vreemde lage m/z-signalen werden eerder waargenomen in de vierpool (quadrupole, Q)-TOF I, II en de LCT MS van Waters MS-instrumenten bij het bestuderen van electrospray spectra van moleculen met een zeer hoge moleculaire massa. De oorsprong van het signaal was onmogelijk te begrijpen door alleen het massaspectrum te bestuderen. Hier konden we, met behulp van de unieke analytische mogelijkheden van TPX-detectoren en het ion-optische SIMION-model van de LCT, dit onbekende signaal identificeren als "secundaire elektronen gevormd door de interactie van intacte MPC-moleculaire ionen met de TOF-behuizing". Deze elektronen verschijnen als een secundaire distributie zowel in het tijd- als in het ruimtedomein.

Het vermogen van de TPX aan de achterkant van de MCP om de pixelclustergrootte te meten die overeenkomt met de detectie van ieder individueel ion, werd gebruikt om het signaal van de MCP op de ionen optische parameters en eigenschappen te begrijpen (**Hoofdstuk 3**). Hierdoor konden we de prestaties van de MCP voor de detectie van individuele ionen karakteriseren in het regime met hoge massa en lage snelheid, waar de detectie-efficiëntie van de MCP lager is. De pixelclustergrootte op de TPX van de secundaire elektronenwolk die door een individueel ion in de MCP wordt gegenereerd wordt benut als een maat voor de MCP-prestaties bij elke m/z-waarde voor de volgende meetbereiken; ionenmassa = 195 tot 802.000 Da, ionensnelheid = 8,4 tot 67,4 km/s, en ionenlading = 1+ tot 72+, en resulteerden in een Poisson-verdeling. De prestaties van de MCP-detector verbeteren bij een toename van de ionenlading, snelheid en energie en verslechteren bij een toename van de ionenmassa, m/z en TOF. De afhankelijkheid van ionen optische parameters zoals TOF-buisspanning, MCP-biasspanning en potentiaalgradiënt tussen achter plaat van de MCP en TPX, op de MCP-voetafdruk van een ion gegenereerde ladingswolk is in detail onderzocht. Deze informatie kan worden gebruikt om een optimale beeldkwaliteit te bereiken wanneer een MCP wordt gebruikt in beeldvormingssystemen, alsook om de efficiëntie van de detectie van native macromoleculaire ionen in het regime met hoge massa en lage snelheid te verbeteren. We konden een vergelijking afleiden de de MCP-prestatie beschrijft op basis van twee onafhankelijke ioneneigenschappen, ionenmassa en lading; pixelclustergrootte/MCP-prestaties $\propto m^{-0.49}q^{0.77}$. Deze vergelijking geeft aan dat de oligomeren van MPC's die bij dezelfde m/z-waarden in het massaspectrum verschijnen, naar verwachting verschillende pixelclustergroottes zullen hebben. Een scheiding op basis van pixelclustergrootte kan worden gebruikt voor de analyse van zeer heterogene native MPC-monsters en vormt een aanvulling op de MS-methoden met één deeltje, zoals ladingsdetectie massaspectrometrie (charge detection mass spectrometry, CDMS).

Hoofdstukken 2 en 3 gebruikten een eerdere generatie TPX-chip uit de TPX-detectorfamilie. Deze werd beperkt door een matige tijdsresolutie (minimaal 10

ns) en single-stop detectie voor elke pixel wat de detectie van ionen met hoge *m/z*-waarden bij hoge ionen belasting belemmerde. In **Hoofdstuk 4** is een TPX3-chip met Silicium (Silicon, Si)-coating, de opvolger van TPX, gebruikt als axiale detector in een lineair MALDI-TOF Ultraflex III MS-instrument. De verbeterde tijdresolutie (1,5625 ns), gelijktijdige meting van tijd-over-drempel (time-over-threshold, TOT) en aankomsttijd (time-of-arrival, TOA), en multihit-mogelijkheden van de TPX3-chip in vergelijking met TPX, maakten het genereren van de TOF/massaspectra mogelijk met een betere S/N-verhouding en verbeterde de gevoeligheid van de hoge *m/z*-detectie in aanwezigheid van lage *m/z*-ionen bij hoge ionen aantallen en detectorspanningen. In tegenstelling tot de vorige detectoropstelling die in hoofdstuk 2 en 3 is besproken, waarbij de TPX-chip direct aan de MCP is gekoppeld, is in hoofdstuk 4 een P47 fosforscherm tussen de MCP en de Si-gecoate TPX3-chip geplaatst. De TPX3-assemblage kan op deze wijze geïnstalleerd worden bij atmosferische druk, wat zorgt voor aanzienlijk verbeterde flexibiliteit, eliminatie van verschillende elementen en flexibele optische projectie van fosforscherm op sensorgebied in vergelijking met de vorige MCP-TPX-opstelling. Met deze experimentele opstelling werd het m/z-bereik aanzienlijk uitgebreid waarbij de intacte enkelvoudig geladen immunoglobuline M (immunoglobulin M, IgM)-ionen 1.000.000 Da naderden. Bovendien maakte het vermogen van de TPX-detector om zowel het TOF-spectrum als de ruimtelijke verdeling van de ionen die op de detector vallen, in combinatie met de toepassing van deflector- en vertragingsspanningen, het onderzoek mogelijk van de metastabiele fragmenten gevormd in verschillende delen van de vluchtbuis. Het unieke vermogen van ruimte en tijd opgeloste detectie om metastabiele fragmenten te detecteren die op verschillende locaties langs de ionen pad zijn gevormd, biedt een interessante manier om de kinetiek van metastabiel ionenverval te bestuderen. Dit naast de mogelijkheid om de invloed van MALDI gerelateerde parameters zoals laserfluxdichtheid, MALDI-matrix en extractiecondities op de metastabiele vervalsnelheid te onderzoeken.

Deze kennis is samengebracht in de ontwikkeling van een uniek Orbitrap/TOF MS instrument voor de uitgebreide structurele en moleculaire karakterisering van MPC's. **Hoofdstuk 5** beschrijft het gedetailleerde ontwerp, de ontwikkeling en evaluatie van het QExactive ultrahoog massabereik (ultra-high mass range, UHMR) Orbitrap/TOF MS-instrument met geïntegreerde UVPD- en TPX-detectiesystemen. De detectiesystemen bestonden uit de MCP-TPX-quad (gebruikt voor onderzoeken in hoofdstukken 2 en 3) en de MCP-P47-TPX3CAM (gebruikt voor studie in Hoofdstuk 4). Dit instrument kan op vier verschillende wijzen bedreven worden. Allen dragen bij aan de meting met hoge massaresolutie en massa-opgeloste beeldvorming van de UVPD-gegenereerde fragmenten van de oorspronkelijke MPC-ionen met behulp van respectievelijk de Orbitrap-massa-analysator en het TOF-TPX3-beeldvormings instrument. UVPD op zowel Orbitrap- als TOF MS-instrumenten met hoge resolutie is al door verschillende groepen gebruikt om het tandem MS-spectrum te verkrijgen dat de

9

structurele en functionele karakterisering van MPC's mogelijk maakt en informatie genereerd over aminozuursequentie, conformatie, stoichiometrie van eiwit-componenten en moleculaire interacties. De beeldvormingsaanpak die is geïmplementeerd met het TPX3-detectie systeem maakt echter de visualisatie mogelijk van de 3D UV-dissociatiegebeurtenis van de MPC's, aangezien de TOF-analysator is ontworpen om de relatieve posities van de fragmenten van de eiwitcomplexen te behouden totdat ze de detector bereiken.

In **Hoofdstuk 6** zijn de niet-covalent gebonden eiwitcomplexen in het midden van de pusher met UV licht gefragmenteerd. De *m*/*z*-opgeloste TPX3-beelden deze fragmenten van bestudeerd met behulp van de het nieuwe Orbitrap/TOF-instrument dat wordt beschreven in Hoofdstuk 5. De *m*/*z*-opgeloste TPX3-beelden werden gebruikt om de energetica van de 3D MPC-dissociatie te bestuderen. De relatieve afstand en hoekverdeling van de product-ionen vergeleken met de impactpositie van de voorloper-MPC-ionen van de *m*/*z*-opgeloste TPX3-beelden zijn cruciaal bij het bepalen van hogere orde structurele kenmerken van de MPC, zoals bindingssterkte, conformatie en de invloed van de ladingstoestand op het gedrag van de MPC's in de gasfase. Bovendien wordt verwacht dat in de toekomst de evaluatie van de *m*/*z*-opgeloste TPX3-beelden na de integratie van andere fragmentatiemethoden zoals dissociatie van elektronenvangst (electron capture dissociation, ECD), dissociatie van elektronenoverdracht (electron transfer dissociation, ETD), oppervlakte-geïnduceerde dissociatie (surface-induced dissociation, SID) en infrarood multifoton dissociatie (infrared multiphoton dissociation, IRMPD) in het Orbitrap/TOF-systeem ook informatie zal opleveren over deze verschillende fragmentatiemechanismen. We waren ook in staat om de ruimtelijk en temporeel (*m*/*z*)-opgeloste detectie van de eiwitcomplex fragmenten te laten zien geproduceerd uit een enkel MMA-ion voor het dimeer β-lactoglobuline (36.5 kDa) en het tetrameer concanavaline A (102 kDa). Het potentieel van dit instrument om het fragmentatieproces op het niveau van een enkel molecuul te onderzoeken, kan worden gebruikt om een grondig begrip van de fragmentatieroutes te krijgen. Het belangrijkste is dat de TPX3-afbeeldingen die worden gegenereerd door de UVPD van tetramere concanavalin A-ionen met een enkele voorloper tot vier monomeersubeenheden bij hoge laserenergie lijken op de projectie van de 3D-geometrie van concanavalin A. De analyse van duizenden van dit soort UVPD-fragment beelden met een enkel ion, *m*/*z*-opgeloste beelden, is bedoeld om de reconstructie van het 3D-moleculaire structurele model van MPC's mogelijk te maken. De verschuiving in de impactpositie in één richting als gevolg van de ionenversnelling in de axiale richting voorafgaand aan het fragmentatieproces moet echter worden gecorrigeerd vóór het reconstructieproces, aangezien deze verschuiving enige vervormingen kan veroorzaken in de resulterende berekende conformatie van de MPC's. Er moeten ook betere rekenhulpmiddelen worden ontwikkeld om verschillende geometrieën aan de 2D-detectorafbeeldingen aan te passen. Deze studie moet worden uitgebreid

naar grotere oligomeren met verschillende conformaties om aan te tonen dat we inderdaad 3D-conformatie informatie verkrijgen met deze methode.

9

REFERENCES
LIST OF PUBLICATIONS
LIST OF ABBREVIATIONS
ACKNOWLEDGEMENTS
CURRICULUM VITAE

A

REFERENCES

1. Robinson, C. V.; Sali, A.; Baumeister, W., The molecular sociology of the cell. *Nature* **2007,** *450* (7172), 973-982.

2. Stollar, E. J.; Smith, D. P., Uncovering protein structure. *Essays in Biochemistry* **2020,** *64* (4), 649-680.

3. Rix, U.; Superti-Furga, G., Target profiling of small molecules by chemical proteomics. *Nature Chemical Biology* **2009,** *5* (9), 616-624.

4. Jore, M. M.; Lundgren, M.; Van Duijn, E.; Bultema, J. B.; Westra, E. R.; Waghmare, S. P.; Wiedenheft, B.; Pul, Ü.; Wurm, R.; Wagner, R., Structural basis for CRISPR RNA-guided DNA recognition by Cascade. *Nature Structural & Molecular Biology* **2011,** *18* (5), 529-536.

5. Shi, W.; Chance, M. R., Metalloproteomics: forward and reverse approaches in metalloprotein structural and functional characterization. *Current Opinion in Chemical Biology* **2011,** *15* (1), 144-148.

6. Marty, M. T.; Hoi, K. K.; Gault, J.; Robinson, C. V., Probing the Lipid Annular Belt by Gas-Phase Dissociation of Membrane Proteins in Nanodiscs. *Angewandte Chemie International Edition* **2016,** *55* (2), 550-554.

7. Skinner, O. S.; Schachner, L. F.; Kelleher, N. L., The Search Engine for Multi-Proteoform Complexes: An Online Tool for the Identification and Stoichiometry Determination of Protein Complexes. *Current Protocols in Bioinformatics* **2016,** *56* (1), 13.30. 1-13.30. 11.

8. Skinner, O. S.; Havugimana, P. C.; Haverland, N. A.; Fornelli, L.; Early, B. P.; Greer, J. B.; Fellers, R. T.; Durbin, K. R.; Do Vale, L. H.; Melani, R. D., An informatic framework for decoding protein complexes by top-down mass spectrometry. *Nature Methods* **2016,** *13* (3), 237-240.

9. Van De Waterbeemd, M.; Tamara, S.; Fort, K. L.; Damoc, E.; Franc, V.; Bieri, P.; Itten, M.; Makarov, A.; Ban, N.; Heck, A. J., Dissecting ribosomal particles throughout the kingdoms of life using advanced hybrid mass spectrometry methods. *Nature Communications* **2018,** 9 (1), 1-12.

10. Sun, P. D.; Foster, C. E.; Boyington, J. C., Overview of protein structural and functional folds. *Current Protocols in Protein Science* **2004,** *35* (1), 17.1. 1-17.1. 189.

11. Kühlbrandt, W., The resolution revolution. *Science* **2014,** *343* (6178), 1443-1444.

12. Shi, Y., A glimpse of structural biology through X-ray crystallography. *Cell* **2014,** *159* (5), 995-1014.

13. Cheng, Y.; Glaeser, R. M.; Nogales, E., How cryo-EM became so hot. *Cell* **2017,** *171* (6), 1229-1231.

14. Murata, K.; Wolf, M., Cryo-electron microscopy for structural analysis of dynamic biological macromolecules. *Biochimica et Biophysica Acta (BBA)-General Subjects* **2018,** *1862* (2), 324-334.

15. Cerofolini, L.; Fragai, M.; Ravera, E.; Diebolder, C. A.; Renault, L.; Calderone, V., Integrative approaches in structural biology: a more complete picture from the combination of individual techniques. *Biomolecules* **2019,** *9* (8), 370.

16. Purslow, J. A.; Khatiwada, B.; Bayro, M. J.; Venditti, V., NMR methods for structural characterization of protein-protein complexes. *Frontiers in Molecular Biosciences* **2020,** *7*, 9.

17. Wu, M.; Lander, G. C., How low can we go? Structure determination of small biological complexes using single-particle cryo-EM. *Current Opinion in Structural Biology* **2020,** *64*, 9-16.

18. Benesch, J. L.; Ruotolo, B. T., Mass spectrometry: come of age for structural and dynamical biology. *Current Opinion in Structural Biology* **2011,** *21* (5), 641-649.

A

19. Liko, I.; Allison, T. M.; Hopper, J. T.; Robinson, C. V., Mass spectrometry guided structural biology. *Current Opinion in Structural Biology* **2016,** *40*, 136-144.

20. Britt, H. M.; Cragnolini, T.; Thalassinos, K., Integration of Mass Spectrometry Data for Structural Biology. *Chemical Reviews* **2021,** *122* (8), 7952-7986.

21. Tamara, S.; den Boer, M. A.; Heck, A. J., High-resolution native mass spectrometry. *Chemical Reviews* **2021,** *122* (8), 7269-7326.

22. Chaudhuri, B. N., Emerging applications of small angle solution scattering in structural biology. *Protein Science* **2015,** *24* (3), 267-276.

23. Trewhella, J., Recent advances in small-angle scattering and its expanding impact in structural biology. *Structure* **2022,** *30* (1), 15-23.

24. Kelly, S. M.; Price, N. C., The use of circular dichroism in the investigation of protein structure and function. *Current Protein and Peptide Science* **2000,** *1* (4), 349-384.

25. Ranjbar, B.; Gill, P., Circular dichroism techniques: biomolecular and nanostructural analyses-a review. *Chemical Biology & Drug Design* **2009,** *74* (2), 101-120.

26. Wu, C. C.; MacCoss, M. J., Shotgun proteomics: tools for the analysis of complex biological systems. *Current Opinion in Molecular Therapeutics* **2002,** *4* (3), 242-250.

27. Aebersold, R.; Mann, M., Mass spectrometry-based proteomics. *Nature* **2003,** *422* (6928), 198.

28. Cristobal, A.; Marino, F.; Post, H.; van den Toorn, H. W.; Mohammed, S.; Heck, A. J., Toward an optimized workflow for middle-down proteomics. *Analytical Chemistry* **2017,** *89* (6), 3318-3325.

29. Sidoli, S.; Garcia, B. A., Middle-down proteomics: a still unexploited resource for chromatin biology. *Expert Review of Proteomics* **2017,** *14* (7), 617-626.

30. Catherman, A. D.; Skinner, O. S.; Kelleher, N. L., Top down proteomics: facts and perspectives. *Biochemical and Biophysical Research Communications* **2014,** *445* (4), 683-693.

31. Chen, B.; Brown, K. A.; Lin, Z.; Ge, Y., Top-down proteomics: ready for prime time? *Analytical Chemistry* **2017,** *90* (1), 110-127.

32. Tran, J. C.; Zamdborg, L.; Ahlf, D. R.; Lee, J. E.; Catherman, A. D.; Durbin, K. R.; Tipton, J. D.; Vellaichamy, A.; Kellie, J. F.; Li, M., Mapping intact protein isoforms in discovery mode using top-down proteomics. *Nature* **2011,** *480* (7376), 254.

33. Gomes, F. P.; Yates III, J. R., Recent trends of capillary electrophoresis-mass spectrometry in proteomics research. *Mass Spectrometry Reviews* **2019,** *38* (6), 445-460.

34. Shen, X.; Yang, Z.; McCool, E. N.; Lubeckyj, R. A.; Chen, D.; Sun, L., Capillary zone electrophoresis-mass spectrometry for top-down proteomics. *TrAC Trends in Analytical Chemistry* **2019,** *120*, 115644.

35. Masson, G. R.; Burke, J. E.; Ahn, N. G.; Anand, G. S.; Borchers, C.; Brier, S.; Bou-Assaf, G. M.; Engen, J. R.; Englander, S. W.; Faber, J., Recommendations for performing, interpreting and reporting hydrogen deuterium exchange mass spectrometry (HDX-MS) experiments. *Nature methods* **2019,** *16* (7), 595-602.

36. Zheng, J.; Strutzenberg, T.; Pascal, B. D.; Griffin, P. R., Protein dynamics and conformational changes explored by hydrogen/deuterium exchange mass spectrometry. *Current Opinion in Structural Biology* **2019,** *58*, 305-313.

37. O'Reilly, F. J.; Rappsilber, J., Cross-linking mass spectrometry: methods and applications in structural, molecular and systems biology. *Nature Structural & Molecular Biology* **2018,** *25* (11), 1000-1008.

38. Iacobucci, C.; Götze, M.; Sinz, A., Cross-linking/mass spectrometry to get a closer view on protein interaction networks. *Current Opinion in Biotechnology* **2020,** *63*, 48-53.

39. Piersimoni, L.; Kastritis, P. L.; Arlt, C.; Sinz, A., Cross-Linking Mass Spectrometry for Investigating Protein Conformations and Protein–Protein Interactions— A Method for All Seasons. *Chemical Reviews* **2021**, *122* (8), 7500-7531.

40. Leney, A. C.; Heck, A. J., Native Mass Spectrometry: What is in the Name? *Journal of the American Society for Mass Spectrometry* **2017**, *28* (1), 5-13.

41. Konijnenberg, A.; Butterer, A.; Sobott, F., Native ion mobility-mass spectrometry and related methods in structural biology. *Biochimica et Biophysica Acta (BBA)-Proteins and Proteomics* **2013**, *1834* (6), 1239-1256.

42. Poltash, M. L.; McCabe, J. W.; Shirzadeh, M.; Laganowsky, A.; Russell, D. H., Native IM-Orbitrap MS: Resolving what was hidden. *TrAC Trends in Analytical Chemistry* **2020**, *124*, 115533.

43. Mistarz, U. H.; Brown, J. M.; Haselmann, K. F.; Rand, K. D., Probing the binding interfaces of protein complexes using gas-phase H/D exchange mass spectrometry. *Structure* **2016**, *24* (2), 310-318.

44. Mistarz, U. H.; Chandler, S. A.; Brown, J. M.; Benesch, J. L.; Rand, K. D., Probing the dissociation of protein complexes by means of gas-phase H/D exchange mass spectrometry. *Journal of The American Society for Mass Spectrometry* **2018**, *30* (1), 45-57.

45. Harris, M. J.; Raghavan, D.; Borysik, A. J., Quantitative evaluation of native protein folds and assemblies by hydrogen deuterium exchange mass spectrometry (HDX-MS). *Journal of The American Society for Mass Spectrometry* **2018**, *30* (1), 58-66.

46. Lanucara, F.; Holman, S. W.; Gray, C. J.; Eyers, C. E., The power of ion mobility-mass spectrometry for structural characterization and the study of conformational dynamics. *Nature Chemistry* **2014**, *6* (4), 281-294.

47. Ben-Nissan, G.; Sharon, M., The application of ion-mobility mass spectrometry for structure/function investigation of protein complexes. *Current Opinion in Chemical Biology* **2018**, *42*, 25-33.

48. Fenn, J. B.; Mann, M.; Meng, C. K.; Wong, S. F.; Whitehouse, C. M., Electrospray ionization for mass spectrometry of large biomolecules. *Science* **1989**, *246* (4926), 64-71.

49. Wilm, M.; Mann, M., Analytical properties of the nanoelectrospray ion source. *Analytical Chemistry* **1996**, *68* (1), 1-8.

50. Nesatyy, V. J., Mass spectrometry evaluation of the solution and gas-phase binding properties of noncovalent protein complexes. *International Journal of Mass Spectrometry* **2002**, *221* (2), 147-161.

51. Iavarone, A. T.; Udekwu, O. A.; Williams, E. R., Buffer loading for counteracting metal salt-induced signal suppression in electrospray ionization. *Analytical Chemistry* **2004**, *76* (14), 3944-3950.

52. Verkerk, U. H.; Kebarle, P., Ion-ion and ion-molecule reactions at the surface of proteins produced by nanospray. Information on the number of acidic residues and control of the number of ionized acidic and basic residues. *Journal of the American Society for Mass Spectrometry.* **2005**, *16* (8), 1325-1341.

53. Macias, L. A.; Santos, I. C.; Brodbelt, J. S., Ion activation methods for peptides and proteins. *Analytical Chemistry* **2019**, *92* (1), 227-251.

54. Sleno, L.; Volmer, D. A., Ion activation methods for tandem mass spectrometry. *Journal of Mass Spectrometry* **2004**, *39* (10), 1091-1112.

55. McLuckey, S. A.; Mentinova, M., Ion/neutral, ion/electron, ion/photon, and ion/ion interactions in tandem mass spectrometry: do we need them all? Are they enough? *Journal of the American Society for Mass Spectrometry* **2011**, *22* (1), 3-12.

56. Karas, M.; Bachmann, D.; Bahr, U.; Hillenkamp, F., Matrix-assisted ultraviolet laser desorption of non-volatile compounds. *Int J Mass Spectrom* **1987**, *78*, 53-68.

A

57.   Mirza, U. A.; Cohen, S. L.; Chait, B. T., Heat-induced conformational changes in proteins studied by electrospray ionization mass spectrometry. *Analytical Chemistry* **1993,** *65* (1), 1-6.

58.   Wenzel, R. J.; Matter, U.; Schultheis, L.; Zenobi, R., Analysis of megadalton ions using cryodetection MALDI time-of-flight mass spectrometry. *Analytical Chemistry* **2005,** *77* (14), 4329-4337.

59.   Weidmann, S.; Barylyuk, K.; Nespovitaya, N.; Mädler, S.; Zenobi, R., A new, modular mass calibrant for high-mass MALDI-MS. *Analytical Chemistry* **2013,** *85* (6), 3425-3432.

60.   Cornett, D. S.; Reyzer, M. L.; Chaurand, P.; Caprioli, R. M., MALDI imaging mass spectrometry: molecular snapshots of biochemical systems. *Nature Methods* **2007,** *4* (10), 828-833.

61.   Chaurand, P.; Latham, J. C.; Lane, K. B.; Mobley, J. A.; Polosukhin, V. V.; Wirth, P. S.; Nanney, L. B.; Caprioli, R. M., Imaging mass spectrometry of intact proteins from alcohol-preserved tissue specimens: bypassing formalin fixation. *Journal of Proteome Research* **2008,** *7* (8), 3543-3555.

62.   Spraggins, J. M.; Rizzo, D. G.; Moore, J. L.; Rose, K. L.; Hammer, N. D.; Skaar, E. P.; Caprioli, R. M., MALDI FTICR IMS of intact proteins: using mass accuracy to link protein images with proteomics data. *Journal of the American Society for Mass Spectrometry* **2015,** 26 (6), 974-985.

63.   Lin, M.; Eberlin, L. S.; Seeley, E. H., Reduced Hemoglobin Signal and Improved Detection of Endogenous Proteins in Blood-Rich Tissues for MALDI Mass Spectrometry Imaging. *Journal of the American Society for Mass Spectrometry* **2022,** *33* (2), 296-303.

64.   Douglas, D.; French, J. B., Collisional focusing effects in radio frequency quadrupoles. *Journal of the American Society for Mass Spectrometry* **1992,** *3* (4), 398-408.

65.   Sobott, F.; Hernandez, H.; McCammon, M. G.; Tito, M. A.; Robinson, C. V., A tandem mass spectrometer for improved transmission and analysis of large macromolecular assemblies. *Analytical Chemistry* **2002,** *74* (6), 1402-7.

66.   Schmidt, A.; Bahr, U.; Karas, M., Influence of pressure in the first pumping stage on analyte desolvation and fragmentation in nano-ESI MS. *Analytical Chemistry* **2001,** *73* (24), 6040-6.

67.   Tahallah, N.; Pinkse, M.; Maier, C. S.; Heck, A. J., The effect of the source pressure on the abundance of ions of noncovalent protein assemblies in an electrospray ionization orthogonal time-of-flight instrument. *Rapid Communications in Mass Spectrometry* **2001,** *15* (8), 596-601.

68.   Chernushevich, I. V.; Thomson, B. A., Collisional cooling of large ions in electrospray mass spectrometry. *Analytical Chemistry* **2004,** *76* (6), 1754-60.

69.   van den Heuvel, R. H.; van Duijn, E.; Mazon, H.; Synowsky, S. A.; Lorenzen, K.; Versluis, C.; Brouns, S. J.; Langridge, D.; van der Oost, J.; Hoyes, J.; Heck, A. J., Improving the performance of a quadrupole time-of-flight instrument for macromolecular mass spectrometry. *Analytical Chemistry* **2006,** *78* (21), 7473-83.

70.   Benesch, J. L.; Ruotolo, B. T.; Simmons, D. A.; Robinson, C. V., Protein complexes in the gas phase: technology for structural genomics and proteomics. *Chemical Reviews* **2007,** *107* (8), 3544-3567.

71.   Mathew, A.; Buijs, R.; Eijkel, G. B.; Giskes, F.; Dyachenko, A.; van der Horst, J.; Byelov, D.; Spaanderman, D. J.; Heck, A. J. R.; Porta Siegel, T.; Ellis, S. R.; Heeren, R. M. A., Ion Imaging of Native Protein Complexes Using Orthogonal Time-of-Flight Mass Spectrometry and a Timepix Detector. *Journal of the American Society for Mass Spectrometry* **2021,** *32* (2), 569-580.

72.   Rose, R. J.; Damoc, E.; Denisov, E.; Makarov, A.; Heck, A. J., High-sensitivity Orbitrap mass analysis of intact macromolecular assemblies. *Nature Methods* **2012,** *9* (11), 1084-6.

73.   Snijder, J.; van de Waterbeemd, M.; Damoc, E.; Denisov, E.; Grinfeld, D.; Bennett,

A.; Agbandje-McKenna, M.; Makarov, A.; Heck, A. J., Defining the stoichiometry and cargo load of viral and bacterial nanoparticles by Orbitrap mass spectrometry. *Journal of the American Chemical Society* **2014,** *136* (20), 7295-7299.

74.	Fort, K. L.; Van de Waterbeemd, M.; Boll, D.; Reinhardt-Szyba, M.; Belov, M. E.; Sasaki, E.; Zschoche, R.; Hilvert, D.; Makarov, A. A.; Heck, A. J., Expanding the structural analysis capabilities on an Orbitrap-based mass spectrometer for large macromolecular complexes. *Analyst* **2018,** *143* (1), 100-105.

75.	Lorenzen, K.; Versluis, C.; van Duijn, E.; van den Heuvel, R. H.; Heck, A. J., Optimizing macromolecular tandem mass spectrometry of large non-covalent complexes using heavy collision gases. *International Journal of Mass Spectrometry* **2007,** *268* (2-3), 198-206.

76.	Nolting, D.; Malek, R.; Makarov, A., Ion traps in modern mass spectrometry. *Mass Spectrometry Reviews* **2019,** *38* (2), 150-168.

77.	Lai, Y. H.; Wang, Y. S., Advances in high-resolution mass spectrometry techniques for analysis of high mass-to-charge ions. *Mass Spectrometry Reviews* **2022**, e21790.

78.	Ben-Nissan, G.; Belov, M. E.; Morgenstern, D.; Levin, Y.; Dym, O.; Arkind, G.; Lipson, C.; Makarov, A. A.; Sharon, M., Triple-stage mass spectrometry unravels the heterogeneity of an endogenous protein complex. *Analytical Chemistry* **2017,** *89* (8), 4708-4715.

79.	Mehaffey, M. R.; Sanders, J. D.; Holden, D. D.; Nilsson, C. L.; Brodbelt, J. S., Multistage ultraviolet photodissociation mass spectrometry to characterize single amino acid variants of human mitochondrial BCAT2. *Analytical Chemistry* **2018,** *90* (16), 9904-9911.

80.	Greisch, J.-F.; Tamara, S.; Scheltema, R. A.; Maxwell, H. W.; Fagerlund, R. D.; Fineran, P. C.; Tetter, S.; Hilvert, D.; Heck, A. J., Expanding the mass range for UVPD-based native top-down mass spectrometry. *Chemical Science* **2019,** *10* (30), 7163-7171.

81.	Gault, J.; Liko, I.; Landreh, M.; Shutin, D.; Bolla, J. R.; Jefferies, D.; Agasid, M.; Yen, H.-Y.; Ladds, M. J.; Lane, D. P., Combining native and 'omics' mass spectrometry to identify endogenous ligands bound to membrane proteins. *Nature Methods* **2020,** *17* (5), 505-508.

82.	Snyder, D. T.; Panczyk, E. M.; Somogyi, A.; Kaplan, D. A.; Wysocki, V., Simple and minimally invasive SID devices for native mass spectrometry. *Analytical Chemistry* **2020,** *92* (16), 11195-11203.

83.	Guilhaus, M., Special feature: Tutorial. Principles and instrumentation in time-of-flight mass spectrometry. Physical and instrumental concepts. *Journal of Mass Spectrometry* **1995,** *30* (11), 1519-1532.

84.	Standing, K., Timing the flight of biomolecules: a personal perspective. *International Journal of Mass Spectrometry* **2000,** *200* (1-3), 597-610.

85.	Mamyrin, B., Time-of-flight mass spectrometry (concepts, achievements, and prospects). *International Journal of Mass Spectrometry* **2001,** *206* (3), 251-266.

86.	Boesl, U., Time-of-flight mass spectrometry: introduction to the basics. *Mass Spectrometry Reviews* **2017,** *36* (1), 86-109.

87.	Scigelova, M.; Makarov, A., Orbitrap mass analyzer–overview and applications in proteomics. *Proteomics* **2006,** *6* (S2), 16-21.

88.	Perry, R. H.; Cooks, R. G.; Noll, R. J., Orbitrap mass spectrometry: instrumentation, ion motion and applications. *Mass Spectrometry Reviews* **2008,** *27* (6), 661-699.

89.	Eliuk, S.; Makarov, A., Evolution of orbitrap mass spectrometry instrumentation. *Annual Review of Analytical Chemistry* **2015,** *8*, 61-80.

90.	Marshall, A. G.; Hendrickson, C. L.; Jackson, G. S., Fourier transform ion cyclotron resonance mass spectrometry: a primer. *Mass Spectrometry Reviews* **1998,** *17* (1), 1-35.

A

91.   Hendrickson, C. L.; Quinn, J. P.; Kaiser, N. K.; Smith, D. F.; Blakney, G. T.; Chen, T.; Marshall, A. G.; Weisbrod, C. R.; Beu, S. C., 21 Tesla Fourier transform ion cyclotron resonance mass spectrometer: a national resource for ultrahigh resolution mass analysis. *Journal of the American Society for Mass Spectrometry* **2015**, *26* (9), 1626-1632.

92.   Nikolaev, E. N.; Kostyukevich, Y. I.; Vladimirov, G. N., Fourier transform ion cyclotron resonance (FT ICR) mass spectrometry: Theory and simulations. *Mass Spectrometry Reviews* **2016**, *35* (2), 219-258.

93.   Tucholski, T.; Ge, Y., Fourier-transform ion cyclotron resonance mass spectrometry for characterizing proteoforms. *Mass Spectrometry Reviews* **2022**, *41* (2), 158-177.

94.   Snijder, J.; Rose, R. J.; Veesler, D.; Johnson, J. E.; Heck, A. J., Studying 18 MDa virus assemblies with native mass spectrometry. *Angewandte Chemie International Edition* **2013**, *52* (14), 4020-3.

95.   Richardson, K.; Hoyes, J., A novel multipass oa-TOF mass spectrometer. *International Journal of Mass Spectrometry* **2015**, *377*, 309-315.

96.   Knauer, S.; Fischer, P.; Marx, G.; Müller, M.; Rosenbusch, M.; Schabinger, B.; Schweikhard, L.; Wolf, R., A multi-reflection time-of-flight setup for the improvement and development of new methods and the study of atomic clusters. *International Journal of Mass Spectrometry* **2019**, *446*, 116189.

97.   Fischer, P.; Schweikhard, L., Multiple-ion-ejection multi-reflection time-of-flight mass spectrometry for single-reference mass measurements with lapping ion species. *Review of Scientific Instruments* **2020**, *91* (2), 023201.

98.   Denisov, E.; Damoc, E.; Lange, O.; Makarov, A., Orbitrap mass spectrometry with resolving powers above 1,000,000. *International Journal of Mass Spectrometry* **2012**, *325*, 80-85.

99.   Liu, H.; Zhang, N.; Wan, D.; Cui, M.; Liu, Z.; Liu, S., Mass spectrometry-based analysis of glycoproteins and its clinical applications in cancer biomarker discovery. *Clinical Proteomics* **2014**, *11* (1), 1-9.

100.   Shaw, J. B.; Lin, T.-Y.; Leach III, F. E.; Tolmachev, A. V.; Tolić, N.; Robinson, E. W.; Koppenaal, D. W.; Paša-Tolić, L., 21 Tesla Fourier transform ion cyclotron resonance mass spectrometer greatly expands mass spectrometry toolbox. *Journal of the American Society for Mass Spectrometry* **2016**, *27* (12), 1929-1936.

101.   Smith, D. F.; Podgorski, D. C.; Rodgers, R. P.; Blakney, G. T.; Hendrickson, C. L., 21 tesla FT-ICR mass spectrometer for ultrahigh-resolution analysis of complex organic mixtures. *Analytical Chemistry* **2018**, *90* (3), 2041-2047.

102.   Savory, J. J.; Kaiser, N. K.; McKenna, A. M.; Xian, F.; Blakney, G. T.; Rodgers, R. P.; Hendrickson, C. L.; Marshall, A. G., Parts-per-billion Fourier transform ion cyclotron resonance mass measurement accuracy with a "walking" calibration equation. *Analytical Chemistry* **2011**, *83* (5), 1732-1736.

103.   Bowman, A. P.; Blakney, G. T.; Hendrickson, C. L.; Ellis, S. R.; Heeren, R. M.; Smith, D. F., Ultra-high mass resolving power, mass accuracy, and dynamic range MALDI mass spectrometry imaging by 21-T FT-ICR MS. *Analytical Chemistry* **2020**, *92* (4), 3133-3142.

104.   Lippens, J. L.; Nshanian, M.; Spahr, C.; Egea, P. F.; Loo, J. A.; Campuzano, I. D., Fourier transform-ion cyclotron resonance mass spectrometry as a platform for characterizing multimeric membrane protein complexes. *Journal of The American Society for Mass Spectrometry* **2017**, *29* (1), 183-193.

105.   Li, H.; Nguyen, H. H.; Ogorzalek Loo, R. R.; Campuzano, I. D.; Loo, J. A., An integrated native mass spectrometry and top-down proteomics method that connects sequence to structure and function of macromolecular complexes. *Nature Chemistry* **2018**, *10* (2), 139-148.

106.   Belov, M. E.; Damoc, E.; Denisov, E.; Compton, P. D.; Horning, S.; Makarov, A. A.; Kelleher, N. L., From protein complexes to subunit backbone fragments: a multi-stage approach to native mass spectrometry.

Analytical chemistry **2013,** *85* (23), 11163-11173.

107. Gault, J.; Donlan, J. A.; Liko, I.; Hopper, J. T.; Gupta, K.; Housden, N. G.; Struwe, W. B.; Marty, M. T.; Mize, T.; Bechara, C., High-resolution mass spectrometry of small molecules bound to membrane proteins. *Nature Methods* **2016,** *13* (4), 333-336.

108. van de Waterbeemd, M.; Fort, K. L.; Boll, D.; Reinhardt-Szyba, M.; Routh, A.; Makarov, A.; Heck, A. J., High-fidelity mass analysis unveils heterogeneity in intact ribosomal particles. *Nature Methods* **2017,** *14* (3), 283-286.

109. Wiza, J. L., Microchannel plate detectors. *Nuclear Instruments and Methods* **1979,** *162* (1-3), 587-601.

110. Matsuura, S.; Umebayashi, S.; Kusuyama, Y.; Natsume, Y.; Oba, K., Compact MCP assemblies for mass spectrometers. *Nuclear Instruments and Methods in Physics Research Section A: Accelerators, Spectrometers, Detectors and Associated Equipment* **1995,** *363* (1-2), 481-484.

111. Jungmann, J. H.; Heeren, R. M., Detection systems for mass spectrometry imaging: A perspective on novel developments with a focus on active pixel detectors. *Rapid Communications in Mass Spectrometry* **2013,** *27* (1), 1-23.

112. Tremsin, A.; Vallerga, J.; Siegmund, O., Overview of spatial and timing resolution of event counting detectors with microchannel plates. *Nuclear Instruments and Methods in Physics Research Section A: Accelerators, Spectrometers, Detectors and Associated Equipment* **2020,** *949*, 162768.

113. Frank, M.; Labov, S. E.; Westmacott, G.; Benner, W. H., Energy-sensitive cryogenic detectors for high-mass biomolecule mass spectrometry. *Mass Spectrometry Reviews* **1999,** *18* (3-4), 155-186.

114. Wenzel, R.; Rohling, U.; Nazabal, A.; Hillenkamp, F., Detector device for high mass ion detection, a method for analyzing ions of high mass and a device for selection between ion detectors. Google Patents: 2013.

115. Keifer, D. Z.; Jarrold, M. F., Single-molecule mass spectrometry. *Mass Spectrometry Reviews* **2017,** *36* (6), 715-733.

116. Spengler, B.; Kirsch, D.; Kaufmann, R.; Karas, M.; Hillenkamp, F.; Giessmann, U., The detection of large molecules in matrix-assisted UV-laser desorption. *Rapid Communications in Mass Spectrometry* **1990,** *4* (9), 301-305.

117. Weidmann, S.; Zenobi, R., High-mass MALDI-MS using ion conversion dynode detectors: Influence of the conversion voltage on sensitivity and spectral quality. *Journal of The American Society for Mass Spectrometry* **2014,** *25* (6), 950-954.

118. Ohkubo, M.; Shigeri, Y.; Kinumi, T.; Saito, N.; Ukibe, M.; Chen, Y.; Kushino, A.; Kurokawa, A.; Sato, H.; Ichimura, S., Fragmentation analysis by superconducting ion detectors in matrix-assisted laser desorption/ionization (MALDI). *Nuclear Instruments and Methods in Physics Research Section A: Accelerators, Spectrometers, Detectors and Associated Equipment* **2006,** *559* (2), 779-781.

119. Aksenov, A. A.; Bier, M. E., The analysis of polystyrene and polystyrene aggregates into the mega dalton mass range by cryodetection MALDI TOF MS. *Journal of the American Society for Mass Spectrometry* **2008,** *19* (2), 219-230.

120. Plath, L. D.; Ozdemir, A.; Aksenov, A. A.; Bier, M. E., Determination of iron content and dispersity of intact ferritin by superconducting tunnel junction cryodetection mass spectrometry. *Analytical Chemistry* **2015,** *87* (17), 8985-8993.

121. Hilton, G. C.; Martinis, J. M.; Wollman, D. A.; Irwin, K. D.; Dulcie, L.; Gerber, D.; Gillevet, P. M.; Twerenbold, D., Impact energy measurement in time-of-flight mass spectrometry with cryogenic microcalorimeters. *Nature* **1998,** *391* (6668), 672-675.

122. Frank, M.; Mears, C.; Labov, S. E.; Benner, W.; Horn, D.; Jaklevic, J.; Barfknecht,

A

A., High-efficiency detection of 66 000 Da protein molecules using a cryogenic detector in a matrix-assisted laser desorption/ionization time-of-flight mass spectrometer. *Rapid Communications in Mass Spectrometry* **1996,** *10* (15), 1946-1950.

123. Rabin, M.; Hilton, G. C.; Martinis, J. M., Application of microcalorimeter energy measurement to biopolymer mass spectrometry. *IEEE Transactions on Applied Superconductivity* **2001,** *11* (1), 242-247.

124. Suzuki, K.; Miki, S.; Shiki, S.; Wang, Z.; Ohkubo, M., Time resolution improvement of superconducting NbN stripline detectors for time-of-flight mass spectrometry. *Applied Physics Express* **2008,** *1* (3), 031702.

125. Casaburi, A.; Esposito, E.; Ejrnaes, M.; Suzuki, K.; Ohkubo, M.; Pagano, S.; Cristiano, R., A 2× 2 mm2 superconducting strip-line detector for high-performance time-of-flight mass spectrometry. *Superconductor Science and Technology* **2012,** *25* (11), 115004.

126. Park, J.; Aksamija, Z.; Shin, H.-C.; Kim, H.; Blick, R. H., Phonon-assisted field emission in silicon nanomembranes for time-of-flight mass spectrometry of proteins. *Nano Letters* **2013,** *13* (6), 2698-2703.

127. Wang, C.-C.; Lai, Y.-H.; Ou, Y.-M.; Chang, H.-T.; Wang, Y.-S., Critical factors determining the quantification capability of matrix-assisted laser desorption/ionization–time-of-flight mass spectrometry. *Philosophical Transactions of the Royal Society A: Mathematical, Physical and Engineering Sciences* **2016,** *374* (2079), 20150371.

128. Luxembourg, S. L.; Mize, T. H.; McDonnell, L. A.; Heeren, R. M., High-spatial resolution mass spectrometric imaging of peptide and protein distributions on a surface. *Analytical Chemistry* **2004,** *76* (18), 5339-44.

129. Ullrich, J.; Moshammer, R.; Dorn, A.; Dörner, R.; Schmidt, L. P. H.; Schmidt-Böcking, H., Recoil-ion and electron momentum spectroscopy: reaction-microscopes. *Reports on Progress in Physics* **2003,** 66 (9), 1463.

130. Froesch, M.; Luxembourg, S. L.; Verheijde, D.; Heeren, R. M., Imaging mass spectrometry using a delay-line detector. *European Journal of Mass Spectrometry* **2010,** *16* (1), 35-45.

131. Klerk, L. A.; Lockyer, N. P.; Kharchenko, A.; MacAleese, L.; Dankers, P. Y.; Vickerman, J. C.; Heeren, R. M., C60+ secondary ion microscopy using a delay line detector. *Analytical chemistry* **2010,** *82* (3), 801-807.

132. Jagutzki, O.; Cerezo, A.; Czasch, A.; Dorner, R.; Hattas, M.; Huang, M.; Mergel, V.; Spillmann, U.; Ullmann-Pfleger, K.; Weber, T., Multiple hit readout of a microchannel plate detector with a three-layer delay-line anode. *IEEE Transactions on Nuclear Science* **2002,** *49* (5), 2477-2483.

133. Campbell, M.; Heijne, E.; Meddeler, G.; Pernigotti, E.; Snoeys, W., A readout chip for a 64/spl times/64 pixel matrix with 15-bit single photon counting. *IEEE Transactions on Nuclear Science* **1998,** *45* (3), 751-753.

134. Llopart, X.; Campbell, M.; Dinapoli, R.; San Segundo, D.; Pernigotti, E., Medipix2: A 64-k pixel readout chip with 55-/spl mu/m square elements working in single photon counting mode. *IEEE Transactions on Nuclear Science* **2002,** *49* (5), 2279-2283.

135. Llopart, X.; Ballabriga, R.; Campbell, M.; Tlustos, L.; Wong, W., Timepix, a 65k programmable pixel readout chip for arrival time, energy and/or photon counting measurements. *Nuclear Instruments and Methods in Physics Research Section A: Accelerators, Spectrometers, Detectors and Associated Equipment* **2007,** *581* (1-2), 485-494.

136. Ballabriga, R.; Campbell, M.; Heijne, E.; Llopart, X.; Tlustos, L.; Wong, W., Medipix3: A 64 k pixel detector readout chip working in single photon counting mode with improved spectrometric performance. *Nuclear Instruments and Methods in Physics Research Section A: Accelerators, Spectrometers, Detectors and Associated Equipment* **2011,** *633*, S15-S18.

137. Poikela, T.; Plosila, J.; Westerlund, T.; Campbell, M.; De Gaspari, M.; Llopart, X.;

Gromov, V.; Kluit, R.; van Beuzekom, M.; Zappon, F.; Zivkovic, V.; Brezina, C.; Desch, K.; Fu, Y.; Kruth, A., Timepix3: a 65K channel hybrid pixel readout chip with simultaneous ToA/ToT and sparse readout. *Journal of Instrumentation* **2014**, *9* (05), C05013.

138. Llopart, X.; Alozy, J.; Ballabriga, R.; Campbell, M.; Casanova, R.; Gromov, V.; Heijne, E.; Poikela, T.; Santin, E.; Sriskaran, V., Timepix4, a large area pixel detector readout chip which can be tiled on 4 sides providing sub-200 ps timestamp binning. *Journal of Instrumentation* **2022**, *17* (01), C01044.

139. Bamberger, C.; Renz, U.; Bamberger, A., Digital imaging mass spectrometry. *Journal of the American Society for Mass Spectrometry* **2011**, *22* (6), 1079-87.

140. Jungmann, J. H.; MacAleese, L.; Visser, J.; Vrakking, M. J.; Heeren, R. M., High dynamic range bio-molecular ion microscopy with the Timepix detector. *Analytical Chemistry* **2011**, *83* (20), 7888-94.

141. Jungmann, J. H.; MacAleese, L.; Buijs, R.; Giskes, F.; De Snaijer, A.; Visser, J.; Visschers, J.; Vrakking, M. J.; Heeren, R. M., Fast, high resolution mass spectrometry imaging using a medipix pixelated detector. *Journal of the American Society for Mass Spectrometry* **2011**, *21* (12), 2023-2030.

142. Jungmann, J. H.; Smith, D. F.; MacAleese, L.; Klinkert, I.; Visser, J.; Heeren, R. M., Biological tissue imaging with a position and time sensitive pixelated detector. *Journal of the American Society for Mass Spectrometry* **2012**, *23* (10), 1679-1688.

143. Ellis, S. R.; Jungmann, J. H.; Smith, D. F.; Soltwisch, J.; Heeren, R. M., Enhanced Detection of High-Mass Proteins by Using an Active Pixel Detector. *Angewandte Chemie International Edition* **2013**, *52* (43), 11261-11264.

144. Jungmann, J. H.; Smith, D. F.; Kiss, A.; MacAleese, L.; Buijs, R.; Heeren, R. M. A., An in-vacuum, pixelated detection system for mass spectrometric analysis and imaging of macromolecules. *International Journal of Mass Spectrometry* **2013**, *341*, 34-44.

145. Kiss, A.; Smith, D. F.; Jungmann, J. H.; Heeren, R. M., Cluster secondary ion mass spectrometry microscope mode mass spectrometry imaging. *Rapid Communications in Mass Spectrometry* **2013**, *27* (24), 2745-2750.

146. Ellis, S. R.; Soltwisch, J.; Heeren, R. M., Time-resolved imaging of the MALDI linear-TOF ion cloud: direct visualization and exploitation of ion optical phenomena using a position- and time-sensitive detector. *Journal of The American Society for Mass Spectrometry* **2014**, *25* (5), 809-19.

147. Soltwisch, J.; Goritz, G.; Jungmann, J. H.; Kiss, A.; Smith, D. F.; Ellis, S. R.; Heeren, R. M., MALDI mass spectrometry imaging in microscope mode with infrared lasers: bypassing the diffraction limits. *Analytical Chemistry* **2014**, *86* (1), 321-5.

148. Syed, S. U.; Eijkel, G. B.; Kistemaker, P.; Ellis, S.; Maher, S.; Smith, D. F.; Heeren, R. M., Experimental investigation of the 2D ion beam profile generated by an ESI octopole-QMS system. *Journal of the American Society for Mass Spectrometry* **2014**, *25* (10), 1780-7.

149. Syed, S. U.; Eijkel, G. B.; Maher, S.; Kistemaker, P.; Taylor, S.; Heeren, R. M., A micropixelated ion-imaging detector for mass resolution enhancement of a QMS instrument. *Analytical and Bioanalytical Chemistry* **2015**, *407* (8), 2055-62.

150. Syed, S. U.; Maher, S.; Eijkel, G. B.; Ellis, S. R.; Jjunju, F.; Taylor, S.; Heeren, R. M., Direct ion imaging approach for investigation of ion dynamics in multipole ion guides. *Analytical Chemistry* **2015**, *87* (7), 3714-3720.

151. Jencic, B.; Sepec, L.; Vavpetic, P.; Kelemen, M.; Rupnik, Z.; Vencelj, M.; Vogel-Mikus, K.; Potocnik, N. O.; Ellis, S. R.; Heeren, R.; Pelicon, P., Stigmatic imaging of secondary ions in MeV-SIMS spectrometry by linear Time-of-Flight mass spectrometer and the TimePix detector. *Nuclear Instruments and Methods in Physics Research Section B: Beam Interactions with Materials and Atoms* **2019**, *452*, 1-6.

152. Körber, A.; Keelor, J. D.; Claes, B. S.; Heeren, R. M.; Anthony, I. G., Fast Mass Microscopy: Mass Spectrometry Imaging of a

A

Gigapixel Image in 34 Minutes. *Analytical Chemistry* **2022**.

153.   Benesch, J. L.; Robinson, C. V., Mass spectrometry of macromolecular assemblies: preservation and dissociation. *Current Opinion in Structural Biology* **2006,** *16* (2), 245-251.

154.   Gardner, M. W.; Brodbelt, J. S., Reduction of chemical noise in electrospray ionization mass spectrometry by supplemental IR activation. *Journal of the American Society for Mass Spectrometry* **2009,** *20* (12), 2206-2210.

155.   Benesch, J. L.; Aquilina, J. A.; Ruotolo, B. T.; Sobott, F.; Robinson, C. V., Tandem mass spectrometry reveals the quaternary organization of macromolecular assemblies. *Chemistry & Biology* **2006,** *13* (6), 597-605.

156.   Stiving, A. Q.; VanAernum, Z. L.; Busch, F.; Harvey, S. R.; Sarni, S. H.; Wysocki, V. H., Surface-induced dissociation: an effective method for characterization of protein quaternary structure. *Analytical Chemistry* **2018,** *91* (1), 190-209.

157.   Wang, G.; Chaihu, L.; Tian, M.; Shao, X.; Dai, R.; de Jong, R. N.; Ugurlar, D.; Gros, P.; Heck, A. J., Releasing nonperipheral subunits from protein complexes in the gas phase. *Analytical Chemistry* **2020,** *92* (24), 15799-15805.

158.   Laskin, J.; Futrell, J. H., Activation of large Ions in FT-ICR mass spectrometry. *Mass spectrometry reviews* **2005,** *24* (2), 135-167.

159.   Brodbelt, J. S., Photodissociation mass spectrometry: new tools for characterization of biological molecules. *Chemical Society Reviews* **2014,** *43* (8), 2757-2783.

160.   Zhou, M.; Wysocki, V. H., Surface induced dissociation: dissecting noncovalent protein complexes in the gas phase. *Accounts of Chemical Research* **2014,** *47* (4), 1010-1018.

161.   Snyder, D. T.; Harvey, S. R.; Wysocki, V. H., Surface-induced Dissociation Mass Spectrometry as a Structural Biology Tool. *Chemical Reviews* **2021**.

162.   Lermyte, F.; Valkenborg, D.; Loo, J. A.; Sobott, F., Radical solutions: Principles and application of electron-based dissociation in mass spectrometry-based analysis of protein structure. *Mass Spectrometry Reviews* **2018,** *37* (6), 750-771.

163.   Riley, N. M.; Coon, J. J., The role of electron transfer dissociation in modern proteomics. *Analytical Chemistry* **2018,** *90* (1), 40-64.

164.   Brodbelt, J. S.; Morrison, L. J.; Santos, I., Ultraviolet photodissociation mass spectrometry for analysis of biological molecules. *Chemical Reviews* **2019,** *120* (7), 3328-3380.

165.   Madsen, J. A.; Kaoud, T. S.; Dalby, K. N.; Brodbelt, J. S., 193-nm photodissociation of singly and multiply charged peptide anions for acidic proteome characterization. *Proteomics* **2011,** *11* (7), 1329-1334.

166.   Shaw, J. B.; Li, W.; Holden, D. D.; Zhang, Y.; Griep-Raming, J.; Fellers, R. T.; Early, B. P.; Thomas, P. M.; Kelleher, N. L.; Brodbelt, J. S., Complete protein characterization using top-down mass spectrometry and ultraviolet photodissociation. *Journal of the American Chemical Society* **2013,** *135* (34), 12646-12651.

167.   O'Brien, J. P.; Li, W.; Zhang, Y.; Brodbelt, J. S., Characterization of native protein complexes using ultraviolet photodissociation mass spectrometry. *Journal of the American Chemical Society* **2014,** *136* (37), 12920-12928.

168.   Morrison, L. J.; Brodbelt, J. S., 193 nm ultraviolet photodissociation mass spectrometry of tetrameric protein complexes provides insight into quaternary and secondary protein topology. *Journal of the American Chemical Society* **2016,** *138* (34), 10849-10859.

169.   Tamara, S.; Dyachenko, A.; Fort, K. L.; Makarov, A. A.; Scheltema, R. A.; Heck, A. J., Symmetry of charge partitioning in collisional and UV photon-induced dissociation of protein assemblies. *Journal of*

the American Chemical Society **2016,** *138* (34), 10860-10868.

170.   Sipe, S. N.; Brodbelt, J. S., Impact of charge state on 193 nm ultraviolet photodissociation of protein complexes. *Physical Chemistry Chemical Physics* **2019,** *21* (18), 9265-9276.

171.   Shockley, W., Currents to conductors induced by a moving point charge. *Journal of Applied Physics* **1938,** *9* (10), 635-636.

172.   Weinheimer, A. J., The charge induced on a conducting cylinder by a point charge and its application to the measurement of charge on precipitation. *Journal of Atmospheric and Oceanic Technology* **1988,** *5* (2), 298-304.

173.   Keifer, D. Z.; Pierson, E. E.; Jarrold, M. F., Charge detection mass spectrometry: weighing heavier things. *Analyst* **2017,** *142* (10), 1654-1671.

174.   Shelton, H.; Hendricks Jr, C.; Wuerker, R., Electrostatic acceleration of microparticles to hypervelocities. *Journal of Applied Physics* **1960,** *31* (7), 1243-1246.

175.   Fuerstenau, S. D.; Benner, W. H., Molecular weight determination of megadalton DNA electrospray ions using charge detection time-of-flight mass spectrometry. *Rapid Communications in Mass Spectrometry* **1995,** *9* (15), 1528-1538.

176.   Schultz, J. C.; Hack, C. A.; Benner, W. H., Mass determination of megadalton-DNA electrospray ions using charge detection mass spectrometry. *Journal of the American Society for Mass Spectrometry* **1998,** *9* (4), 305-313.

177.   Gamero-Castaño, M., Induction charge detector with multiple sensing stages. *Review of Scientific Instruments* **2007,** *78* (4), 043301.

178.   Gamero-Castaño, M., Retarding potential and induction charge detectors in tandem for measuring the charge and mass of nanodroplets. *Review of Scientific Instruments* **2009,** *80* (5), 053301.

179.   Smith, J. W.; Siegel, E. E.; Maze, J. T.; Jarrold, M. F., Image charge detection mass spectrometry: pushing the envelope with sensitivity and accuracy. *Analytical Chemistry* **2011,** *83* (3), 950-956.

180.   Barney, B. L.; Daly, R. T.; Austin, D. E., A multi-stage image charge detector made from printed circuit boards. *Review of Scientific Instruments* **2013,** *84* (11), 114101.

181.   Benner, W. H., A gated electrostatic ion trap to repetitiously measure the charge and m/z of large electrospray ions. *Analytical Chemistry* **1997,** *69* (20), 4162-4168.

182.   Contino, N. C.; Jarrold, M. F., Charge detection mass spectrometry for single ions with a limit of detection of 30 charges. *International Journal of Mass Spectrometry* **2013,** *345*, 153-159.

183.   Elliott, A. G.; Merenbloom, S. I.; Chakrabarty, S.; Williams, E. R., Single particle analyzer of mass: a charge detection mass spectrometer with a multi-detector electrostatic ion trap. *International Journal of Mass Spectrometry* **2017,** *414*, 45-55.

184.   Harper, C. C.; Elliott, A. G.; Oltrogge, L. M.; Savage, D. F.; Williams, E. R., Multiplexed charge detection mass spectrometry for high-throughput single ion analysis of large molecules. *Analytical Chemistry* **2019,** *91* (11), 7458-7465.

185.   Kafader, J. O.; Melani, R. D.; Senko, M. W.; Makarov, A. A.; Kelleher, N. L.; Compton, P. D., Measurement of Individual Ions Sharply Increases the Resolution of Orbitrap Mass Spectra of Proteins. *Analytical Chemistry* **2019,** *91* (4), 2776-2783.

186.   Worner, T. P.; Snijder, J.; Bennett, A.; Agbandje-McKenna, M.; Makarov, A. A.; Heck, A. J. R., Resolving heterogeneous macromolecular assemblies by Orbitrap-based single-particle charge detection mass spectrometry. *Nature Methods* **2020,** *17* (4), 395-398.

187.   Kafader, J. O.; Melani, R. D.; Durbin, K. R.; Ikwuagwu, B.; Early, B. P.; Fellers, R. T.; Beu, S. C.; Zabrouskov, V.; Makarov, A. A.; Maze, J. T.; Shinholt, D. L.; Yip, P. F.; Tullman-Ercek, D.; Senko, M. W.; Compton, P. D.;

A

Kelleher, N. L., Multiplexed mass spectrometry of individual ions improves measurement of proteoforms and their complexes. *Nature Methods* **2020,** *17* (4), 391-394.

188.   Miller, L. M.; Jarrold, M. F., Charge detection mass spectrometry for the analysis of viruses and virus-like particles. *Essays in Biochemistry* **2022.**

189.   Smith, R. D.; Cheng, X.; Bruce, J. E.; Hofstadler, S. A.; Anderson, G. A., Trapping, Detection and Reaction of Very Large Single Molecular-Ions   by   Mass-Spectrometry. *Nature* **1994,** *369* (6476), 137-139.

190.   Bruce, J.; Cheng, X.; Bakhtiar, R.; Wu, Q.; Hofstadler, S.; Anderson, G.; Smith, R., Trapping, detection, and mass measurement of individual ions in a Fourier transform ion cyclotron resonance mass spectrometer. *Journal of the American Chemical Society* **1994,** *116* (17), 7839-7847.

191.   Chen, R.; Wu, Q.; Mitchell, D. W.; Hofstadler, S. A.; Rockwood, A. L.; Smith, R. D., Direct charge number and molecular weight determination of large individual ions by electrospray ionization Fourier transform ion cyclotron resonance mass spectrometry. *Analytical Chemistry* **1994,** *66* (22), 3964-3969.

192.   Chen, R.; Cheng, X.; Mitchell, D. W.; Hofstadler, S. A.; Wu, Q.; Rockwood, A. L.; Sherman, M. G.; Smith, R. D., Trapping, detection, and mass determination of coliphage T4 DNA ions by electrospray ionization Fourier transform ion cyclotron resonance mass spectrometry. *Analytical Chemistry* **1995,** *67* (7), 1159-1163.

193.   Cheng, X.; Camp, D. G.; Wu, Q.; Bakhtiar, R.; Springer, D. L.; Morris, B. J.; Bruce, J. E.; Anderson, G. A.; Edmonds, C. G.; Smith, R. D., Molecular weight determination of plasmid DNA using electrospray ionization mass spectrometry. *Nucleic Acids Research* **1996,** *24* (11), 2183-2189.

194.   Wuerker, R. F.; Shelton, H.; Langmuir, R., Electrodynamic containment of charged particles. *Journal of Applied Physics* **1959,** *30* (3), 342-349.

195.   Hars, G.; Tass, Z., Application of quadrupole ion trap for the accurate mass determination of submicron size charged particles. *Journal of Applied Physics* **1995,** *77* (9), 4245-4250.

196.   Schlemmer, S.; Illemann, J.; Wellert, S.; Gerlich, D., Nondestructive high-resolution and absolute mass determination of single charged particles in a three-dimensional quadrupole trap. *Journal of Applied Physics* **2001,** *90* (10), 5410-5418.

197.   Peng, W.-P.; Yang, Y.-C.; Kang, M.-W.; Lee, Y. T.; Chang, H.-C., Measuring masses of single bacterial whole cells with a quadrupole ion trap. *Journal of the American Chemical Society* **2004,** *126* (38), 11766-11767.

198.   Peng, W.-P.; Yang, Y.-C.; Lin, C.-W.; Chang, H.-C., Molar mass and molar mass distribution of polystyrene particle size standards. *Analytical Chemistry* **2005,** *77* (21), 7084-7089.

199.   Nie, Z.; Tzeng, Y. K.; Chang, H. C.; Chiu, C. C.; Chang, C. Y.; Chang, C. M.; Tao, M. H., Microscopy-based mass measurement of a single whole virus in a cylindrical ion trap. *Angewandte Chemie* **2006,** *118* (48), 8311-8314.

200.   Peng, W. P.; Yang, Y. C.; Kang, M. W.; Tzeng, Y. K.; Nie, Z.; Chang, H. C.; Chang, W.; Chen, C. H., Laser-induced acoustic desorption mass spectrometry of single bioparticles.   *Angewandte   Chemie International Edition* **2006,** *45* (9), 1423-1426.

201.   Burg, T. P.; Godin, M.; Knudsen, S. M.; Shen, W.; Carlson, G.; Foster, J. S.; Babcock, K.; Manalis, S. R., Weighing of biomolecules, single cells and single nanoparticles in fluid. *Nature* **2007,** *446* (7139), 1066-1069.

202.   Naik, A. K.; Hanay, M.; Hiebert, W.; Feng, X.; Roukes, M. L., Towards single-molecule   nanomechanical   mass spectrometry. *Nature Nanotechnology* **2009,** *4* (7), 445-450.

203.   Hanay, M. S.; Kelber, S.; Naik, A.; Chi, D.; Hentz, S.; Bullard, E.; Colinet, E.; Duraffourg, L.;   Roukes,   M.,   Single-protein nanomechanical mass spectrometry in real time. *Nature Nanotechnology* **2012,** *7* (9), 602-608.

204.   Sage, E.; Brenac, A.; Alava, T.; Morel, R.; Dupré, C.; Hanay, M. S.; Roukes, M. L.; Duraffourg, L.; Masselon, C.; Hentz, S., Neutral particle mass spectrometry with nanomechanical systems. *Nature Communications* **2015,** 6 (1), 1-5.

205.   Malvar, O.; Ruz, J.; Kosaka, P. M.; Domínguez, C. M.; Gil-Santos, E.; Calleja, M.; Tamayo, J., Mass and stiffness spectrometry of nanoparticles and whole intact bacteria by multimode nanomechanical resonators. *Nature Communications* **2016,** 7 (1), 13452.

206.   Sage, E.; Sansa, M.; Fostner, S.; Defoort, M.; Gély, M.; Naik, A. K.; Morel, R.; Duraffourg, L.; Roukes, M. L.; Alava, T., Single-particle mass spectrometry with arrays of frequency-addressed nanomechanical resonators. *Nature Communications* **2018,** 9 (1), 3283.

207.   Dominguez-Medina, S.; Fostner, S.; Defoort, M.; Sansa, M.; Stark, A.-K.; Halim, M. A.; Vernhes, E.; Gely, M.; Jourdan, G.; Alava, T., Neutral mass spectrometry of virus capsids above 100 megadaltons with nanomechanical resonators. *Science* **2018,** 362 (6417), 918-922.

208.   Stachiv, I.; Machů, Z.; Ševeček, O.; Tuhovcak, O.; Kotoul, M.; Jeng, Y.-R., Resolving measurement of large (~ GDa) chemical/biomolecule complexes with multimode nanomechanical resonators. *Sensors and Actuators B: Chemical* **2022,** 353, 131062.

209.   Lai, S.-H.; Reynaud, A.; Zhang, N.-N.; Kwak, M.; Vysotskyi, B.; Dominguez-Medina, S.; Fortin, T.; Clement, K.; Defoort, M.; Lee, T. G., Characterizing Nanoparticle Mass Distributions Using Charge-Independent Nanoresonator Mass Spectrometry. *The Journal of Physical Chemistry C* **2022,** 126 (49), 20946-20953.

210.   Chen, F.; Gülbakan, B.; Weidmann, S.; Fagerer, S. R.; Ibáñez, A. J.; Zenobi, R., Applying mass spectrometry to study non-covalent biomolecule complexes. *Mass Spectrometry Reviews* **2016,** 35 (1), 48-70.

211.   Fagerquist, C. K.; Sultan, O., Induction and identification of disulfide-intact and disulfide-reduced β-subunit of Shiga toxin 2 from Escherichia coli O157: H7 using MALDI-TOF-TOF-MS/MS and top-down proteomics. *Analyst* **2011,** 136 (8), 1739-1746.

212.   Sturiale, L.; Palmigiano, A.; Silipo, A.; Knirel, Y. A.; Anisimov, A. P.; Lanzetta, R.; Parrilli, M.; Molinaro, A.; Garozzo, D., Reflectron MALDI TOF and MALDI TOF/TOF mass spectrometry reveal novel structural details of native lipooligosaccharides. *Journal of Mass Spectrometry* **2011,** 46 (11), 1135-1142.

213.   Oros, D.; Ceprnja, M.; Zucko, J.; Cindric, M.; Hozic, A.; Skrlin, J.; Barisic, K.; Melvan, E.; Uroic, K.; Kos, B., Identification of pathogens from native urine samples by MALDI-TOF/TOF tandem mass spectrometry. *Clinical Proteomics* **2020,** 17 (1), 1-9.

214.   Fagerquist, C. K.; Dodd, C. E., Top-down proteomic identification of plasmid and host proteins produced by pathogenic Escherichia coli using MALDI-TOF-TOF tandem mass spectrometry. *PLOS One* **2021,** 16 (11), e0260650.

215.   Kooijman, P. C.; Mathew, A.; Ellis, S. R.; Heeren, R. M. A., Infrared Laser Desorption and Electrospray Ionisation of Non-Covalent Protein Complexes: Generation of Intact, Multiply Charged Species. *Analysis & Sensing* **2021,** 1 (1), 44-47.

216.   Hellwig, N.; Martin, J.; Morgner, N., LILBID-MS: using lasers to shed light on biomolecular architectures. *Biochemical Society Transactions* **2022,** 50 (3), 1057-1067.

217.   Addie, R. D.; Balluff, B.; Bovée, J. V.; Morreau, H.; McDonnell, L. A., Current state and future challenges of mass spectrometry imaging for clinical research. In *Analytical Chemistry*, ACS Publications: 2015.

218.   Jackson, S. N.; Woods, A. S., Imaging of noncovalent complexes by MALDI-MS. *Journal of The American Society for Mass Spectrometry* **2013,** 24 (12), 1950-1956.

219.   Griffiths, R. L.; Cooper, H. J., Direct tissue profiling of protein complexes: toward native mass spectrometry imaging. *Analytical Chemistry* **2016,** 88 (1), 606-609.

A

220. Griffiths, R. L.; Sisley, E. K.; Lopez-Clavijo, A. F.; Simmonds, A. L.; Styles, I. B.; Cooper, H. J., Native mass spectrometry imaging of intact proteins and protein complexes in thin tissue sections. *International Journal of Mass Spectrometry* **2019,** *437,* 23-29.

221. Hale, O. J.; Cooper, H. J., Native mass spectrometry imaging and in situ top-down identification of intact proteins directly from tissue. *Journal of the American Society for Mass Spectrometry* **2020,** *31* (12), 2531-2537.

222. Hale, O. J.; Cooper, H. J., Native mass spectrometry imaging of proteins and protein complexes by nano-DESI. *Analytical Chemistry* **2021,** *93* (10), 4619-4627.

223. Hale, O. J.; Hughes, J. W.; Sisley, E. K.; Cooper, H. J., Native Ambient Mass Spectrometry Enables Analysis of Intact Endogenous Protein Assemblies up to 145 kDa Directly from Tissue. *Analytical Chemistry* **2022,** *94* (14), 5608-5614.

224. Zemaitis, K. J.; Velickovic, D.; Kew, W.; Fort, K. L.; Reinhardt-Szyba, M.; Pamreddy, A.; Ding, Y. L.; Kaushik, D.; Sharma, K.; Makarov, A. A.; Zhou, M. W.; Pasa-Tolic, L., Enhanced Spatial Mapping of Histone Proteoforms in Human Kidney Through MALDI-MSI by High-Field UHMR-Orbitrap Detection. *Analytical Chemistry* **2022,** *94* (37), 12604-12613.

225. Papanastasiou, D.; Kounadis, D.; Lekkas, A.; Orfanopoulos, I.; Mpozatzidis, A.; Smyrnakis, A.; Panagiotopoulos, E.; Kosmopoulou, M.; Reinhardt-Szyba, M.; Fort, K.; Makarov, A.; Zubarev, R. A., The Omnitrap Platform: A Versatile Segmented Linear Ion Trap for Multidimensional Multiple-Stage Tandem Mass Spectrometry. *J Am Soc Mass Spectrom* **2022,** *33* (10), 1990-2007.

226. Heck, A. J., Native mass spectrometry: a bridge between interactomics and structural biology. *Nature Methods* **2008,** *5* (11), 927-33.

227. Heck, A. J.; Van Den Heuvel, R. H., Investigation of intact protein complexes by mass spectrometry. *Mass Spectrometry Reviews* **2004,** *23* (5), 368-89.

228. Sharon, M.; Robinson, C. V., The role of mass spectrometry in structure elucidation of dynamic protein complexes. *Annual Review of Biochemistry* **2007,** *76,* 167-93.

229. Yin, S.; Loo, J. A., Top-down mass spectrometry of supercharged native protein–ligand complexes. *International Journal of Mass Spectrometry* **2011,** *300* (2-3), 118-122.

230. Hanson, C. L.; Robinson, C. V., Protein-nucleic acid interactions and the expanding role of mass spectrometry. *Journal of Biological Chemistry* **2004,** *279* (24), 24907-10.

231. Tito, M. A.; Tars, K.; Valegard, K.; Hajdu, J.; Robinson, C. V., Electrospray time-of-flight mass spectrometry of the intact MS2 virus capsid. *Journal of the American Chemical Society* **2000,** *122* (14), 3550-3551.

232. Verentchikov, A. N.; Ens, W.; Standing, K. G., Reflecting time-of-flight mass spectrometer with an electrospray ion source and orthogonal extraction. *Analytical Chemistry* **1994,** *66* (1), 126-33.

233. Guilhaus, M.; Selby, D.; Mlynski, V., Orthogonal acceleration time-of-flight mass spectrometry. *Mass Spectrometry Reviews* **2000,** *19* (2), 65-107.

234. Campbell, M.; Collaboration, M., 10 years of the Medipix2 Collaboration. *Nuclear Instruments and Methods in Physics Research Section A: Accelerators, Spectrometers, Detectors and Associated Equipment* **2011,** *633,* S1-S10.

235. Esposito, M.; Jakubek, J.; Mettivier, G.; Pospisil, S.; Russo, P.; Solc, J., Energy sensitive Timepix silicon detector for electron imaging. *Nuclear Instruments and Methods in Physics Research Section A: Accelerators, Spectrometers, Detectors and Associated Equipment* **2011,** *652* (1), 458-461.

236. Wong, W.; Alozy, J.; Ballabriga, R.; Campbell, M.; Kremastiotis, I.; Llopart, X.; Poikela, T.; Sriskaran, V.; Tlustos, L.; Turecek, D., Introducing Timepix2, a frame-based pixel detector readout ASIC measuring energy deposition and arrival time. *Radiation Measurements* **2019,** 106230.

237.   Al Darwish, R.; Marcu, L.; Bezak, E., Overview of current applications of the Timepix detector in spectroscopy, radiation and medical physics. *Applied Spectroscopy Reviews* **2020,** *55* (3), 243-261.

238.   Clark, A. T.; Crooks, J. P.; Sedgwick, I.; Turchetta, R.; Lee, J. W.; John, J. J.; Wilman, E. S.; Hill, L.; Halford, E.; Slater, C. S.; Winter, B.; Yuen, W. H.; Gardiner, S. H.; Lipciuc, M. L.; Brouard, M.; Nomerotski, A.; Vallance, C., Multimass velocity-map imaging with the Pixel Imaging Mass Spectrometry (PImMS) sensor: an ultra-fast event-triggered camera for particle imaging. *The Journal of Physical Chemistry A* **2012,** *116* (45), 10897-903.

239.   Sobott, F.; Robinson, C. V., Characterising electrosprayed biomolecules using tandem-MS—the noncovalent GroEL chaperonin assembly. *International Journal of Mass Spectrometry* **2004,** *236* (1-3), 25-32.

240.   van Duijn, E.; Simmons, D. A.; van den Heuvel, R. H.; Bakkes, P. J.; van Heerikhuizen, H.; Heeren, R. M.; Robinson, C. V.; van der Vies, S. M.; Heck, A. J., Tandem mass spectrometry of intact GroEL-substrate complexes reveals substrate-specific conformational changes in the trans ring. *Journal of the American Chemical Society* **2006,** *128* (14), 4694-702.

241.   Uetrecht, C.; Watts, N. R.; Stahl, S. J.; Wingfield, P. T.; Steven, A. C.; Heck, A. J., Subunit exchange rates in Hepatitis B virus capsids are geometry- and temperature-dependent. *Physical Chemistry Chemical Physics* **2010,** *12* (41), 13368-71.

242.   Brasch, M.; de la Escosura, A.; Ma, Y.; Uetrecht, C.; Heck, A. J.; Torres, T.; Cornelissen, J. J., Encapsulation of phthalocyanine supramolecular stacks into virus-like particles. *Journal of the American Chemical Society* **2011,** *133* (18), 6878-6881.

243.   Uetrecht, C.; Barbu, I. M.; Shoemaker, G. K.; Van Duijn, E.; Heck, A. J., Interrogating viral capsid assembly with ion mobility–mass spectrometry. *Nature Chemistry* **2011,** *3* (2), 126.

244.   Snijder, J.; Uetrecht, C.; Rose, R. J.; Sanchez-Eugenia, R.; Marti, G. A.; Agirre, J.; Guerin, D. M. A.; Wuite, G. J. L.; Heck, A. J. R.; Roos, W. H., Probing the biophysical interplay between a viral genome and its capsid. *Nature Chemistry* **2013,** *5* (6), 502-509.

245.   Vykydal, Z.; Visschers, J.; Tezcan, D. S.; De Munck, K.; Borgers, T.; Ruythooren, W.; De Moor, P., The RELAXd project: Development of four-side tilable photon-counting imagers. *Nuclear Instruments and Methods in Physics Research Section A: Accelerators, Spectrometers, Detectors and Associated Equipment* **2008,** *591* (1), 241-244.

246.   van Duijn, E.; Bakkes, P. J.; Heeren, R. M.; van den Heuvel, R. H.; van Heerikhuizen, H.; van der Vies, S. M.; Heck, A. J., Monitoring macromolecular complexes involved in the chaperonin-assisted protein folding cycle by mass spectrometry. *Nature Methods* **2005,** *2* (5), 371-6.

247.   Jungmann, J. H.; Gijsbertsen, A.; Visser, J.; Visschers, J.; Heeren, R. M.; Vrakking, M. J., A new imaging method for understanding chemical dynamics: efficient slice imaging using an in-vacuum pixel detector. *Review of Scientific Instruments* **2010,** *81* (10), 103112.

248.   Akiba, K.; Artuso, M.; Badman, R.; Borgia, A.; Bates, R.; Bayer, F.; van Beuzekom, M.; Buytaert, J.; Cabruja, E.; Campbell, M.; Collins, P.; Crossley, M.; Dumps, R.; Eklund, L.; Esperante, D.; Fleta, C.; Gallas, A.; Gandelman, M.; Garofoli, J.; Gersabeck, M.; Gligorov, V. V.; Gordon, H.; Heijne, E. H. M.; Heijne, V.; Hynds, D.; John, M.; Leflat, A.; Llin, L. F.; Llopart, X.; Lozano, M.; Maneuski, D.; Michel, T.; Nicol, M.; Needham, M.; Parkes, C.; Pellegrini, G.; Plackett, R.; Poikela, T.; Rodrigues, E.; Stewart, G.; Wang, J. C.; Xing, Z., Charged particle tracking with the Timepix ASIC. *Nuclear Instruments and Methods in Physics Research B* **2012,** *661* (1), 31-49.

249.   Anton, G.; Gebert, U.; Michel, T.; Rugheimer, T. K., A hybrid photodetector using the Timepix semiconductor assembly for photoelectron detection. *Nuclear Instruments and Methods in Physics Research Section A: Accelerators, Spectrometers, Detectors and Associated Equipment* **2009,** *602* (1), 205-208.

250.   Long, J. M.; Furch, F. J.; Dura, J.; Tremsin, A. S.; Vallerga, J.; Schulz, C. P.;

A

Rouzee, A.; Vrakking, M. J. J., Ion-ion coincidence imaging at high event rate using an in-vacuum pixel detector. *The Journal of Chemical Physics* **2017**, *147* (1), 013919.

251. Rostom, A. A.; Fucini, P.; Benjamin, D. R.; Juenemann, R.; Nierhaus, K. H.; Hartl, F. U.; Dobson, C. M.; Robinson, C. V., Detection and selective dissociation of intact ribosomes in a mass spectrometer. *Proceedings of the National Academy of Sciences* **2000**, *97* (10), 5185-90.

252. Bruce, J. E.; Anderson, G. A.; Udseth, H. R.; Smith, R. D., Large Molecule Characterization Based upon Individual Ion Detection with Electrospray Ionization-FTICR Mass Spectrometry. *Analytical Chemistry* **1998**, *70* (3), 519-25.

253. Makarov, A.; Denisov, E., Dynamics of ions of intact proteins in the Orbitrap mass analyzer. *Journal of the American Society for Mass Spectrometry* **2009**, *20* (8), 1486-95.

254. Beuhler, R.; Friedman, L., Low noise, high voltage secondary emission ion detector for polyatomic ions. *International Journal of Mass Spectrometry and Ion Physics* **1977**, *23* (2), 81-97.

255. Versluis, C.; van der Staaij, A.; Stokvis, E.; Heck, A. J.; de Craene, B., Metastable ion formation and disparate charge separation in the gas-phase dissection of protein assemblies studied by orthogonal time-of-flight mass spectrometry. *Journal of the American Society for Mass Spectrometry*. **2001**, *12* (3), 329-36.

256. Brunelle, A.; Chaurand, P.; Della-Negra, S.; Le Beyec, Y.; Parilis, E., Secondary Electron Emission Yields from a CsI Surface Under Impacts of Large Molecules at Low Velocities ($5 \times 10^3 - 7 \times 10^4$ ms^{-1}). *Rapid Communications in Mass Spectrometry* **1997**, *11* (4), 353-362.

257. Liu, R.; Li, Q.; Smith, L. M., Detection of large ions in time-of-flight mass spectrometry: effects of ion mass and acceleration voltage on microchannel plate detector response. *Journal of The American Society for Mass Spectrometry*. **2014**, *25* (8), 1374-83.

258. Brouard, M.; Halford, E.; Lauer, A.; Slater, C. S.; Winter, B.; Yuen, W. H.; John, J. J.; Hill, L.; Nomerotski, A.; Clark, A.; Crooks, J.; Sedgwick, I.; Turchetta, R.; Lee, J. W.; Vallance, C.; Wilman, E., The application of the fast, multi-hit, pixel imaging mass spectrometry sensor to spatial imaging mass spectrometry. *Review of Scientific Instruments* **2012**, *83* (11), 114101.

259. Vallance, C., Multi-mass velocity-map imaging studies of photoinduced and electron-induced chemistry. *Chemical Communications* **2019**, *55* (45), 6336-6352.

260. Frojdh, E.; Campbell, M.; De Gaspari, M.; Kulis, S.; Llopart, X.; Poikela, T.; Tlustos, L., Timepix3: first measurements and characterization of a hybrid-pixel detector working in event driven mode. *Journal of Instrumentation* **2015**, *10* (01), C01039.

261. Zhao, A.; van Beuzekom, M.; Bouwens, B.; Byelov, D.; Chakaberia, I.; Cheng, C.; Maddox, E.; Nomerotski, A.; Svihra, P.; Visser, J.; Vrba, V.; Weinacht, T., Coincidence velocity map imaging using Tpx3Cam, a time stamping optical camera with 1.5 ns timing resolution. *Review of Scientific Instruments* **2017**, *88* (11), 113104.

262. Bergmann, B.; Billoud, T.; Burian, P.; Broulim, P.; Leroy, C.; Lesmes, C.; Manek, P.; Meduna, L.; Pospisil, S.; Sopczak, A.; Suk, M., Relative luminosity measurement with Timepix3 in ATLAS. *Journal of Instrumentation* **2020**, *15* (1), C01039.

263. Sanglier, S.; Leize, E.; Dorsselaer, A.; Zal, F., Comparative ESI-MS study of~ 2.2 MDa native hemocyanins from deep-sea and shore crabs: from protein oligomeric state to biotope. *Journal of the American Society for Mass Spectrometry* **2003**, *14* (5), 419-429.

264. Ilag, L. L.; Videler, H.; McKay, A. R.; Sobott, F.; Fucini, P.; Nierhaus, K. H.; Robinson, C. V., Heptameric (L12) 6/L10 rather than canonical pentameric complexes are found by tandem MS of intact ribosomes from thermophilic bacteria. *Proceedings of the National Academy of Sciences* **2005**, *102* (23), 8192-8197.

265. Geno, P.; Macfarlane, R., Secondary electron emission induced by

impact of low-velocity molecular ions on a microchannel plate. *Int J Mass Spectrom* **1989,** 92, 195-210.

266.   Meier, R.; Eberhardt, P., Velocity and ion species dependence of the gain of microchannel plates. *Int J Mass Spectrom* **1993,** *123* (1), 19-27.

267.   Westmacott, G.; Frank, M.; Labov, S.; Benner, W., Using a superconducting tunnel junction detector to measure the secondary electron emission efficiency for a microchannel plate detector bombarded by large molecular ions. *Rapid Communications in Mass Spectrometry* **2000,** *14* (19), 1854-1861.

268.   Chen, X.; Westphall, M. S.; Smith, L. M., Mass spectrometric analysis of DNA mixtures: instrumental effects responsible for decreased sensitivity with increasing mass. *Analytical Chemistry* **2003,** *75* (21), 5944-5952.

269.   Beuhler, R.; Friedman, L., Threshold studies of secondary electron emission induced by macro-ion impact on solid surfaces. *Nuclear Instruments and Methods* **1980,** *170* (1-3), 309-315.

270.   Beuhler, R. J., A comparison of secondary electron yields from accelerated water cluster ions (M/z< 50 000) striking Al2O3 and copper surfaces. *Journal of Applied Physics* **1983,** *54* (7), 4118-4126.

271.   Axelsson, J.; Parilis, E.; Reimann, C.; Sullivan, P.; Sundqvist, B., Electron emission from conducting surfaces impacted by multiply-charged polyatomic ions. *Nuclear Instruments and Methods in Physics Research Section B: Beam Interactions with Materials and Atoms* **1995,** *101* (4), 343-356.

272.   Westmacott, G.; Ens, W.; Standing, K., Secondary ion and electron yield measurements for surfaces bombarded with large molecular ions. *Nuclear Instruments and Methods in Physics Research Section B: Beam Interactions with Materials and Atoms* **1996,** *108* (3), 282-289.

273.   Ponchut, C.; Clément, J.; Rigal, J.-M.; Papillon, E.; Vallerga, J.; LaMarra, D.; Mikulec, B., Photon-counting X-ray imaging at kilohertz frame rates. *Nuclear Instruments and Methods in Physics Research Section A: Accelerators, Spectrometers, Detectors and Associated Equipment* **2007,** *576* (1), 109-112.

274.   Platkevic, M.; Cermak, P.; Jakubek, J.; Pospisil, S.; Stekl, I.; Vykydal, Z.; Zemlicka, J.; Leroy, C.; Allard, P.; Bergeron, G. In *Characterization of charge collection in various semiconductor sensors with energetic protons and Timepix device*, IEEE Nuclear Science Symposium Conference Record, IEEE: 2011; pp 4715-4719.

275.   Whyntie, T.; Harrison, M. In *Simulation and analysis of the LUCID experiment in the Low Earth Orbit radiation environment*, Journal of Physics: Conference Series, IOP Publishing: 2014; p 022038.

276.   Stoffle, N.; Pinsky, L.; Kroupa, M.; Hoang, S.; Idarraga, J.; Amberboy, C.; Rios, R.; Hauss, J.; Keller, J.; Bahadori, A., Timepix-based radiation environment monitor measurements aboard the International Space Station. *Nuclear Instruments and Methods in Physics Research Section A: Accelerators, Spectrometers, Detectors and Associated Equipment* **2015,** *782*, 143-148.

277.   Vallerga, J.; McPhate, J.; Tremsin, A.; Siegmund, O., High-resolution UV, alpha and neutron imaging with the Timepix CMOS readout. *Nuclear Instruments and Methods in Physics Research Section A: Accelerators, Spectrometers, Detectors and Associated Equipment* **2008,** *591* (1), 151-154.

278.   Tremsin, A.; Vallerga, J.; McPhate, J.; Siegmund, O., Optimization of high count rate event counting detector with Microchannel Plates and quad Timepix readout. *Nuclear Instruments and Methods in Physics Research Section A: Accelerators, Spectrometers, Detectors and Associated Equipment* **2015,** *787*, 20-25.

279.   Ballabriga, R.; Campbell, M.; Llopart, X., Asic developments for radiation imaging applications: The medipix and timepix family. *Nuclear Instruments and Methods in Physics Research Section A: Accelerators, Spectrometers, Detectors and Associated Equipment* **2018,** *878*, 10-23.

280.   Yamamura, Y.; Muraoka, K., Over-cosine angular distributions of sputtered

A

atoms at normal incidence. *Nuclear Instruments and Methods in Physics Research Section B: Beam Interactions with Materials and Atoms* **1989**, *42* (2), 175-181.

281.   Gudmundsson, J. T., Physics and technology of magnetron sputtering discharges. *Plasma Sources Science and Technology* **2020**, *29* (11), 113001.

282.   Mantus, D. S.; Morrison, G. H., Ion image detection with a microchannel plate evaluated by using a charge coupled device camera. *Analytical Chemistry* **1990**, *62* (11), 1148-1155.

283.   Michalet, X.; Siegmund, O.; Vallerga, J.; Jelinsky, P.; Millaud, J.; Weiss, S., Detectors for single-molecule fluorescence imaging and spectroscopy. *Journal of Modern Optics* **2007**, *54* (2-3), 239-281.

284.   Jungmann, J. H.; Heeren, R. M., Emerging technologies in mass spectrometry imaging. *Journal of Proteomics* **2012**, *75* (16), 5077-5092.

285.   Tremsin, A.; Vallerga, J., Unique capabilities and applications of Microchannel Plate (MCP) detectors with Medipix/Timepix readout. *Radiation Measurements* **2020**, *130*, 106228.

286.   Edgar, M. L.; Kessel, R.; Lapington, J. S.; Walton, D. M., Spatial charge cloud distribution of microchannel plates. *Review of Scientific Instruments* **1989**, *60* (12), 3673-3680.

287.   Tremsin, A.; Siegmund, O., Spatial distribution of electron cloud footprints from microchannel plates: Measurements and modeling. *Review of Scientific Instruments* **1999**, *70* (8), 3282-3288.

288.   Tremsin, A. S.; Siegmund, O. H. In *Charge cloud asymmetry in detectors with biased MCPs*, X-Ray and Gamma-Ray Instrumentation for Astronomy XII, International Society for Optics and Photonics: 2002; pp 127-138.

289.   Saito, M.; Saito, Y.; Asamura, K.; Mukai, T., Spatial charge cloud size of microchannel plates. *Review of Scientific Instruments* **2007**, *78* (2), 023302.

290.   Mathew, A.; Eijkel, G. B.; Anthony, I. G.; Ellis, S. R.; Heeren, R. M., Characterization of Microchannel Plate Detector Response for the Detection of Native Multiply Charged High Mass Single Ions in Orthogonal-Time-of-Flight Mass Spectrometry Using a Timepix Detector. *Journal of Mass Spectrometry* **2022**, *57* (4), e4820.

291.   Fisher-Levine, M.; Nomerotski, A., TimepixCam: a fast optical imager with time-stamping. *Journal of Instrumentation* **2016**, *11* (03), C03016.

292.   Nomerotski, A.; Chakaberia, I.; Fisher-Levine, M.; Janoska, Z.; Takacs, P.; Tsang, T., Characterization of TimepixCam, a fast imager for the time-stamping of optical photons. *Journal of Instrumentation* **2017**, *12* (01), C01017.

293.   Nomerotski, A., Imaging and time stamping of photons with nanosecond resolution in Timepix based optical cameras. *Nuclear Instruments and Methods in Physics Research Section A: Accelerators, Spectrometers, Detectors and Associated Equipment* **2019**, *937*, 26-30.

294.   Fisher-Levine, M.; Boll, R.; Ziaee, F.; Bomme, C.; Erk, B.; Rompotis, D.; Marchenko, T.; Nomerotski, A.; Rolles, D., Time-resolved ion imaging at free-electron lasers using TimepixCam. *Journal of Synchrotron Radiation* **2018**, *25* (2), 336-345.

295.   Cheng, C.; Vindel-Zandbergen, P.; Matsika, S.; Weinacht, T., Electron correlation in channel-resolved strong-field molecular double ionization. *Physical Review A* **2019**, *100* (5), 053405.

296.   Lam, H. V. S.; Yarlagadda, S.; Venkatachalam, A.; Wangjam, T. N.; Kushawaha, R. K.; Cheng, C.; Svihra, P.; Nomerotski, A.; Weinacht, T.; Rolles, D., Angle-dependent strong-field ionization and fragmentation of carbon dioxide measured using rotational wave packets. *Physical Review A* **2020**, *102* (4), 043119.

297.   Cheng, C.; Forbes, R.; Howard, A. J.; Spanner, M.; Bucksbaum, P. H.; Weinacht, T., Momentum-resolved above-threshold ionization of deuterated water. *Physical Review A* **2020**, *102* (5), 052813.

298.	Liu, Y.; Rozgonyi, T.; Marquetand, P.; Weinacht, T., Excited-state dynamics of CH2I2 and CH2IBr studied with UV-pump VUV-probe momentum-resolved photoion spectroscopy. *The Journal of Chemical Physics* **2020**, *153* (18), 184304.

299.	Debrah, D. A.; Stewart, G. A.; Basnayake, G.; Nomerotski, A.; Svihra, P.; Lee, S. K.; Li, W., Developing a camera-based 3D momentum imaging system capable of 1 Mhits/s. *Review of Scientific Instruments* **2020,** *91* (2), 023316.

300.	Allum, F.; Cheng, C.; Howard, A. J.; Bucksbaum, P. H.; Brouard, M.; Weinacht, T.; Forbes, R., Multi-Particle Three-Dimensional Covariance Imaging:"Coincidence" Insights into the Many-Body Fragmentation of Strong-Field Ionized D2O. *The Journal of Physical Chemistry Letters* **2021,** *12* (34), 8302-8308.

301.	Visser, J.; Van Beuzekom, M.; Boterenbrood, H.; Van Der Heijden, B.; Muñoz, J.; Kulis, S.; Munneke, B.; Schreuder, F., SPIDR: a read-out system for Medipix3 & Timepix3. *Journal of Instrumentation* **2015,** *10* (12), C12028.

302.	Winter, B.; King, S.; Brouard, M.; Vallance, C., A fast microchannel plate-scintillator detector for velocity map imaging and imaging mass spectrometry. *Review of Scientific Instruments* **2014,** *85* (2), 023306.

303.	Vidarsson, G.; Dekkers, G.; Rispens, T., IgG subclasses and allotypes: from structure to effector functions. *Frontiers in Immunology* **2014,** *5*, 520.

304.	Li, Y.; Wang, G.; Li, N.; Wang, Y.; Zhu, Q.; Chu, H.; Wu, W.; Tan, Y.; Yu, F.; Su, X.-D., Structural insights into immunoglobulin M. *Science* **2020,** *367* (6481), 1014-1017.

305.	Chen, X.; Westphall, M. S.; Smith, L. M., Mass spectrometric analysis of DNA mixtures: instrumental effects responsible for decreased sensitivity with increasing mass. *Analytical Chemistry* **2003,** *75* (21), 5944-52.

306.	Sipe, D. M.; Plath, L. D.; Aksenov, A. A.; Feldman, J. S.; Bier, M. E., Characterization of mega-dalton-sized nanoparticles by superconducting tunnel junction cryodetection mass spectrometry. *ACS Nano* **2018,** *12* (3), 2591-2602.

307.	Wood, D.; Burleigh, R. J.; Smith, N.; Bortoletto, D.; Brouard, M.; Burt, M.; Nomerotski, A.; Plackett, R.; Shipsey, I., Ion Microscope Imaging Mass Spectrometry Using a Timepix3-Based Optical Camera. *Journal of the American Society for Mass Spectrometry* **2022,** *33* (12), 2328-2332.

308.	Karas, M.; Bahr, U.; Strupat, K.; Hillenkamp, F.; Tsarbopoulos, A.; Pramanik, B. N., Matrix dependence of metastable fragmentation of glycoproteins in MALDI TOF mass spectrometry. *Analytical Chemistry* **1995,** *67* (3), 675-679.

309.	Spengler, B., Post-source decay analysis in matrix-assisted laser desorption/ionization mass spectrometry of biomolecules. *Journal of Mass Spectrometry* **1997,** *32* (10), 1019-1036.

310.	Laskin, J.; Lifshitz, C., Kinetic energy release distributions in mass spectrometry. *Journal of Mass Spectrometry* **2001,** *36* (5), 459-478.

311.	Brown, R. S.; Carr, B. L.; Lennon, J. J., Factors that influence the observed fast fragmentation of peptides in matrix-assisted laser desorption. *Journal of the American Society for Mass Spectrometry* **1996,** *7* (3), 225-232.

312.	Szilágyi, Z.; Varney, J. E.; Derrick, P. J.; Vékey, K., Dependence of matrix-assisted laser desorption/ionization post-source decay spectra on laser power. *Rapid Communications in Mass Spectrometry* **1998,** *12* (8), 489-492.

313.	Gabelica, V.; Schulz, E.; Karas, M., Internal energy build-up in matrix-assisted laser desorption/ionization. *Journal of Mass Spectrometry* **2004,** *39* (6), 579-593.

314.	Lössl, P.; van de Waterbeemd, M.; Heck, A. J., The diverse and expanding role of mass spectrometry in structural and molecular biology. *The EMBO Journal* **2016,** *35* (24), 2634-2657.

A

315.   Olsen, J. V.; de Godoy, L. M.; Li, G.; Macek, B.; Mortensen, P.; Pesch, R.; Makarov, A.; Lange, O.; Horning, S.; Mann, M., Parts per million mass accuracy on an Orbitrap mass spectrometer via lock mass injection into a C-trap. *Molecular & Cellular Proteomics* **2005,** *4* (12), 2010-2021.

316.   Shinholt, D. L.; Anthony, S. N.; Alexander, A. W.; Draper, B. E.; Jarrold, M. F., A frequency and amplitude scanned quadrupole mass filter for the analysis of high m/z ions. *Review of Scientific Instruments* **2014,** *85* (11), 113109.

317.   Zuth, C.; Vogel, A. L.; Ockenfeld, S.; Huesmann, R.; Hoffmann, T., Ultrahigh-resolution mass spectrometry in real time: atmospheric pressure chemical ionization Orbitrap mass spectrometry of atmospheric organic aerosol. *Analytical Chemistry* **2018,** *90* (15), 8816-8823.

318.   Calabrese, A. N.; Radford, S. E., Mass spectrometry-enabled structural biology of membrane proteins. *Methods* **2018,** *147*, 187-205.

319.   Benesch, J. L., Collisional activation of protein complexes: picking up the pieces. *Journal of the American Society for Mass Spectrometry* **2009,** *20* (3), 341-348.

320.   Makarov, A. A.; Heeren, R. M.; Albert, J., Method for determining the structure of a macromolecular assembly. US patent numbers US10,032,618 and US 10,373,817.

321.   Zhou, M.; Liu, W.; Shaw, J. B., Charge movement and structural changes in the gas-phase unfolding of multimeric protein complexes captured by native top-down mass spectrometry. *Analytical Chemistry* **2019,** *92* (2), 1788-1795.

322.   Mathew, A.; Keelor, J. D.; Eijkel, G. B.; Anthony, I. G. M.; Long, J.; Prangsma, J.; Heeren, R. M. A.; Ellis, S. R., Time-Resolved Imaging of High Mass Proteins and Metastable Fragments Using Matrix-Assisted Laser Desorption/Ionization, Axial Time-of-Flight Mass Spectrometry, and TPX3CAM. *Analytical Chemistry* **2023,** *95* (2), 1470-1479.

323.   Sen, R.; Hirvonen, L. M.; Zhdanov, A.; Svihra, P.; Andersson-Engels, S.; Nomerotski, A.; Papkovsky, D., New luminescence lifetime macro-imager based on a Tpx3Cam optical camera. *Biomedical Optics Express* **2020,** *11* (1), 77-88.

324.   Aglagul, D.; Kaufman, B.; Cheng, C.; Weinacht, T.; Saule, T.; Trallero-Herrero, C. A.; Nomerotski, A., A simple approach for characterizing the spatially varying sensitivity of microchannel plate detectors. *Review of Scientific Instruments* **2022,** *93* (7), 075108.

325.   Cheng, C.; Moğol, G.; Weinacht, T.; Nomerotski, A.; Trallero-Herrero, C., 3D velocity map imaging of electrons with TPX3CAM. *Review of Scientific Instruments* **2022,** *93* (1), 013003.

326.   O'Brien, J. P.; Needham, B. D.; Henderson, J. C.; Nowicki, E. M.; Trent, M. S.; Brodbelt, J. S., 193 nm ultraviolet photodissociation mass spectrometry for the structural elucidation of lipid A compounds in complex mixtures. *Analytical Chemistry* **2014,** *86* (4), 2138-2145.

327.   Fort, K. L.; Dyachenko, A.; Potel, C. M.; Corradini, E.; Marino, F.; Barendregt, A.; Makarov, A. A.; Scheltema, R. A.; Heck, A. J., Implementation of ultraviolet photodissociation on a benchtop Q exactive mass spectrometer and its application to phosphoproteomics. *Analytical Chemistry* **2016,** *88* (4), 2303-2310.

328.   Cleland, T. P.; DeHart, C. J.; Fellers, R. T.; VanNispen, A. J.; Greer, J. B.; LeDuc, R. D.; Parker, W. R.; Thomas, P. M.; Kelleher, N. L.; Brodbelt, J. S., High-throughput analysis of intact human proteins using UVPD and HCD on an orbitrap mass spectrometer. *Journal of Proteome Research* **2017,** *16* (5), 2072-2079.

329.   Brodie, N. I.; Huguet, R.; Zhang, T.; Viner, R.; Zabrouskov, V.; Pan, J.; Petrotchenko, E. V.; Borchers, C. H., Top-down hydrogen–deuterium exchange analysis of protein structures using ultraviolet photodissociation. *Analytical Chemistry* **2018,** *90* (5), 3079-3082.

330.   Kelly, R. T.; Tolmachev, A. V.; Page, J. S.; Tang, K.; Smith, R. D., The ion funnel: theory, implementations, and applications.

Mass Spectrometry Reviews **2010**, *29* (2), 294-312.

331.   Leiminger, M.; Feil, S.; Mutschlechner, P.; Ylisirniö, A.; Gunsch, D.; Fischer, L.; Jordan, A.; Schobesberger, S.; Hansel, A.; Steiner, G., Characterisation of the transfer of cluster ions through an atmospheric pressure interface time-of-flight mass spectrometer with hexapole ion guides. *Atmospheric Measurement Techniques* **2019**, *12* (10), 5231-5246.

332.   Alberts, B., The cell as a collection of protein machines: preparing the next generation of molecular biologists. *Cell* **1998**, *92* (3), 291-294.

333.   Smith, L. M.; Agar, J. N.; Chamot-Rooke, J.; Danis, P. O.; Ge, Y.; Loo, J. A.; Paša-Tolić, L.; Tsybin, Y. O.; Kelleher, N. L.; Proteomics, C. f. T.-D., The human proteoform project: defining the human proteome. *Science Advances* **2021**, *7* (46), eabk0734.

334.   Van Berkel, W. J.; Van Den Heuvel, R. H.; Versluis, C.; Heck, A. J., Detection of intact megaDalton protein assemblies of vanillyl-alcohol oxidase by mass spectrometry. *Protein Science* **2000**, *9* (3), 435-439.

335.   Allison, T. M.; Reading, E.; Liko, I.; Baldwin, A. J.; Laganowsky, A.; Robinson, C. V., Quantifying the stabilizing effects of protein–ligand interactions in the gas phase. *Nature communications* **2015**, *6* (1), 1-10.

336.   Ma, X.; Lai, L. B.; Lai, S. M.; Tanimoto, A.; Foster, M. P.; Wysocki, V. H.; Gopalan, V., Uncovering the stoichiometry of Pyrococcus furiosus RNase P, a multi-subunit catalytic ribonucleoprotein complex, by surface-induced dissociation and ion mobility mass spectrometry. *Angewandte Chemie International Edition* **2014**, *53* (43), 11483-11487.

337.   Harvey, S. R.; Seffernick, J. T.; Quintyn, R. S.; Song, Y.; Ju, Y.; Yan, J.; Sahasrabuddhe, A. N.; Norris, A.; Zhou, M.; Behrman, E. J., Relative interfacial cleavage energetics of protein complexes revealed by surface collisions. *Proceedings of the National Academy of Sciences* **2019**, *116* (17), 8143-8148.

338.   Heck, A. J.; Chandler, D. W., Imaging techniques for the study of chemical reaction dynamics. *Annual Review of Physical Chemistry* **1995**, *46* (1), 335-372.

339.   Jungmann, J.; Gijsbertsen, A.; Visser, J.; Visschers, J.; Heeren, R.; Vrakking, M., A new imaging method for understanding chemical dynamics: Efficient slice imaging using an in-vacuum pixel detector. *Review of Scientific Instruments* **2010**, *81* (10), 103112.

340.   Suits, A. G., Invited review article: photofragment imaging. *Review of Scientific Instruments* **2018**, *89* (11), 111101.

341.   Mathew, A.; Giskes, F.; Lekkas, A.; Greisch, J. F.; Eijkel, G. B.; Anthony, I. G. M.; Fort, K.; Heck, A. J. R.; Papanastasiou, D.; Makarov, A. A.; Ellis, S. R.; Heeren, R. M. A., An Orbitrap/Time-of-Flight Mass Spectrometer for Photofragment Ion Imaging and High-Resolution Mass Analysis of Native Macromolecular Assemblies. *Journal of the American Society for Mass Spectrometry* **2023**, *34* (7), 1359-1371.

342.   Dodds, E. D.; Hagerman, P. J.; Lebrilla, C. B., Fragmentation of singly protonated peptides via a combination of infrared and collisional activation. *Analytical Chemistry* **2006**, *78* (24), 8506-8511.

343.   Mistarz, U. H.; Bellina, B.; Jensen, P. F.; Brown, J. M.; Barran, P. E.; Rand, K. D., UV photodissociation mass spectrometry accurately localize sites of backbone deuteration in peptides. *Analytical Chemistry* **2018**, *90* (2), 1077-1080.

344.   R. Julian, R., The mechanism behind top-down UVPD experiments: making sense of apparent contradictions. *Journal of The American Society for Mass Spectrometry* **2017**, *28* (9), 1823-1826.

345.   Susa, A. C.; Xia, Z.; Williams, E. R., Native mass spectrometry from common buffers with salts that mimic the extracellular environment. *Angewandte Chemie International Edition* **2017**, *56* (27), 7912-7915.

346.   Ventouri, I. K.; Malheiro, D. B.; Voeten, R. L.; Kok, S.; Honing, M.; Somsen, G. W.; Haselberg, R., Probing protein denaturation during size-exclusion

A

chromatography using native mass spectrometry. *Analytical Chemistry* **2020,** *92* (6), 4292-4300.

347.   van Dongen, W. D.; Heck, A. J., Binding of selected carbohydrates to apo-concanavalin A studied by electrospray ionization mass spectrometry. *Analyst* **2000,** *125* (4), 583-589.

348.   Zhou, M.; Dagan, S.; Wysocki, V. H., Impact of charge state on gas-phase behaviors of noncovalent protein complexes in collision induced dissociation and surface induced dissociation. *Analyst* **2013,** *138* (5), 1353-1362.

349.   Lermyte, F.; Williams, J. P.; Brown, J. M.; Martin, E. M.; Sobott, F., Extensive charge reduction and dissociation of intact protein complexes following electron transfer on a quadrupole-ion mobility-time-of-flight MS. *Journal of the American Society for Mass Spectrometry* **2015,** *26* (7), 1068-1076.

350.   Rathore, D.; Dodds, E. D., Collision-induced release, ion mobility separation, and amino acid sequence analysis of subunits from mass-selected noncovalent protein complexes. *Journal of The American Society for Mass Spectrometry* **2014,** *25* (9), 1600-1609.

351.   Hardman, K. D.; Ainsworth, C. F., Structure of concanavalin A at 2.4-Ang resolution. *Biochemistry* **1972,** *11* (26), 4910-4919.

352.   Alves, S.; Fournier, F.; Afonso, C.; Wind, F.; Tabet, J.-C., Gas-phase ionization/desolvation processes and their effect on protein charge state distribution under matrix-assisted laser desorption/ionization conditions. *European Journal of Mass Spectrometry* **2006,** *12* (6), 369-383.

353.   Schulz, E.; Karas, M.; Rosu, F.; Gabelica, V., Influence of the matrix on analyte fragmentation in atmospheric pressure MALDI. *Journal of the American Society for Mass Spectrometry* **2006,** *17* (7), 1005-1013.

354.   Selman, M. H.; Hoffmann, M.; Zauner, G.; McDonnell, L. A.; Balog, C. I.; Rapp, E.; Deelder, A. M.; Wuhrer, M., MALDI-TOF-MS analysis of sialylated glycans and glycopeptides using 4-chloro-α-cyanocinnamic acid matrix. *Proteomics* **2012,** *12* (9), 1337-1348.

355.   Indelicato, S.; Bongiorno, D.; Indelicato, S.; Drahos, L.; Turco Liveri, V.; Turiák, L.; Vékey, K.; Ceraulo, L., Degrees of freedom effect on fragmentation in tandem mass spectrometry of singly charged supramolecular aggregates of sodium sulfonates. *Journal of Mass Spectrometry* **2013,** *48* (3), 379-383.

356.   Quintyn, R. S.; Yan, J.; Wysocki, V. H., Surface-induced dissociation of homotetramers with D2 symmetry yields their assembly pathways and characterizes the effect of ligand binding. *Chemistry & Biology* **2015,** *22* (5), 583-592.

357.   van Schayck, J. P.; van Genderen, E.; Maddox, E.; Roussel, L.; Boulanger, H.; Fröjdh, E.; Abrahams, J.-P.; Peters, P. J.; Ravelli, R. B., Sub-pixel electron detection using a convolutional neural network. *Ultramicroscopy* **2020,** *218*, 113091.

358.   van Schayck, J. P.; Zhang, Y.; Knoops, K.; Peters, P. J.; Ravelli, R. B., Integration of an event-driven timepix3 hybrid pixel detector into a cryo-em workflow. *Microscopy and Microanalysis* **2023,** *29* (1), 352-363.

359.   Huang, J. J.; Weinstock, D.; Hirsh, H.; Bouck, R.; Zhang, M.; Gorobtsov, O. Y.; Okamura, M.; Harder, R.; Cha, W.; Ruff, J. P., Disorder dynamics in battery nanoparticles during phase transitions revealed by operando single-particle diffraction. *Advanced Energy Materials* **2022,** *12* (12), 2103521.

360.   Aoyagi, S.; Aoyagi, A.; Takeda, H.; Osawa, H.; Sumitani, K.; Imai, Y.; Kimura, S., Position and electric field dependent local lattice strain detected by nanobeam x-ray diffraction on a relaxor ferroelectric single crystal. *Physical Review B* **2022,** *105* (2), 024101.

361.   Ling, Y.; Sun, T.; Guo, L.; Si, X.; Jiang, Y.; Zhang, Q.; Chen, Z.; Terasaki, O.; Ma, Y., Atomic-level structural responsiveness to environmental conditions from 3D electron

diffraction. *Nature Communications* **2022**, *13* (1), 6625.

362. Kang, C.; Yang, K.; Zhang, Z.; Usadi, A. K.; Calabro, D. C.; Baugh, L. S.; Wang, Y.; Jiang, J.; Zou, X.; Huang, Z., Growing single crystals of two-dimensional covalent organic frameworks enabled by intermediate tracing study. *Nature Communications* **2022**, *13* (1), 1370.

363. Cheng, C.; Singh, V.; Matsika, S.; Weinacht, T., Strong Field Double Ionization of Formaldehyde Investigated Using Momentum Resolved Covariance Imaging and Trajectory Surface Hopping. *The Journal of Physical Chemistry A* **2022**, *126* (40), 7399-7406.

364. Nomerotski, A.; Chekhlov, M.; Dolzhenko, D.; Glazenborg, R.; Farella, B.; Keach, M.; Mahon, R.; Orlov, D.; Svihra, P., Intensified Tpx3Cam, a fast data-driven optical camera with nanosecond timing resolution for single photon detection in quantum applications. *Journal of Instrumentation* **2023**, *18* (01), C01023.

365. Vidyapin, V.; Zhang, Y.; England, D.; Sussman, B., Characterisation of a single photon event camera for quantum imaging. *Scientific Reports* **2023**, *13* (1), 1009.

366. Davino, M.; McManus, E.; Helming, N. G.; Cheng, C.; Moğol, G.; Rodnova, Z.; Harrison, G.; Watson, K.; Weinacht, T.; Gibson, G. N., A plano–convex thick-lens velocity map imaging apparatus for direct, high resolution 3D momentum measurements of photoelectrons with ion time-of-flight coincidence. *Review of Scientific Instruments* **2023**, *94* (1), 013303.

367. Jannis, D.; Hofer, C.; Gao, C.; Xie, X.; Béché, A.; Pennycook, T. J.; Verbeeck, J., Event driven 4D STEM acquisition with a Timepix3 detector: Microsecond dwell time and faster scans for high precision and low dose applications. *Ultramicroscopy* **2022**, *233*, 113423.

A

LIST OF PUBLICATIONS

This thesis is based on the following publications

1. **Mathew, A.**; Buijs, R.; Eijkel, G. B.; Giskes, F.; Dyachenko, A.; van der Horst, J.; Byelov, D.; Spaanderman, D. J.; Heck, A. J. R.; Porta Siegel, T.; Ellis, S. R.; Heeren, R. M. A., Ion Imaging of Native Protein Complexes Using Orthogonal Time-of-Flight Mass Spectrometry and a Timepix Detector. *Journal of the American Society for Mass Spectrometry* **2021**, *32* (2), 569-580.

2. **Mathew, A.**; Eijkel, G. B.; Anthony, I. G. M.; Ellis, S. R.; Heeren, R. M. A., Characterization of Microchannel Plate Detector Response for the Detection of Native Multiply Charged High Mass Single Ions in Orthogonal Time-of-Flight Mass Spectrometry Using a Timepix Detector. *Journal of Mass Spectrometry* **2022**, *57* (4), e4820.

3. **Mathew, A.**; Keelor, J. D.; Eijkel, G. B.; Anthony, I. G. M; Long, J.; Prangsma, J.; Heeren, R. M. A; Ellis, S. R., Time-Resolved Imaging of High Mass Proteins and Metastable Fragments Using Matrix-Assisted Laser Desorption/Ionization, Axial Time-of-Flight Mass Spectrometry, and TPX3CAM, *Analytical Chemistry* **2023**, *95* (2), 1470-1479.

4. **Mathew, A.**; Giskes, F.; Lekkas, A.; Greisch, J. -F.; Eijkel, G. B.; Anthony, I. G. M.; Fort, K. L.; Heck, A. J. R.; Papanastasiou, D.; Makarov, A. A.; Ellis, S. R.; Heeren, R. M. A., An Orbitrap/Time-of-Flight Mass Spectrometer for Photofragment Ion Imaging and High-Resolution Mass Analysis of Native Macromolecular Assemblies. *Journal of the American Society for Mass Spectrometry* **2023**, 34 (7), 1359-1371.

5. **Mathew, A.**; Giskes, F.; Eijkel, G. B.; Anthony, I. G. M; Papanastasiou, D.; Heck, A. J. R.; Makarov, A. A.; Ellis, S. R.; Heeren, R. M. A., Towards Geometric Structural Elucidation of Macromolecular Assemblies Using Single Ion Imaging Mass Spectrometry and Ultraviolet Photodissociation. Manuscript in preparation.

Other publications

1. Kooijman, P. C.; **Mathew, A.**; Ellis, S. R.; Heeren, R. M. A., Infrared Laser Desorption and Electrospray Ionization of Non-Covalent Protein Complexes: Generation of Intact, Multiply Charged Species. *Analysis & Sensing* **2021**, *1* (1), 44-47.

2. Gijsbers, A.; Vinciauskaite, V.; Siroy, A.; Gao, Y.; Tria, G.; **Mathew, A.**; Sanchez-Puig, N.; Lopez-Iglesias, C.; Peters, P. J.; Ravelli, R. B. G., Priming

Mycobacterial ESX-Secreted Protein B to Form a Channel-Like Structure. *Current Research in Structural Biology* **2021,** *3*, 153-164.

3. Flynn, C.; Wilhelm, A.; Schneider, E.; Rößler, J.; Leuthner, M.; Tosheska , S.; Knoops, K.; **Mathew, A.;** King, S.; Reisbeck, M.; Haydn, O.; Grill, S.; Zeidler, R.; Hammerschmidt, W.; Lopez-Iglesias, C.; Heeren, R. M. A.; Kiechle, M.; Wilhelm, O.; Knolle, P. A.; Höchst, B., Detection of HER2-Positive Extracellular Vesicles in Plasma from Breast Cancer Patients Using Flow-Cytometry, **2023***, Manuscript submitted.

4. Hadavi, D.; Ng, C. Y.; Zhao, Y.; **Mathew, A.;** Anthony, I. G. M.; Cuypers, E.; Porta Siegel, T.; Honing, M., Buffer 4-Ethylmorpholine/acetate Maintains Solution-Phase Folding for Native Mass Spectrometry of Proteins and Proteins Complexes, Manuscript submitted.

5. Schneider, E.; Flynn, C.; Rößler, J.; Baumann, T.; Rothfuß, C.; Erber, J.; Fricke, L.; Campbell, B.; Feuerherd, M.; Knoops, K.; **Mathew, A.;** Tan, S.; Pichlmair, A.; Protzer, U.; Brisson, A.R.; Moretti, A.; Heeren, R. M. A.; Hammerschmidt, W.; Zeidler, R.; Wilhelm, O.; Knolle, P. A.; Höchst, B., Progress Prediction of Covid-19 by Multiparametric Analysis of Extracellular Vesicle by Flow Cytometry, Manuscript in preparation.

Contributions to conferences and scientific meetings

Oral presentations

1. **Mathew, A.;** Eijkel, G. B.; Giskes, F.; van der Horst, J.; Langridge, D.; Barendregt, A.; Heck, A. J. R.; Porta Siegel, T.; Ellis, S. R.; Heeren, R. M. A., Ion Imaging of Native Protein Complexes Using Time-of-Flight Mass Spectrometry and a Timepix Detector, *Physics@veldhoven* **2021**.

2. **Mathew, A.;** Giskes, F.; Eijkel, G. B.; Lekkas, A.; Kounadis, D.; Orfanopoulos, J.; Fort, K. L.; Keelor, J. D.; Long, J.; Prangsma, J.; Heck, A. J. R.; Papanastasiou, D.; Makarov, A. A.; Ellis, S. R.; Heeren, R. M. A., Single Ion Imaging of Biomacromolecules in Mass Spectrometry Using Timepix Detector, *International Workshop on Radiation Imaging Detectors (iWoRiD*) **2021**.

3. **Mathew, A.;** Giskes, F.; Greisch, J. -F.; Eijkel, G. B.; Lekkas, A.; Kounadis, D.; Orfanopoulos, J.; Fort, K. L.; Keelor, J. D.; Prangsma, J.; Heck, A. J. R.; Papanastasiou, D.; Makarov, A. A.; Ellis, S. R.; Heeren, R. M. A., Structural Analysis of Biomacromolecules in Mass Spectrometry Using Timepix Detector and UV Photodissociation, *NWO CHAINS* **2021**.

A

4. **Mathew, A.;** Giskes, F.; Greisch, J. -F.; Eijkel, G. B.; Anthony, I. G. M; Lekkas, A.; Fort, K. L.; Prangsma, J.; Papanastasiou, D.; Heck, A. J. R.; Makarov, A. A.; Ellis, S. R.; Heeren, R. M. A., Mass-Resolved Imaging and Structural Analysis of Biomacromolecules in Mass Spectrometry Using Timepix Detector and UV Photodissociation, *Physics@veldhoven* **2022**.

5. **Mathew, A.;** Giskes, F.; Greisch, J. -F.; Eijkel, G. B.; Anthony, I. G. M; Lekkas, A.; Fort, K. L.; Prangsma, J.; Papanastasiou, D.; Heck, A. J. R.; Makarov, A. A.; Ellis, S. R.; Heeren, R. M. A., Structural Analysis of Biomacromolecular assemblies in Mass Spectrometry Using Timepix Detector and UV Photodissociation, *Dutch Society for Mass Spectrometry (NVMS) Meeting* **2022**.

6. **Mathew, A.;** Giskes, F.; Greisch, J. -F.; Eijkel, G. B.; Anthony, I. G. M; Lekkas, A.; Fort, K. L.; Prangsma, J.; Papanastasiou, D.; Heck, A. J. R.; Makarov, A. A.; Ellis, S. R.; Heeren, R. M. A., Pixelated Detectors for the Molecular Structural Analysis and Photofragment Ion Imaging of Biomacromolecular Assemblies, *Medipix Consortium Meeting* **2022**.

7. **Mathew, A.;** Giskes, F.; Lekkas, A.; Greisch, J. -F.; Eijkel, G. B.; Anthony, I. G. M; Fort, K. L.; Prangsma, J.; Papanastasiou, D.; Heck, A. J. R.; Makarov, A. A.; Ellis, S. R.; Heeren, R. M. A., Single Ion Fragment Imaging and Molecular Structural Analysis of Biomacromolecules in Mass Spectrometry Using Timepix Detector and UV Photodissociation, *International Mass Spectrometry Conference* (IMSC) **2022**.

Poster presentations

1. **Mathew, A.**; Porta Siegel, T.; Eijkel, G. B.; Giskes, F.; Heck, A. J. R.; Heeren, R. M. A.; Ellis, S. R., Mass-Resolved Imaging of Proteins and Protein Complexes Using Orthogonal Time-of-Flight Combined with a Timepix Detector, *M4i Workshop on Mass Spectrometry Imaging* **2018**.

2. Gijsbers, A.; **Mathew, A.;** Siroy, A.; Ellis, S. R.; Ravelli, R. B. G.; Heeren, R. M. A.; Peters, P. J., Oligomerization of the Mycobacterium Tuberculosis ESX-1 Secreted Protein B (EspB), *NVK Structural Biology Symposium* **2019.**

3. **Mathew, A.**; Porta Siegel, T.; Eijkel, G. B.; Giskes, F.; Heck, A. J. R.; Heeren, R. M. A.; Ellis, S. R., Spatially Resolved Detection of Proteins and Protein Complexes Using Orthogonal Time-of-Flight Combined with a Timepix Detector, *Mass Spectrometry School in Biotechnology and Medicine (MSBM)* **2019**.

4. **Mathew, A.;** Eijkel, G. B.; Giskes, F.; Heck, A. J. R.; Porta Siegel, T.; Heeren, R. M. A.; Ellis, S. R., Mass-Resolved Imaging of Biomacromolecular

Assemblies Using Orthogonal Time-of-Flight Combined with a Timepix Detector, *MERLN Ph.D. Symposium* **2019.**

5. **Mathew, A.;** Porta Siegel, T.; Eijkel, G. B.; Keelor, J. D.; Giskes, F.; Heck, A. J. R.; Heeren, R. M. A.; Ellis, S. R., Imaging Macromolecules in Mass Spectrometers Using Timepix Detector Technology, *Physics@veldhoven* **2020**.

6. **Mathew, A.;** Eijkel, G. B.; Giskes, F.; Keelor, J. D.; Anthony, I. G. M; Long, J.; Lekkas, A.; Fort, K. L.; Prangsma, J.; Papanastasiou, D.; Heck, A. J. R.; Makarov, A. A.; Ellis, S. R.; Heeren, R. M. A., A Method for the Structural Analysis and Mass Resolved Imaging of Biomacromolecular Assemblies in Mass Spectrometry Using Timepix Detector, *American Society for Mass Spectrometry (ASMS) Conference* **2021**.

A

LIST OF ABBREVIATIONS

ADC	Analog-to-digital converter
AI-ETD	Activated ion ETD (IRMPD followed by ETD)
AP MS	Affinity purification mass spectrometry
ASIC	Application-specific integrated circuit
ATP	Adenosine triphosphate
BSA	Bovine serum albumin
BSHV	Bakeable safe high-voltage
C	Correction lens/Einzel lens
CCD	Charge coupled device
CCS	Collision cross-section
CDMS	Charge detection mass spectrometry
CHCA	a-cyano-4-hydroxycinnamic acid
CID	Collision-induced dissociation
CMOS	Complementary metal oxide semiconductor
cpp	Counts per pixel
Cryo-EM	Cryogenic-electron microscopy
D	Dimer
DC	Direct current
DESI	Desorption electrospray ionization
DHA	2',6'-dihydroxyacetophenone
DHB	2, 5-dihydroxybenzoic acid
DLD	Delay-line detector
DNA	Deoxyribonucleic acid
DOF	Degrees of freedom
ECD	Electron capture dissociation
EDTA	Ethylenediaminetetraacetic acid
EID	Electron induced dissociation
EL	Einzel lens/correction lens
EM	Electron multiplier
EmI	Electron meta-ionization
EMR	Extended mass range
ERMS	Energy-resolved mass spectrometry
ESI	Electrospray ionization
ETD	Electron transfer dissociation
EThCD	ETD supplemented with HCD

FT-ICR	Fourier transform-ion cyclotron resonance
GUI	Graphical user interface.
H	Hydrogen/hexamer/hexapole
HB	Hydrogen bond
H/D	Hydrogen/deuterium
HAA	Hydrogen atom attachment
HAPS	Hybrid active pixel detector
HC	Heavy chain
HCD	Higher-energy collisional dissociation
HDX-MS	Hydrogen-deuterium exchange mass spectrometry
HM	High mass
HRF MS	Hydroxyl radical footprinting mass spectrometry
HV	High voltage
IA	Interface area
IAD	Ion activated dissociation
ICD	Inductive charge detector
IgA	Immunoglobulin A
IgG	Immunoglobulin G
IgM	Immunoglobulin M
IM-MS	Ion mobility mass spectrometry
IR	Infrared
ITO	Indium tin oxide
KE	Kinetic energy
L	Lens
LAESI	Laser ablation electrospray ionization
LC	Liquid chromatography/ Light chain
LESA	Liquid extraction surface analysis
LILBID	Laser-induced liquid bead ion desorption
LQ-trap	Linear quadrupole trap
M	Monomer
m/z	Mass-to-charge
MALDI	Matrix-assisted laser desorption/ionization
MCP	Microchannel plate
MMA	Macromolecular assembly
MPC	Multiproteoform complex
MPX	Medipix
MS	Mass spectrometry/spectrometer

MS/MS	Tandem mass spectrometry
MW	Molecular weight
MWCO	Molecular weight cutoff
NCE	Normalized collision energy
NEMS	Nanoelectromechanical systems
nESI	Nano-electrospray ionization
NMR	Nuclear magnetic resonance
nMS	Native mass spectrometry
O-TOF	Orthogonal time-of-flight
P	Phosphor screen/pentamer
PA	Proton affinity
PD	Photodissociation
PFI	Photofragment ion imaging
PIE	Pulsed ion extraction
PImMS	Pixel imaging mass spectrometry
PSD	Post-source decay
Q	Quadrupole/Quadrupole trap/Tetramer
QE	Quantum efficiency
QIT	Quadrupole ion trap
q-TOF	Quadrupole time-of-flight
ReLAXD	High-resolution large-area X-ray detector
RF	Radiofrequency
RMS	Root mean square
RNA	Ribonucleic acid
R-TOF	Reflectron time-of-flight
S/N	Signal-to-noise
SA	Sinapinic acid
SB	Salt bridge
SEM	Secondary electron multiplier
Si	Silicon
SID	Surface-induced dissociation
SIMS	Secondary ion mass spectrometry
SPIDR	Speedy pixel detector readout
SSLD	superconducting stripline detector
STJ	Superconducting tunnel junction
T	Trimer
TDC	Time-to-digital converter

TEM	Transmission electron microscopy
TFA	Trifluoroacetic acid
TOA	Time-of-arrival
TOF	Time-of-flight
TOT	Time-over-threshold
TPX	Timepix
TPX3	Timepix3
TPX3CAM	Timepix3 based camera
TTL	Transistor-transistor logic
UHMR	Ultra-high mass range
UV	Ultraviolet
UVPD	Ultraviolet photodissociation
XL-MS	Chemical cross-linking mass spectrometry
XSA	Cross-strip anode

A

ACKNOWLEDGEMENTS

Embarking on a Ph.D. journey is a profound, long-term commitment, demanding ample patience, unwavering motivation, and steadfast hope. I consider myself incredibly fortunate as I was surrounded by the perfect combination of people, in the right place, and at just the right time during this journey. The importance of a supportive supervisory team cannot be overstated; dear **Ron** and **Shane**, you both have played a pivotal role in shaping the researcher and the person I am today, and I cannot thank you enough for your guidance and support throughout this entire process. Selecting someone like me, with a vastly different background, for such a challenging project alongside a team of MS instrumentation experts that any budding researcher could only dream of, requires immense courage. The initial months in a foreign country, amidst an international, interdisciplinary group, learning and applying new things every day, was quite challenging for me. Yet, you both showed incredible patience and encouragement, celebrating each small step I took forward. You made the transition smooth and comfortable. You have been an invaluable source of support and a calming presence during our discussions with collaborators and at conferences. Both of you set a wonderful example not only as accomplished scientists but also as great human beings. I have been deeply inspired by how you value your families and manage to strike a perfect balance between your personal and work lives – something I am still learning. **Shane**, when you had to move back to Australia in my second year, it was tough for me. Nevertheless, the strong foundation you laid in the early stages of the project was very crucial in bringing the project to its current position. Even after you moved back, you remained actively involved and fulfilled your role as co-promoter. I would like to see your departure as something that mold me as independence researcher at very early stage of my career. **Ron**, you seamlessly took over my daily supervision from that point onwards. When I asked for bimonthly meetings, you willingly held weekly meetings with me, always making time amidst your busy schedule. You are my go-to person for both research-related matters and personal concerns. The enthusiasm of both of you for our project and the way you presented me to others have been instrumental in building my career and expanding my network. Sure, we had a few disagreements, especially during the writing process and final stages of the Ph.D., but looking back, those moments were overshadowed by the incredible journey we had together. Thank you for everything!

Dear **Frans** and **Gert**, I truly could not have done my PhD without both of you. There were times when I thought of even moving to your office, considering the countless hours I spent in your office. When you moved to L5, it was a relief as it saved a considerable amount of my energy spend by commuting between floors. **Frans**, your years of experience in vacuum systems and exceptional talent in mechanical coupling played a crucial role in making our complex integrated instrument systems work seamlessly. I would bring you some vague ideas, and you would work your magic, turning them into incredible mechanical assemblies. Your skills are truly unique, and I cannot help but feel a bit worried about finding someone with your expertise when I move to a different place and continue in the field of analytical instrumentation. **Gert**, just a four letter Dutch name, which I still struggle to pronounce correctly. Your proficiency in TPX data processing has

been unmatched. From the early days of the Medipix collaboration at AMOLF, through the different generations of MPX/TPX detector ASICs and various data acquisition software, you have always adapted quickly and efficiently. Each time I came to you with more complex tasks, your enthusiasm grew, leading to endless fascinating conversations. You happily work on it and ensure they were done right, which is truly awe-inspiring. I must admit, though, that I hold you responsible for not letting me explore my programming skills after my Masters, as you always took care of everything on that side.

Dear **Ronny**, you have been my go-to person for anything related to proteomics, even after me spending so many years in structural proteomics. When I first started, I had almost zero knowledge about most of the facilities in our lab, but you were patient and kind enough to explain everything to me. Your help during the setting up of native MS in Orbitrap UHMR, for protein purification, accompanying me to visit to Hecklab at Utrecht during the advanced MS course were invaluable. I still remember how others in the advanced MS course identified me as the one who came with the "smart guy" :) Dear **Annemarie**, thanks you for taking care of all my orders and all the help in both the IMS and Surgery labs. No matter how strange and difficult the ordering was with some vendors, you always managed to find a way to get what I wanted and kept me informed throughout the process.

Dear **IDEE members**, you have been my go-to people whenever I encounter a technical problem or could not find something in Frans's storage space. I have approached most of you at least once, and you have consistently been helpful, no matter how last minute or complex the situation was. Your technical support has been invaluable, especially given the nature of the project. I want to mention a few names specifically: **Pascal**, **Simon**, **Caro**, **Maurice Huinck**, **Mark**, **Paul Dizij**, **Lou**, **Etienne**, and **Paul Laeven** - thank you all for your constant support.

Dear **Roel Spätjens** and **Denis**, thank you for graciously allowing me to use the micropipette puller and oven in your departments over the years. Your generosity has saved me a lot of money on nESI needles. Dear **Cristina and Patrick**, your help in optimizing the settings of the puller in the first year of my Ph.D. has been invaluable.

Dear **Ian**, I wanted to express my sincere appreciation for all the help and support you have provided since joining our group in 2019, especially considering Shane's absence. We have had fascinating discussions about my projects, particularly on TPX3 data. You never hesitate to step in whenever you sense that I need assistance, and your help has been crucial in various aspects, whether it is TPX3 data processing, troubleshooting experimental setups, laser alignment, or reviewing my articles and thesis chapters. Your passion for teaching and talent for delivering exceptional presentations are also truly inspiring. Dear **Tiff**, thank you for your help in bringing the LCT to running condition after many years of non-operation. The data files from your previous measurements and notes played a crucial role in making the entire setting up process so much easier and smoother. Looking at the resulting publication now, I can confidently say that all the effort was entirely worth it. Dear **Joel**, I can't thank you enough for making the process of setting up the new MCP-P47-TPX3CAM much less painful than I anticipated. Your dedication and involvement in everything from the design to

A

implementation and obtaining the first set of data, alongside the team at ASI, was truly commendable. When you moved back to the US, you translated your knowledge effectively, and I see the results reflected in my TPX3CAM publications.

Dear **Dimitris**, working closely with you and the entire Fasmatech team on the conceptualization, ion-optics design, construction, and preliminary testing of the Orbitrap-TOF instrument has been an absolute joy. The early days of my Ph.D., with frequent visits to Athens and your lab, hold cherished memories. Your thorough training in the TOF part was pivotal in propelling me this far in my journey. Each discussion with you has broadened my horizons, and I am grateful for the wealth of knowledge I have gained. I would like to extend my special gratitude to dear **Alex**, **Diamantis**, **John**, and **Christos**, who readily addressed my numerous questions.

Dear **Alexander** and **Albert**, I consider myself incredibly fortunate to have had the opportunity to work with such accomplished and well-respected scientists. Your interest in our TTW project, constant encouragement, and engaging discussions fueled my determination to achieve more and strive for excellence. I am particularly thankful to both of you for being a part of my PhD defense committee, sparing time from your busy schedules. **Alexander**, you have been a true inspiration, solidifying my decision to pursue a career in MS instrumentation. I am well aware of the challenges that I will face, but I am sure that this field is the one that will bring me immense happiness. Dear **Kyle**, I am indebted for being a dependable source of assistance at Thermo, helping me whenever I encountered questions related to the Orbitrap MS and external instrument settings. **Albert**, when I commenced my Ph.D., I had little knowledge of structural proteomics, but your generous support, offering me multiple visits to your lab at Utrecht to explore native MS facility with dear **Sem** and delve into the UVPD experimental setup and MS and MS/MS data acquisition and analysis software with dear **Jeff**, broadened my horizons significantly. **Jeff**, your willingness and patience to answer my endless questions related to UVPD or other MS/MS techniques have been extremely helpful in shaping my understanding of structural proteomics. I will forever be grateful for your assistance, including your visit to Maastricht to help me set up the UVPD. Dear **Arjan**, I appreciate the effort you put into performing experiments on the standard LCT at Utrecht with various proteins and MS settings.

Dear ASI members - **Jingming**, **Jord**, and **Thorbjoern** - working closely with you throughout my Ph.D. was a pleasure. Your expertise in hardware and software development and tailored solutions using TPX-based detection technology have left an indelible mark on my Ph.D. Your contributions have been invaluable, and there is not a single chapter in my thesis without TPX-based detectors.

I would like to extend my gratitude to the rest of my co-authors, including dear **Ronald Buijs** for providing me the details on the electronics design of LCT-TPX system, dear **Jerre** for engaging discussions related to the LCT, and dear **Andrey**, **Dimitry**, and **Dirk** for their contributions in the initial stages of the LCT-TPX project.

To the rest of the NWO TTW 15575 committee members – dear **Kirsten**, **Christophe**, **Garry**, **Filip**, **Bram**, **Erik**, **Hans Brouwer**, **Wilfried**, and **Bastiaan**, our biannual

meetings have been an incredible source of motivation and drive for my Ph.D. Your support, positivity, and enthusiasm about my work have constantly pushed me to achieve more, and I am grateful for that.

Dear **David**, thank you for providing the LCT ion optics model and for the enlightening discussions on "ghost peaks" in LCT. Dear **Samy**, your expertise in Orbitrap MS technical details, protein purification, and MS analysis have been a great help during my initial years of Ph.D. Dear **Maurice Janssen**, meeting you in person at IMSC-2022 was a pleasure, and I am sincerely grateful for your keen interest in my project and the generous time you invested in helping me understand the energetics of photofragments of MMAs.

Dear **Leonor**, you have been an excellent student and working with you was an absolute pleasure. Your dedication and talent have made my life so much easier. I wish you all the best in your pursuit of Masters, and I look forward to the possibility of working with you again in the future.

Throughout my Ph.D., I had the wonderful opportunity to work with external collaborators, where I utilized native MS as a tool to address their relevant biological questions. Some of these collaborations resulted in publications, while others had to be halted due to several reasons. This was a new and exciting experience for me, which helped me in improving my understanding of native MS and MMA structures while introducing me to a vast array of techniques for retrieving molecular structural details of biomolecules. I am deeply grateful to dear **Raimond**, **Peter Peters**, **Carmen López Iglesias**, **Ye**, **Kèvin**, **Hans Duimel**, **Abril**, **Axel**, **Nuria**, **Sneha**, **Lyanne**, **Vanesa**, **Isabelle**, **Miriam**, **Bastian**, **Percy**, **Ikhlas**, **Matt**, **Mangesh**, and **Ashwani** for the valuable discussions, allowing me to be part of your research, and enriching my knowledge.

Dear **Maarten**, your generosity in allowing me to attend your lecture on "Analytical Science and Technology" during my first year was immensely beneficial, considering me coming from a different field. Our conversations over the years have been enlightening, and they significantly contributed in broadening my understanding of biomolecules and analytical techniques. Thank you for serving as the chair of my Ph.D. thesis assessment committee and for making the review process a calming experience. I would like to extend my gratitude to **Prof. dr. Eline Kooi**, **Prof. dr. Anouk Rijs**, and **Dr. Ljiljana Pasa-Tolic** for being part of my assessment committee and dedicating time from your busy schedules to review my Ph.D. thesis.

Dear **Helen**, I am immensely grateful for the countless ways you have supported me since my selection to M4i. Your positive energy, caring nature, and constant help have made my life at M4i much smoother. Dear **Anita** and **Nicole**, I really appreciate the help you have offered during the times when Helen was not available.

Dear **Sef**, I would like to express my gratitude for taking care of the financial aspects of my project and supporting me in various ways. Your quick action in arranging things has been a tremendous help. I still remember how considerate you were when I encountered that accident during my first week at Maastricht. Your kind gesture of connecting me to the Indian community at MERLN when I was missing my culture in the beginning of my Ph.D. meant a lot to me.

A

things. **Romy**, though our time together in the office was limited due to my lab work, your dedication to your research and the way you manage your responsibilities both at work and as a mother of two have left a profound impact on me. **Pien**, when Sylvia left, I was a bit sad, but you turned out to be an amazing office mate and a great friend. Our engaging, nice and fun conversations have made workdays more enjoyable. And, of course, we've managed to accomplish a good amount of work too! **Eva**, even though you come to our office only once a week, our conversations have been uniquely diverse and thought-provoking. Your insights and perspectives have enriched my understanding of several subjects. Dear **Sabine**, though you are not a direct office mate, the proximity of our offices and our shared connection with one of my officemates have brought us closer. I have always enjoyed our chats, especially during the borrels – they have been a lot of fun.

Dear **Jian-Hua**, you have been an amazing friend, and I cannot express enough how much fun and joy you have brought into my life. From countless hours spent together at work to our lunch and dinner gatherings, and fun evenings, every moment has been unforgettable. Your ability to light up any group with just a couple of sentences is truly remarkable. With you, I have never felt insecure or hesitant, and your presence have encouraged me to step out of my comfort zone, allowing me to be my true self. We have never run out of topics for conversation, and sometimes we had to reluctantly end our chats. You have seen my crazy side to some extent and listened to my silly thoughts, and I am grateful for the understanding and laughter we have shared during our time in Maastricht. Even though you are moving to Leiden, I am sure that our friendship will remain strong and enduring.

Dear **Navya**, **Mudita**, and **Sneha**, having fellow Indians like you at M4i has enriched my experience here in ways beyond words. Despite our different perspectives and diverse cultural backgrounds, which is something that was expected considering the rich diversity of India, we have found common interests and a deep understanding of one another. **Navya**, your arrival in the Nanoscopy group brought me immense joy as I finally got connected with someone from Kerala and the warmth of our culture, and speaking Malayalam with you was truly a relief. You have been with me through ups and downs, both in work and personal life, and your presence and advice have been invaluable during difficult times. I will always cherish the unforgettable holidays we spent together in Europe. Thank you for bringing **Rohit** and **Vyshakh** to our trips as well as to our lives. **Mudita**, when you joined our M4i-IMS group, I was thrilled to have another Indian companion. Your vibrant energy and talkative nature never fail to amaze me, leaving me as a listener most of the time when I am with you. You surprised me with the unexpected level of maturity you have shown during our time in Amsterdam (may not be the only time), taking care of all of us without uttering a word. Your constant check-ins, concern, and unwavering support, especially during my illness, evoked feelings of warmth and a sense of being at home. **Sneha**, even though you have been in Maastricht for less than a year, you have already impressed me with how easily you connect and enjoy spending time with new people. You have proven to be a fantastic listener, always there to lend a listening ear and offer encouraging words, making me feel better about most of

A

ACKNOWLEDGEMENTS

my actions and decisions. Your remarkable level of patience and unwavering positive attitude towards life is something that constantly inspires me.

Dear **Pmax**, the moments we shared together, particularly outside of work during food gatherings and fun-filled conversations, have been a blast. Your presence has added so much joy to our outings, and it is a pity that you had to finish your Ph.D. and leave us so soon. Dear **Charles**, my nearest neighbor from work (now that Min has moved), my go-to-person for any housing issues, your noble gesture of dropping me home after late-night gatherings is something I truly appreciate, an act of care that reminds me of my culture. Our chitchats and get-togethers have been so enjoyable. Thanks to both you and **Pmax**, I have learned a lot about French culture from you people, leaving me with a wonderful impression. Dear **Min**, living in the same building as you has been a blessing, especially during times when I was sick or needed assistance with university-related matters and housing issues. Taking care of Yuan and Qiu when you were in Portugal was a new and nice experience for me, which I unexpectedly enjoyed, and it has now made me consider having a cat of my own in the future.

Dear **Darya**, one of the things I truly appreciate about our friendship is our ability to have both fun-filled and lighthearted conversations, as well as serious and deep ones. It is remarkable how well you understand my struggles, as we come from cultures where women face different yet serious challenges. I admire your strength and independence, especially in advocating for the freedom of Iranian women. Dear **Ben**, you have been a supportive and motivating friend, always ready to share valuable insights about research and beyond. Your perspective on academia and industry has been valuable, which helped/will help me make important career decisions. Dear **Britt**, You have been an unwavering source of help, not just for me, but for all of us - your impressive list of co-authored publications stands as a testament to that. Right from the very beginning, you have been there for me, consoling me at the hospital after my accident during my first week here, even when you had to leave to Amsterdam. Your approachability and attentive listening during times of worry was truly comforting.

To rest of my M4i colleagues, dear **Aljoscha** (Thank you for the insightful discussions on TPX detectors), **Amol**, **Andrej**, **Andrew**, **Anton**, **Benjamin** (Thank you for all the help related to the data analysis and interpretation of glycan clusters spectra), **Berta**, **Brenda**, **Bo**, **Bryn** (Thank you for providing me company at lab on the weekends), **Che Yee**, **Chris**, **Edith**, **Eva Cuypers**, **Fabian**, **Fred**, **Florian**, **Isabeau**, **Kasper Krestensen**, **Kasper Krijnen**, **Kim**, **Kimberly**, **Klara**, **Kristel**, **Laura van der Vloet**, **Laura van Hese**, **Layla**, **Lennart**, **Lidia**, **Lieke**, **Lucia**, **Mariya**, **Marta**, **Maxime**, **Michele**, **Michelle**, **Michiel**, **Naomi**, **Paul van Schayck**, **Peilang** (Thank you for providing me the peptide samples), **Philippe Massonnet**, **Pieter Kooijman**, **Roel**, **Rob**, **Saleh**, **Sebastiaan**, **Stephanie**, **Theo**, **Tim** (Thank you for helping with the lipid data analysis), **Tialfi**, **Yuandi** (Thank you for providing me company at work on the weekends), and **Yue** (Thank you for your help with ChimeraX), as well as to non-M4i colleagues, dear **Anne**, **Annet**, **Bas**, **Evi**, **Hanne**, **Hans van Eijk**, **Janine**, **Jean**, **Kees**, **Leanne**, **Lin**, **Mo**, **Philippe Vangrieken**, **Remon**, **Roxanne**, **Sander**, **Steven**, **Veerle**, and **Yan**, and to all other M4i -guests and students, it has been an absolute pleasure getting to know you. Thank you for the delightful conversations, fun times and memorable moments we have shared. **Darya**, **Pieter Kooijman**,

256

Berta, **Bo**, **Che Yee**, **Isabeau**, **Laura van der Vloet, Lidia**, **Maarten**, **Michiel** and **Yuandi**, thank you all for the incredible opportunity to be part of your research projects, and the knowledge and experience I gained from working together with you.

To my beloved Koperwiek family - dear **Maria**, **Yvonne**, **Mary**, **Maaike**, **Aracely**, **Carmen**, **Anabel**, **Inez**, **Alexandra**, and **Constanza**, and to dear **Shan shan**, since the moment I moved to Maastricht, you all welcomed me with open arms to the Netherlands, creating a warm and supportive environment that felt like home. Your genuine curiosity about Indian culture and your eagerness to help me embrace Dutch and European culture truly touched my heart. You have been with me through this Ph.D. journey, understanding my hectic and stressful work schedule and offering unwavering support. The beauty of our relationship lies in the fact that even if we do not talk for a long time, when we reconnect, it feels like we never missed a beat. You all hold a special place in my heart, and I genuinely consider Koperwiek as my second home. Thank you for always being there for me. Dear **Chinnamma Aunty**, **Sona Chechy**, **Swapna Chechy**, **Tom Chettayi**, **Gemy Chettayi**, and the **kids** - being away from my real home and the rest of my family from India was not easy, but you made it more bearable with by frequently connecting with me through visits and calls. Your presence here is a big relief for Pappa and Amma. To dear **Anu Achan**, **Anu Chechy**, **Anitha Chechy**, and the rest of the **Malayali community in Maastricht**, and to dear **Sarfaraz** and **Tulasi**, thank you for making me feel less homesick and for understanding of my hectic work schedule and willingness to accommodate our interactions. To all my dear **friends**, **family**, and **teachers in India**, your continuous support and motivation throughout this journey have been invaluable. Whether it was through phone calls or text messages, you were there whenever I needed help, and you made this experience smoother for me.

Last but certainly not least, my dearest **Pappa**, **Amma**, and **Appoos**, thanking you is the most challenging part of writing this thesis. We, as a family, have always had an unspoken understanding of appreciation, love, care and support that only we can truly comprehend. Yet, I am gonna give it a try to convey how truly grateful I am for everything. When I was so attached to my home country and found comfort in staying and building a career there, you all encouraged and convinced me to pursue a Ph.D. abroad. The unwavering support and flexibility you provided in making my career decisions, a privilege not easily afforded to many from our traditional part of India, have been truly empowering. Your pride and genuine happiness in all my achievements over the years have been a constant source of motivation. Although I can share the moments of happiness with others, you are the ones who hold the perfect key to alleviating the several meltdowns I had experienced during my Ph.D. Talking to you brings a sense of peace and resolution that no one else can provide. Thanks for always being there for me, for being my pillars of strength, and for the immeasurable love, care and support you have given me throughout this journey.

A

CURRICULUM VITAE

Anjusha Mathew was born on the 16th of October, 1994 in Kannur, Kerala, India. She completed her pre-university education in 2012, majoring in Science with a focus on Physics, Chemistry, Mathematics, and Biology, from her home district Wayanad, Kerala. She moved to Thiruvananthapuram, Kerala in the same year to pursue her higher studies. She obtained her Bachelor of Technology degree in Applied Electronics and Instrumentation from the College of Engineering Thiruvananthapuram (CET), University of Kerala in 2016 by securing second rank in the university. During her undergraduate years, she gained her technical skills by working on several projects that focused on developing the basic prototypes of gesture vocalizer, autonomous object tracking system (Bachelor's thesis), etc.

In 2016, she started her Master's at the Indian Institute of Space Science and Technology (IIST), Thiruvananthapuram, with a goal to combine her interest in technology with science. She graduated with a Master of Technology degree in Earth System Sciences in 2018 earning first rank. During her postgraduate studies, she spent two months at the Space Physics Laboratory, Vikram Sarabhai Space Centre (VSSC), Thiruvananthapuram, by developing a fuzzy logic-based PID methodology for parameter control in an aerosol humidograph instrument. Her Master's project focused on the design, development, and preliminary testing of the engineering model of ARIS (Advanced Retarding Potential Analyzer for Ionospheric Studies), which was aimed for the structural and compositional studies of ionosphere. This project provided her the perfect opportunity to combine the instrumentation skills acquired during her Bachelor's into the field of space science, further fueling her desire to pursue a research career in scientific instrumentation. ARIS underwent further development, and was included as one of the payloads of the Indian Space Research Organization (ISRO)'s PSLV C45 PS-4 (2019) and PSLV C55 PS-4 (2023) orbital missions and will be a part of the upcoming Mangalyaan-2 and Shukrayaan-1 missions for the Martian and Venusian ionospheric studies, respectively.

In 2018, she relocated to Maastricht, the Netherlands to pursue her Ph.D. research in analytical instrumentation at the Maastricht MultiModal Molecular Imaging (M4i) Institute in Maastricht University under the supervision of Prof. dr. Ron Heeren and Dr. Shane Ellis. Her doctoral work focused on the technological developments in mass spectrometry (MS) towards unraveling the molecular structure of multiproteoform assemblies (MPCs) by bringing together the aspects of soft-ionization techniques, high-mass analyzers, ion dissociation methods, and

position-sensitive detectors. The results of the research performed during her Ph.D. are presented in this thesis. During this period, she has collaborated with numerous institutes and companies, producing five first-authored and five collaborative papers. Part of her Ph.D. research was presented at national (Physics@veldhoven, CHAINS, NVMS, etc.) and international (iWoRiD, ASMS, IMSC, etc.) conferences.

In 2023, she started as a postdoctoral fellow at M4i Institute, where her research focuses on retrieving the higher-order structural features of MPCs using the MS-based instrument developed during her Ph.D.

A